EFFICIENT AND PHYSICALLY CONSISTENT ELECTROMAGNETIC MACROMODELING OF HIGH-SPEED INTERCONNECTS EXHIBITING GEOMETRIC UNCERTAINTIES

BY

JOON HYUNG CHUNG

DISSERTATION

Submitted in partial fulfillment of the requirements
for the degree of Doctor of Philosophy in Electrical and Computer Engineering
in the Graduate College of the
University of Illinois at Urbana-Champaign, 2012

Urbana, Illinois

Doctoral Committee:

Professor Andreas C. Cangellaris, Chair
Professor Jose E. Schutt-Aine
Professor Jennifer T. Bernhard
Associate Professor Deming Chen

ABSTRACT

We propose new methodologies to improve the current state-of-the-art in macromodeling techniques pertinent to the rational function interpolation of broadband electromagnetic responses of linear, passive, multiport, high-speed interconnect networks.

First, we propose and demonstrate a new methodology that combines the efficiency of low-frequency and high-frequency resistance and inductance extraction for electrically-short interconnects using magneto-quasi-static field solvers with the accuracy of rational function interpolation using the Vector Fitting method to generate accurate SPICE-compatible dispersive macromodels for multiple, coupled wire bonds. Computational efficiency in the development of the macromodel is achieved by limiting the application of the field solver to only low frequencies, at which field penetration inside the wires is accurately resolved with a coarse discretization of the cross section of the wires, and to frequencies high enough that the skin effect is well developed and a surface impedance condition suffices to capture the frequency dependence of the wire resistance and inductance due to the skin effect.

Second, we investigate ways in which the computational cost of enforcing passivity of the generated multiport macromodel can be reduced. More specifically, two strategies were examined. The first one involved transfer function matrix element-by-element passivity assessment and enforcement. The second considered transfer

function matrix bock-wise passivity enforcement. Our investigation of the two strategies and comparison to the full transfer matrix (common pole) passivity enforcement option, helped illustrate advantages and shortcomings of the various options. In summary, the advantage of working with a single set of poles often outweighs the computational savings associated with element-by-element and block-wise fitting for the case of networks with a large number of ports.

Third, we examine ways to improve the quality and physical consistency of the original data while at the same time both pruning them in a manner that preserves the accuracy of the rational fit and reducing the computational cost of the fitting process. Toward this we propose and demonstrate an adaptive sampling Vector Fitting algorithm, which adaptively reduces the number of the original sample data subject to the constraint that the causality of the data is ensured. In addition, in order to reduce the computational cost of the Vector Fitting process, we introduce the Vector Fitting via Repeated Random Sampling (VFRS) algorithm. VFRS achieves significant reduction in the computational cost of the Vector Fitting process by extracting the poles used for the rational fit of the complete set of samples through the rational function fitting of subsets of randomly selected samples.

Finally, a fast methodology is introduced for the assessment of the impact of the electromagnetic loading by adjacent wiring on a high-speed channel, in the presence of uncertainty in the geometry of the wiring layout. This is achieved by employing the mathematical framework of stochastic collocation and parametric macromodeling to provide for a computationally efficient development of a passive, broadband,

stochastic electromagnetic macromodel of the channel over the random space defined by the random variables that define the uncertainty of the routing of the adjacent wiring.

To Jeesuk Kim and my mom

ACKNOWLEDGMENTS

I am greatly indebted to my advisor, Professor Andreas C. Cangellaris, for his support, direction of this work and most of all, his patience and guidance throughout my graduate studies. I also want to thank Qualcomm, Inc., and U.S. Army Resesarch Laboratory for sponsorship of this research. I would like to extend special thanks to Dr. Jerry Aguirre at Kyocera America, Dr. Mehyar Khazei at Qualcomm, Inc., Dr. Myoung Joon Choi, Dr. Jayong Koo, and Vishram Pandit at Intel Corp., for their mentorship and support. I would like to thank the members of my Ph.D committee: Professor Jose Schutt-Aine, Professor Jennifer Bernhard, and Associate Professor Deming Chen for their advice and feedback on this work.

I would like to thank many present and former colleagues in the ECE department that have shaped and influenced my life. I would especially like to thank Dr. In Jae Chung from Apple, Dr. Se-Jung Moon from Intel Corp., and Juan Ochoa for friendship, support and valuable discussions. I would also like to acknowledge and thank many friends from Covenant Fellowship Church for their support and prayers over the years. I especially thank Stanley Wu, Irene Wu, Ben Cheng, Fanny Lee, and Soo Young Kim.

I would like to express my gratitude to my beloved wife Jeesuk for her loving support, patience and companionship, and my son Daniel for being a joy in our lives. I also thank my parents and my brother for their love and faith in me. Finally, I would like to praise and thank God for guiding me and becoming the source of my strength.

TABLE OF CONTENTS

LIST OF TABLES

LIST OF FIGURES

CHAPTER 1

INTRODUCTION

1.1 Background of the High-Speed Interconnect Macromodeling

The rapid growth of very large scale integration (VLSI) technology has continuously challenged the state-of-the-art physical design process of electronic systems, from semiconductor processing, materials, and chip-level design, to interconnect designs that include packaging structures, printed circuit boards, vias, bond wires, ball grid arrays, backplanes, and power/ground planes. As the latest technological trends have evidently pushed toward higher integration of functionality and a reduction of on-chip feature size, often resulting in an integration of 100 billion to 1 trillion transistors per chip mark, the complexity of the interconnect design and density on the package and board level have also increased significantly. In addition, the switching speed of the processors has steadily increased with switching times down to a few tens of picoseconds range and information throughput in the order of several tens of gigabits across different levels of integration [1]-[11].

Two observations are drawn from the technological trends. First, signal integrity and power integrity have become crucial in high-speed, high-performance broadband applications, as the length of interconnects has become a significant fraction of the signal wavelength (greater than one-tenth of the signal wavelength). As the physical extent of the interconnect becomes long enough for information to travel between the driver and receiver circuit, distributed transmission line effects such as signal attenuation, reflection, overshoot, undershoot, ringing, crosstalk, and

radiation become too dominant to ignore. Thus, the interconnects can no longer be approximated by the lumped circuits, as the distributed electromagnetic interference of the system, if not well-designed, can potentially result in logic glitches and distortion of the signal that fail to meet the design specification [1]-[5], [11]. Second, the advances in the semiconductor process, materials, and high-complexity, high-density circuitry necessitate the development of appropriate computer-aided design (CAD) methods to correctly model the electrical behaviors and interactions of the chip and interconnects, accounting for all the electromagnetic phenomena involved. Despite significant research efforts and progress to date, the complexity of appropriate modeling of electromagnetic phenomena in the high-density IC environment has made it very difficult to develop efficient design techniques even for the current state of the art simulation tools.

One of the major bottlenecks occurs because of the difference in how semiconductor devices and circuits and interconnects are modeled. The frequency domain, through the mathematical framework of network analysis, is the most natural way to analyze the electromagnetic attributes of the passive linear interconnect structures. On the other hand, the nonlinear devices are best analyzed in time domain. Popular non-linear solvers such as SPICE [12] have a limited set of models for transmission lines and, in general, no high-frequency behavior of many of the interconnect structures present in a packaged electronic system. Therefore, a simultaneous frequency/time-domain co-simulation of the chip and interconnects is needed to accurately capture distributed electromagnetic effects in the integrated system.

Another major bottleneck occurs due to the direct consequence of the mixed-domain co-simulation. Many efforts to address the incompatibility of distributed electromagnetic models of high-speed interconnect with SPICE have led to the development of field-centric approaches [1],

using methods such as FDTD, TLM, and time-domain finite element methods to rigorously solve the electromagnetic field quantities of the interconnects during the numerical integration in time and updating the voltages and currents of the drivers and receivers in sync with the field quantities. The frequency-domain simulation of large interconnects involves several LU decomposition algorithms and forward-backward substitution at each frequency point, and the time-domain simulations use trapezoidal rule to solve a non-linear set of difference equations at each time point with Newton iteration and several LU decompositions [13]. Therefore, the mixed-domain solvers required to model the electromagnetic effects are in general computationally expensive for component simulation and even prohibitive for a complicated system-level simulation composed of multiple blocks of interconnect components with drivers and receivers.

The aforementioned considerations make evident the need for an alternative approach to alleviate the major difficulties of mixed-domain simulation. In many applications, we see that understanding the macroscopic behavior of the components and the overall system, namely the input and the output behavior of the individual interconnect block and ICs, is sufficient, while no information from the internal component may be available. More specifically, in the case of interconnect structures, network theory analysis in which the admittance, impedance, and scattering matrix are used to describe the broadband electromagnetic behavior of the multiport interconnects, provides for an abstraction of the physical structure in terms of a relationship between input and output quantities at the ports. The frequency-dependent matrix is obtained either from analytical and numerical solutions from computational modeling or from measurements. In this approach, electromagnetic modeling becomes a preprocessing step to the time-domain simulation. The frequency-dependent matrix available at a set of discrete frequency

bandwidths of interests is either utilized in the time-domain simulation by applying inverse Fourier transform together with recursive convolution [14], or represented as a rational transfer function of frequency by applying least squares interpolation-based techniques [15]–[36] and converted as SPICE compatible equivalent circuit netlist [82],[83]. By approximating the frequency-dependent or time-dependent system response data, this new approximated model replaces the original infinite-order system by a smaller-order model with similar input and output relationship. The model then can be used to generate spectra and waveforms for signal or power integrity analysis, or the model is coupled with other circuit model blocks for global simulation. Furthermore, post-processing techniques can be applied to enforce or improve the simulation performance.

The main advantage of this approach is that it represents component-level behavior of the input and output ports, while providing the most compact mathematical formulation by reducing the number of equations involved, thereby improving CPU time. The output interconnect model of the proposed approach is highly modular. These interconnect models may be used and combined in sub-circuit format and are compatible with presently popular CAD tools such as SPICE [13]. Therefore, the integration of the frequency/time domain with many different component models becomes accessible and easy to implement. This approach is called macromodeling, and the development of efficient high-speed interconnect macromodeling techniques is the main focus of this dissertation.

Within the macromodeling community in the past ten years, many critical issues have been raised by the industry, which has spent significant time and effort to advance the macromodeling high-speed passive interconnects [37]–[39]. The first issue is in obtaining an accurate representation of the original frequency interpolated data of the high-speed passive model.

Accurate behavioral modeling of high-speed interconnects was hampered because of the numerical ill-conditioning of the rational function fitting due to the broadband nature of high-speed interconnects. Attempts to improve the numerical conditioning resulted in efforts that use linear frequency scaling [19],[23], orthogonal polynomials [20],[24], a combination of low-pass, band-pass, and high-pass filters [18], and other system identification techniques [17]. However, these methods are still unsuitable for an accurate modeling of the frequency response of the complex broadband system or a broadband measurement data set that includes the noise in non-rational form. In 1999, an iterative linear least-squares approximation method called Vector Fitting (VF) [21] was introduced by Gustavsen. It has gained wide popularity as a means to generate rational function interpolation of broadband responses of high-speed interconnects and package electromagnetic models. The major advantage of the VF algorithm is its robustness in iteratively effectively replacing an initial guess of the poles of the system with an improved set of poles. The accuracy of the VF method has improved over the years through several advances, including improving the pole relocating properties [25],[26] by introducing orthonormal basis functions [28] for all sets of poles; including iterative weighting functions [19],[33],[34] to the least squares fitting process; and introducing possibilities in sampled frequency data partitioning and fitting techniques [18],[19],[93],[94].

The second issue is the numerical cost and the robustness of the macromodeling of the high-speed passive structures. This second issue cannot be separated from the first, as efficiency of modeling necessitates accuracy of modeling. A vast improvement over the original VF algorithm in terms of its computational inefficiency when applied to the macromodeling of multi-port interconnect systems resulted from reducing the calculation of residues during the iterative pole calculation process [27]. With the large set of port models, element-by-element

fitting as well as block-wise fitting [32] have been introduced to reduce the computational time and improve the efficiency of the fitting. Partitioning [93],[94] has also been explored not only as a way to increase the accuracy of the fitting, but also to increase computational efficiency. For a structure with many ports with oversampled data, many adaptive sampling algorithms [84]-[90] have been introduced to further reduce the computation cost while maintaining the accuracy of the fitting.

The third issue is ensuring the physical consistency of the macromodel [40]-[46], thus ensuring its realness, stability, causality and passivity. These constraints are crucial barometers to check the theoretical consistency of our numerically approximated model. A violation of any of the four constraints would result in an erroneous and non-physical macromodel [40]. The standard VF algorithm resolves realness by utilizing complex-conjugate pole pairs [21], and achieves stability by flipping the unstable poles [21]. However, VF does not have internal algorithms to correct causality or passivity violation in the original data. Many efficient passivity [53]-[70] and causality correction [75]-[81] algorithms have been developed as post-processing correction steps to fix the passivity and causality violation that leads to unstable time-domain simulation. These post-processing steps ensure physical consistency of the macromodel.

The fourth issue is the development of a reliable stochastic/parametric macromodel [101]-[127]. Variability in several subdomains of the system, including geometric information such as layout, width, length of the wiring and electrical and material properties of the interconnect design are common during the manufacturing or early design stage. Needless to say, correct assessment of the system response in the presence of uncertainty or variability is a critical step in assuring a successful design as well as providing reliable design guidelines for future products. Standard Monte Carlo method and Design of Experiment (DoE) [101] are among the popular

techniques in statistical analysis to account for variability in critical design parameters. Despite their popularity, the slow convergence of the Monte Carlo [108],[109] method and excessive computation time of DoE [99] when dealing with high-dimensional random spaces call for a more efficient stochastic macromodeling technique. Recently, there has been a heavy focus on developing efficient stochastic modeling of high-speed interconnects using polynomial chaos [103]-[110], stochastic collocation [111],[112], and combination of both methods [117],[118] for low- to high-dimensional systems. In addition to the advances in stochastic modeling, another significant research effort has been devoted to developing an accurate and efficient parameterized macromodel that parameterizes poles, residues, state space or descriptor representation of the macromodel [119]-[127]. This parameterized modeling technique also needs to guarantee the physical consistency of the parameterized model, such as stability and passivity, over the parameterized domains [119]-[122].

The fifth and final important issue in macromodeling is to ensure the compatibility of the macromodel with circuit analysis and simulation tools. The model should be available for use as either pole-residue, pole-zero, or state space form for simultaneous time integration through efficient recursive convolution [80] and modified nodal analysis [81] with linear and nonlinear IO devices, or as an equivalent SPICE circuit netlist [82],[83] for co-simulation with other nonlinear models in CAD software such as HSPICE, or in Verilog-A description for high-level mixed-domain simulation.

1.2 Research Objectives and Contributions

Despite progress to date in broadband macromodeling of high-speed interconnects, several issues and challenges remain where new ideas and advances are needed. Some of them have been addressed as part of the research pursuits documented in this dissertation.

First, a methodology that combines a field-solver with rational function approximation technique to efficiently and accurately model electrically small dispersive multi-port interconnect structure was developed [51]. The fast field solver of [47] is used to obtain the low- and high-frequency behavior of the impedance matrix representation of the structure, and VF is used as an interpolator to interpolate accurately the mid-frequency behavior band by exploiting the electrically small nature of the structure. Of specific interest are bond wires, flip-chip and ball grid array interconnects, where the electrical length is small and thus an electrical model in terms of frequency-dependent inductance and resistance matrices and a capacitance matrix are appropriate. A magneto-quasistatic field solver is used to capture the frequency-dependence of the elements of the resistance and inductance matrices. However, the significant cost involved with the extraction by the field-solver due to discretization of the interior of the interconnect structure proves that this is not an attractive approach. The proposed method resolves this problem by relying on the use of a surface impedance boundary condition on the conductor at a high-frequency regime where the skin depth is much smaller than the cross-sectional dimensions of the structure to avoid discretizing the interior, and utilizing rational function approximation (VF) to interpolate the per-unit-length impedance matrix over the intermediate frequency band regime, while relying on extracted per-unit-length resistance and inductance matrices from a low- and high-frequency regime. Multiple coupled bond wires are used as examples to demonstrate the efficiency of the methodology compared to conventional method.

Second, a passivity assessment and enforcement technique of the ***S***-parameter tabulated data is investigated for three different fitting approaches, namely, common-pole fitting, element-by-element fitting, and block-wise fitting of multi ***S***-parameter tabulated data. This study is motivated by the fact that the conventional approach of passivity assessment and enforcement of

the multi-port interconnect structure is carried out through only common-pole rational function approximation and is often combined with model-order reduction for a large-order structure. Though passivity enforcement using common-pole fitting may be effective for small to mid-range multi-port data structures, it may not be feasible for over-determined, large-order sets of tabulated data. Rather, block-wise and element-by-element fitting in conjunction with the block-wise and element-by-element passivity enforcement techniques may effectively reduce memory requirements and/or the computational cost of generating the macromodel. First, the cost of these three fitting methods is considered in the context of both sparse VF setting [23] and fast VF [27] setting. Then, the cost of the three fitting methods with passivity assessment and passivity enforcement via iterative perturbation approach [63] is examined.

Third, two different methodologies for the systematic and accuracy-preserving reduction of large sets of broadband measured or calculated interconnects data are presented. Many algorithms are available to reduce large sets of sampled data [84]-[95]. One of the methods we propose is unique in the sense that it adaptively reduces and reuses some of its frequency samples and the corresponding $\boldsymbol{S}$ parameter data [88]. It adopts an adaptive sampling approach by initially using lowest, highest, and midpoint frequency samples, generating the associated causal and stable transfer functions, and then selecting additional frequency points between the used adjacent frequency samples in a manner that ensures improvement in fitting accuracy. The second approach not only reduces the computational time and the memory requirements but also improves the overall accuracy of the fitting by a random generation of the oversampled original data with a choice of the number of frequency samples per set and the number of random generation sets [95]. Once randomly generated samples of the original data are fitted with a rational function approximation algorithm such as VF, all the corresponding poles of each

random generation set are accumulated to fit the original response. The benefit of this approach is its computational efficiency in fitting broadband multi-port systems. Unlike conventional macromodeling techniques, which require the model to be fit exactly with poles that correctly represent the original poles of the model, this technique does not depend on accuracy of the fit for each randomly chosen set. Rather, the proposed methodology depends on sufficient number of generated sets with random number of samples.

Finally, an efficient stochastic macromodeling technique [113] is introduced for the fast assessment of the impact of electromagnetic loading by surrounding wiring on the transmission properties of a high-speed channel. This methodology makes use of standard macromodeling technique for incorporating the uncertain geometrical and layout surrounding parameters in the vicinity of the channel, in the frequency-dependent macromodel of the high-speed channel. For the case where the adjacent topography can be described in terms of a few random variables, stochastic collocation techniques on multi-dimensional tensor grids are used to generate the macromodel. This method is investigated with several interconnects examples, and the advantage of this method over Monte Carlo method is discussed in the context of these example studies.

1.3 Organization of the Dissertation

This document is organized as follows. In Chapter 2, a survey of macromodeling algorithms in the context of the development of the VF algorithm over the past decade is presented. Included in the discussion are the mathematical requirements pertinent to the physical consistency of the macromodel, namely of realness, stability, passivity, and causality of the transfer function of the linear, passive system.

Chapter 3 presents the fast methodology for the extraction of frequency-dependent per-unit-length resistance and inductance matrices for multiconductor interconnects over a broad frequency range, from dc to multi-GHz frequencies.

Chapter 4 introduces element-by-element and block-wise passivity assessment and enforcement algorithms via an iterative residue perturbation method for tabulated $\boldsymbol{S}$ parameter data.

Chapter 5 introduces a robust technique to reduce large sets of densely distributed frequency samples of tabulated multiport passive $\boldsymbol{S}$ –parameter matrix data, while preserving the causality of the original dense model.

Chapter 6 introduces a new methodology for vector fitting, called VF via Repeated Random Sampling (VFRS). This technique is proposed as yet another possible approach for reducing the computation time associated with rational function fitting of large data sets. The performance of the proposed approach is assessed through comparisons to standard VF and other cost-reduction rational function techniques.

Chapter 7 introduces a fast stochastic macromodeling technique of a high-speed interconnect channel in the presence of electromagnetic loading by neighborhood wiring that lacks specificity in its routing and topography for it to be described in a deterministic fashion. Example studies are presented to validate the proposed approach and examine its attributes in the context of early-stage noise aware interconnect design.

The dissertation concludes with a summary of the main contributions and ideas for future work in Chapter 8.

CHAPTER 2

BACKGROUND

2.1 Introduction

A macromodel of a high-speed interconnect in frequency domain is a system identification or approximation process that represents the I/O response of the data in a simplified mathematical format using suitable basis functions. Since it is common for the I/O transfer function of a high-speed interconnect multiport to be represented in terms of its scattering (***S***), admittance (***Y***), or impedance (***Z***) matrix in frequency domain, the macromodel concerns extraction of the appropriate response of our transfer function that contains many resonances in terms of its poles and residues. Rational function interpolation [15]-[36], in which the basis functions are defined as a quotient of polynomials, is the most popular approach for macromodeling of a linear, passive and time-invarient system and devices in frequency domain.

Care must be taken to preserve the numerical accuracy of the modeled data, so that the macromodel can capture the response of the broadband system appropriately. This becomes a challenging task for broadband data with rich resonant behavior over a wide frequency band. Accuracy in the development of the macromodel is important for correct time and frequency-domain simulation. Needless to say, macromodeling of the original high-speed interconnect system becomes a wasted effort if the physical consistency of the model is not guaranteed. Therefore, the fundamental properties of realness, stability, causality, and passivity [39]-[46] of the system have to be assured in order for our macromodel to be physically consistent. There are studies [40],[43] that prove that passivity is the strongest requirement to guarantee the physical

consistency of a given model, since passivity implies causality, stability, and unitary boundedness. The passivity constraint, which can be violated due to measurement errors or numerical errors, can be restored by several efficient techniques to enforce a self-consistent model of the original data in our macromodeling process.

In addition to the physical consistency of the macromodel, accurate estimation of the frequency bandwidth over which the macromodel should be accurate becomes necessary in order to ensure the accuracy of time-domain simulation. The most straightforward approach to handle the tabulated data for transient analysis is to use an inverse Fourier transform (IFFT) on the frequency data to obtain its time-domain counterpart and convolve with the terminations and sources in time domain. Convolution-based approaches, while straightforward, have several disadvantages [75]. The number of time samples required for a desired level of accuracy is high, thus making a convolution-based approach a computationally expensive approach for a multiport broadband macromodel. Also, much care needs to be given to avoid aliasing in IFFT [14]. In addition, extrapolation and low-pass filtering of the frequency-domain data to reduce the time-domain ripple associated with IFFT often results in causality violation, which results in physically inconsistent model [14]. The second and more efficient and popular approach to model the frequency-domain data is via rational function approximation [15]-[36]. This approach is robust and computationally efficient enough to handle multiport data in comparison to the convolution-based approach, and avoids all the difficulties pertinent to the previous approach, as long as the physical consistency of the rational function approximation is preserved.

Several challenges existed in the past to guarantee a numerically reliable macromodel of the tabulated data via rational function approximation. The first issue had to do with the fact that tabulated data was modeled in a least-squares sense, as its nonlinear cost function had to be

minimized. Several techniques such as Kalman [24] and Levi [15] were used to solve a linear variation of the nonlinear cost-function. However, these approaches have convergence problems, and it has been shown that an iterative least-squares technique such as Sanathanan-Koerner [16] gave a much improved fitting over the aforementioned approaches for high-order systems. The second issue was the appropriate choice of the optimal basis functions which has significant impact on the numerical accuracy of the macromodel. The traditional way of solving a least squares problem was to calculate the coefficients of the macromodel by solving Vandermonde-like equations [17]. The problem with this approach was that the numerical conditioning of the fitting deteriorated quickly with a high-order and broadband system. To improve the numerical conditioning, several families of orthogonal polynomials such as Chebyshev polynomials of first and second kind [20], and Clenshaw and Lancos-based orthogonal basis [24] were proposed. Even though these basis functions provided improvement in fitting accuracy, several problems such as ill-conditioning and lack of computational efficiency still hampered the accuracy of the complex broadband interconnect model.

In 1999, Gustavsen introduced vector fitting (VF) [21], a robust and efficient iterative linear least-squares technique that significantly improved some of the previously mentioned ill-conditioning of the broadband data approximation evident with a Vandermonde-like matrix. Using a pole relocation technique, VF identifies and improves the fitting iteratively by replacing the previous real or complex conjugate poles with an improved set of poles. Since 1999, VF has become a standard in macromodeling many applications, such as packages, transmission lines, and power cables. Also, many techniques have been combined with the VF algorithm to handle a more complex broadband system with better accuracy and computational efficiency.

In this chapter, the fundamental properties of stability, causality, and passivity and their relations to building a physically consistent macromodel are reviewed, along with a discussion of the VF algorithm. Then, three different rational function fitting techniques, namely, common-pole fitting, element-by-element fitting, and block-wise fitting, are discussed. The computational cost of each method will be compared with the sparse vector fitting and fast vector fitting tools.

2.2 Requirements of Physically Consistent Macromodeling

The system that we characterize is a linear, time-invariant electrical *N* port network, which has $(N/2 \times 1)$ input vector $\boldsymbol{x}(t)$ and $(N/2 \times 1)$ output vector $\boldsymbol{y}(t)$. In time domain, the response at the i^{th} port of output vector $\boldsymbol{y}(t)$ due to the input vector $\boldsymbol{x}_j(t)$ at the j^{th} port is given by the convolution, where $\boldsymbol{h}_{ij}(t)$ is the ijth element of the impulse transfer matrix.

$$\boldsymbol{y_i}(t) = \boldsymbol{h}_{ij}(t) * \boldsymbol{x}_j(t) = \int_{-\infty}^{+\infty} \boldsymbol{h_{ij}}(t-\tau)\, \boldsymbol{x_j}(\tau) d\tau \tag{2.1}$$

The time domain of the *N* port I/O system is properly represented in Laplace domain by using bilateral Laplace transform as the following Equation (2.2), where $s = \sigma + j\omega \, \epsilon \, ROC$ (region of convergence). The unilateral Laplace transform neglects any part of the signal for $t < 0$, making it impossible to assess conditions for a causal system. Thus, it is necessary to extend the time integration to $-\infty$.

$$\boldsymbol{Y}(s) = \boldsymbol{H}(s)\boldsymbol{X}(s), \quad \boldsymbol{H}(s) = \int_{-\infty}^{+\infty} \boldsymbol{h}(t)\, e^{-\boldsymbol{st}} dt \tag{2.2}$$

The equivalent representation in Fourier domain is restricted to the imaginary axis $s = j\omega$ only, when the integral of the Fourier transform in (2.3) converges. We review the concept of stability, causality, and passivity in both time and frequency domain.

$$\boldsymbol{Y}(j\omega) = \boldsymbol{H}(j\omega)\boldsymbol{X}(j\omega), \quad \boldsymbol{H}(j\omega) = \int_{-\infty}^{+\infty} \boldsymbol{h}(t)\, e^{-j\omega \boldsymbol{t}} dt \tag{2.3}$$

2.2.1 Stability

The stability of the system is guaranteed when the output of the system is bounded for all bounded input [14]. From the several definitions of stability, the well-known bounded-input bounded-output (BIBO) stability is adopted for our purposes in the time domain for the LTI system.

$$\int_{-\infty}^{+\infty} \left| h_{ij}(t) \right| dt < +\infty \tag{2.4}$$

In frequency domain, two conditions of Laplace transform have to be satisfied to meet the stability of the system. First, the *ROC* of its transfer matrix $\boldsymbol{H}(s)$ has to include the imaginary axis. Second, $\boldsymbol{H}(\infty)$ has to be bounded. Both conditions entail a practical rule of the stable system with its poles having a negative real part.

2.2.2 Causality

An LTI system is causal if and only if all the elements $h_{ij}(t)$ of its impulse matrix $\boldsymbol{h}(t)$ are zero for t <0. This concept shows that the effect cannot precede the cause. For every input $\boldsymbol{x}(t)$ that vanishes for $t < t_0$, the output $\boldsymbol{y}(t)$ also vanishes for $t < t_0$ [40].

$$\boldsymbol{h}(t) = 0, \quad t < 0 \tag{2.5}$$

We explore the definition of causality in frequency domain through Laplace and Fourier transform, respectively. The causality condition of $\boldsymbol{H}(s)$ in bilateral Laplace transform shows that the following two properties need to be satisfied [41]:

(1) *ROC* is a strip parallel to the imaginary axis, in the complex $s = \sigma + j\omega$ plane. For the system to be causal the function needs to be analytic inside its *ROC* and *ROC* needs to be a half plane open on the right ($Re\{s\} > \sigma_0$).

(2) Each element of the transfer matrix $\boldsymbol{H}(s)$ does not grow faster than a polynomial for $Re\{s\} > \sigma_0$.

In a Fourier domain, the causal impulse matrix response $\boldsymbol{h}(t)$ leads to the following equation [45],[46]:

$$\boldsymbol{H}(j\omega) = \frac{1}{j\pi} pv \int_{-\infty}^{+\infty} \frac{\boldsymbol{H}(j\omega')}{\omega - \omega'} d\omega' \tag{2.6}$$

where the integral converges despite the singularity for $\omega = \omega'$, $\boldsymbol{H}(j\omega) = \boldsymbol{U}(\omega) + j\boldsymbol{V}(\omega)$ and pv is the Cauchy principal value. Each element of transfer matrix $\boldsymbol{H}(j\omega)$ is divided into frequency response of real and imaginary parts that are dependent on each other. This interdependency between the real and imaginary values is known as Kramers-Krönig relations, and constitutes a necessary and sufficient condition for causality.

$$\begin{aligned} \boldsymbol{U}(\omega) &= \frac{1}{\pi} pv \int_{-\infty}^{+\infty} \frac{\boldsymbol{V}(j\omega')}{\omega - \omega'} d\omega' \\ \boldsymbol{V}(\omega) &= \frac{1}{\pi} pv \int_{-\infty}^{+\infty} \frac{\boldsymbol{U}(j\omega')}{\omega - \omega'} d\omega' \end{aligned} \tag{2.7}$$

2.2.3 Passivity

The original definition of passivity of a physical system is related to a system unable to generate energy. For an *N*-port network scattering parameter representation in time domain, the instantaneous power is given by the expression in (2.8), where $\boldsymbol{a}(\tau)$ and $\boldsymbol{b}(\tau)$ are incident and reflected waves at the ports [43].

$$\int_{-\infty}^{t} \boldsymbol{a}^{\boldsymbol{T}}(\tau)\boldsymbol{a}(\tau) - \boldsymbol{b}^{\boldsymbol{T}}(\tau)\boldsymbol{b}(\tau)\, d\tau \geq 0 \tag{2.8}$$

Equation (2.8) is satisfied, and the system is causal, if the system absorbs more energy than it generates, and generation of the energy occurs after absorption for all *t* in a system. This equation shows that a non-causal system that first generates energy and then absorbs it is strictly considered as a passivity violated system [46]. Therefore, all passive LTI systems are also

causal. The passivity condition of the scattering matrix $\boldsymbol{S}(s)$ in the frequency domain is satisfied if and only if all the following three conditions are fulfilled [40].

(1) Each element of $\boldsymbol{S}(j\omega)$ is analytic in $\Re e(s) > 0$, and the dispersion relations in (2.7) hold.
(2) $\boldsymbol{I} - \boldsymbol{S}^{\boldsymbol{H}}(j\omega)\boldsymbol{S}(j\omega)$ is a nonnegative-definite matrix for all s such that $\Re e(s) > 0$.
(3) $\boldsymbol{S}(-j\omega) = \boldsymbol{S}^{*}(j\omega)$.

The first condition shows that dispersion relations in frequency domain have to be fulfilled to guarantee causality which is a pre-requisite for passivity. The second condition shows the unitary boundedness of the scattering representation to control passivity of the system behavior where $\Re e(s) > 0$. The third condition, where '$*$' denotes complex conjugation, is a sufficient and necessary condition to guarantee $S_{ij}(t)$ real in time domain. A rational and analytic system $\boldsymbol{S}(s)$ in $\Re e(s) > 0$ automatically satisfies causality, thereby only requiring the second and third conditions for the system to be passive.

2.3 Vector Fitting

Vector Fitting (VF) is one of the most robust and efficient rational function interpolation techniques, based on a reformulation of polynomial based Sanathanan-Koerner [16] iteration. The major advantage of VF is its formulation of the rational approximation process, cast in terms of iterative relocation of the poles. A set of rational functions (partial fraction) are used as its basis function instead of set of polynomial basis functions s^n to improve the conditioning of the system. In addition, stability of the poles can be enforced by a pole flipping scheme in VF.

We consider a passive *N*-port transfer matrix $\boldsymbol{H}$(s) in Equation (2.9). Our transfer function is represented as the sum of partial fraction basis functions with real or complex conjugate pairs of residues $c_{p,ij}$, poles a_p and real constant term $H_{\infty,ij}$, where *i,j=1,…N*. The intent of the VF is to

estimate the coefficients of the non-linear equation in (2.9) of the original transfer function over a given frequency interval. We note that the non-linear equation in (2.9) in terms of the unknown poles a_p can be solved sequentially as a linear equation in the following three steps.

$$\{\boldsymbol{H}(\boldsymbol{s})\}_{ij} = \sum_{p=1}^{N}\left(\frac{c_{p,ij}}{s-a_p}\right) + H_{\infty,ij} \tag{2.9}$$

The first step concerns the identification of a set of poles of the original non-linear equation as a linear equation in the least squares sense. For this purpose, let us denote a scalar auxiliary function $\sigma(s)$ and our approximated response $(\boldsymbol{\sigma H})(s)$ in (2.10) with a rational function of order *N*, sharing common set of starting poles $\bar{a}_p$.

$$\sigma(s) = \sum_{p=1}^{N}\left(\frac{\tilde{r}_p}{s-\bar{a}_p}\right) + 1$$

$$\left\{\boldsymbol{H}(\boldsymbol{s})_{\boldsymbol{fit}}\right\}_{ij} \approx (\boldsymbol{\sigma H})(s) = \sum_{p=1}^{N}\left(\frac{r_{p,ij}}{s-\bar{a}_p}\right) + d_{ij} \tag{2.10}$$

We select an initial *N* number of poles $\bar{a}_p$ that span the frequency bandwidth uniformly. A typical choice of initial poles $\bar{a}_p$ and $\bar{a}_{p+1}$ for the complex conjugate pair poles is made such that it will have a weak attenuation for all frequency bandwidths of interest in order to avoid ill-conditioning. Equation (2.11) shows the relation between the real and the imaginary parts of a complex pole pair. The parameter *v* is chosen so that the poles are close to the imaginary axis. This number gives a well-conditioned initial basis functions for the entire frequency range of interest.

$$\bar{a}_n = -\bar{\alpha}_n + j\bar{\beta}_n, -\bar{a}_{n+1} = -\bar{\alpha}_n - j\bar{\beta}_n$$

$$\{\bar{\alpha}_n\} = v\{\bar{\beta}_n\} \tag{2.11}$$

Then, the following condition in (2.12) is enforced in a least squares sense by using the available data $\boldsymbol{H}(\boldsymbol{s})$ from s=s_0,…., s_k. Substituting (2.10) into (2.12), the solution becomes an over-determined least-squares linear problem of the system in (2.14). The solutions of linear least squares system in (2.13) provide the residues $\tilde{r}_p$ of the auxiliary function $\sigma(s)$ as well as the residues and constant coefficients of $\{\boldsymbol{H}(\boldsymbol{s})_{\boldsymbol{fit}}\}_{ij}$. The details that define each matrix comprising the over-determined least-squares solution follow in (2.14) ~ (2.17).

$$(\boldsymbol{\sigma H})(s) = \sigma(s)\boldsymbol{H}(s) \tag{2.12}$$

$$\left(\sum_{p=1}^{N}\left(\frac{r_p}{s-\bar{a}_p}\right)+d_{ij}\right)=\left(\sum_{p=1}^{N}\left(\frac{\tilde{r}_p}{s-\bar{a}_p}\right)+1\right)\{\boldsymbol{H}(\boldsymbol{s})\}_{ij} \tag{2.13}$$

$$\mathbf{A}_f \cdot \boldsymbol{u} = \boldsymbol{b}_f \tag{2.14}$$

$$\mathbf{A}_f = \begin{bmatrix} \boldsymbol{X_f} & 0 & 0 & 0 & \boldsymbol{X_{f,1}} \\ 0 & \boldsymbol{X_f} & 0 & 0 & \boldsymbol{X_{f,2}} \\ 0 & 0 & \ddots & 0 & \vdots \\ 0 & 0 & 0 & \boldsymbol{X_f} & \boldsymbol{X_{f,K}} \end{bmatrix}, \mathbf{X}_f = \begin{bmatrix} Re(\mathbf{X'}_f) \\ Im(\mathbf{X'}_f) \end{bmatrix}, \mathbf{X}_{f,k} = \begin{bmatrix} Re(\mathbf{X'}_{f,k}) \\ Im(\mathbf{X'}_{f,k}) \end{bmatrix} \tag{2.15}$$

$$\mathbf{X'}_f = \begin{bmatrix} \frac{1}{s_1-\bar{a}_1} & \cdots & \frac{1}{s_1-\bar{a}_N} & 1 \\ \vdots & \ddots & \vdots & \vdots \\ \frac{1}{s_{M_f}-\bar{a}_1} & \cdots & \frac{1}{s_{M_f}-\bar{a}_N} & 1 \end{bmatrix}, \mathbf{X'}_{f,k} = \begin{bmatrix} \frac{-\boldsymbol{H}_k(s_1)}{s_1-\bar{a}_1} & \cdots & \frac{-\boldsymbol{H}_k(s_1)}{s_1-\bar{a}_N} \\ \vdots & \ddots & \vdots \\ \frac{-\boldsymbol{H}_k(s_{M_f})}{s_{M_f}-\bar{a}_1} & \cdots & \frac{-\boldsymbol{H}_k(s_{M_f})}{s_{M_f}-\bar{a}_N} \end{bmatrix} \tag{2.16}$$

$$\boldsymbol{u} = [\boldsymbol{u}_1^T \ \ldots \ \boldsymbol{u}_k^T \ \tilde{\boldsymbol{u}}^T]^T, \ \boldsymbol{u_k} = \left[\boldsymbol{r}_{1,k} \ \ldots \ \boldsymbol{r}_{N,k} \ d_k\right]^T, \ \tilde{\boldsymbol{u}} = [\tilde{\boldsymbol{r}}_{1,k} \ \ldots \ \tilde{\boldsymbol{r}}_{N,k}]^{\boldsymbol{T}}$$

$$\boldsymbol{b}_f = \left[\boldsymbol{b}_{f,1}^T \ \ldots \ \boldsymbol{b}_{f,k}^T \ \right]^T, \qquad \boldsymbol{b}_{f,k} = \left[\boldsymbol{H}_k(s_1) \ldots \boldsymbol{H}_k\left(s_{N_s}\right)\right]^{\boldsymbol{T}}$$

$$\boldsymbol{H}_k(s) = \begin{bmatrix} Re(\boldsymbol{H}_k(s)) \\ Im(\boldsymbol{H}_k(s)) \end{bmatrix}, \text{ k=}\textit{1, 2,..., K.} \tag{2.17}$$

For an N_p-port system with M_f frequency samples and N common poles, K numbers of elements [$K = (N_p)^2$] of transfer functions $\boldsymbol{H}(s)$ are separated by real and imaginary vector and stacked into a single column vector $\boldsymbol{b_f}$. $\boldsymbol{A_f}$ is a sparse matrix that contains K by $K+1$ numbers of block $\boldsymbol{X}$, where the size of the individual block matrix is denoted by $2M_f$ *by N+1*. This formulations result in a large sparse matrix [23] with the size *2(*M_f *K) by [(N+1)K +* N *]*. The size of the sparse matrix often becomes a problem for estimating multiport passive networks due to the memory constraint and computation time needed to solve the matrix. With initial guess of the poles, N number of residues of the auxiliary function need to be calculated. To preserve the real coefficients of the transfer function, a linear combination of $\phi_P(s)$ and $\phi_{P+1}(s)$ has to be formed to make the poles and residues complex conjugate pairs, where $-a_{p+1} = -a_p^*$ and $-r_{p+1} = -r_p^*$. Thus, a linear combination of two modified basis functions $\phi_p(s)$ and $\phi_{p+1}(s)$ is shown as below in (2.18) followed by the least-squares formulation $\boldsymbol{Ax} = \boldsymbol{b}$ in (2.19).

$$\Phi_p(s) = \frac{1}{s-\bar{a}_p} + \frac{1}{s-\bar{a}_{p+1}}, \qquad \Phi_{p+1}(s) = \frac{j}{s-\bar{a}_p} - \frac{j}{s-\bar{a}_{p+1}} \tag{2.18}$$

$$A = \begin{bmatrix} \Phi_1(s_1) & \Phi_2(s_1) & \cdots & \Phi_{p-1}(s_1) & \Phi_p(s_1) & 1 & s_1 & -f(s_1)\Phi_1(s_1) & -f(s_1)\Phi_2(s_1) & \cdots & -f(s_1)\Phi_{p-1}(s_1) & -f(s_1)\Phi_p(s_1) \\ \Phi_1(s_2) & \Phi_2(s_2) & \cdots & \Phi_{p-1}(s_2) & \Phi_p(s_2) & 1 & s_2 & -f(s_2)\Phi_1(s_2) & -f(s_2)\Phi_2(s_2) & \cdots & -f(s_2)\Phi_{p-1}(s_2) & -f(s_2)\Phi_p(s_2) \\ \vdots & \vdots & \ddots & \vdots & \vdots & \vdots & \vdots & \vdots & \vdots & \ddots & \vdots & \vdots \\ \Phi_1(s_k) & \Phi_2(s_k) & \cdots & \Phi_{p-1}(s_k) & \Phi_p(s_k) & 1 & s_k & -f(s_k)\Phi_1(s_k) & -f(s_k)\Phi_2(s_k) & \cdots & -f(s_k)\Phi_{p-1}(s_k) & -f(s_k)\Phi_p(s_k) \end{bmatrix}$$

$$\boldsymbol{x} = \left[\Re e(c_1)\ \Im m(c_1) \ldots \Re e(c_p)\ \Im m(c_p) \quad d \quad \Re e(\tilde{c}_1)\ \Im m(\tilde{c}_1) \ldots \Re e(\tilde{c}_p)\ \Im m(\tilde{c}_p)\right]^T$$

$$\boldsymbol{b} = [H(s_1)\ H(s_2) \ldots\ H(s_k)]^T$$

$$\begin{bmatrix} \Re e(\boldsymbol{A}) \\ \Im m(\boldsymbol{A}) \end{bmatrix} \boldsymbol{x} = \begin{bmatrix} \Re e(\boldsymbol{b}) \\ \Im m(\boldsymbol{b}) \end{bmatrix} \tag{2.19}$$

The second step of VF determines the relocated poles of the system during SK iterations. We call this step a pole-relocation step. The system augmented as the rational functions with N number of predefined initial poles in (2.10) is reformulated as the following pole-zero representation.

$$(\boldsymbol{\sigma H})(s) = \sum_{p=1}^{P}\left(\frac{r_p^{(t)}}{s-\bar{a}_p}\right) + d_{ij} = \frac{\prod_{p=1}^{P-1}\left(s-z_{p,n}^{(t)}\right)}{\prod_{p=1}^{P}(s-\bar{a}_p)} \tag{2.20a}$$

$$\sigma(s) = \sum_{p=1}^{P}\left(\frac{\tilde{r}_p^{(t)}}{s-\bar{a}_p}\right) + 1 = \frac{\prod_{p=1}^{P}\left(s-z_{p,d}^{(t)}\right)}{\prod_{p=1}^{P}(s-\bar{a}_p)} \tag{2.20b}$$

After the two equations of $(\boldsymbol{\sigma H})(s)$ and $\sigma(s)$ in (2.20) are parameterized, the common poles, $\bar{a}_p$, are cancelled out and $\boldsymbol{H}(s)$ can be calculated as the fraction of the zeros of two functions. Thus, the zeros of the initial scaling function $\sigma(s)$ become the new common poles $\bar{a}_p$ of the transfer matrix $\boldsymbol{H}(s)$ in its first SK iteration step. In each iteration step, respective zeros of the scaling function in the previous steps are used as the relocated, improved set of poles of the subsequent steps. This relationship between the poles and the zeros is shown in Equation (2.21). Finally, zeros of $\sigma(s)$ are easily computed by solving the eigenvalues of the matrix $\boldsymbol{K}$ in (2.22), where

$$\boldsymbol{H}(s) = \frac{\boldsymbol{\sigma}(s)\boldsymbol{H}(s)}{\boldsymbol{\sigma}(s)} = \frac{\prod_{p=1}^{P-1}\left(s-z_{p,n}^{(t)}\right)/\prod_{p=1}^{P}(s-a_p)}{\prod_{p=1}^{P}\left(s-z_{p,d}^{(t)}\right)/\prod_{p=1}^{P}(s-a_p)} = \frac{\prod_{p=1}^{P-1}\left(s-z_{p,n}^{(t)}\right)}{\prod_{p=1}^{P}\left(s-z_{p,d}^{(t)}\right)} \tag{2.21}$$

$$\boldsymbol{K} = (\boldsymbol{A} - \boldsymbol{B}\overline{\boldsymbol{C}}^{\boldsymbol{T}}) \tag{2.22}$$

$\boldsymbol{A}$ is a diagonal matrix that contains the poles on each iteration step, $\boldsymbol{B}$ is a column vector of ones and $\overline{\boldsymbol{C}}^{\boldsymbol{T}}$ is a row-vector containing the residues of $\sigma(s)$. The minimal state space representation of the pole-residue model $\sigma(s)$ is given in (2.23).

$$s\boldsymbol{I}\boldsymbol{X}(s) = \boldsymbol{A}\boldsymbol{X}(s) + \boldsymbol{B}\boldsymbol{U}(s)$$

$$\boldsymbol{Y}(s) = \boldsymbol{C}\boldsymbol{X}(s) + \boldsymbol{D}\boldsymbol{U}(s) \tag{2.23}$$

If a_p and a_{p+1} are complex conjugate pairs, the above state space representation of the linear combination is converted into a real-only model, given as

$$\widehat{\boldsymbol{A}} = \begin{bmatrix} \Re e(-\boldsymbol{a_p}) & \Im m(-\boldsymbol{a_p}) \\ -\Im m(-\boldsymbol{a_p}) & \Re e(-\boldsymbol{a_p}) \end{bmatrix}, \widehat{\boldsymbol{B}} = \begin{bmatrix} 2 \\ 0 \end{bmatrix}, \widehat{\boldsymbol{C}} = [\Re e(\tilde{r}_p) \quad \Im m(\tilde{r}_p)] \, , \widehat{\boldsymbol{D}} = 0. \tag{2.24}$$

Note that iterations to find the optimum relocated poles are stopped when the desired accuracy of the least squares solution is reached. Typically, 3 to 5 iterations are enough to reach convergence if we are given enough poles.

The final step of VF, after N_{iter} number of SK iteration steps and identifying the number and the location of the poles that preserves the accuracy of the fit, concerns the calculation of the residues of $\boldsymbol{H}(s)$ in (2.9)**.** This again gives the over-determined linear least squares problem of the form $\boldsymbol{Ax} = \boldsymbol{b}$ and completes the VF process.

2.4 Common-Pole, Element-by-Element and Block-wise Fitting

In this section, we compare the size of the matrix and the computational cost of our interpolated model on VF solution based on common-pole fitting, element-by-element fitting and block-wise fitting of a stable, linear time-invariant, but possibly non-passive *N*-port system represented as an ***S***-parameter rational function approximated matrix, ***S***(s). An element-by-element fitting allows different sets of poles for each element in the matrix to be fitted. Block-wise fitting, which is similar to element-by-element fitting, allows different sets of poles for each block (group of elements) in the matrix to be fitted. The first comparison will be made in the sparse matrix solver used in sparse VF [23], followed by the second comparison using the QR decomposition used in fast VF [27]. These comparisons will provide a guideline to what fitting

techniques will be the most numerically efficient approaches for rational interpolation of a broadband electromagnetic multi-port system.

2.4.1 Comparison of three VF fitting strategies in sparse matrix VF solver

Let us recall a stable, linear time-invariant *N*-port **S** parameter matrix $\boldsymbol{S}(\mathrm{s})$**,** mathematically represented in pole-residue form in (2.25a), where N_p denotes the order of common pole, and $r_{m,ij}$ and q_m denote residue and common-pole matrices. Equation (2.25b) shows the elements of $\boldsymbol{S}(\mathrm{s})$ in terms of element-by-element approximation, where {i,j} denote row and column of an element, N_{ij} denote the order of the element {i,j} of element-by-element fitting, $r_{m,ij}$, $q_{m,ij}$ are m^{th} residues and poles of element {i,j}, and d_{ij} is a constant generated by rational function fit. Equation (2.25c) shows a rational function approximation for block-wise fitting, where it combines characteristics of both common-pole fitting and element-by-element fitting. This has similarities with the column-wise fitting [23],[32], such that groups of elements are fitted separately with different poles with respect to the rational function approximation, $\boldsymbol{S_{fit}}(\mathrm{s})$. However, unlike column-wise fitting, this approach offers the advantage that choosing groups that share common poles is not limited to columns of $\boldsymbol{S_{fit}}(\mathrm{s})$ only, but is extended to any elements in $\boldsymbol{S_{fit}}(\mathrm{s})$. Equation (2.25c) shows *k* number of groups fitted with common poles, where each group contains respective number of elements {i,j} of $\boldsymbol{S_{fit}}(\mathrm{s})$.

$$\left\{\boldsymbol{S_{fit}}(\mathrm{s})\right\}_{\mathrm{ij}} = \sum_{\mathrm{m}=1}^{\mathrm{N_p}} \frac{\mathbf{r_{m,ij}}}{\mathrm{s}-\mathbf{q_m}} + \mathbf{d}_{\mathrm{ij}} \tag{2.25a}$$

$$\left\{\boldsymbol{S_{fit}}(\mathrm{s})\right\}_{\mathrm{ij}} = \sum_{\mathrm{m}=1}^{\mathrm{N_{ij}}} \frac{\mathbf{r_{m,ij}}}{\mathrm{s}-\mathbf{q_{m,ij}}} + \mathbf{d}_{\mathrm{ij}} \tag{2.25b}$$

$$\left\{\boldsymbol{S_{fit}}(\mathrm{s})\right\}_{\mathrm{k}} = \sum_{\mathrm{m}=1}^{\mathrm{N_{p,k}}} \frac{\mathbf{r_m}}{\mathrm{s}-\mathbf{q_m}} + \mathbf{d}_{\mathrm{k}} \ , \ \boldsymbol{S_{fit}}(\mathrm{s}) = \{\boldsymbol{S_{fit}}(\mathrm{s})_1, \ldots \boldsymbol{S_{fit}}(\mathrm{s})_{\mathrm{k}}\} \tag{2.25c}$$

The least square formulation of the *N* port system, represented by its rational function $\boldsymbol{H}(\mathrm{s})$, where the residues, poles, and constants are denoted by $\{\boldsymbol{r}_{m,ij}\}$, $\{\boldsymbol{q}_{m,ij}\}$, and $\{\boldsymbol{d}_{ij}\}$, is based on

Equations (2.14) to (2.19). A closer look at (2.14) and the matrix $\mathbf{A}_f$ suggests that it is in a block triangular form. The matrix $\mathbf{A}_f$ is sparse, but each block of $\mathbf{X}_f$ and $\mathbf{X}_{f,k}$ is dense. The least squares problem is over-determined, and all the blocks are rectangular. Each component vector $\boldsymbol{u}_k^T$ of scalar vector $\boldsymbol{u}$ is composed of residues and constants of each element. Next, recognizing the fact that VF is an iterative three-step process, we make an estimate of the memory storage and computation time for each VF step. For common-pole matrix fitting with M_f samples, K elements, and N poles for a passive N_p port system, the following three-step operation of the least-squares fitting designated as (2.14) is carried out.

1) The first process involves calculation of common poles for sparse VF. First, the coefficient of the scaling function $\boldsymbol{\sigma}(\mathrm{s})$ is calculated by solving the least squares matrix $\boldsymbol{A}_f \cdot \boldsymbol{u} = \boldsymbol{b}_f$ in (2.14), where $\boldsymbol{A}_f$ is a sparse matrix of dimension $(2M_fK) \times ((N+1)K + N)$, and K is ${N_p}^2$. If we account for N_{iter} number of iterations, the computation time of solving $\mathbf{A}_f$ is proportional to $O\big((2M_fK) \times ((N+1)K + N))\big) \times N_{iter}$. For the purpose of comparing different fitting strategies, we call this process step 1.
2) Second, new common poles (zeros) for the scaling function $\boldsymbol{\sigma}(\mathrm{s})$ are calculated by calculating the eigenvalues of a matrix of dimension $(N \times N)$ (e.g. $\{q_m\} = eig(\boldsymbol{A}\text{-}\boldsymbol{b}\tilde{d}^{-1}\tilde{\boldsymbol{r}}^T)$). If we are to account for N_{iter} number of iterations, the calculation of the computation time is proportional to $O\,(N \times N) \times N_{iter}$. This step is called step 2.
3) The second process involves calculation of residues with the new poles by solving the least squares matrix $\boldsymbol{A}_f \cdot \boldsymbol{u} = \boldsymbol{b}_f$, where $\boldsymbol{A}_f$ has dimension $(2M_fK) \times \big((N+1)K\big)$ and the computation time proportional to $O\big((2M_fK) \times ((N+1)K)\big) \times N_{iter}$. This process is called step 3.

For element-by-element fitting with M_f samples, K elements, and N_k poles and N_{iter} number of iterations for a passive N_p port system, sparse matrix of the least squares fitting in (2.14) is no longer needed as each element can be cast into the least squares fitting in the form (2.26), which requires the following three-step operation:

$$\boldsymbol{A}_{f,k} \cdot \boldsymbol{u}_k = \boldsymbol{b}_{f,k} \tag{2.26}$$

$$\boldsymbol{A}_f = \left[\boldsymbol{X}_f \;\; \boldsymbol{X}_{f,k}\right], \mathbf{X}_f = \begin{bmatrix} Re(\boldsymbol{X'}_f) \\ Im(\boldsymbol{X'}_f) \end{bmatrix}, \mathbf{X}_{f,k} = \begin{bmatrix} Re(\boldsymbol{X'}_{f,k}) \\ Im(\boldsymbol{X'}_{f,k}) \end{bmatrix}$$

$$\mathbf{X'}_f = \begin{bmatrix} \frac{1}{s_1 - q_{1,k}} & \cdots & \frac{1}{s_1 - q_{N_k,k}} & 1 \\ \vdots & \ddots & \vdots & \vdots \\ \frac{1}{s_{M_f} - q_{1,k}} & \cdots & \frac{1}{s_{M_f} - q_{N_k,k}} & 1 \end{bmatrix}, \quad \mathbf{X'}_{f,k} = \begin{bmatrix} \frac{-\boldsymbol{H}_k(s_1)}{s_1 - q_{1,k}} & \cdots & \frac{-\boldsymbol{H}_k(s_1)}{s_1 - q_{N_k,k}} \\ \vdots & \ddots & \vdots \\ \frac{-\boldsymbol{H}_k(s_{M_f})}{s_{M_f} - q_{1,k}} & \cdots & \frac{-\boldsymbol{H}_k(s_{M_f})}{s_{M_f} - q_{N_k,k}} \end{bmatrix}$$

$$\boldsymbol{u} = \left[\boldsymbol{r}_{1,k} \; \ldots \; \boldsymbol{r}_{N_k,k} \; d_k \; \tilde{\boldsymbol{r}}_{1,k} \; \ldots \; \tilde{\boldsymbol{r}}_{N_k,k}\right]^{\boldsymbol{T}}, \qquad \boldsymbol{b}_{f,k} = \left[\boldsymbol{H}_k(s_1) \ldots \boldsymbol{H}_k\left(s_{M_f}\right)\right]^{\boldsymbol{T}},$$

$$\boldsymbol{H}_k(s) = \begin{bmatrix} Re(\boldsymbol{H}_k(s)) \\ Im(\boldsymbol{H}_k(s)) \end{bmatrix}, k=1, 2, \ldots, K. \tag{2.27}$$

1) First, the coefficient of the scaling function $\boldsymbol{\sigma}(\mathrm{s})$ is calculated by solving the least squares matrix $\boldsymbol{A}_f \cdot \boldsymbol{u} = \boldsymbol{b}_f$ in (2.14), where $\boldsymbol{A}_f$ is a dense matrix of dimension $(2M_f) \times (2N_k + 1)$. Since we fit *K* elements individually, if we account for N_{iter} number of iterations, calculation of computation time of $\boldsymbol{A}_f$ is proportional to $\sum_{k=1}^{K} O\big((2M_f) \times (2N_k + 1)\big) \times N_{iter}$.
2) Second, new element-by-element poles (zeros) for the scaling function $\boldsymbol{\sigma}(\mathrm{s})$ are calculated by calculating the eigenvalues of a matrix of dimension $(N_k \times N_k)$ (e.g. $\{q_m\} = eig(\boldsymbol{A}\text{-}\boldsymbol{b}\tilde{d}^{-1}\tilde{\boldsymbol{r}}^T)$). If we are to account for *K* elements and N_{iter} number of iterations, calculation of computation time is proportional to $\sum_{k=1}^{K} O\big((N_k \times N_k)\big) \times N_{iter}$.
3) The second process involves calculation of residues with the new poles by solving the least squares matrix $\boldsymbol{A}_f \cdot \boldsymbol{u} = \boldsymbol{b}_f$, where $\boldsymbol{A}_f$ has dimension $(2M_f) \times (N_k + 1)$ and the computational time proportional to $\sum_{k=1}^{K} O\left((2M_f) \times (N_k + 1)\right) \times N_{iter}$.

For block-wise fitting with M_f samples, *K* elements, *M* number of blocks of common poles, T_i number of elements for each block *i*, where $\sum_{i=1}^{M} T_i = K$, N_{T_i} common poles for a block of T_i elements, and N_{iter} number of iterations for a passive N_p port system, the common-pole least squares fitting in (2.14) and the element-by-element least squares fitting in (2.26) are combined

to form block-wise fitting. Block-wise sparse matrix VF also requires three successive steps which follow the procedure below.

1) First, the coefficients of the scaling function $\boldsymbol{\sigma}(s)$ are calculated by solving the least squares matrix $\boldsymbol{A}_f \cdot \boldsymbol{u} = \boldsymbol{b}_f$ in (4.5), where $\boldsymbol{A}_f$ is reduced matrix of dimension $(2M_f T_i) \times \left(\left(N_{T_i}+1\right)T_i + N_{T_i}\right)$. Since we fit M blocks of common poles, if we account for N_{iter} number of iterations, the computation time of $\boldsymbol{A}_f$ is proportional to $\sum_{i=1}^{M} O\left(\left((2M_f T_i) \times \left(\left(N_{T_i}+1\right)T_i + N_{T_i}\right)\right)\right) \times N_{iter}$.
2) Second, the new poles (zeros) for the scaling function $\boldsymbol{\sigma}(s)$ are calculated by calculating the eigenvalues of a matrix of dimension $(N_{T_i} \times N_{T_i})$ (e.g. $\{q_m\} = eig(\boldsymbol{A}\text{-}\boldsymbol{b}\tilde{d}^{-1}\tilde{\boldsymbol{r}}^T)$). If we are to account for K elements and N_{iter} number of iterations, calculation of computation time is proportional to $\sum_{i=1}^{M} O(N_{T_i} \times N_{T_i}) \times N_{iter}$.
3) The third process involves calculation of residues with the new poles by solving the least squares matrix $\boldsymbol{A}_f \cdot \boldsymbol{u} = \boldsymbol{b}_f$ where $\boldsymbol{A}_f$ has dimension $(2M_f T_i) \times \left(\left(N_{T_i}+1\right)T_i\right)$ and has computational time proportional to $\sum_{i=1}^{M} O((2M_f T_i) \times \left(N_{T_i}+1\right)T_i) \times N_{iter}$.

We first compare the maximum storage requirement of $\boldsymbol{A}_f$ for all three fitting techniques for the sparse matrix VF setting. For the sake of generality, if we assign equal number of poles N for all three fitting techniques, the maximum storage requirement based on common-pole fitting is K times greater than element-by-element fitting and roughly K/T_i times greater than block-wise fitting. Therefore, in terms of memory and storage requirements, element-by-element and block-wise fitting is considered a better option than the common-pole fitting. Table 2.1 summarizes the maximum storages of common-pole, element-by-element, and block-wise fitting for sparse VF that require M_f frequency samples, N common poles, K number of elements, N_{iter} number of

iterations, N_k element-by-element poles, and N_{T_i} block-wise poles for M groups of each having T_i elements.

Next, the operation time at each step for the common-pole, element-by-element, and block-wise fitting is examined. For an *m* by *n* matrix $\boldsymbol{A}_f$, the "\" operator in Matlab solves the least squares solution by using the householder method that requires about $2mn^2 - 2n^3/3$ flops [96]. If $\boldsymbol{A}_f$ is a $2M_f$ by *2N* matrix (separating real and imaginary components), the calculation of the coefficients of the scaling function $\boldsymbol{\sigma}(\mathrm{s})$ requires about $16M_fN^2 - 16N^3/3$ flops. On the other hand, the eigenvalue calculation of an $N \times N$ matrix via Hessenberg reduction and QR iteration requires about $10N^3$ flops [96]. Since $M_f \gg N$ in general, calculation of the coefficient of the scaling function $\boldsymbol{\sigma}(\mathrm{s})$ is the most time-consuming part of the sparse VF process. Table 2.2 summarizes the flops counts of common-pole, element-by-element, and block-wise sparse VF of a system that require M_f frequency samples, *N* common poles, *K* number of elements, N_{iter} number of iterations, N_k element-by-element poles for *K* elements, N_{T_i}common poles for a group composed of T_i elements. In general, fewer than 5 iterations are needed (N_{iter}) for the VF process. For sparse VF of an over-determined system with samples M_f much greater than N, step 1 is the dominant process, followed by steps 3 and 2. Estimation of the computation time of step 1 is roughly $\big((N+1)K+N\big)/\big((N+1)K\big)\big)^2$ times step 3, and roughly $2M_fK^2/N$ times step 2. Since step 1 is dominant, we consider the overall computational cost of the sparse VF based on the computation flop count of step 1. As shown in step 1 of Table 2.2, assuming that the number of poles are same for all three strategies, the overall flop count of the element-by-element fitting for all elements is at least 1/*K* times that of common-pole fitting, and is comparable to block-wise fitting. Again, this proves that under the sparse VF of a multiport system, element-by-

element and block-wise fitting approaches have computational advantages over common-pole fitting.

Table 2.1: Comparison of the maximum storage size of common-pole, element-by-element and block-wise fitting of sparse VF.

Maximum Storage Size	Step 1	Step 2	Step 3
Common-pole	$(2M_fK) \times ((N+1)K + N)$	$(N \times N)$	$(2M_fK) \times \big((N+1)K\big)$
Element-by-element	$(2M_f) \times (2N_k + 1)$	$(N_k \times N_k)$	$(2M_f) \times (N_k + 1)$
Block-wise	$(2M_fT_i) \times \Big(\big(N_{T_i}+1\big)T_i + N_{T_i}\Big)$	$(N_{T_i} \times N_{T_i})$	$(2M_fT_i) \times \big((N_k+1)T_i\big)$

Table 2.2: Comparison of the computation time (flop count) of common-pole, element-by-element and block-wise fitting of sparse VF.

Computation time (flop count)	Step 1	Step 2	Step 3
Common-pole	$\approx (4M_fK)((N+1)K+N)^2 \times N_{iter}$	$10N^3 \times N_{iter}$	$\approx (4M_fK)((N+1)K)^2 \times N_{iter}$
Element-by-element	$\approx \sum_{k=1}^{K} \big((4M_f)(2N_k+1)^2 \times N_{iter}\big)$	$\sum_{k=1}^{K} 10N_k^3 \times N_{iter}$	$\approx \sum_{k=1}^{K} \big((4M_f)(N_k+1)^2\big) \times N_{iter}$
Block-wise	$\approx \sum_{i=1}^{M} \Big((4M_fT_i)\Big(\big(N_{T_i}+1\big)T_i + N_{T_i}\Big)^2 \times N_{iter}\Big)$	$\sum_{i=1}^{M} 10N_{T_i}^3 \times N_{iter}$	$\approx \sum_{i=1}^{M} \Big((4M_fT_i)\Big(\big(N_{T_i}+1\big)T_i\Big)^2\Big) \times N_{iter}$

2.4.2 Comparison of three VF fitting strategies in fast matrix VF solver

The fast VF technique [27] has replaced sparse VF by introducing QR decomposition to reduce the computational cost. The least squares solution of fast VF is implemented with (2.26)

and (2.27) for pole and residue identification steps, and the system equation $\boldsymbol{A_f \cdot u = b_f}$ is solved via QR decomposition denoted as (2.28a) and (2.28b).

$$\boldsymbol{A_f = QR} \tag{2.28a}$$

$$\boldsymbol{u \cong R \backslash (Q^T b)} \tag{2.28b}$$

As we know, for multi-port systems, the solution of the pole identification step (step1) can be time-consuming and memory-demanding when sparse VF is used. This is true because the matrix computation involved with the matrix size is $(2M_f K) \times ((N+1)K + N)$, where M_f is the total number of the frequency samples, K is the total number of elements, and N is the order of the system, which increases dramatically with the number of elements. This problem is overcome using the fast implementation, which recognizes the fact that we only need to calculate the free variables associated with the scaling function $\boldsymbol{\sigma}(\mathrm{s})$, instead of the whole sparse matrix. The result is a smaller and compact block structure of the system which is formed and solved independently via QR decomposition. This leads to a new system matrix that has as many columns as there are free variables in $\boldsymbol{\sigma}(\mathrm{s})$. As an example, we consider the fitting of four elements. The system matrix for the pole identification step has the form (2.29) and we are only interested in calculation of $\boldsymbol{x_5}$, the variables of residue term in $\boldsymbol{\sigma}(\mathrm{s})$.

$$\begin{bmatrix} \boldsymbol{A} & 0 & 0 & 0 & \boldsymbol{B_1} \\ 0 & \boldsymbol{A} & 0 & 0 & \boldsymbol{B_2} \\ 0 & 0 & \boldsymbol{A} & 0 & \boldsymbol{B_3} \\ 0 & 0 & 0 & \boldsymbol{A} & \boldsymbol{B_4} \end{bmatrix} \begin{bmatrix} \boldsymbol{x_1} \\ \boldsymbol{x_2} \\ \boldsymbol{x_3} \\ \boldsymbol{x_4} \\ \boldsymbol{x_5} \end{bmatrix} = \begin{bmatrix} \boldsymbol{b_1} \\ \boldsymbol{b_2} \\ \boldsymbol{b_3} \\ \boldsymbol{b_4} \\ \boldsymbol{b_5} \end{bmatrix} \tag{2.29}$$

As the first step, we consider the following equation in (2.30), and following QR decomposition in (2.31), where the superscripts 1 and 2 denote upper and lower partition of the vector.

$$\boldsymbol{A_f x} = [\boldsymbol{A} \;\; \boldsymbol{B_1}] \begin{bmatrix} \boldsymbol{x_1} \\ \boldsymbol{x_5} \end{bmatrix} = \boldsymbol{b_1} \tag{2.30}$$

$$\begin{bmatrix} \boldsymbol{R_{11}} & \boldsymbol{R_{12}} \\ \boldsymbol{0} & \boldsymbol{R_{22}} \end{bmatrix} \begin{bmatrix} \boldsymbol{x_1} \\ \boldsymbol{x_5} \end{bmatrix} = \boldsymbol{Q}^T \begin{bmatrix} \boldsymbol{b_1^1} \\ \boldsymbol{b_1^2} \end{bmatrix} = \begin{bmatrix} \boldsymbol{y_1^1} \\ \boldsymbol{y_1^2} \end{bmatrix} \tag{2.31}$$

From (2.31), the following relation $\boldsymbol{R_{22}x_5 = y_1^2}$ is formed, and the same formulation is built for all four elements, which results the equivalent form of (2.32), where the lower partition matrix $\boldsymbol{R_{22}}$ of each element is stacked up. According to the example, we see that both maximum storage size and the computation time in fast VF are significantly reduced due to reduction of the size of the original sparse matrix in standard matrix fitting into reduced dense matrix fitting.

$$\begin{bmatrix} \boldsymbol{R_{22,1}} \\ \boldsymbol{R_{22,2}} \\ \boldsymbol{R_{22,3}} \\ \boldsymbol{R_{22,4}} \end{bmatrix} \boldsymbol{x_5} = \begin{bmatrix} \boldsymbol{y_1^2} \\ \boldsymbol{y_2^2} \\ \boldsymbol{y_3^2} \\ \boldsymbol{y_4^2} \end{bmatrix} \tag{2.32}$$

Equations (2.30) to (2.32) show the three-step process of step 1, which is equivalent to the calculation of coefficient of the scaling function $\boldsymbol{\sigma}(s)$ by solving the least squares matrix $\boldsymbol{A_f \cdot u = b_f}$. The flop count of the process in Matlab is different from sparse VF since QR decomposition is used instead of "\". For a matrix $\mathbf{A}_f$ of size *m* by *n*, QR factorization of (2.30) accounts for $2mn^2$ flops [96]. The next process in (2.31), where we multiply the transpose of Q to b matrix, accounts for *2mn* flops. Finally, (2.32), stacking up *kn/2* by *n/2* reduced $\boldsymbol{R}$ matrix, where *k* is the number of elements and using backward substitution to find the coefficient of $\boldsymbol{\sigma}(s)$, accounts for $kn^2/4$ flops. Since fast VF utilizes each dense and compact block matrix for QR decomposition, instead of the sparse matrix of whole elements, there will be significant reduction of the flop counts. For an *n* by *n* matrix, the eigenvalue calculation of the matrix via Hessenberg reduction and QR iteration requires roughly $10n^3$ flops. The finalized residue of the scaling function in step 3 uses "\" operator which requires $2mn^2$ flops for an *m* by *n* matrix.

Tables 2.3 and 2.4 compare the maximum storage size and the flop counts of steps 1, 2, and 3 for common-pole, element-by-element and block-wise fitting of fast VF. For common-pole fast

VF, M_f samples, K elements, N poles and N_{iter} iterations for a passive N_p-port system are used. For element-by-element fitting, M_f samples, K elements, N_k poles and N_{iter} iterations for a passive N_p-port system are used. Finally, for block-wise fitting, M_f samples, K elements, M number of blocks of common poles, T_i number of elements per block, where $\sum_{i=1}^{M} T_i = K$, N_{T_i} poles for a block of T_i elements, and N_{iter} number of iterations for a passive N_p port system are used.

Table 2.3: Comparison of the maximum storage size of common-pole, element-by-element and block-wise fitting of fast VF.

Maximum Storage Size	Step 1	Step 2	Step 3
Common-pole	$(2M_f) \times (2N + 1)$	$(N \times N)$	$(2M_f) \times (N + 1)$
Element-by-element	$(2M_f) \times (2N_k + 1)$	$(N_k \times N_k)$	$(2M_f) \times (N_k + 1)$
Block-wise	$(2M_f) \times \left(2N_{T_i} + 1\right)$	$(N_{T_i} \times N_{T_i})$	$(2M_f) \times \left(N_{T_i} + 1\right)$

Table 2.4: Comparison of the computation time (flop count) of common-pole, element-by-element and block-wise fitting of fast VF.

Computation time (flop count)	Step 1	Step 2	Step 3
Common-pole	$\approx \left(4M_f(2N + 1)^2\right) \times N_{iter}$	$10N^3 \times N_{iter}$	$\approx \left(4M_f(N + 1)^2\right) \times N_{iter}$
Element-by-element	$\approx \sum_{k=1}^{K} \left(\left(4M_f(2N_k + 1)^2\right) \times N_{iter}\right)$	$\sum_{k=1}^{K} 10N_k^3 \times N_{iter}$	$\approx \sum_{k=1}^{K} \left(4M_f(N_k + 1)^2\right) \times N_{iter}$
Block-wise	$\approx \sum_{i=1}^{M} \left(\left(4M_f\left(2N_{T_i} + 1\right)^2\right) \times N_{iter}\right)$	$\sum_{i=1}^{M} 10N_{T_i}^3 \times N_{iter}$	$\approx \sum_{i=1}^{M} \left(4M_f\left(N_{T_i} + 1\right)^2\right) \times N_{iter}$

CHAPTER 3

A FAST METHODOLOGY FOR THE SYNTHESIS OF MULTI-PORT EQUIVALENT CIRCUIT MODEL FOR MULTICOUPLED BOND WIRES

3.1 Introduction

Accurate prediction of high-frequency effects such as crosstalk and distortions in high-speed interconnects is strongly dependent on the accurate modeling of the frequency-dependent resistance and inductance parameters of interconnects. For multi-port interconnect systems with three-dimensional geometrical information present, a full-wave or quasi-static solver is necessary to accurately capture the high-frequency effects, such as current crowding and proximity effects that will lead to a reliable computation of a frequency-dependent impedance matrix. Fast Henry [47] is one of the more popular methods for the solution of the magneto-quasistatic integral equation to compute frequency-dependent inductance and resistance matrices for coupled interconnects. Once the frequency-dependent impedance matrices are accurately extracted at a set of frequencies over the bandwidth of interest, vector fitting (VF) [21],[25],[27] may be used to generate rational function approximations to the frequency-dependent per-unit-length impedance matrix of a multi-conductor interconnect [48],[49].

Due to their electrically small lengths, the electrical modeling of interconnects for signal and power integrity analysis is customarily done making use of three-dimensional capacitance, resistance, and inductance extractors. Such an approach has been shown to lead to accurate models up to frequencies at which the wire electrical length (length in wavelengths) remains below 0.25. For such ***RLC*** modeling, the primary cost of the development of the equivalent circuit is associated with the calculation of the frequency-dependent resistance and inductance matrices. In particular, in order to capture accurately the frequency dependence of these matrices, the field solver used must comprehend accurately the field penetration inside the wires. Irrespective of the type of solver used (integral equation based or finite element based), the two frequency regimes at which resistance and inductance extraction is the fastest are: a) frequencies low enough for the skin depth in the metallization to be comparable to or larger than the wire cross-sectional dimensions, and b) frequencies high enough for the skin depth to be much smaller than the cross-sectional dimensions of the wire. For the former, a coarse discretization of the wires suffices for accurate resistance and inductance extraction while, for the latter, use of a surface impedance boundary condition eliminates the need for discretizing the interior of the wires. This observation motivates the possibility of relying on extracted values for $\boldsymbol{R}(\omega)$ and $\boldsymbol{L}(\omega)$ obtained only at these two frequency regimes to describe the dispersive properties of the synthesized circuit over the entire frequency bandwidth of interest. More specifically, the proposed approach is to use extracted values of $\boldsymbol{R}(\omega)$ and $\boldsymbol{L}(\omega)$ obtained at these two frequency regimes in a VF-based rational interpolation to approximate $\boldsymbol{R}(\omega)$ and $\boldsymbol{L}(\omega)$ of the electrically short interconnects over the entire frequency bandwidth. The feasibility of such an approach is examined in this chapter.

3.2 A Fast Methodology of Multi-port Modeling of Bond Wires with Frequency-Dependent Losses

Figure 3.1 (a) depicts a representative geometry of a group of bond wires. Quasi-static, integral equation-based solvers are used for the extraction of the capacitance, inductance, and resistance matrices of the coupled bond wires. For the case of the magneto-quasi-static problem that is solved for the calculation of the inductance and resistance matrices, we distinguish between two frequency regimes: a) a low-frequency regime that extends over the range of frequencies for which skin depth is larger or at the order of the wire diameter, and b) a high-frequency regime that encompasses the range of frequencies for which the skin depth is a small fraction of the wire diameter. In the low-frequency regime, use of a filament discretization of the wires for the discretization of the volumetric current density $\mathbf{j}$ in the wires is economical. The pertinent magneto-quasi-static integral equation is in (3.1) [50].

$$\frac{\mathbf{j}(\mathbf{r})}{\sigma} + \frac{j\omega\mu}{4\pi}\int_V \frac{\mathbf{j}(\mathbf{r}')}{|\mathbf{r}-\mathbf{r}'|}dv' = -\nabla\Phi, \quad \mathbf{r}\in V \tag{3.1}$$

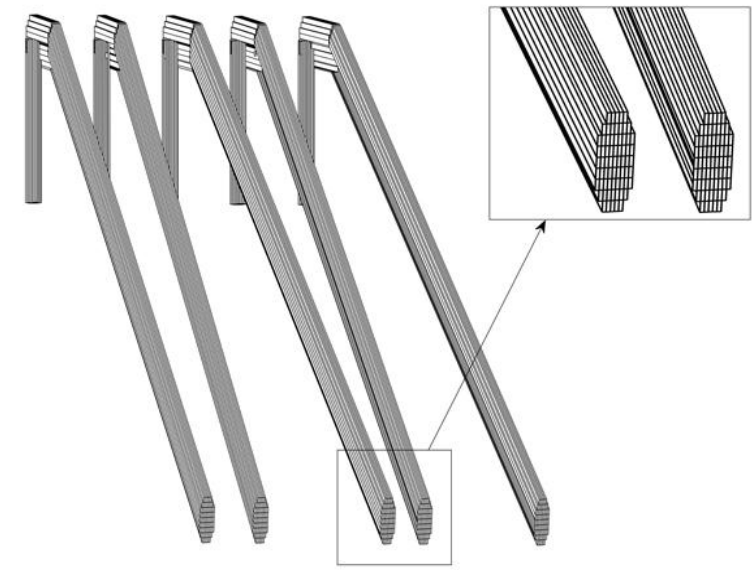

(a)

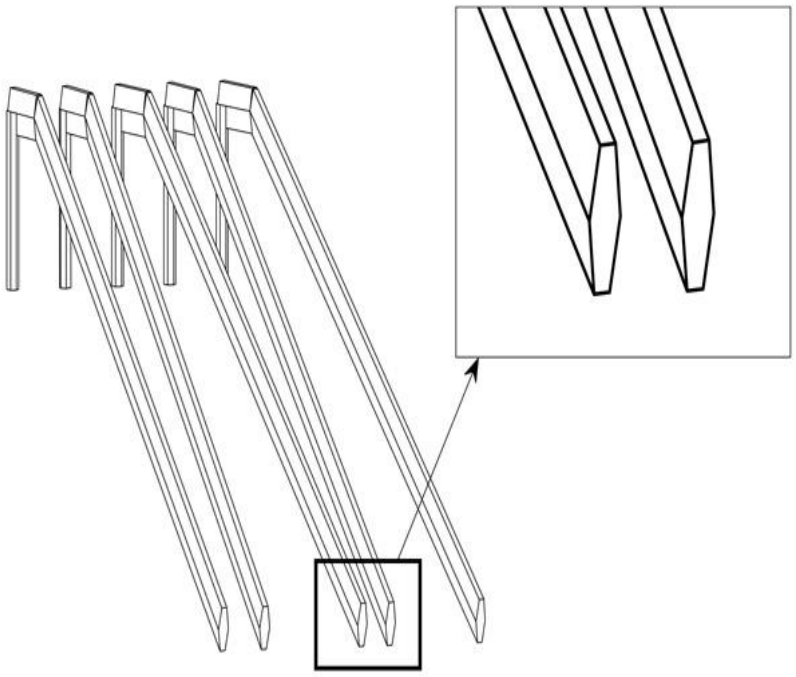

(b)

Figure 3.1: Geometry and discretization of the bond wires. (a) Volumetric discretization of the wires at low frequency regime and (b) discretization of the wires using Leontovich's surface impedance boundary at high frequency regime.

Through a standard Galerkin process the discrete form of (3.1) leads to a matrix equation of the form (3.2), where $i, j = 1, ..., N$, and δ_{ij} is the Kronecker's delta and N is the number of filaments.

$$[R]_{ij} = \frac{l_i \delta_{ij}}{\sigma a_i}, \; [L]_{ij} = \frac{j\omega\mu}{4\pi V_j} \int_{V_j} \frac{\mathbf{l}_i \cdot \mathbf{l}_j}{|\mathbf{r}_i^c - \mathbf{r}'|} dv', \; [V]_i = \Phi(\mathbf{r}_i^a) - \Phi(\mathbf{r}_i^b),$$

$$([R] + j\omega[L])[I] = [V] \tag{3.2}$$

The quantity $[V]_i$ denotes the difference of the nodal potentials at the end points of the ith filament. Augmenting the above linear systems with the discrete form of the charge conservation equation, $\nabla \cdot \mathbf{j} = 0$, enforced at each one of the n nodes formed by the junction of different conductor segments, closes the system for the calculation of the N filament currents and the n nodal potentials [47].

In the high-frequency regime, if the wires are discretized volumetrically according to skin-depth, the model may result in a matrix equation of a very large dimension. To circumvent this problem at the frequencies when the skin-depth is substantially smaller than cross-sectional dimensions of the wires, one can reduce the volumetric integral equation (3.1) to its surface counterpart with the use of an appropriate impedance boundary condition,

$$Z_s \mathbf{J}(\mathbf{r}) + \frac{j\omega\mu}{4\pi} \int_S \frac{\mathbf{J}(\mathbf{r}')}{|\mathbf{r} - \mathbf{r}'|} ds' = -\nabla\Phi, \quad \mathbf{r} \in S, \tag{3.3}$$

where $Z_s = (1+i)\sqrt{\omega\mu_0 / (2\sigma)}$ is the Leontovich's surface impedance [50]. This integral equation can be discretized using the boundary element method of moments. As depicted in Fig. 3.1 (b), confinement of the unknown functions to the surfaces of the wires results in a matrix equation of substantially smaller size, thus allowing for expedient extraction of the ***R*** and ***L*** parameters at high frequencies.

For the case of the capacitance extraction, the integral equation of electrostatics with respect to the unknown charge density is given as (3.4), where $q(\boldsymbol{r}) = \sum_{j=1}^{N} Q_j / a_j$ and a_j is the cross-sectional area of j th filament. This integral equation is reduced to a matrix form $\left[\bar{C}\right]\cdot\left[Q\right]=\left[\Phi\right]$ with delta-function at the centroid $\mathbf{r}_i^c$ of the i th surface element, where capacitance and the nodal voltage matrices are defined as (3.5).

$$\frac{1}{4\pi\varepsilon_0}\int_S \frac{q(\mathbf{r}')}{|\mathbf{r}-\mathbf{r}'|}ds' = \Phi(\mathbf{r}), \quad \mathbf{r}\in S \tag{3.4}$$

$$\left[\bar{C}\right]_{ij} = \frac{1}{4\pi\varepsilon_0}\sum_{j=1}^{N}\frac{Q_j}{a_j}\int_{S_j}\frac{1}{|\mathbf{r}_i^c-\mathbf{r}'|}ds', \quad \left[\Phi\right]_i = \Phi(\mathbf{r}_i^c), \ i, j = 1,\ldots, N \tag{3.5}$$

The extracted values of $\boldsymbol{R}(\omega)$ and $\boldsymbol{L}(\omega)$ at the low- and high-frequency regimes are used as input to a rational function-fitting algorithm [21] to yield a rational function interpolation over the bandwidth of interest, including the intermediate frequency band over which $\boldsymbol{R}(\omega)$ and $\boldsymbol{L}(\omega)$ were not computed through the solution of the magneto-quasi-static equation. More specifically, since the diagonal elements of the impedance matrix for the coupled bond wires exhibit the strongest dependence with frequency, rational function interpolations are generated for these terms in the form of [48],[49],

$$Z_{kk}(s) = R_{kk}(s) + sL_{kk}(s) = R_0^{(kk)} + sL_0^{(kk)} + \sum_{m=1}^{Q_1} R_m^{(kk)}\left(s - P_m\right)^{-1} \tag{3.6}$$

where $s = j\omega$. VF simultaneously fits all elements in $\boldsymbol{Z}(s)$ and makes no assumptions about the frequency dependence of the elements due to the generality of the form (3.6). Because the frequency variation of the elements in the impedance matrix is smooth, it required VF about 1 ~ 5 real poles to fit the element impedance. An equivalent circuit representation of (3.6) - depicted in Figure 3.2 by each branch formed by the series connection of a resistor, an inductor and Q_1

$R\|L$ circuits - follows immediately from (3.6) by noting that it can be recast in the following form:

$$Z_{kk}(s) = \bar{R}_0^{(kk)} + sL_0 + \sum_{m=1}^{Q_1} \bar{R}_m^{(k)} s(s - P_m)^{-1} \tag{3.7}$$

$$\bar{R}_0^{(kk)} = R_0^{(kk)} - \sum_{m=1}^{Q_1} \left(\frac{R_m^{(kk)}}{P_m}\right), \bar{R}_m^{(kk)} = \frac{R_m^{(kk)}}{P_m}, \bar{L}_m^{(kk)} = \frac{-R_m^{(kk)}}{P_m^2} \tag{3.8}$$

In the above equations, expressions for the elements of the equivalent circuit in terms of the terms in the rational function interpolation in (3.6) are provided. As far as the mutual impedances are concerned, the values computed at the highest frequency of interest are used for the definition of the equivalent circuit. These then, together with the extracted terminal capacitances, are used to complete the multi-port, equivalent circuit for the coupled bond wires depicted in Figure 3.2.

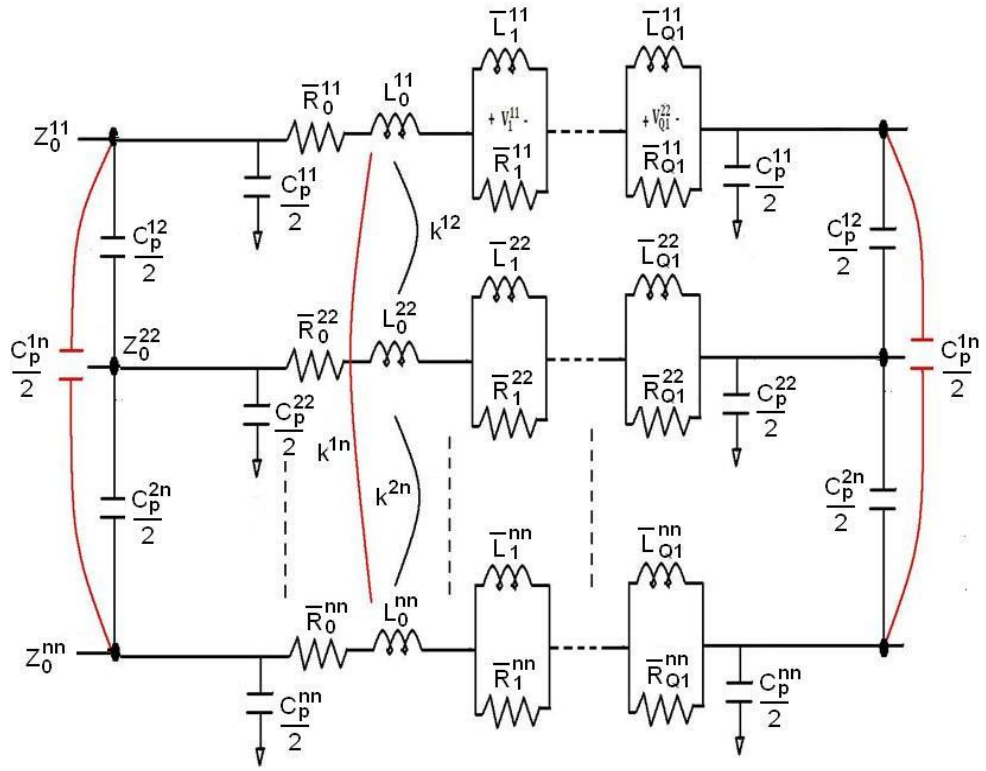

Figure 3.2: Equivalent circuit representation of n coupled bond wires.

3.3 Validation Studies

To demonstrate the effectiveness of the proposed methodology, three distinct examples of multiport bond wires with increasing complexity are tested. Two methodologies are compared. First, computation time of the standard technique (RLCG3D) that uses 3-D magneto-quasistatic integral equation-based ***RLC*** extractor and subsequent rational function fitting synthesis to generate SPICE-equivalent netlist is compared with the proposed fast methodology that utilizes effective discretization of the low-frequency regime and surface impedance boundary condition of the high-frequency regime with ensuing interpolation of the mid-band frequency regime by VF algorithm. Second, the accuracy of the proposed methodology will be tested through comparisons of the transient responses of signal propagation through the interconnects using the aforementioned two models.

3.3.1 Four coupled Cu bond wires

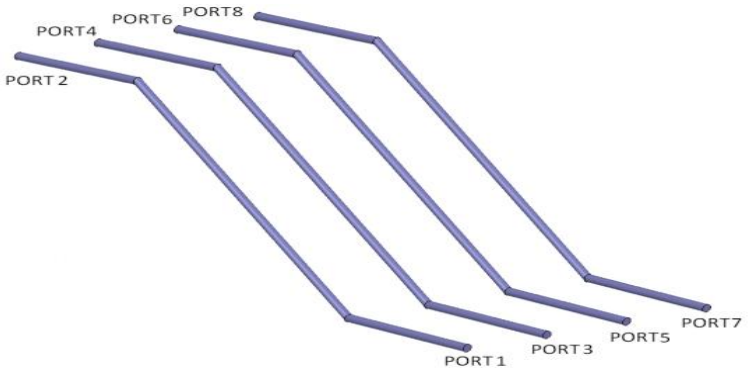

Figure 3.3: An eight-port circuit involving four coupled Cu bond wires.

The first numerical example concerns the geometry of four coupled Cu bond wires depicted in Figure 3.3. The wire radius is 10^{-2} mm, each bond wire is 1.1983 mm long, the axis-to-axis distance between adjacent wires is 0.2 mm, and the surrounding medium is air. A ground plane is

present below the wires, placed at a distance of 1 mm from the bottom side of the wires. Depicted in Figure 3.4 is the comparison of the resistance and reactance versus frequency for one of the bond wires over the 2 GHz frequency bandwidth of interest calculated using the proposed method, with those obtained using the 3D extractors. One real pole is used for approximation of each impedance element. The RMS (root mean square) error in the fitting of the impedance elements is 0.008, and a very good agreement between the two methodologies is observed.

A typical choice of boundary frequency of the low-frequency regime is chosen such that the skin depth δ is approximately 0.15 ~ 0.2 times the diameter of the wire. The starting frequency of the high-frequency regime is such that the skin depth δ is less than 0.1 times the diameter of the wire. The frequency-dependent resistance and inductance matrices are extracted for 39 different frequency intervals from 10 MHz to 2 GHz for 3D extractors. For our proposed methodology, frequency-dependent resistance and inductance matrices are extracted for 25 different frequencies in the range 10 MHz to 0.5 GHz and 3 frequencies in the interval 1 GHz to 2 GHz, leaving VF to interpolate the medium frequency regime from 0.5 GHz to 1 GHz. Table 3.1 compares the computation time of the two approaches. Judging from Table 3.1 and Figure 3.4, the proposed methodology clearly has a numerical advantage in comparison to the standard 3D extractor.

Table 3.1: Comparison of the computation time between standard methodology and our proposed methodology for a four coupled bond wire.

Intel Core 2 Duo CPU 2.1 GHz, 0.97 GB RAM	Computational time
Standard Methodology	154 minutes 28 seconds
Proposed Methodology	12 minutes 46 seconds

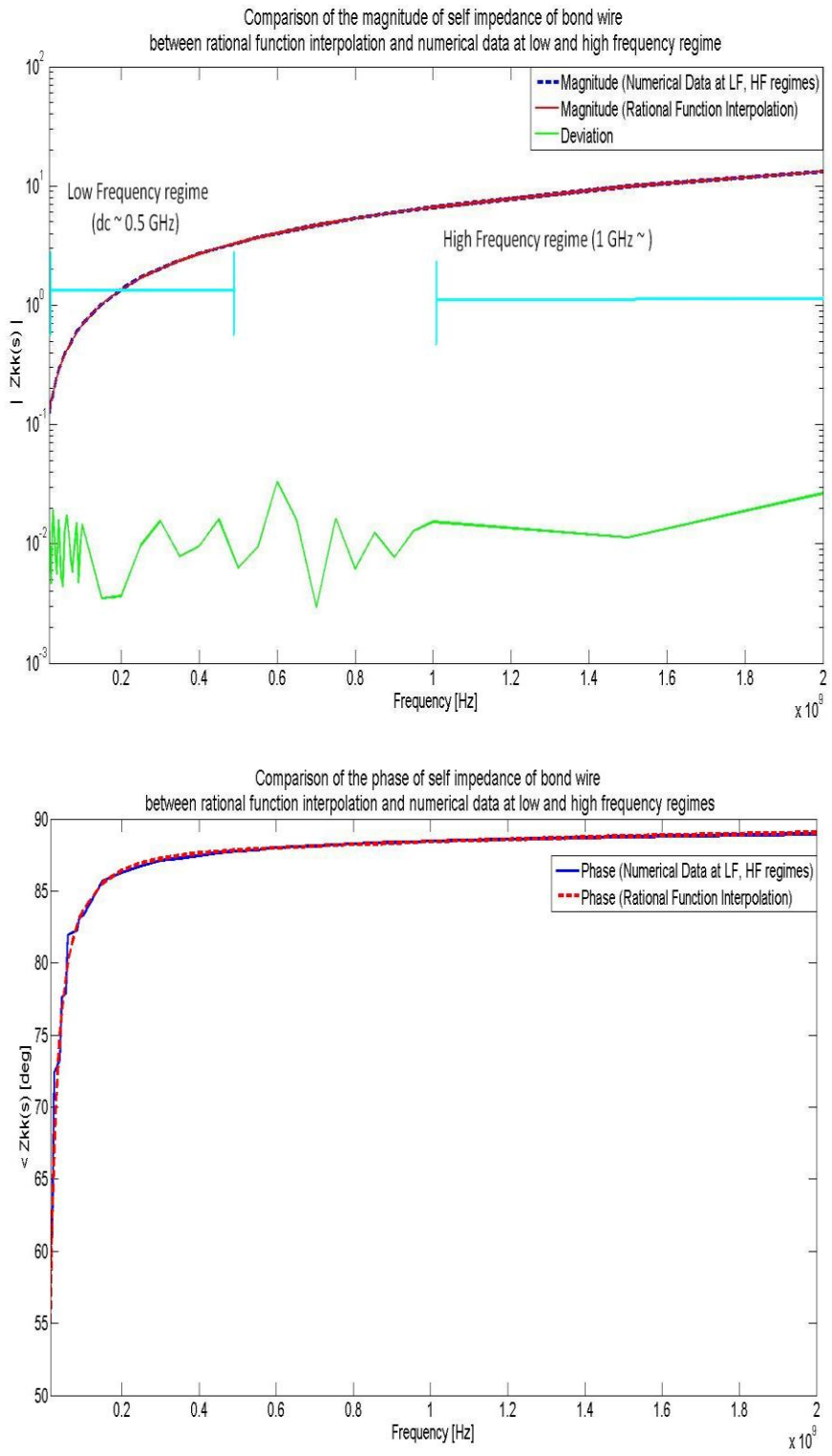

Figure 3.4: Comparison of the frequency-dependent resistance (top) and reactance (down) for one of the four bond wires of Figure 3.3.

Next, the synthesized equivalent multiport is used with a set of source and load conditions to perform a transient simulation using SPICE. With reference to Figure 3.3, a voltage source with input impedance of 50 Ω is connected at Port 1. All remaining ports are terminated at 50 Ω. The excitation waveform is a pulse train of period 2 ns, pulse width 1 ns, rise and fall times of 0.2 ns, and amplitude of 2 V. The resulting waveforms at several of the ports are depicted in Figures 3.5 and 3.6. The generated responses have been computed using two different synthesized circuits. One of the circuits was synthesized using the proposed methodology. The other was synthesized using resistance and inductance matrix data computed by the 3D quasi-static extractors over the entire frequency band. The two sets of responses are in very good agreement for both the driven and victim wires.

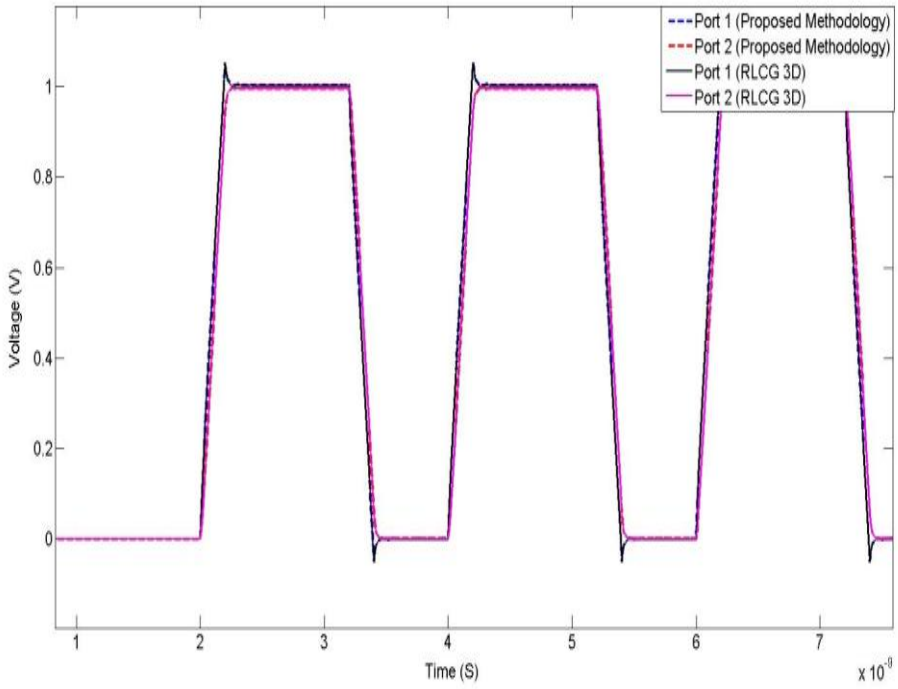

Figure 3.5: Transient responses at Ports 1 and 2.

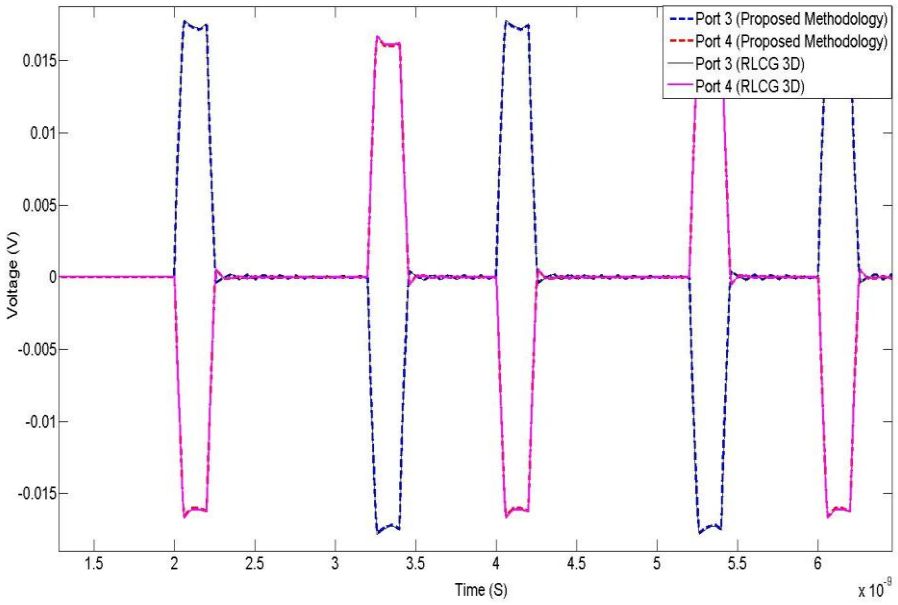

Figure 3.6: Transient responses at Ports 3 and 4.

3.3.2 Twelve coupled bond wires

The second numerical example concerns the geometry of twelve coupled Cu bond wires depicted in Figure 3.7. The wire radius is 10^{-2} mm, and the wire lengths are 1.3008 mm, 1.1983 mm, and 0.7981 mm, respectively. The axis-to-axis distance between adjacent wires ranges from 0.5 mm to 0.75 mm and the surrounding medium is air. A ground plane is present below the wires, placed at a distance of 1 mm from the bottom side of the wires.

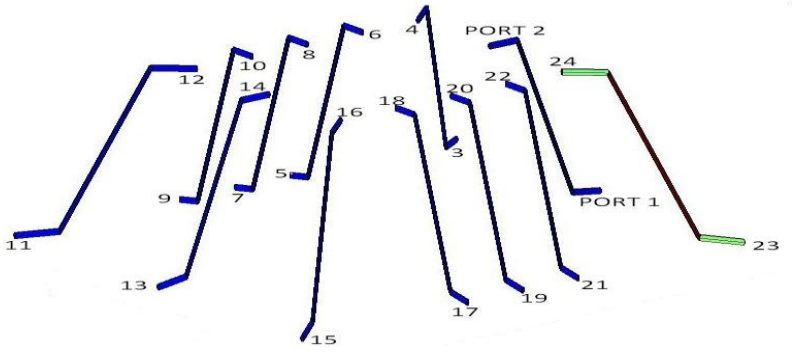

Figure 3.7: Twelve coupled Cu bond wires with 24 ports.

Figure 3.8 shows the comparison of the resistance and reactance versus frequency for one of the bond wires over the 5 GHz frequency bandwidth of interest calculated using the proposed method, with those obtained using the 3D extractors. The rms (root mean square) error in the fitting of the impedance elements is 0.0191, and again a very good agreement between the two methodologies is observed. The frequency-dependent resistance and inductance matrices are extracted for 30 different frequencies from 100 MHz to 5 GHz for 3D extractors. The frequency-dependent resistance and inductance matrices are extracted for 10 different frequencies in the interval 100 MHz to 500 MHz, and 3 frequencies in the interval from 3 GHz to 5 GHz, leaving VF to interpolate the medium frequency regime from 0.5 GHz to 3 GHz. Table 3.2 compares the computation time of the two approaches and demonstrates the computational efficiency of the proposed methodology.

Table 3.2: Comparison of the computation time between standard methodology and our proposed methodology for a twelve coupled bond wire.

Intel Core 2 Duo CPU 4 GHz, 8 GB RAM	Computational time
Standard Methodology	~ 11 hours
Proposed Methodology	~ 3 hours

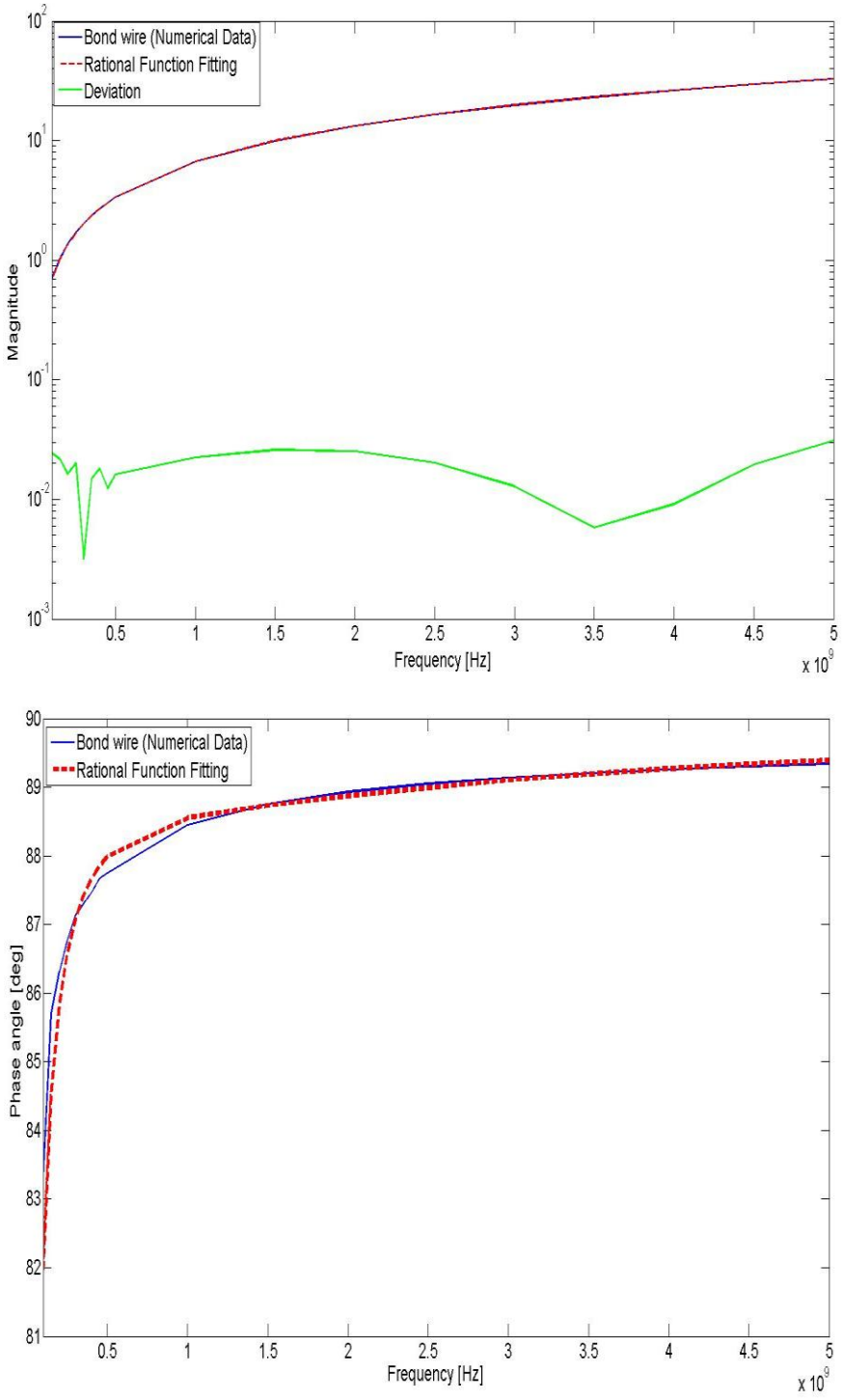

Figure 3.8: Comparison of the frequency-dependent resistance (top) and reactance (down) for one of the twelve wire bonds of Figure 3.7.

Next, the synthesized equivalent multiport with the same setting as the previous one is used with a volatge source input impedance of 50 Ω connected at Port 1, and remaining ports terminated at 50 Ω. The excitation waveform of a pulse train of period 2 ns, pulse width 1 ns, rise and fall times of 0.2 ns and amplitude of 2 V is applied at Port 1. The resulting waveforms of our methodology at several of the ports are depicted in Figures 3.9 and 3.10.

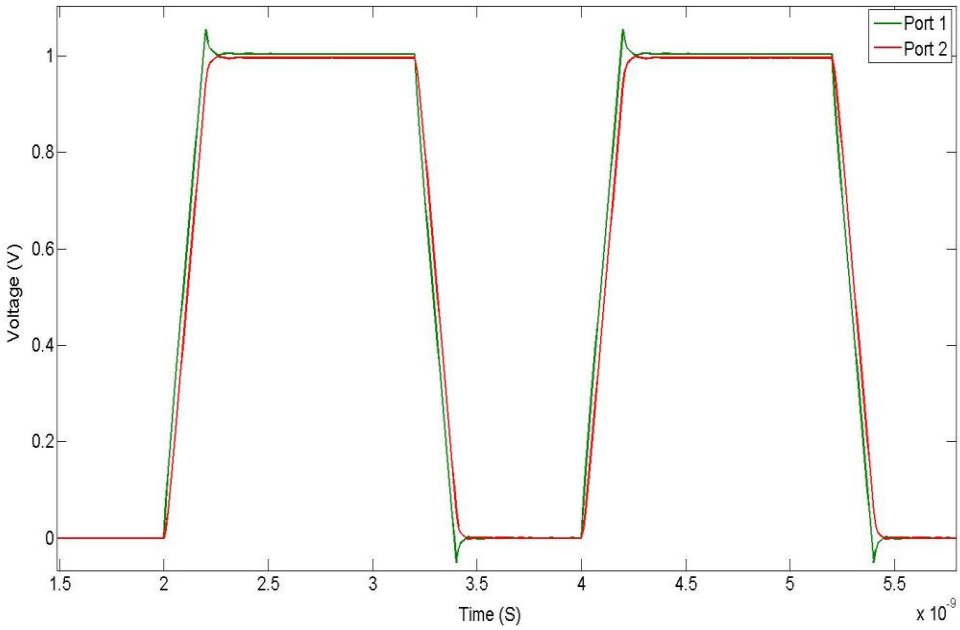

Figure 3.9: Transient responses at Ports 1 and 2.

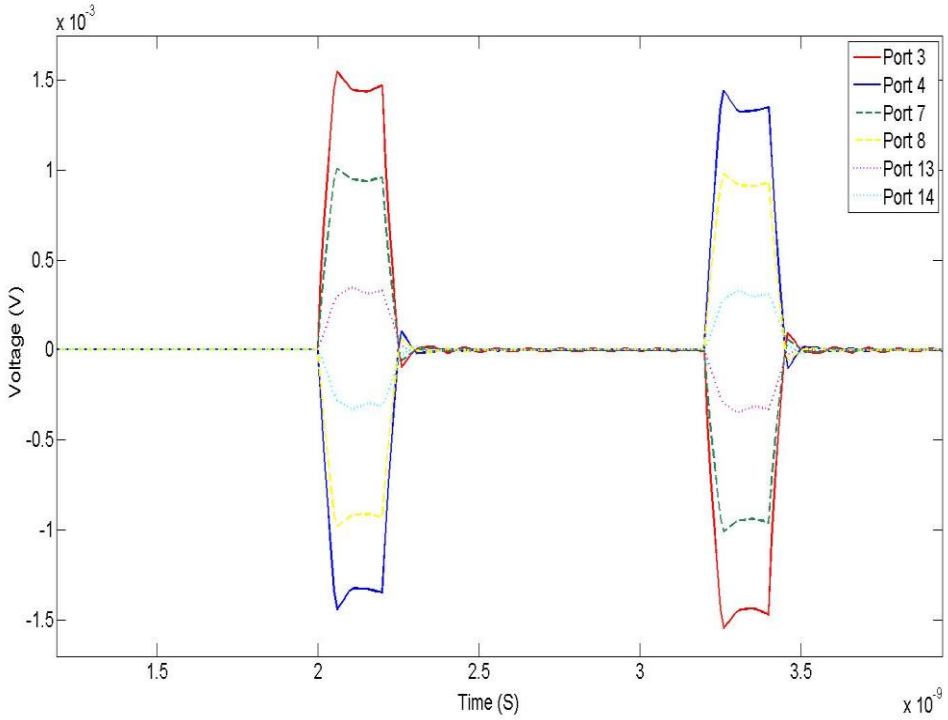

Figure 3.10: Transient responses at ports 3, 4, 7, 8, 13 and 14 (victim wires).

3.3.3 Fourteen bond wires in inhomogeneous medium

The third numerical example in Figure 3.11 concerns the geometry of a partitioned 14-coupled Cu bond wire group that connects to RF pins of a commercial package. The wire radius is 2.5×10^{-2} mm and two different groups of wire length of 0.9551 mm and 0.2323 mm exist. The axis-to-axis distance between adjacent wires for both groups is 0.11 mm. Figure 3.12 shows the cross-sectional view of the substrate. There are two different layers of thickness 0.9×10^{-3} mm and 0.385×10^{-3} mm and relative permittivity 4.2 and 3.9. The bond wires are located at the top of the signal plane BT. A ground plane is present below the wires, placed at a distance of 0.385 mm from the bottom side of the wires.

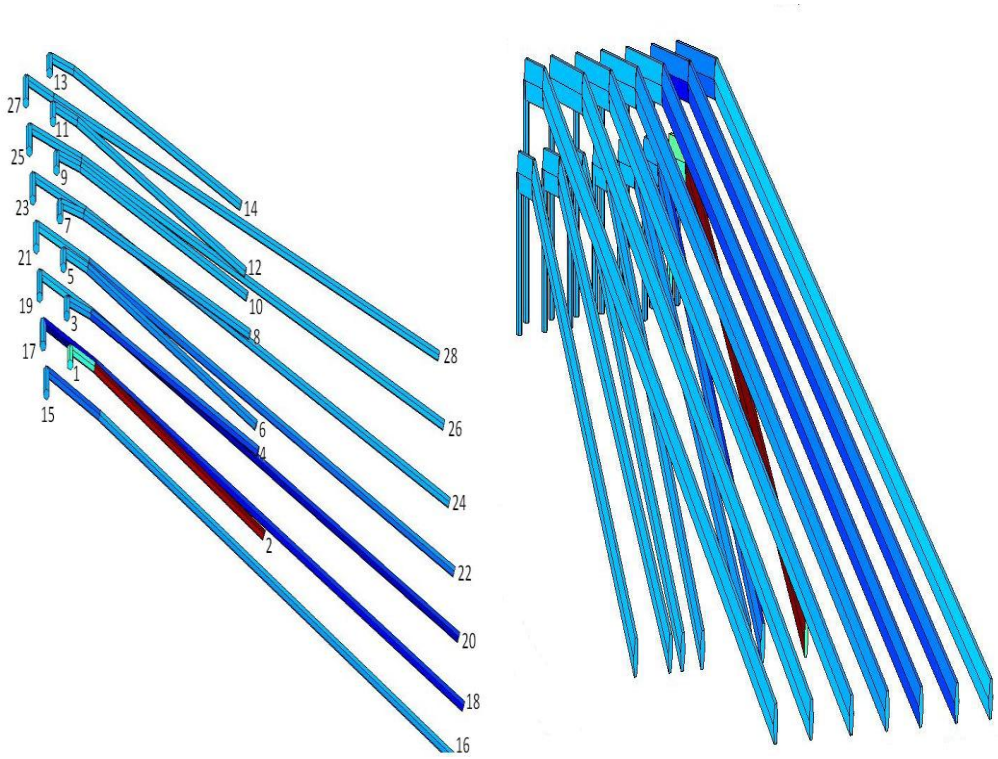

Figure 3.11: Fourteen coupled Cu bond wires for RF pins, with 28 ports.

AIR		Extends to infinity
Modified Epoxy	$e_r = 4.2$	0.9×10^{-3} mm
Signal Plane 1 (BT)	$e_r = 3.9$	0.25×10^{-3} mm
BT	$e_r = 3.9$	0.135×10^{-3} mm
AIR		Extends to infinity

Ground Plane

Figure 3.12: Cross-section of the commercial package.

The frequency-dependent resistance and inductance matrices are extracted for 6 different frequencies in the interval 100 MHz to 500 MHz and 1 frequency at 2 GHz for 3D extractors.

The frequency-dependent resistance and inductance matrices are interpolated between 500 MHz and 2 GHz with 2 real pole fitting. It results in RMS error less than 0.009, and a good fitting of the impedance matrix is observed. For transient simulation, the synthesized equivalent multiport is used with volatge source input impedance of 50 Ω connected at Port 1, and remaining ports terminated at 50 Ω. The excitation waveform of a pulse train of period 2 ns, pulse width 1 ns, rise and fall times of 0.2 ns, and amplitude of 2 V is applied at Port 1. The resulting waveforms at several of the ports are depicted in Figures 3.13 and 3.14.

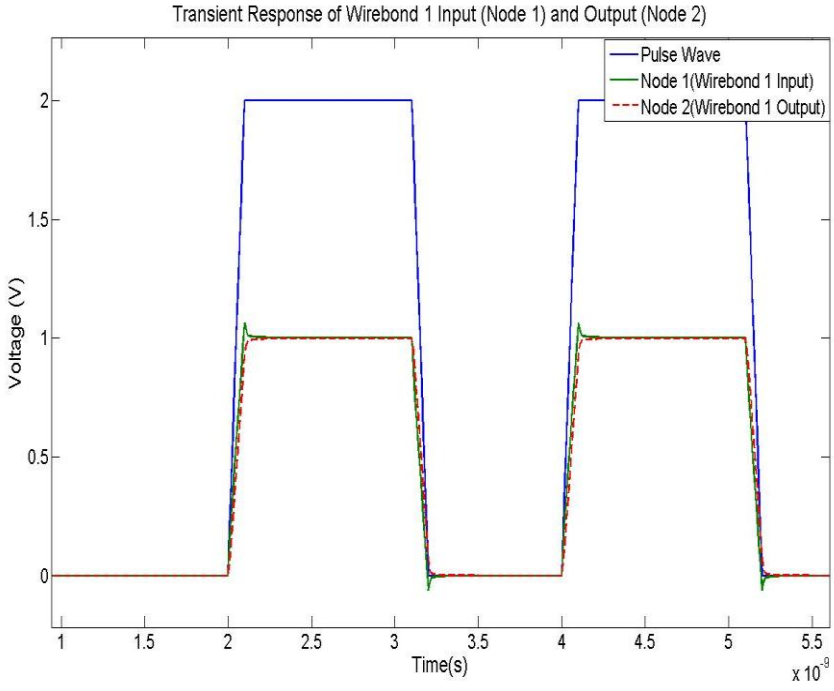

Figure 3.13: Transient responses at Ports 1 and 2.

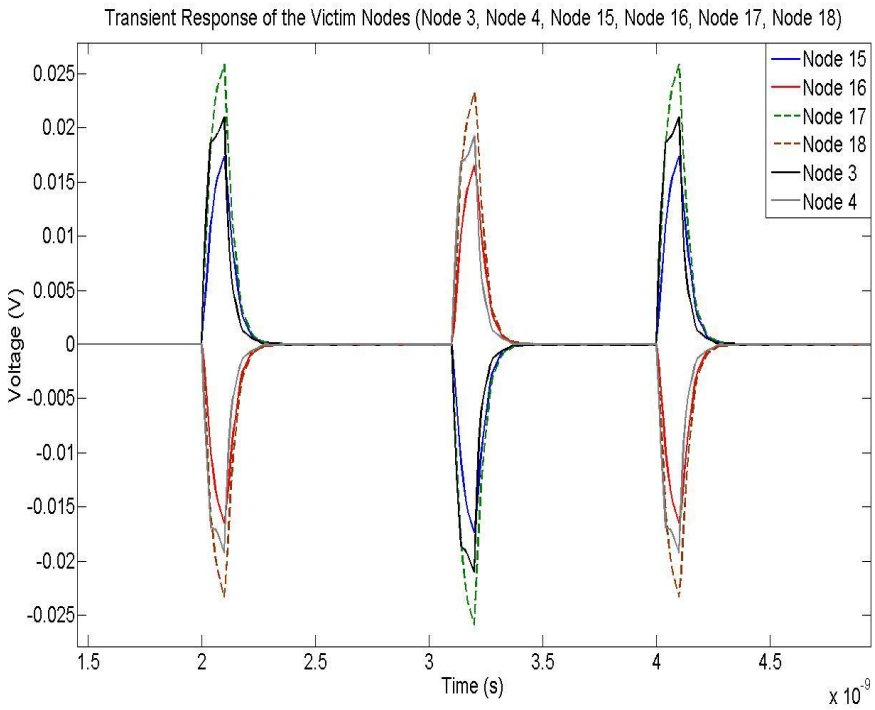

Figure 3.14: Transient responses at Ports 3, 4, 15, 16, 17, and 18 (victim wires).

3.4 Summary

In summary, we have proposed a computationally efficient scheme for the development of an equivalent RLC circuit representation of coupled bond wires of arbitrary configuration and number, valid over frequency bandwidths for which the wire length is small compared to the wavelength. The frequency-dependent resistance and inductance matrices of the wires are computed at the lower frequency band and the highest frequency band over the interval of interest through the solution of a magneto-quasi-static, three-dimensional boundary value problem. For the former, use of a low-density volumetric grid at a subset of frequencies at which the skin depth is larger than or at most comparable to wire cross-sectional dimensions results in fast computation of $\boldsymbol{R}(\omega)$ and $\boldsymbol{L}(\omega)$. For the latter, the skin depth being much smaller than the cross-sectional dimensions of the wires permits the use of a surface impedance boundary

condition and eliminates the need for volumetric discretization. These sets of values are then used in conjunction with a rational function fitting algorithm to interpolate the reduced sets of frequency samples over the entire frequency bandwidth of interest and generate the desired multi-port equivalent circuit subsequently.

Comparison of the computation time of a standard RLCG 3D extractor that relies on a volumetric discretization of the wires and our methodology over three sets of bond wire structure proves that our methodology is 4 – 10 times more efficient than the brute force approach. Through empirical studies, it was found that the optimal application of our methodology would be the case where the electrical length of our bond wires is less than 0.25 times the wavelength, and cases that would require one to two real poles for rational approximation. In this chapter, an efficient methodology for the synthesis of electrically small dispersive multi-port structures was proposed combining a magneto-quasi-static RLGC extractor and VF.

CHAPTER 4

PASSIVITY ASSESSMENT AND ENFORCEMENT OF TABULATED S-PARAMETER MATRIX

4.1 Introduction

A system that is passive implies that the system cannot generate more energy than it absorbs. Rational function interpolation of the passive system should always result in a passivity preserving macromodel. However, there are two distinct cases where the passivity condition may be violated. The first case happens when the original model does not preserve the passivity condition. This happens for measurement data with critical measurement errors due to miscalibration or improper measurement techniques, or for numerical data with incorrect interpolation and numerical errors. In this case, the subsequent rational function interpolation of such a model, however accurately it may interpolate the model, results in a passivity-violating and physically inconsistent macromodel. This is clearly demonstrated in [52] through rational interpolation of a non-passive model resulting in an unstable system, even when the model is cascaded with a stable and passive network. The second case happens when the measured or simulated data preserves passivity, but passivity is violated in the process of rational function interpolation. This happens due to the fact that rational interpolation techniques [15-36] do not guarantee the passivity of the identified transfer function, even if the original data satisfies the passivity requirement at the desired frequency bandwidth. The second case happens to interconnect structures that are electrically small and have low loss in their broadband frequency

spectrum. The passivity of the macromodel is an important property that must be checked and preserved as a post-processing step of rational function interpolation for accurate time-domain representation of the model.

Several different passivity enforcement techniques have been presented for multi-port tabulated data [53]-[69], and developing a robust passivity enforcement technique is still an on-going research topic. A passivity enforcement technique can be classified into one of two groups, based on whether it is a local or a global scheme. The first group [53],[56] enforces the passivity at given discrete frequency samples only. These algorithms take a local approach for passivity violation at a particular frequency band. Therefore, any attempt for passivity correction at some frequency band may lead to a new passivity violation at other frequency points. The second group [57]-[68] takes a global approach for passivity enforcement of the model such that the passivity condition from minimum to maximum frequency band is guaranteed by means of Hamiltonian eigenvalue perturbation. The passivity enforcement techniques vary widely from convex optimization [57] to quadratic programming [53]-[56], residue perturbation [59],[60],[63], pole perturbation [61],[62], modal perturbation [55], direct identification of passive model from data samples [69], and others [68]. The aforementioned passivity assessment and enforcement techniques rely on common-pole fitting of the transfer function matrix.

For a large complex multi-port system that has a broadband frequency content with rich resonance behavior represented by a tabulated $\boldsymbol{S}$ parameter matrix, macromodeling with common set of poles may pose many challenges which include issues with computational efficiency and accuracy due to memory constraints, and lack of the quality of the data due to presence of noise. To resolve this problem, element-by-element rational function interpolation [56] was introduced applying the passivity enforcement technique via quadratic programming [53] for the $\boldsymbol{Y}$ matrix.

In addition, block-wise rational function interpolation can be useful for preserving passivity of our system in a computationally efficient manner. Rather than applying the same order of poles for all elements in the matrix, element-by-element fitting allows different sets of poles for each element in the matrix to be fitted, and it is an attractive feature for fitting aforementioned complex systems. Block-wise fitting, on the other hand allows different sets of poles for each block (group of elements) in the matrix to be fitted. Ref. [56] presents an element-by-element admittance matrix fitting with each element having same number of poles. In many cases, the general state space form of the element-by-element or block-wise approximation needs to be known and applied for the case where each element or each block has different orders of poles. Also, a passivity assessment and enforcement technique involving sweeping along the frequency for eigenvalues of Re{$\mathbf{Y}(\omega)$} cannot be guaranteed in the entire frequency domain, as passivity may still be violated at different sets of frequencies. The Hamiltonian matrix [71],[72], which determines the boundary frequency values of passivity violation from the state space representation of the rational fit without the frequency sweep, is widely used with many passivity enforcement techniques, including perturbation of Hamiltonian matrix, residues and poles [59]-[68]. However, the techniques that involve Hamiltonian matrix and perturbation approaches are based on common-pole fitting. The objective of this chapter is to demonstrate the efficiency of the element-by-element and block-wise fitting with different orders in its element or block and how element-by-element or block-wise state space parameters can be used in Hamiltonian matrix and passivity enforcement techniques using iterative method via perturbation of residues [63]. We apply different fitting and passivity enforcements in this study in sparse VF and fast VF. The reason for introducing two sets of VF techniques is based on major computational improvements of the rational approximation techniques, from large sparse matrix least squares fitting [53] to

computationally efficient reduced matrix fitting using QR decomposition [27]. Also, the aforementioned element-by-element fitting [56] and the expediency of the method are only based on a sparse matrix solver [53]. Thus, it is worthwhile to investigate how efficient element-by-element and block-wise fitting and the following passivity enforcement are with respect to the common-pole fitting and passivity enforcement.

4.2 State Equation Representation of Linear Networks for Common-Pole, Element-by-Element, and Block-wise Fitting

The state space equation of the common pole approximation is written as follows:

$$\boldsymbol{S}_{\mathbf{fit}}(\mathrm{s}) = \boldsymbol{C}(\mathrm{s}\boldsymbol{I} - \boldsymbol{A})^{-1}\boldsymbol{B} + \boldsymbol{D} \tag{4.1}$$

The elements of $\boldsymbol{A}$ and $\boldsymbol{C}$ are composed of either real or complex conjugate pairs. Simply, $\boldsymbol{A}$ is a diagonal matrix that holds the common poles $\{a_m\}$, repeated as many times as $\boldsymbol{S_{fit}}$ has columns. For example, if $\boldsymbol{S_{fit}}(\mathrm{s})$ represents a two-port structure, common poles that diagonally fill the matrix $\boldsymbol{A}$ are repeated twice. Matrix $\boldsymbol{C}$ holds the elements of the residue matrices $\{\boldsymbol{r_m}\}$. Matrix $\boldsymbol{B}$ is a selector matrix that contains both vectors of ones and zeros that associate each input to a separate block (column set) in $\boldsymbol{A}$ and $\boldsymbol{C}$. Let us consider a two-port system for which the fast VF with common poles results in a rational function of order 3. The following explicit state space form in (4.2) is expected from 3 common poles of 2-port system:

$$\boldsymbol{A} = \mathrm{diag}(p_1\ \ p_2\ \ p_3\ \ p_1\ \ p_2\ \ p_3)\,, \quad \boldsymbol{B^T} = \begin{bmatrix} 1 & 1 & 1 & 0 & 0 & 0 \\ 0 & 0 & 0 & 1 & 1 & 1 \end{bmatrix},$$
$$\boldsymbol{C} = \begin{bmatrix} r_{1,11} & r_{2,11} & r_{3,11} & r_{1,12} & r_{2,12} & r_{3,12} \\ r_{1,21} & r_{2,21} & r_{3,21} & r_{1,22} & r_{2,22} & r_{3,22} \end{bmatrix}, \quad \boldsymbol{D} = \begin{bmatrix} \mathrm{D}_{11} & \mathrm{D}_{12} \\ \mathrm{D}_{21} & \mathrm{D}_{22} \end{bmatrix} \tag{4.2}$$

The element-by-element pole-residue model in (2.36b) in matrix form can be written in a state space form as follows:

$$\boldsymbol{S_{fit}}(\mathrm{s}) = \boldsymbol{C_{e.e.}}(\boldsymbol{sI} - \boldsymbol{A_{e.e.}})^{-1}\boldsymbol{B_{e.e.}} + \boldsymbol{D_{e.e.}} \tag{4.3}$$

The state space parameters $\boldsymbol{A}_{\mathbf{e.e.}}$, $\boldsymbol{C}_{\mathbf{e.e.}}$ and $\boldsymbol{B}_{\mathbf{e.e.}}$ of the element-by-element fitting of the scattering matrix are different from those generated by the common-pole fitting. Assuming an N-port matrix with $N_{\mathrm{i,j}}$ order for each element, the matrices $\boldsymbol{A}_{\mathbf{e.e.}}$, $\boldsymbol{C}_{\mathbf{e.e.}}$ and $\boldsymbol{B}_{\mathbf{e.e.}}$ have a generalized state matrix form as follows:

$$\mathbf{A}_{\mathbf{e.e.}} = \mathrm{diag}\left(\mathbf{P}_{11} \ldots \mathbf{P}_{1N} \ldots \mathbf{P}_{N1} \ldots \mathbf{P}_{NN}\right),$$

$$\mathbf{B}_{\mathbf{e.e.}}{}^{\mathrm{T}} = \begin{bmatrix} \mathbf{I}_{11} & \mathbf{0}_{12} & \cdots & \mathbf{0}_{1N} & \cdots & \mathbf{I}_{N1} & \mathbf{0}_{N2} & \cdots & \mathbf{0}_{NN} \\ \mathbf{0}_{11} & \mathbf{I}_{12} & \cdots & \mathbf{0}_{1N} & \cdots & \mathbf{0}_{N1} & \mathbf{I}_{N2} & \cdots & \mathbf{0}_{NN} \\ \vdots & \vdots & \ddots & \vdots & \cdots & \vdots & \vdots & \ddots & \vdots \\ \mathbf{0}_{11} & \mathbf{0}_{12} & \cdots & \mathbf{I}_{1N} & \cdots & \mathbf{0}_{N1} & \mathbf{0}_{N2} & \cdots & \mathbf{I}_{NN} \end{bmatrix},$$

$$\mathbf{C}_{\mathbf{e.e.}} = \begin{bmatrix} \mathbf{R}_{11} \ldots \mathbf{R}_{1N} & \mathbf{0}_{21} \ldots \mathbf{0}_{2N} \ldots \mathbf{0}_{N1} \ldots \mathbf{0}_{NN} \\ \mathbf{0}_{11} \ldots \mathbf{0}_{1N} & \mathbf{R}_{21} \ldots \mathbf{R}_{2N} \ldots \mathbf{0}_{N1} \ldots \mathbf{0}_{NN} \\ \vdots \quad \vdots \quad \vdots & \vdots \quad \vdots \quad \vdots \quad \vdots \quad \vdots \quad \vdots \\ \mathbf{0}_{11} \ldots \mathbf{0}_{1N} & \mathbf{0}_{21} \ldots \mathbf{0}_{2N} \ldots \mathbf{R}_{N1} \ldots \mathbf{R}_{NN} \end{bmatrix},$$

$$\mathbf{D}_{\mathbf{e.e.}} = \mathbf{D} = \begin{bmatrix} \mathrm{D}_{11} & \cdots & \mathrm{D}_{1N} \\ \vdots & \ddots & \vdots \\ \mathrm{D}_{N1} & \cdots & \mathrm{D}_{NN} \end{bmatrix}. \tag{4.4}$$

The state matrix $\boldsymbol{A}_{\mathbf{e.e.}}$ is a diagonal matrix with dimensions $\left(\sum_{\mathrm{i}=1}^{N}\sum_{\mathrm{j}=1}^{N} N_{ij}\right)$ by $\left(\sum_{\mathrm{i}=1}^{N}\sum_{\mathrm{j}=1}^{N} N_{ij}\right)$. Block matrix $\boldsymbol{P}_{\mathbf{ij}}$ of $\boldsymbol{A}_{\mathbf{e.e.}}$ is an N_{ij} by N_{ij} diagonal matrix with N_{ij} number of poles. Matrix $\boldsymbol{B}_{\boldsymbol{e.e.}}^{\boldsymbol{T}}$, which relates the input variables to the state variables, is an N by $\left(\sum_{\mathrm{i}=1}^{N}\sum_{\mathrm{j}=1}^{N} N_{ij}\right)$ matrix composed of row vectors of 1's and 0's. The block $\boldsymbol{I}_{\mathbf{ij}}$ and $\mathbf{0}_{\mathbf{ij}}$ of $\boldsymbol{B}_{\mathbf{e.e.}}$ are row vectors with size N_{ij}. Matrix $\boldsymbol{C}_{\mathbf{e.e.}}$, which relates the state variables to output variables, is an N by $\left(\sum_{\mathrm{i}=1}^{N}\sum_{\mathrm{j}=1}^{N} N_{ij}\right)$ matrix that holds row vectors of residues and 0's. Constant D matrix is an N by N matrix. The state space representation of block-wise fitting is equivalent to that of element-by-element fitting.

As an example, we show a state space representation of a 2-port device, in which the first group of elements $\{\boldsymbol{S}_{\mathbf{11}}(\mathrm{s}), \boldsymbol{S}_{\mathbf{22}}(\mathrm{s})\}$ have 40 complex conjugate poles diagonalized as $\boldsymbol{P}_{\mathbf{1}}$ and second group of elements $\{\boldsymbol{S}_{\mathbf{12}}(\mathrm{s}), \boldsymbol{S}_{\mathbf{21}}(\mathrm{s})\}$ have 20 complex conjugate poles diagonalized as $\boldsymbol{P}_{\mathbf{2}}$

in (4.5). $\boldsymbol{P_1}$ is a diagonalized matrix of 40 complex poles $\{p_{1,p1,}, p_{2,p1}, p_{3,p1} \dots p_{40,p1}\}$, and $\boldsymbol{R_{11}}$ is a row vector of 40 residues $\{r_{1,r11}, r_{2,r11}, r_{3,r11} \dots r_{40,r11}\}$.

$$\mathbf{A_{e.e.}} = \mathrm{diag}(\,\mathbf{P_1}\ \mathbf{P_2}\ \mathbf{P_2}\ \mathbf{P_1}\,),$$
$$\mathbf{B_{e.e.}}^{\mathrm{T}} = \begin{bmatrix} \mathbf{I_1} & \mathbf{0_2} & \mathbf{I_2} & \mathbf{0_1} \\ \mathbf{0_1} & \mathbf{I_2} & \mathbf{0_2} & \mathbf{I_1} \end{bmatrix},$$
$$\mathbf{C_{e.e.}} = \begin{bmatrix} \mathbf{R_{11}} & \mathbf{R_{12}} & \mathbf{0_{21}} & \mathbf{0_{22}} \\ \mathbf{0_{11}} & \mathbf{0_{12}} & \mathbf{R_{21}} & \mathbf{R_{22}} \end{bmatrix},$$
$$\mathbf{D_{e.e.}} = \mathbf{D} = \begin{bmatrix} D_{11} & D_{12} \\ D_{21} & D_{22} \end{bmatrix}. \tag{4.5}$$

The state space matrices $\boldsymbol{A}$ and $\boldsymbol{C}$, in all three different types of fitting are represented in complex numbers. These matrices can also be expressed in terms of only real numbers via a similarity transformation [73]. Equation (4.6) shows the corresponding matrices $\widehat{\boldsymbol{A}}$ and $\widehat{\boldsymbol{C}}$ via similarity transform. The same procedure is applied to the element-by-element and block-wise fitted state space matrices, $\boldsymbol{A_{e.e.}}$ and $\boldsymbol{C_{e.e.}}$. The state space representation based on element-by-element and block-wise fitting will produce slightly asymmetrical $\boldsymbol{S_{fit}}$, since a different pole set will be obtained for the different blocks.

$$\widehat{\boldsymbol{A}} = \begin{bmatrix} Re\{a\} & Im\{a\} \\ -Im\{a\} & Re\{a\} \end{bmatrix},\ \widehat{\boldsymbol{C}} = [Re\{\boldsymbol{c}\} \quad Im\{\boldsymbol{c}\}]\ ,\ \widehat{\boldsymbol{b}} = \begin{bmatrix} 2Re\{\boldsymbol{b}^T\} \\ -2Im\{\boldsymbol{b}^T\} \end{bmatrix} = \begin{bmatrix} 2\boldsymbol{b}^T \\ \boldsymbol{0}^T \end{bmatrix} \tag{4.6}$$

4.3 Passivity Assessment for Common-Pole, Element-by-Element and Block-wise Fitting

The rational approximation model through the previous step is stable, but passivity of the model has to be checked and corrected if the macromodel violates the condition. The passivity

condition for the S matrix is defined in (4.7) as its singular values $\boldsymbol{\sigma}$ at all provided frequency bands in (4.8) are unitary bounded [43].

$$\left(\boldsymbol{I} - \boldsymbol{S}^{H}(j\omega)\boldsymbol{S}(j\omega)\right) \geq 0 \quad \forall\, \omega \tag{4.7}$$

$$\max_{\omega} \boldsymbol{\sigma}\left(\boldsymbol{S}(j\omega)\right) \leq 1 \quad \forall\, \omega \tag{4.8}$$

The method above is ideally the most straightforward way to test the passivity of the system by checking whether the singular values at all frequencies are unitary bounded or not. However, this relies on the frequency samples and it is impossible to perform this test from DC to infinity. Therefore, what is needed is a passivity test independent of the frequency samples. State space matrices can be used for this purpose, and they can provide the global passivity test and identify the passivity violation regions of the system irrespective of the frequency samples. The boundary of the passivity violation region can be detected by computing the eigenvalues of the Hamiltonian matrix $\boldsymbol{M}$ in (4.9) [71] by ensuring that it has no imaginary eigenvalues, where $\boldsymbol{R} = \boldsymbol{D}^{\boldsymbol{T}}\boldsymbol{D} - \boldsymbol{I}$ and $\boldsymbol{Q} = \boldsymbol{D}\boldsymbol{D}^{\boldsymbol{T}} - \boldsymbol{I}$.

$$\boldsymbol{M} = \begin{bmatrix} \boldsymbol{A} - \boldsymbol{B}\boldsymbol{R}^{-1}\boldsymbol{D}^{\boldsymbol{T}}\boldsymbol{C} & -\boldsymbol{B}\boldsymbol{R}^{-1}\boldsymbol{B}^{\boldsymbol{T}} \\ \boldsymbol{C}^{\boldsymbol{T}}\boldsymbol{Q}^{-1}\boldsymbol{C} & -\boldsymbol{A}^{\boldsymbol{T}} + \boldsymbol{C}^{\boldsymbol{T}}\boldsymbol{D}\boldsymbol{R}^{-1}\boldsymbol{B}^{\boldsymbol{T}} \end{bmatrix} \tag{4.9}$$

For element-by-element and block-wise approximations, the Hamiltonian matrix $\boldsymbol{M}_{\mathbf{e.e.}}$ is obtained by substituting the element-by-element state matrices in (4.10), where $\boldsymbol{R}_{\mathbf{e.e.}} = \boldsymbol{D}_{\mathbf{e.e.}}^{\mathbf{T}}\boldsymbol{D}_{\mathbf{e.e.}} - \boldsymbol{I}$ and $\boldsymbol{Q}_{\mathbf{e.e.}} = \boldsymbol{D}_{\mathbf{e.e.}}\boldsymbol{D}_{\mathbf{e.e.}}^{\mathbf{T}} - \boldsymbol{I}$. The frequency band where passivity is violated is found by checking the imaginary eigenvalue $j\omega$ of the Hamiltonian matrix. Due to the noise, no eigenvalues that correspond to the crossover frequencies of Hamiltonian matrix will exactly have imaginary value [58],[72]. Therefore, the crossover frequencies are selected with the eigenvalues that have a very small ratio of real part divided by imaginary part, and which are symmetric only with the real axis.

$$\boldsymbol{M_{e.e.}} = \begin{bmatrix} \boldsymbol{A_{e.e.} - B_{e.e.} R_{e.e.}^{-1} D_{e.e.}^{T} C_{e.e.}} & \boldsymbol{-B_{e.e.} R_{e.e.}^{-1} B_{e.e.}^{T}} \\ \boldsymbol{C_{e.e.}^{T} Q_{e.e.}^{T} C_{e.e.}} & \boldsymbol{-A_{e.e.}^{T} + C_{e.e.}^{T} D_{e.e.} R_{e.e.}^{-1} B_{e.e.}^{T}} \end{bmatrix} \tag{4.10}$$

The difference between (4.10) and (4.9) lies in the size of the Hamiltonian matrix. For comparison, assume rational approximation with M_f samples, K elements, and N poles for a passive N_p port system. The size of the Hamiltonian matrix $\boldsymbol{M}$ for the common-pole fitting is $2NN_p$ by $2NN_p$. If we assume that we fit with N poles for all of our elements for element-by-element or block-wise fitting, the size of the Hamiltonian matrix $\boldsymbol{M}$ is $2NN_p^2$ by $2NN_p^2$. This in fact will be the worst case study for element-by element fitting or block-wise fitting. However, the advantage of the element-by-element or block-wise fitting is to use different and possibly fewer orders of poles for some fitted elements or blocks of elements rather than using the same order for all the elements. In general, the size of the Hamiltonian matrix for element-by-element or block-wise fitting will be greater than the size of the common-pole fitting.

4.4 Passivity Enforcement for Common-Pole, Element-by-Element and Block-wise Fitting

After the detection of the passivity violation region, the passivity enforcement algorithm [63] is applied in the following steps. Singular value decomposition of $\boldsymbol{S}(j\omega)$, where $\boldsymbol{U}$ and $\boldsymbol{V}^*$ are unitary matrices and $\sum$ is a positive, real-valued diagonal matrix that contains the singular values, is carried out in (4.11). For the sake of avoiding repetition, we only present the case for element-by-element and block-wise fitting. However, all the equations have the same form.

$$\boldsymbol{S_{fit}}(j\omega_{eval}) = \boldsymbol{C_{e.e.t+1}}(j\omega_{eval}\boldsymbol{I} - \boldsymbol{A_{e.e.}})^{-1}\boldsymbol{B_{e.e.}} + \boldsymbol{D_{e.e.}} = \boldsymbol{U}\sum\boldsymbol{V}^* \tag{4.11}$$

For singular values of the diagonal matrix $\sum$ violating unitary bound, a new set of violating parameter $\boldsymbol{S_{viol}}(j\omega)$ is constructed by introducing the diagonal matrix $\sum_{\boldsymbol{viol}}$ in (4.12), which is

obtained by subtracting the predefined tolerance parameter (e.g. 0.999) to the singular value greater than 1 of the original diagonal matrix $\sum$ in (4.13).

$$\boldsymbol{S_{fit\_viol}}(j\omega_{eval}) = \boldsymbol{U}\boldsymbol{\sum_{viol}}\boldsymbol{V}^{*} \tag{4.12}$$

$$\boldsymbol{\sum_{viol}} = \boldsymbol{\sum\gamma} - \boldsymbol{\Psi} \tag{4.13}$$

The parameters $\boldsymbol{\gamma}$ and $\boldsymbol{\Psi}$ in (4.14) are square diagonal matrices, and the value of δ, a pre-defined tolerance parameter, is chosen slightly smaller than 1 (for e.g. 0.999).

$$\begin{aligned} \boldsymbol{\gamma}|_{ii,\sum_{ii}\leq\delta} &= 0 \; \boldsymbol{\gamma}|_{ii,\sum_{ii}>\delta} = 1 \\ \Psi|_{ii,\sum_{ii}\leq\delta} &= 0 \; \Psi|_{ii,\sum_{ii}>\delta} = \delta \end{aligned} \tag{4.14}$$

A new set of $\boldsymbol{C_{\mathbf{e.e.viol}}}$ is computed by fitting $\boldsymbol{S_{\mathbf{viol}}}$(jω) at all provided frequency bandwidths using the same set of poles used in the original macromodel to make the state-space model passive. Once $\boldsymbol{C_{\mathbf{e.e.viol}}}$ is computed, $\boldsymbol{C_{\mathbf{e.e.t+1}}}$ is updated by subtracting the $\boldsymbol{C_{\mathbf{e.e.viol}}}$ from $\boldsymbol{C_{\mathbf{e.e.t}}}$. In this way, the residues of the element-by-element matrix $\boldsymbol{C_{\mathbf{e.e.}}}$ are perturbed and this process is iterated until all the singular values at provided frequency bandwidths are unitary bounded. This step is shown in (4.15). Asymptotic passivity $\left(\boldsymbol{S_{\mathbf{fit}}}(\infty)\right)$ enforcement [64] is done similarly by taking singular value decomposition of the matrix $\boldsymbol{D_{\mathbf{e.e.}}}$ before passivity enforcement of the $\boldsymbol{S}$(jω) matrix.

$$\begin{aligned} \boldsymbol{S_{fit\_viol}}(j\omega_{eval}) &= \boldsymbol{C_{e.e.viol}}(j\omega_{eval}\boldsymbol{I} - \boldsymbol{A_{e.e.}})^{-1}\boldsymbol{B_{e.e.}} \\ \boldsymbol{C_{e.e.t+1}} &= \boldsymbol{C_{e.e.t}} - \boldsymbol{C_{e.e.viol}} \end{aligned} \tag{4.15}$$

4.5 Validation Studies

For validation and comparison purposes of the passivity assessment and enforcement techniques with element-by-element and block-wise fitting, three examples of measurement and

simulated data are considered. Note that all simulations were performed using a 2.1 GHz processor with 1 GB RAM.

4.5.1 Two-port co-planar waveguide measurement

Measurement data of a 2-port co-planar waveguide with 400 samples from 45 MHz to 50 GHz is considered as a first example. The measurement has uniform sampling with Δf = 124.8875 MHz. Vector fitting [21],[25],[27] which uses SK iterative technique [16] is used to fit each element or groups of common poles independently of the others to generate an accurate model. Unstable poles are flipped, guaranteeing stable rational function fit for each element or blocks of the S-parameter matrix. Three fitting strategies in two different VF environments (sparse VF and fast VF) are considered as comparison purpose. First, in a sparse VF environment [23], 150 complex conjugate common poles were used to fit the asymmetric model, resulting in a very accurate fitting with computational time of 27.015 s and the RMS error of 0.00358. Element-by-element fitting with 60, 20, 24 and 58 complex conjugate poles for S_{11}, S_{12}, S_{21} and S_{22} resulted in a comparable RMS error of 0.004128 with computational time of 13.688 s. Block-wise fitting with two groups having 60 common poles for S_{11}, S_{22} and 24 common poles for S_{12} and S_{21} resulted in RMS error of 0.004154 with computational time of 12.658 s. Table 4.1 shows the summary of the three fitting strategies in sparse VF.

The experiment proves the assumption that there are computational advantages of using element-by-element and block-wise fitting over the common-pole fitting, as the size of the sparse least squares matrix can be considerably reduced to a dense element or blocks of elements matrix. From the extensive discussion of the computation order and the flop count of each fitting strategy within each process of the two-step sparse VF algorithm in the previous section, we can expect the computational time disparity of common-pole fitting with element-by-element and

block-wise fitting to significantly increase as the number of ports and frequency samples of the macromodel increase.

Next, the same number of poles for common-pole, element-by-element and block-wise fitting are applied in the fast VF environment. As expected, the computation time in fast VF was significantly reduced compared to sparse VF, and a speedup factor of 4 ~ 8 was observed for all three fitting strategies due to reduction of the sparse matrix. The numerical convergence of the fast VF is superior to the sparse VF, and it will require fewer poles to fit the system while preserving the accuracy. Note that 50 complex conjugate common poles resulted in computation time of 3.29032 s with RMS error of 0.0021492. Element-by-element fitting with 60, 20, 24, 58 complex conjugate poles resulted in computation time of 6.118404 s with RMS error of 0.0022744. Finally, block-wise fitting with 60 and 24 complex conjugate poles resulted in computation time of 3.725553s with RMS error of 0.0023084. In fast VF, common-pole fitting and block-wise fitting are more computationally efficient for a small-order, mid-size frequency sampled 2-port system. Table 4.2 shows the summary of the three fitting strategies in fast VF.

Table 4.1: Comparison of number of poles, RMS error, and computation time for common-pole, element-by-element and block-wise fitting for sparse VF

Sparse Vector Fitting	Number of poles needed	RMS error	Rational approximation time
Common-pole fitting	150 c.c. poles	0.00358	27.015 s
Element-by-element fitting	60, 20, 24, 58 c.c. poles	0.004128	13.688 s
Block-wise fitting	60, 24 c.c. poles	0.004154	12.658 s

Table 4.2: Comparison of number of poles, RMS error, and computation time for common-pole, element-by-element and block-wise fitting for fast VF

Fast Vector Fitting	Number of poles needed	RMS error	Rational approximation time
Common-pole fitting	50 c.c. poles	0.0021492	3.29032 s
Element-by-element fitting	60, 20, 24, 58 c.c. poles	0.0022744	6.118404 s
Block-wise fitting	60, 24 c.c. poles	0.0023084	3.725553s

The reason for such a sharp contrast compared to the sparse VF can only be explained by the fact that the total flop count and computation time of step 1 do not dominate the overall computational cost more than in other steps in fast VF setting, due to the huge reduction of the size of the least squares matrix. Because of this reduction, the least squares matrix that we use is already small, and taking even further reduction of this reduced matrix by using element-by-element fitting has no computational advantage, since element-by-element fitting will reduce the size of the matrix even further but will require K number of least squares fitting of elements from (4.9) to (4.11). Compared to the common-pole fitting, element-by-element fitting takes K more iterations. When the size of the least squares matrix is reduced, the contribution of iterations becomes more important to the overall computation time, and although element-by-element fitting may bring more size and memory advantage, common-pole or block-wise fitting gives a better result. From now on, only fast VF will be considered due to the vast performance improvement over sparse VF.

Figure 4.1 shows the element-by-element and original magnitude and the phase of the measured 2-port S parameter model. The differences between the magnitude and phase fitting of the co-planar waveguide for three fitting strategies were minimal as the RMS errors indicate. In

this figure, only element-by-element fitting results are shown. A very good agreement is observed.

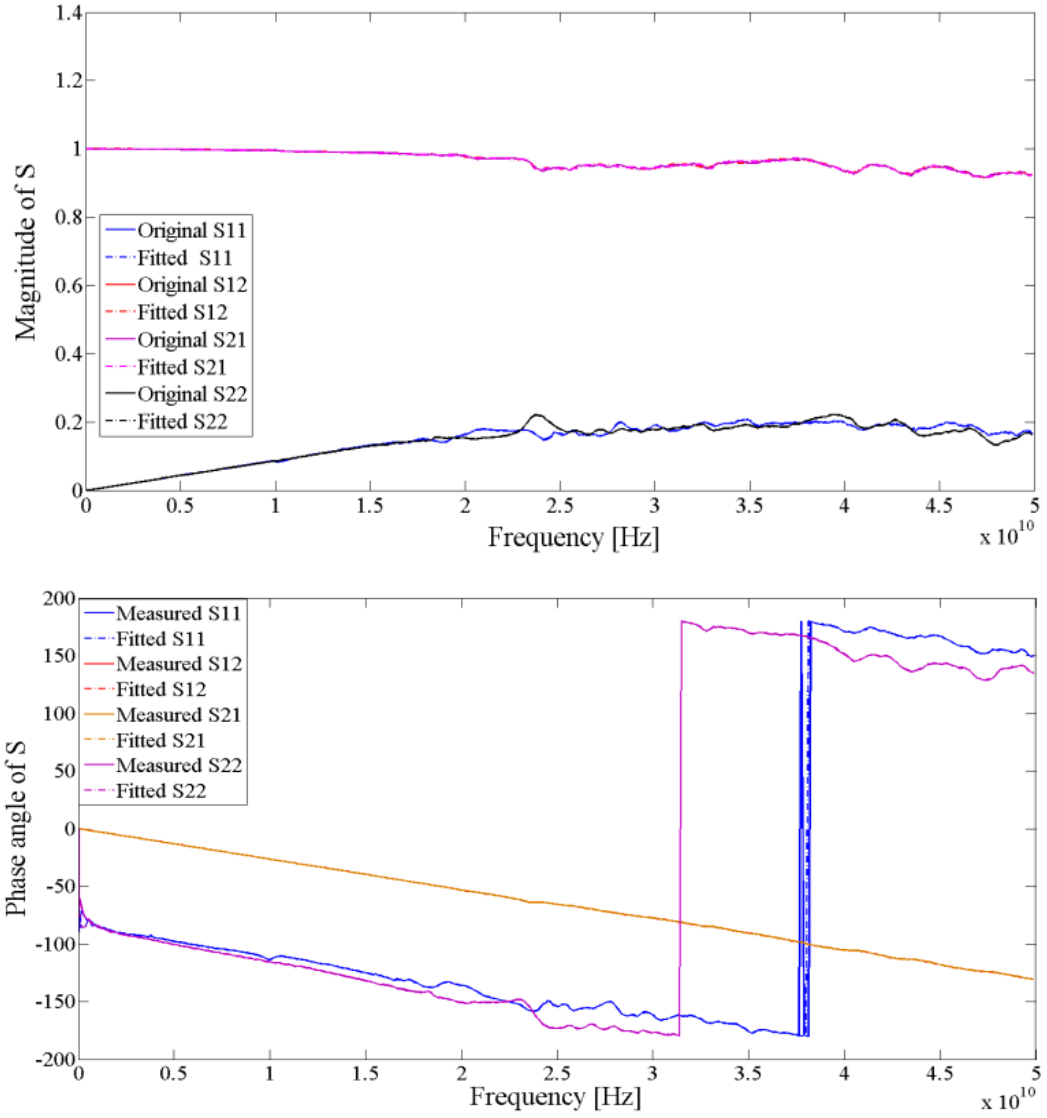

Figure 4.1: Comparison of the magnitude (top) and phase (bottom) of the measurement data and element-by-element fitting.

The top of Figure 4.2 shows the eigenvalue distribution of the Hamiltonain matrix for common-pole, element-by-element, and block-wise fittings. For the purpose of clarity, an enlarged view of the eigenvalue spread near the imaginary axis showing the imaginary eigenvalues and passivity violation is shown on the bottom of Figure 4.2. The numerical values of passivity violated

regions are summarized in Table 4.3 and are further verified by singular value decomposition in Figure 4.3. All three strategies result in two passivity violation regions, and the difference between passivity violation regions according to the three methods is minimal.

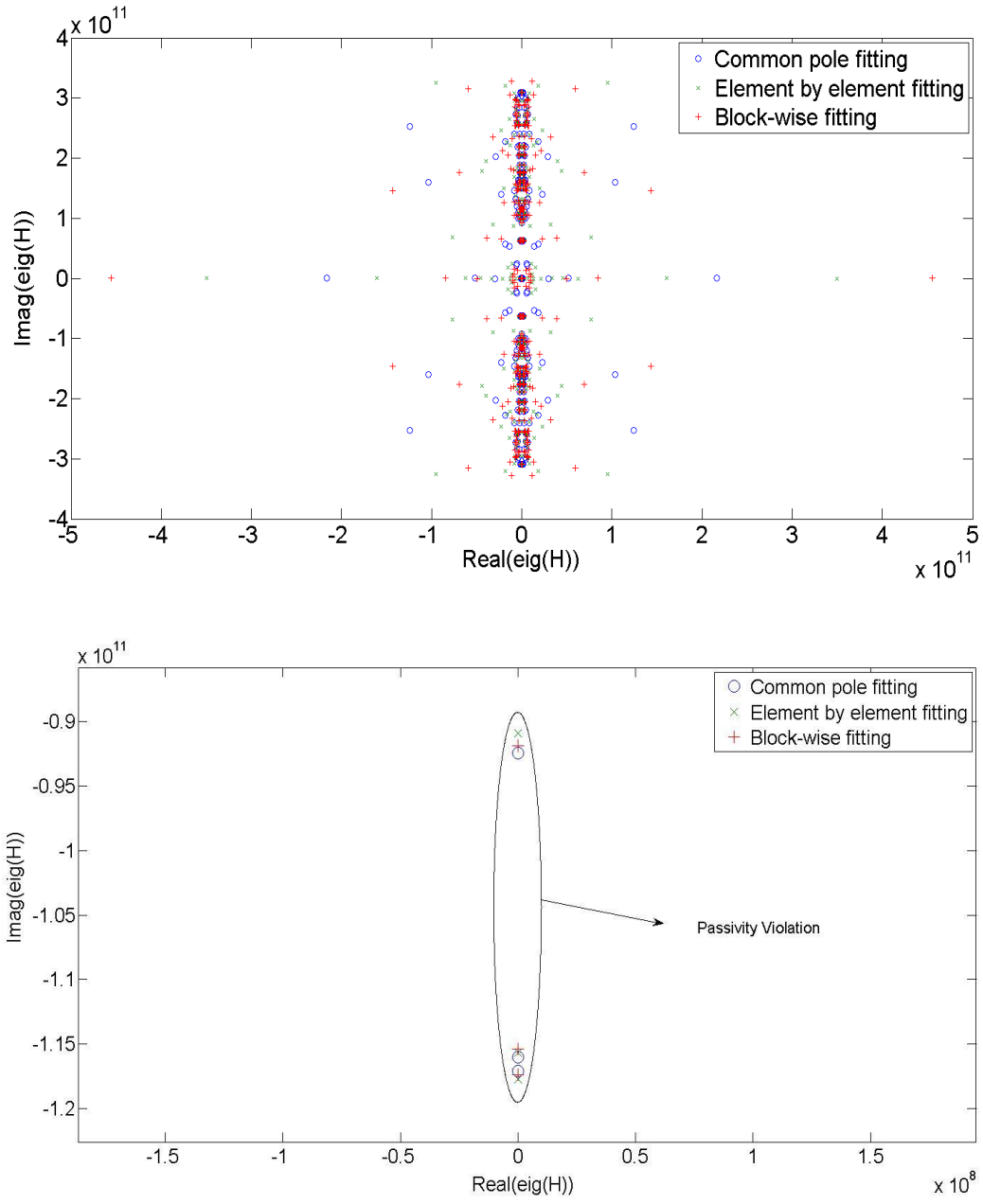

Figure 4.2: Comparison of the eigenvalues of Hamiltonian distribution (top) and passivity violation region (bottom) for common-pole, element-by-element and block-wise fitting.

Table 4.3: Comparison of passivity violation region according Hamiltonian matrix for common-pole, element-by-element and block-wise fitting

Passivity assessment	Passivity violation regions
Common-pole fitting	dc ~ 14.709 GHz, 18. 461 ~ 18.613 GHz
Element-by-element fitting	dc ~ 14.467 GHz, 18.405 ~ 18.736 GHz
Block-wise fitting	dc ~ 14.625 GHz, 18.367 ~ 18.683 GHz

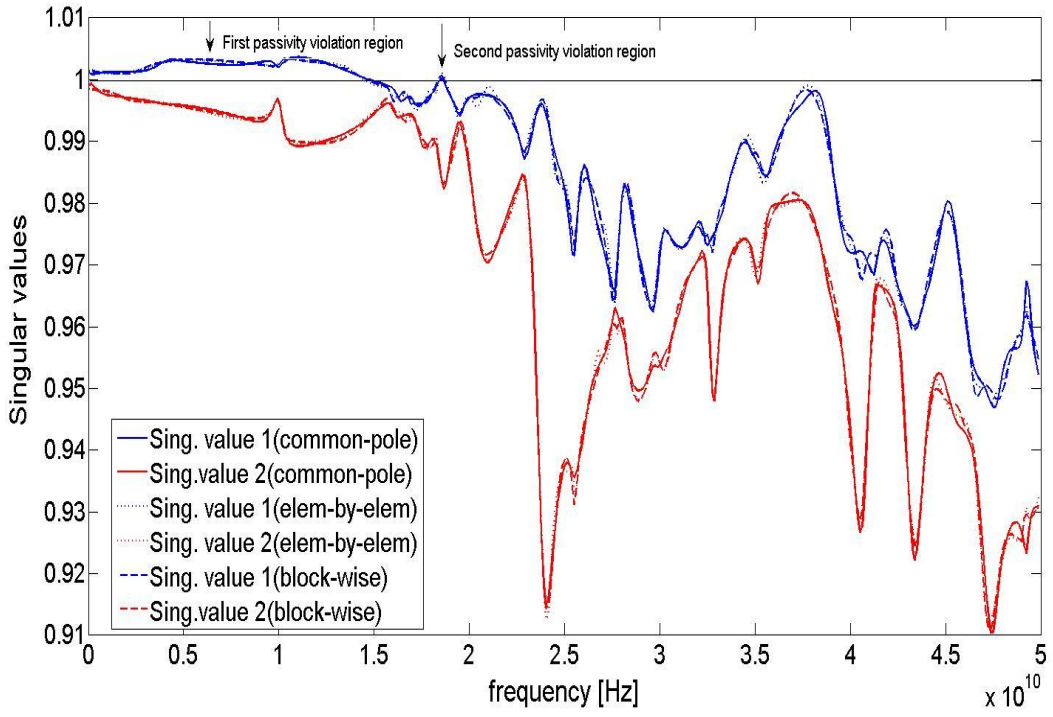

Figure 4.3: Comparison of the passivity violation regions for common-pole, element-by-element and block-wise fitting through singular value decomposition.

After two passivity violation frequency bands are detected, an iterative residue perturbation approach is applied to common-pole, element-by-element, and block-wise fitted state space representation, to enforce passivity. Figure 4.4 shows the result of the singular values of common-pole, element-by-element, and block-wise passivity enforcement scheme after two iterations have taken place, and Figure 4.5 shows the maximum singular values of three

enforcement techniques with respect to two iterations. We see the monotonic decrease of the maximum singular value for all three techniques as the number of iteration steps increase during the passivity enforcement scheme. It took three iterations for element-by-element fitting while it took two iterations for other techniques. Table 4.4 summarizes the computation time of passivity assessment and passivity enforcement for three different techniques. Literally, there is not much difference among the three techniques in terms of computational efficiency.

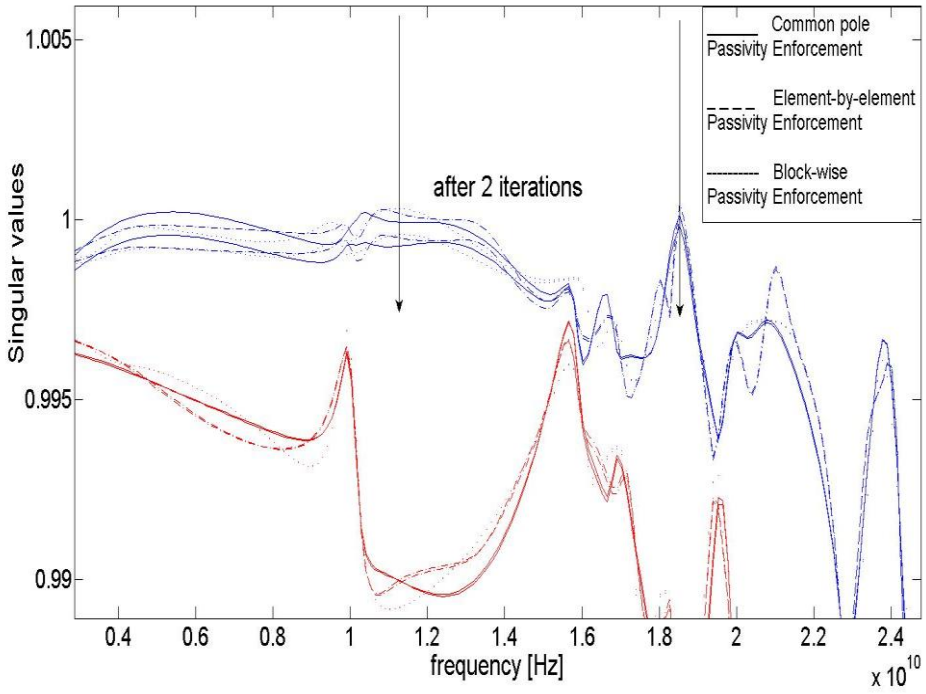

Figure 4.4: Passivity enforcement for common-pole, element-by-element and block-wise fitting after two iterations.

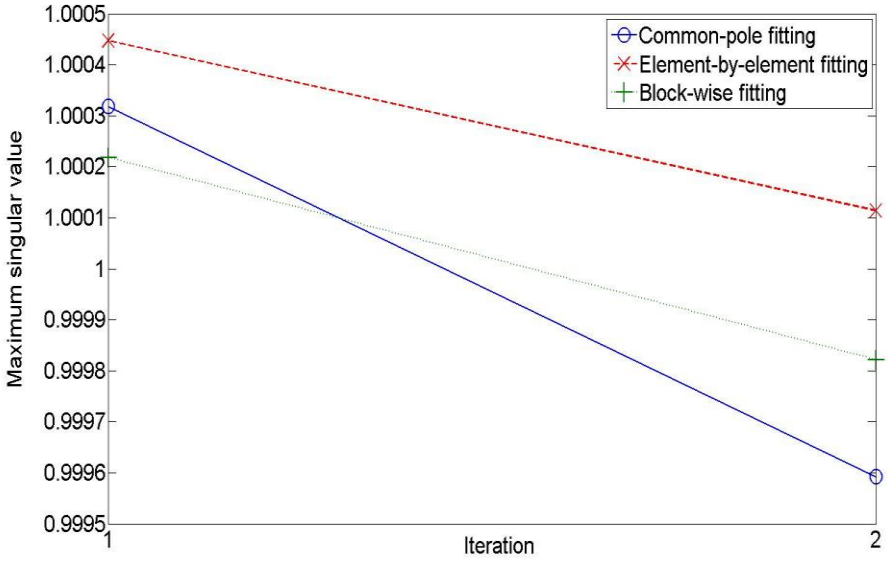

Figure 4.5: Maximum singular value of the 2-port coplanar waveguide for common-pole, element-by-element and block-wise passivity enforcement in each iteration step.

Table 4.4: Comparison of the computation time of passivity assessment (Hamiltonian matrix) and passivity enforcement (iterative perturbation of residues) of common-pole, element-by-element and block-wise rational approximation models.

	Passivity assessment	Passivity enforcement
Common-pole fitting	0.214337 s	0.80412 s
Element-by-element fitting	0.751283 s	0.576519 s
Block-wise fitting	0.747763 s	0.358611 s

Lastly, Figure 4.6 shows the magnitude of S_{11} and S_{12} after passivity enforcement has been applied for three techniques. The passivity enforcement via iterative residue technique enforces passivity of the original spectrum while maintaining the accuracy of the initial spectrum.

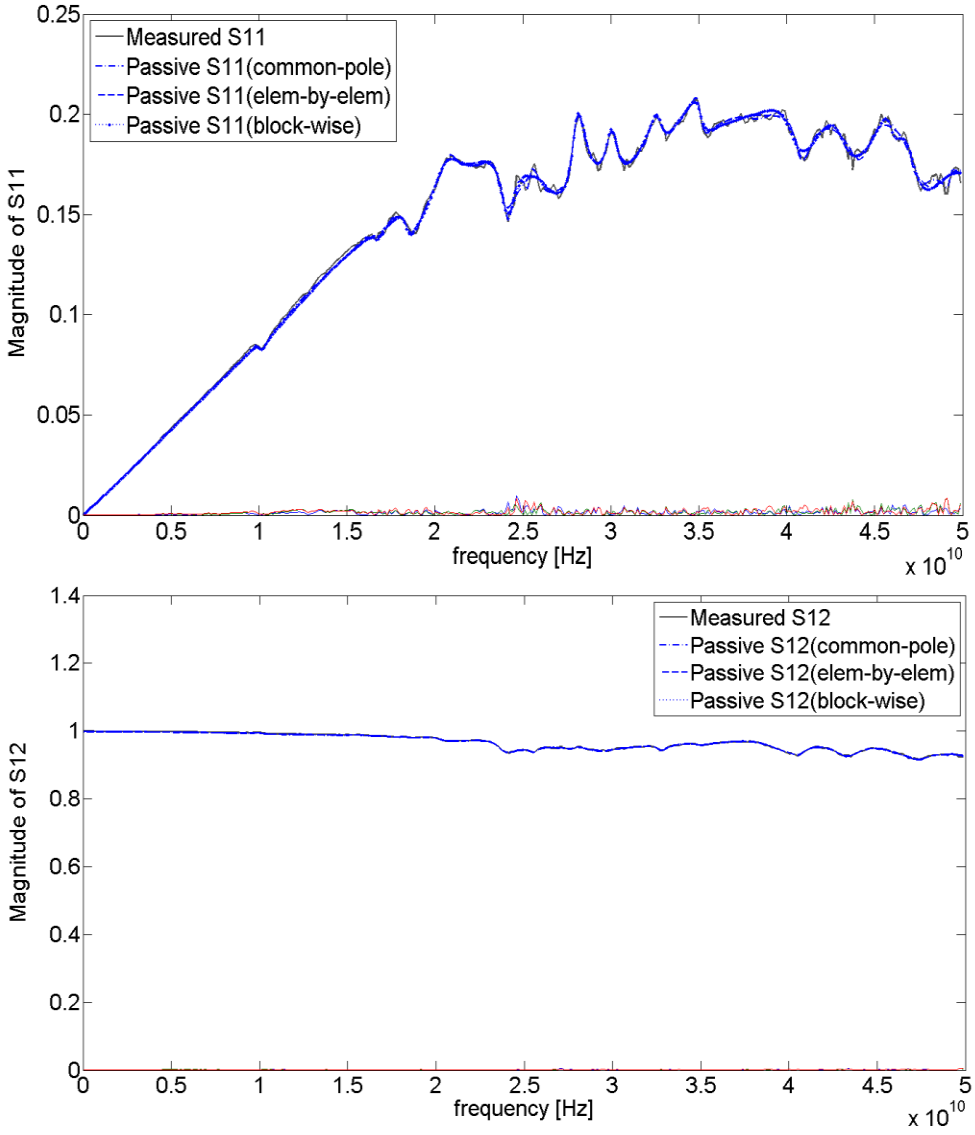

Figure 4.6: Magnitude of S_{11} (top) and S_{12} (bottom) after passivity enforcement for common-pole, element-by-element, and block-wise rational interpolation.

Hence, from the passivity assessment and enforcement comparison in Table 4.4 and from the magnitude of S_{11} and S_{12} after passivity enforcement, we see that element-by-element and block-wise fitting and subsequent passivity enforcement techniques are reliable alternatives to the well-known common-pole passivity enforcement technique not only in terms of preserving the accuracy of the solution, but also in terms of the computation efficiency.

4.5.2 Four-port package example

In the second example, 4-port package structure with two power and ground pins, VDD and VDDO placed and extended over different layers through vias are considered. The output $\boldsymbol{S}$ parameter matrix was simulated through SPEED 2000 of Sigrity from 10 MHz to 2 GHz in 545 uniform frequency samples. DC extrapolation [74] was applied to this model and 66 non-uniform samples from DC to 2 MHz were added to the existing samples, making 611 samples in total. In this example, we attempt to verify the accuracy of the rational approximation, the computational efficiency and robustness of the passivity assessment and enforcement methodologies in common-pole, element-by-element, and block-wise fast VF and compare each equivalent netlist model in time domain. We first use three different stable rational function approximations of the $\boldsymbol{S}$ matrix while applying the same number of poles. For common-pole fitting, 20 complex conjugate poles are applied. For element-by-element fitting, 20 complex conjugate poles for each element are applied. Lastly, for block-wise fitting, two groups are applied, the first with 4 elements (S_{11}, S_{22}, S_{33}, S_{44}) and the second with 12, each having 20 common complex conjugate poles. Common-pole fitting with 20 poles resulted in 6.321486 seconds with RMS error of 0.001388. Element-by-element fitting with 20 poles resulted in 33.177491 seconds with RMS error of 0.00059057. Finally, block-wise fitting of two groups, each having 20 common poles, resulted in 7.20477 seconds with RMS error of 0.0011048. Using the same order, element-by-element fitting gives the most accurate solution, since least squares fitting of each element is done with optimal and flexible pole placement. Block-wise is a hybrid of element-by-element and common-pole fitting, as it will allow better fitting accuracy than common-pole fitting with less computation time than element-by-element fitting. In terms of computation time, element-by-element fitting will be the most time-consuming as it requires rational function fit of each

element. Block-wise fitting gives good accuracy while reducing computation time to fit multiport systems.

Next, we use common-pole, element-by-element and block-wise fitting to meet the required RMS error of 0.001. Table 4.5 summarizes the pole order, RMS error, and the computation time to achieve the RMS error threshold. Again, we see that the common-pole fitting strategy gives the greatest computational advantage, while block-wise fitting with two groups is a close second.

Table 4.5: Comparison of number of poles, RMS error, and computation time for common pole, element-by-element and block-wise fitting for fast VF.

Fast Vector Fitting	Number of poles needed	RMS error	Rational approximation time
Common pole fitting	22 c.c. poles	0.00096687	5.865177 s
Element-by-element fitting	$N_e = \begin{bmatrix} 10 & 20 & 20 & 10 \\ 20 & 10 & 16 & 20 \\ 20 & 16 & 20 & 20 \\ 10 & 20 & 20 & 20 \end{bmatrix}$	0.00094247	25.86676 s
Block-wise fitting	$N_e = \begin{bmatrix} 18 & 20 & 20 & 18 \\ 20 & 18 & 18 & 20 \\ 20 & 18 & 20 & 20 \\ 18 & 20 & 20 & 20 \end{bmatrix}$ <u>Two groups:</u> First group with 18 common poles (S_{11}, S_{14}, S_{22}, S_{23}, S_{32}, S_{41}) Second group with 20 common poles (S_{12}, S_{13}, S_{21}, S_{24}, S_{31}, S_{33}, S_{34}, S_{42}, S_{43}, S_{44})	0.0009946	7.281168 s

Figure 4.7 shows the distribution of the eigenvalues of Hamiltonian matrix of three fitting strategies, and Table 4.6 shows the passivity violation regions of three fitting strategies. The passivity violation regions for element-by-element (23.98 MHz ~ 33.16 MHz) and block-wise

fitting (23.263 MHz ~ 32.3 MHz) were greater than the passivity violation region for common pole (21.31 MHz ~ 23.066 MHz) fitting for this example. Figure 4.8 shows the singular values of the three different rational function fit of the S matrix, and verifies that the passivity violation regions for each fit are same as predicted by the Hamiltonian matrix.

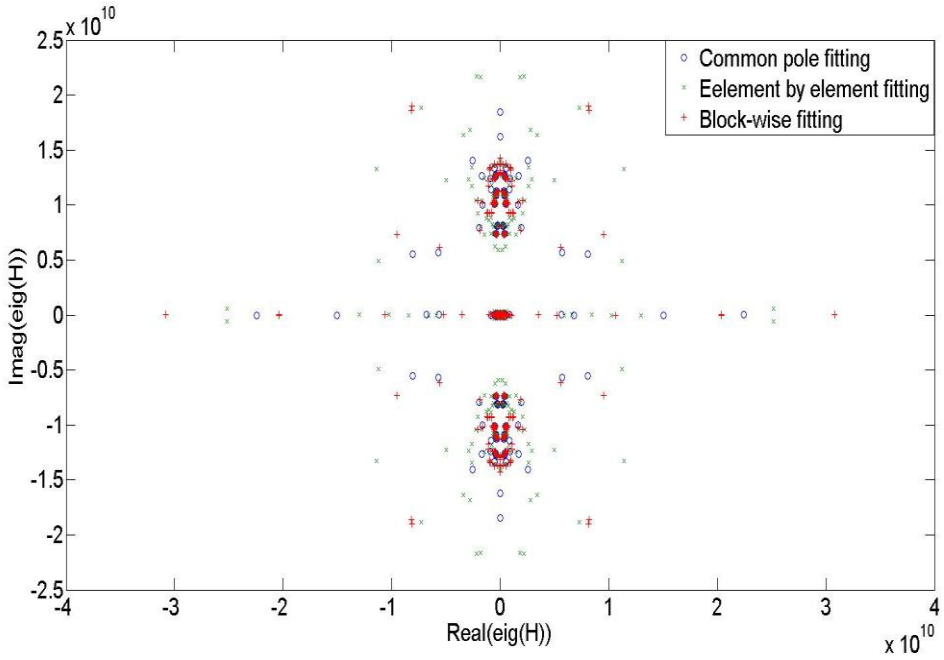

Figure 4.7: Comparison of the eigenvalues of Hamiltonian distribution (top) and passivity violation region (bottom) for common-pole, element-by-element and block-wise fitting.

Table 4.6: Comparison of passivity violation region according Hamiltonian matrix for common-pole, element-by-element and block-wise fitting.

Passivity assessment	Passivity violation regions
Common-pole fitting	21.31 MHz ~ 23.066 MHz
Element-by-element fitting	23.98 MHz ~ 33.16 MHz
Block-wise fitting	23.263 MHz ~ 32.3 MHz

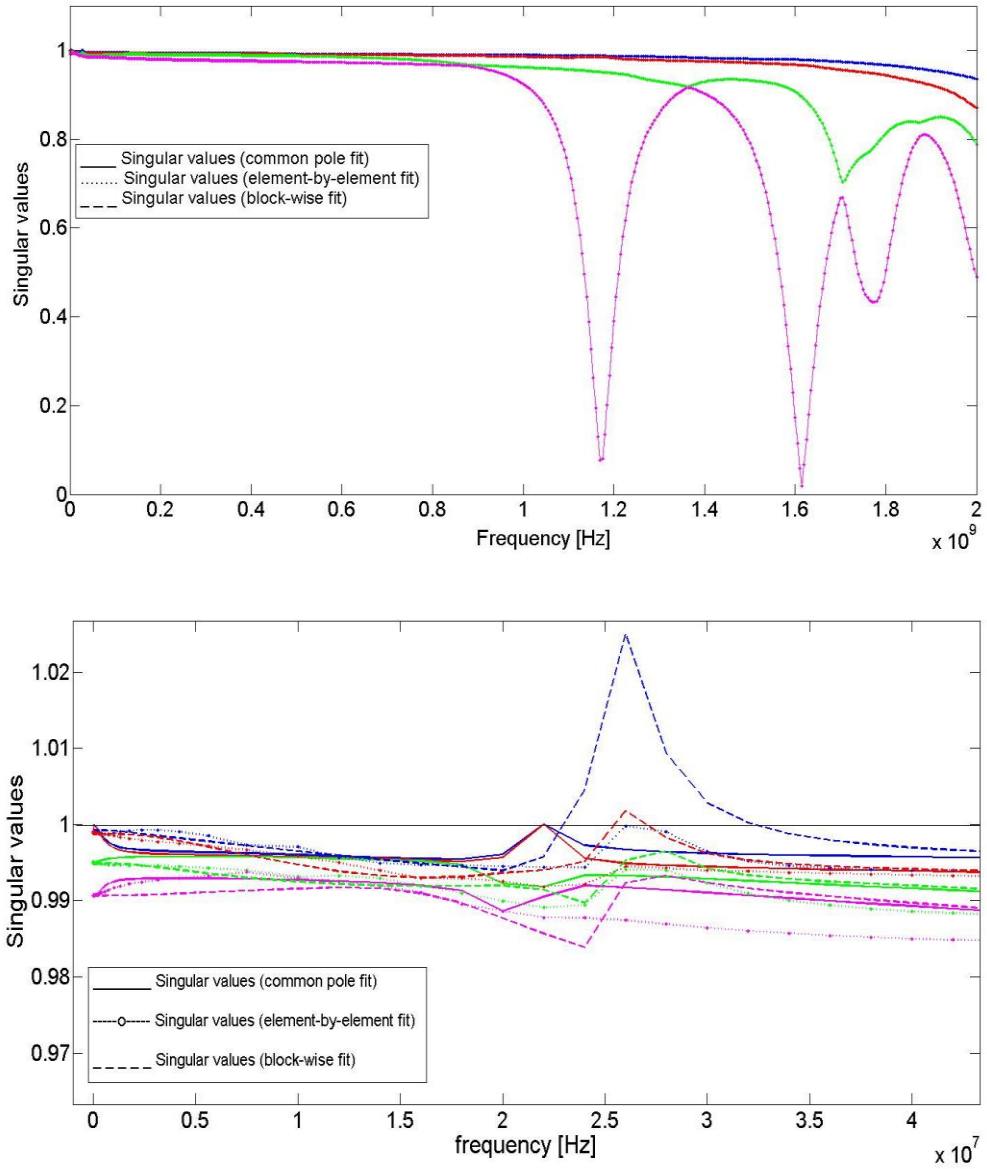

Figure 4.8: Comparison of the passivity violation regions (top) and close look at passivity violation region (bottom) for common-pole, element-by-element and block-wise fitting through singular value decomposition.

Figure 4.9 compares the passivity enforcement of three fitting strategies. It took 9 iterations for both common-pole and block-wise passivity enforcement schemes and 8 iterations for element-by-element passivity enforcement scheme to suppress the frequency regions where singular values greater than 1 and passivity violation occur.

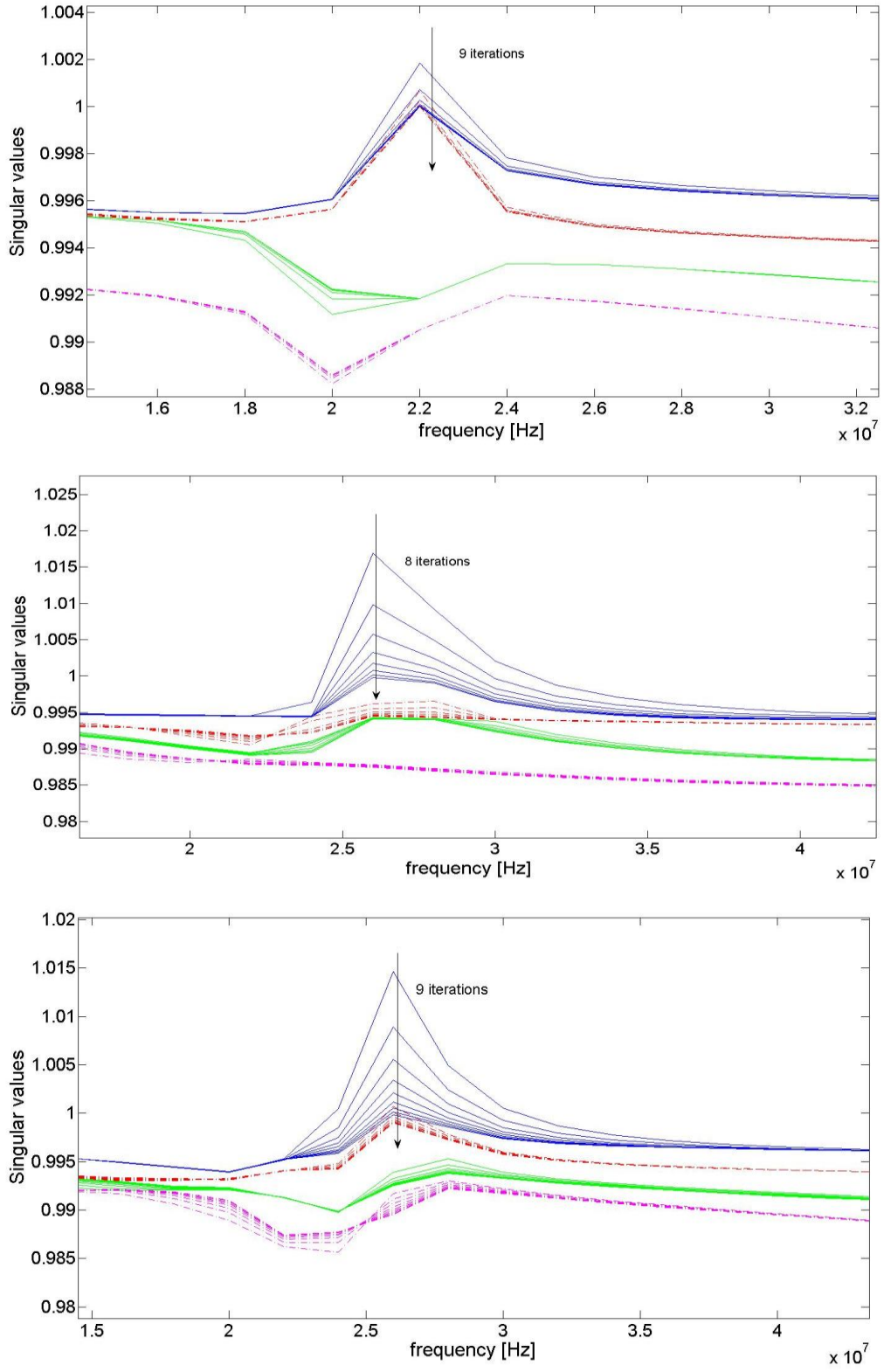

Figure 4.9: Passivity enforcement for common-pole (top), element-by-element (middle) and block-wise (bottom) fitting.

Figure 4.10 shows the changes of maximum singular values of common pole, element-by-element, and block-wise passivity enforcement techniques with respect to the number of iterations. For example, the maximum singular value of block-wise fitting decreases monotonically from 1.015to 0.998 in 9 iterations.

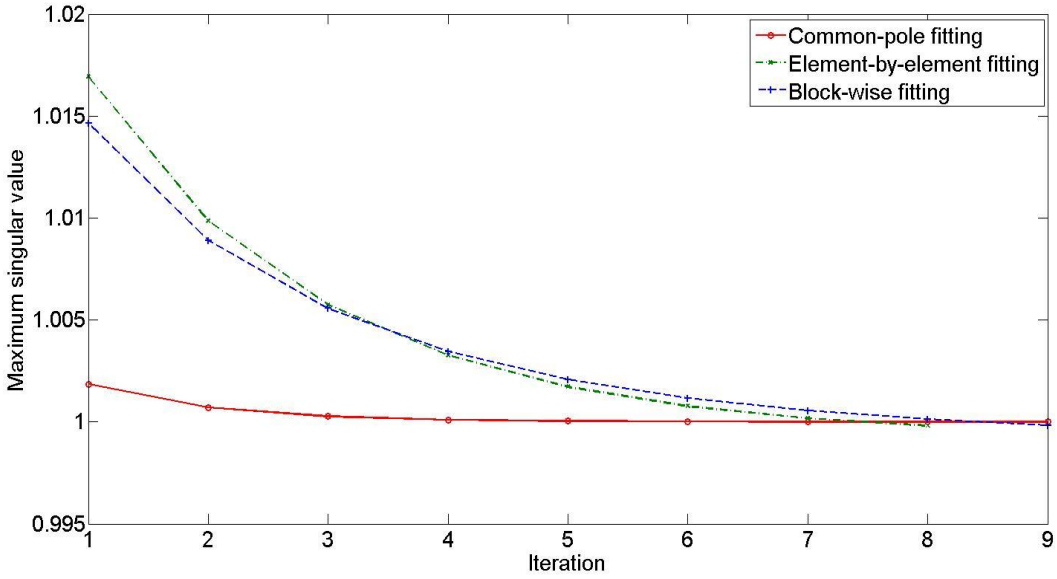

Figure 4.10: Maximum singular value comparison of common-pole, element-by-element, and block-wise passivity enforcement techniques with respect to the number of iterations used for residue perturbation

Table 4.7 compares the computation time of passivity assessment and passivity enforcement techniques for three fitting strategies. The size of the Hamiltonian matrix for common-pole, element-by-element, and block-wise representation is 176×176 , 544×544, and 616×616, respectively, and hence gives common-pole fitting ~ 10 times more edge than the element-by-element and block-wise fitting. The passivity enforcement scheme depends actually on how tolerance factor δ (usually set up as 0.999) is defined. If the tolerance factor is greater than the threshold defined above but less than 1, it will result in smaller $\sum_{viol}$, $\boldsymbol{S}_{fit\_viol}$, and $\boldsymbol{C}_{e.e.viol}$. Since in each iteration step, subsequent passivity violation residues based on the tolerance factor

will be subtracted from the initial residues, greater threshold results in smaller changes in the residues per iteration. This results in a greater number of residue perturbations and increase of computation time for enforcing passivity of the original model. However, at the same time, this has benefits such that passivity enforcement can better approximate the original curve, while making changes, compared to using a smaller tolerance factor.

Table 4.7: Comparison of the computation time of passivity assessment (Hamiltonian matrix) and passivity enforcement (iterative perturbation of residues) of common-pole, element-by-element and block-wise rational approximation models.

	Passivity assessment	Passivity enforcement
Common-pole fitting	0.215222 s	7.164465 s
Element-by-element fitting	2.095468 s	6.565856 s
Block-wise fitting	3.169443 s	6.948339 s

Figure 4.11 shows the magnitude and phase of S12 and S14 after passivity enforcement has been applied. We see that there is a minimal difference between the original S matrix, and the result of common-pole, element-by-element and block-wise fitting and subsequent passivity enforcement. After the passivity enforcement, the state space representation of 4 port package system can further be extended in terms of SPICE-compatible equivalent netlist. Figure 4.12 shows the circuit termination and the transient response based on common-pole fitting, element-by-element fitting, and block-wise fitting and passivity enforcement. Port 1 is defined as power pin VDD in layer 1, and port 4 the same power pin VDD in layer 27. Ports 2 and 3 are defined as ground pin VDDO in layer 1 and 27, respectively. Figure 4.12 shows three different transient simulation cases with common-poles, element-by-element, and block-wise fitting. The configuration is such that the transient response given by applying input pulse wave of 1 V with 2ns rise/fall time at port 1. All other ports are terminated with 50 Ω. The transient responses of

all four ports of three different SPICE equivalent netlists based on different fitting and passivity enforcement techniques show very good agreement with each other.

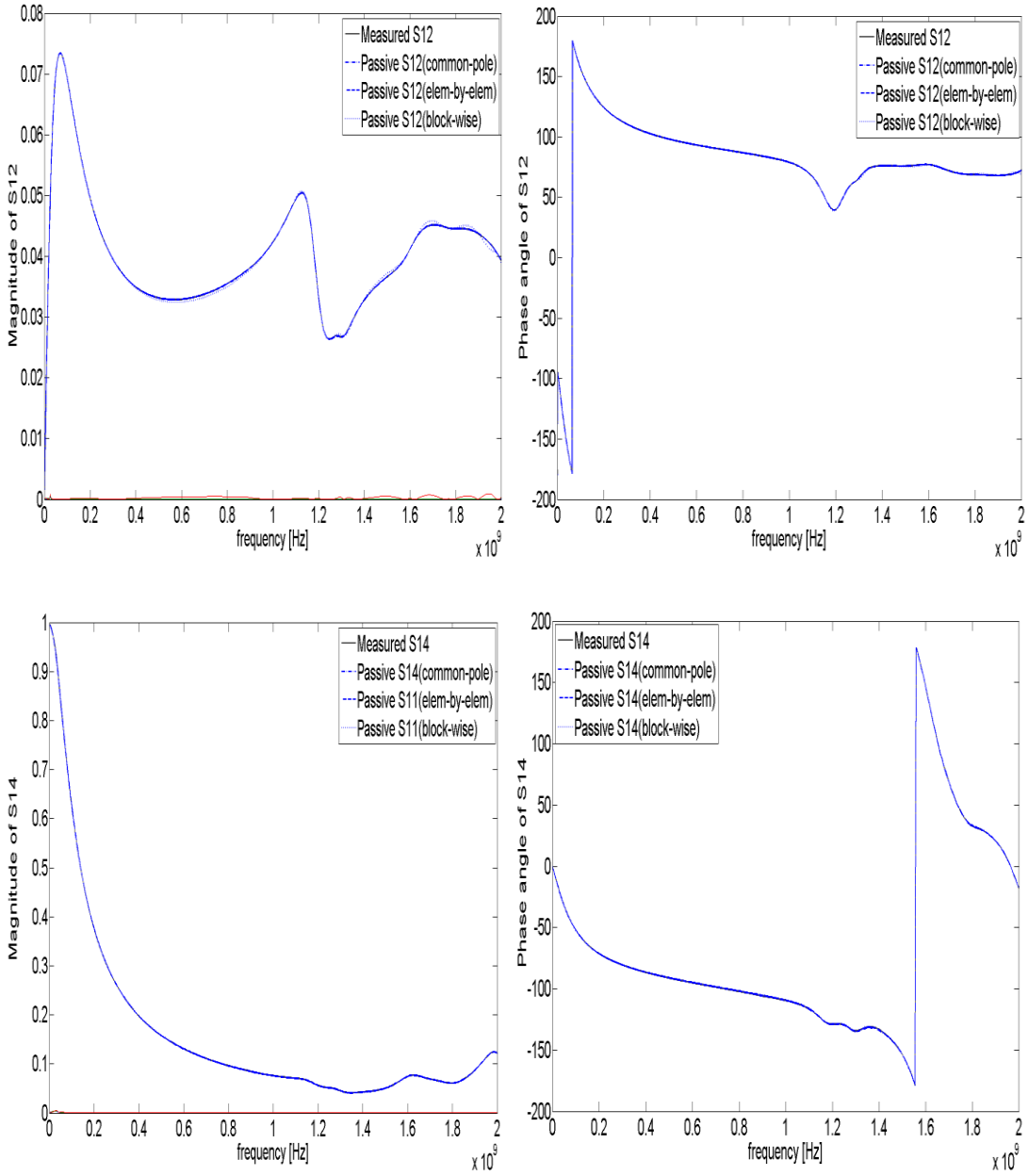

Figure 4.11: Magnitude and phase of S12 (top) and S14 (bottom) after passivity enforcement for common-pole, element-by-element, and block-wise rational interpolation.

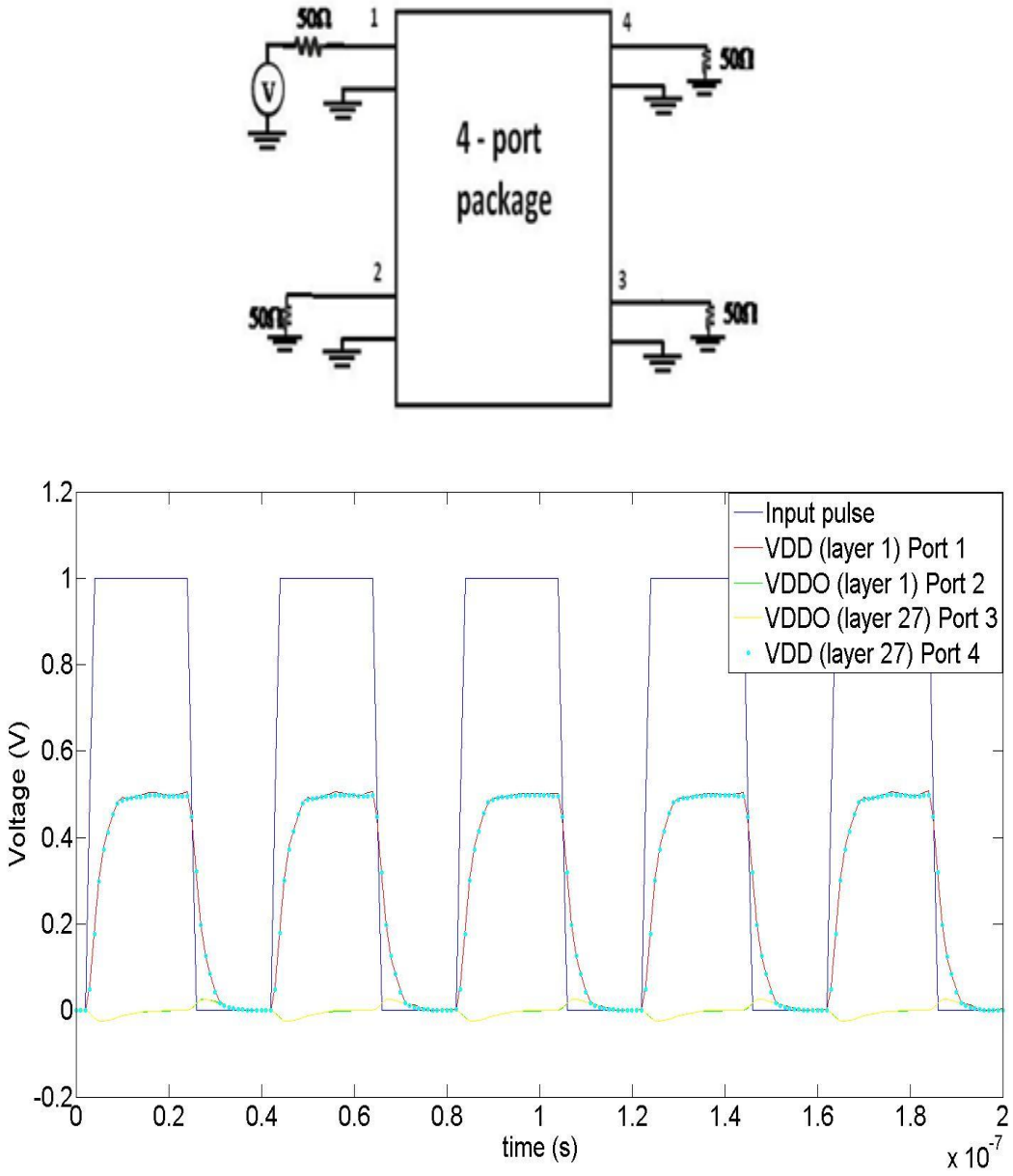

Figure 4.12: A 4-port package network representation (above) and the subsequent transient response of passivity enforced common-pole, element-by-element and block-wise fitting.

4.6 Summary

In this section, two different options of rational function fitting, namely element-by-element fitting and block-wise fitting with respective passivity assessment and enforcement techniques, were considered as an alternative to common-pole fitting and passivity enforcement technique.

In sparse VF setting, it was observed that element-by-element and block-wise fitting of the system actually resulted in a more accurate macromodel with fewer poles than the common-pole fitting. It was also observed that these two approaches presented huge improvement in computational efficiency over the common-pole fitting. In terms of rational function approximation, common-pole and block-wise fitting are regarded as more efficient than element-by-element fitting due to less iteration with the least squares elements involved. In terms of memory and space allocation, element-by-element fitting and block-wise fitting are considered better techniques than common-pole fitting. We have also applied three different fitting techniques in passivity assessment and enforcement schemes, and compared the accuracy and robustness of these models. A robust iterative residue perturbation passivity enforcement technique was chosen because of its simplicity and distinctive computational advantages over other passivity enforcement techniques. Based on the 2-port and 4-port examples, a global passivity assessment through Hamiltonian matrix was achieved, and passivity violation regions were detected. It was shown that state space representation and Hamiltonian matrix of the common-pole fitting were smaller than element-by-element and block-wise representation. All three fittings in frequency domain after the passivity enforcement were compared to the original S matrix model that was not passive. The curves from the Figures suggest that they are in excellent agreement.

It shows that the block-wise fitting, element-by-element fitting and the passivity enforcement techniques bring certain benefits (either time or storage) over common-pole fitting. Note that the passivity enforcement technique has been tested with small and mid-size ports with reasonable number of frequency samples. For large number of ports with rich resonant behavior that requires large order, further reduction of the original model is necessary.

CHAPTER 5

ADAPTIVE SAMPLING OF BROADBAND INTERCONNECT STRUCTURES

5.1 Introduction

Recently, significant emphasis has been put on the development and advancement of robust methodologies for the passive, rational-function fitting of broadband, electromagnetic responses of interconnect structures associated with the signal and power distribution networks of packaged electronic systems. These methodologies are expected to handle both numerically computed and measured data, quantified either in terms of a transient electromagnetic response or a broadband frequency sweep. Algorithms like VF and its derivatives [21]-[36] have become the computer tools of choice in the community for achieving the rational function fit. The computational efficiency, accuracy, and numerical robustness of these algorithms are strongly dependent on the number of sampling frequencies at which the data is obtained. This is especially true in the case of multi-port networks with broadband responses spanning a few tens of GHz. Therefore, we are interested in systematic methodologies that reduce the number of frequency samples in describing the interconnect response while preserving the accuracy of macromodeling. Such a methodology is proposed and demonstrated in this chapter.

Several efficient and systematic ways of picking and selecting the reduced frequency samples of the original electromagnetic response of high-speed interconnect structure have been proposed [84]-[94], resulting in computationally efficient rational approximation of broadband transfer

matrix. In [85], an adaptive knot is placed at the mean of the selected samples while extending spline interpolation iteratively to reduce the size of the frequency samples and the ensuing matrix needed for rational function fitting. In [84], a reduced set of samples are determined adaptively by rational interpolation and from the evaluation of the error estimates of the corresponding spectra with the original spectra in a recursive manner. In [86] and [87], frequency samples are iteratively chosen and the sample size is refined such that singular values of the macromodel based on the adaptive sampling are less than unity. In another words, the passivity of the macromodel that represents the system is guaranteed, as the frequency samples are chosen adaptively.

In order for the adaptive sampling methodology to be effective, two important criteria have to be met. First, it is necessary that the technique reduce the overall cost of the rational function approximation, while preserving the accuracy of the original data. The number of rows of the least squares matrix, $\boldsymbol{Au = b}$, is $2N$, where N is the number of frequency samples that depicts the discrete samples of the broadband data. The standard VF algorithm involves multiple iterations of three steps, namely, pole identification, eigenvalue decomposition, and residue identification. The numerical computation at each one of the three stages of the rational function interpolation involves matrix operations, the cost of which depends on the number of frequency samples of the original interconnect data. Thus, reduction of the number of samples reduces the matrix size, memory, and the computational cost involved with the manipulation of the matrices involved in these stages.

Second, it is also important for the reduced model to preserve the physical consistency of the original system. While this constraint is rigorously checked and corrected at the passivity enforcement stage of the macromodeling, it would be very useful for the reduced sampled model

to provide the means to quickly assess and show if the data used for the model under development describe a physically consistent system. This gives an insight into whether the measurement or simulation data that depicts the high-speed passive interconnect models has a physical meaning, before proceeding to the next stage of the macromodeling.

In this chapter, a new methodology [88] is presented that provides solutions to the aforementioned two issues. This methodology provides for a systematic and accuracy-preserving reduction of large sets of measured or numerically extended data quantifying the broadband frequency response of passive electromagnetic structures. The proposed methodology is different from other approaches in that it provides for an adaptive sampling approach that uses Blumer's index [90] to check for the causality of the original system. If the original system is not causal and thus not passive, this will be reflected by the Blumer's index of the reduced number of frequency samples in adaptive sampling steps. The proposed methodology is also useful for enhancing the computational efficiency and improving numerical robustness and accuracy of rational function fitting for the synthesis of equivalent circuit representations of interconnect structures.

5.2 Adaptive Sampling Strategy

The proposed methodology makes use of the adaptive sampling idea proposed by Blumer for minimizing the number of frequency points at which the numerical calculation of the causal electromagnetic transfer function of a transmission line system should be calculated [90]. Subsequently, application of this method to expedite broadband CW measurements was reported in [89]. For our purposes, we are interested in exploring the applicability of the approach to reducing a given set of calculated or measured data describing the electromagnetic response of a causal, multi-port electromagnetic network of the type encountered in the signal distribution

networks of packaged electronic systems. In the following, we review the methodology in the context of such an application.

Blumer's idea is founded on the fact that for a causal transfer function the real and imaginary parts of its spectrum are constrained by the Hilbert transform relationship. Let $F(\omega)$ be frequency response of causal transfer function, and let $U(\omega)$ and $V(\omega)$ depict the real and imaginary components of $F(\omega)$. Knowing that $U(\omega)$ and $V(\omega)$ are the Hilbert transforms of each other and each is square integrable, energy conservation has to be satisfied through Parseval's theorem. Equations (5.1) and (5.2) below explain the detailed steps of the Parseval's theorem between real and imaginary component of the spectra in frequency domain, while (5.3) shows the result of energy conservation.

$$\int_0^\infty |U(\omega)|^2\, d\omega = \int_0^\infty \frac{1}{\pi} pv \int_0^\infty \frac{V(s)}{\omega - s} ds \frac{1}{\pi} pv \int_0^\infty \frac{V(t)}{\omega - t} dt\, d\omega$$
$$= \int_0^\infty \int_0^\infty \frac{1}{\pi^2} \int_0^\infty \frac{d\omega}{(\omega - s)(\omega - t)} V(s) ds V(t) dt \tag{5.1}$$

$$\frac{1}{\pi^2} \int_0^\infty \frac{d\omega}{(\omega - s)(\omega - t)} = \delta(s - t) \tag{5.2}$$

$$\int_0^\infty |U(\omega)|^2 d\omega = \int_0^\infty |V(\omega)|^2 d\omega \tag{5.3}$$

In view of (5.3), Blumer proposed the use of the following Blumer index, *B*, as a means of assessing the accuracy of a set of discrete data for the electromagnetic spectrum under consideration.

$$B = \left\{ 1 - \left| \frac{\sum_{\omega_i=\omega_{min}}^{\omega_{max}} |U(\omega_i)|^2 \Delta\omega_i - \sum_{\omega_i=\omega_{min}}^{\omega_{max}} |V(\omega_i)|^2 \Delta\omega_i}{\sum_{\omega_i=\omega_{min}}^{\omega_{max}} |U(\omega_i)|^2 \Delta\omega_i + \sum_{\omega_i=\omega_{min}}^{\omega_{max}} |V(\omega_i)|^2 \Delta\omega_i} \right| \right\} \times 100(\%) \tag{5.4}$$

Clearly, the above expression has been written for the case of discrete spectra. For the case of continuous spectra the summations are replaced by the integrals in Equation (5.3). The ideal value of the Blumer index is 100 %; hence, a number of discrete samples will be deemed adequate if the calculated Blumer index is sufficiently close to 100 %. The use of the Blumer index in implementing a systematic methodology for reducing the number of frequency samples necessary for the accurate description of the electromagnetic transfer function is discussed next through the aid of the flow diagram presented in Figure 5.1. With the given transfer function, $F(\omega)$ is uniformly or non-uniformly sampled over the bandwidth $\omega_{min} \leq \omega \leq \omega_{max}$, and we define an initial set of three frequencies points, namely, ω_{min}, ω_{max}, and $\omega_m \approx (\omega_{min} + \omega_{max})/2$. The ≈ sign indicates that the frequency sample closest to the midpoint of the frequency interval is assigned as the third frequency ω_m. This initial set of frequency points will be augmented in an iterative fashion with additional frequency points selected from the available data making use of the discrete spectral derivative of the given discrete data defined according to the Equation (5.5),

$$\Delta F_i = \frac{F(\omega_i) - F(\omega_{i-1})}{\omega_i - \omega_{i-1}}, \qquad i = 1,2,\dots,N_p - 1 \tag{5.5}$$

where N_p is the number of the frequency samples in the discrete spectrum of the electromagnetic transfer function. Following [89], let ΔF_{max} and ΔF_{min}be, respectively, the maximum and the minimum discrete spectral derivative magnitudes from the set in Equation (5.5). Then, the following equation is used to define the number of additional samples $(N_{aug})_k$ to be used in each interval defined by consecutive data points, ω_{k-1}, ω_k,

$$(N_{aug})_k = 1 + \left[m \frac{|\Delta F_k| - |\Delta F_{min}|}{|\Delta F_{max}| - |\Delta F_{min}|} \right] \tag{5.6}$$

where $[\bullet]$ denotes the integer function and m is an integer, the choice of which dictates the density of additional points introduced in each interval. In this manner, the regions where the spectrum is smooth and not varying much, ΔF_i is close to ΔF_{min}, and the number of new sampling points added is close to 1. On the other hand, regions where the spectrum is varying sharply (such as the large slopes values of the curve), ΔF_i is close to ΔF_{max}, and the number of new sampling points added is close to $(1 + m)$. Once the augmented set of points has been obtained, the Blumer index is computed. If its value is acceptable and if the absolute value of the difference between the original and adaptive sampled magnitude, $\left|F_{original}(\omega) - F_{adap}(\omega)\right|$ meets the threshold RMS error limit, then the iterative process terminates. Otherwise, the process continues with the insertion of additional points within each interval of consecutive frequency data in the updated data set. Once the adaptive samples are determined for the element of transfer matrix in frequency domain, the same adaptive sampling process is repeated for N^2 elements, where *N* is the number of ports, and adaptive samples from each element are combined to form final reduced sample set for *N*-port tabulated data. Figure 5.2 shows the flowchart of the finalized adaptive sampling. Once the reduced set is determined, VF can be used to represent the reduced set in terms of rational approximation, and a SPICE compatible equivalent circuit can be generated.

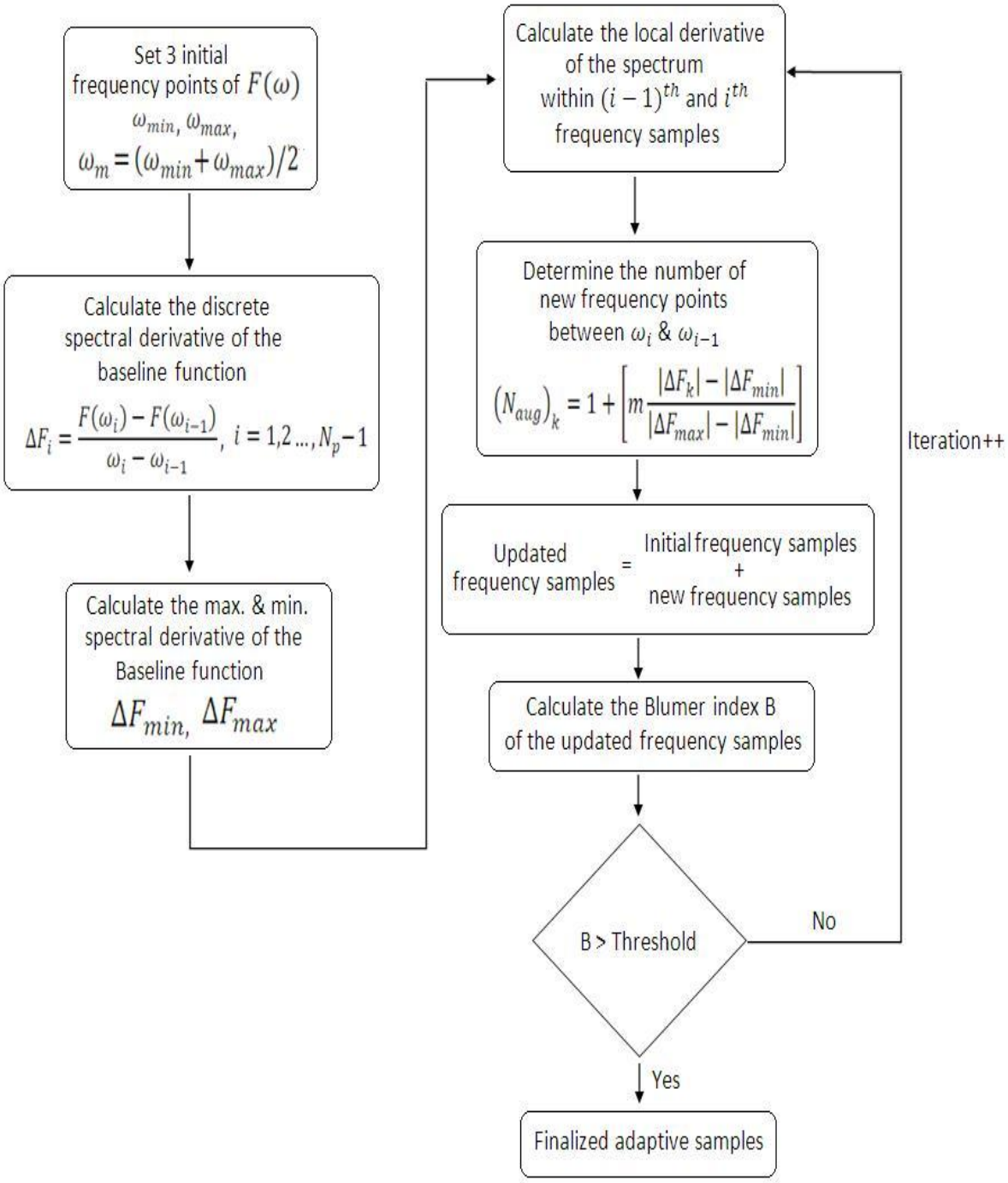

Figure 5.1: Flowchart of adaptive sampling process for each element.

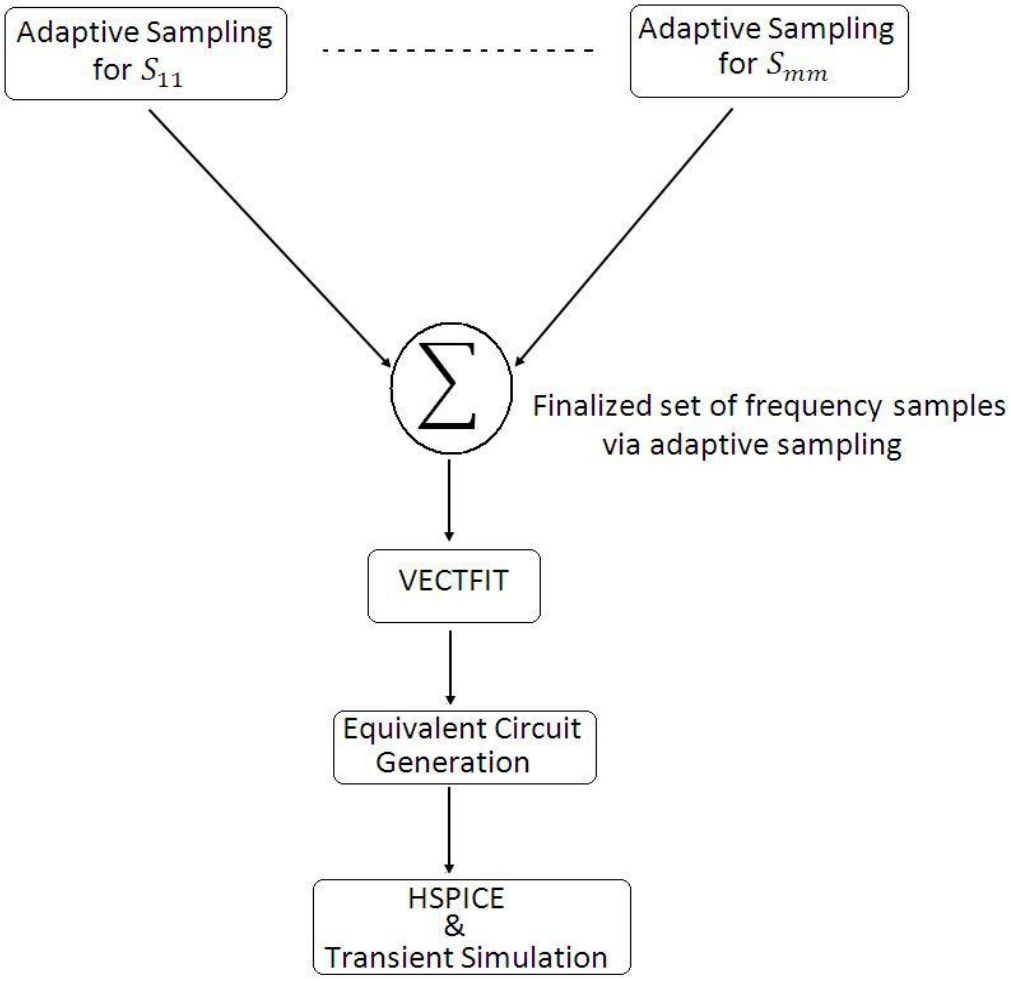

Figure 5.2: Flowchart of adaptive sampling process for multi-port tabulated S matrix.

5.3 Validation Studies

Next three examples are presented from the application of the proposed methodology to the reduction of discrete frequency data describing the measured spectra of electromagnetic responses. The numerical efficiency and computational cost of adaptive sampling VF is compared to standard VF. All simulations were done with 2.1 GHz Pentium processor with 1 GB RAM.

5.3.1 Two-port RF board example

The first example is for the scattering parameters of an unknown RF board interconnect, which was simulated in HFSS. Its scattering parameters were measured at 2001 frequency samples uniformly distributed over the bandwidth 10 MHz - 20 GHz. Figure 5.3 compares the magnitude of S_{12} of the original 2001 uniformly sampled data with that obtained using a set of 535 non-uniformly distributed points obtained after the fourth iteration of the process described above with m = 4, yielding a Blumer index of 98.2509%. A very good agreement is observed. The two sets of data were subsequently processed using VF with a passivity assessment and enforcement algorithm [63] to generate rational function fits for the scattering parameters of the two-port, which in turn were used for the development of an equivalent circuit for use in SPICE [82].

Since there is no *a priori* knowledge of the order of the tabulated data, the order of the model should be determined by the quality of the fitting of VF. If the RMS error of N order rational fit does not meet the RMS error threshold value of 3×10^{-3} for this example, then the order of the fit is increased by 2 and the whole VF process is iterated automatically until the final order chosen satisfies the RMS threshold. A rough estimate of the initial order of the system is determined in order to avoid unnecessary multiple loops of iterations and ensuing computational burden. The initial order is determined by the following algorithm. For common-pole fitting, the number n of local minima, ω_{min}^{n}, of the magnitude of S_{11} are detected by setting a threshold parameter δ, and locating the peaks and valleys, where there are points lower/higher by δ on both sides. Then the initial poles are placed at

$$p_n = (-a \pm j)\omega_{min}^{n}\,, \tag{5.7}$$

where the real part $a \ll 1$ is chosen such that starting poles are predominantly imaginary. This is a typical starting pole choice in VF and it guarantees good numerical stability of the VF condition. As iterations take place during the VF process to relocate the optimum poles, the real parts of the starting poles will change such that they closely approximate the original data.

Comparison of the performance of the VF algorithm in fitting the two sets of data using the same number of poles is documented in Table 5.1. Both sets required 62 poles to meet the RMS error threshold. The computation time for the adaptively sampled reduced set was 56.32506 s, which is 2.518 speed-up in comparison to the standard VF. The synthesized equivalent circuit was used in SPICE for a transient simulation, with one end of the line match terminated and the other driven by a voltage source of input resistance of 50 Ω and generating a pulse train waveform of 2 V with pulse delay of 2 ns, rise/fall time of 0.2 ns, pulse width of 800 ps, and period of 1600 ps. The calculated near- and far-end responses are in very good agreement as clearly depicted in Figure 5.4.

Table 5.1: Comparison of uniformly sampled set and reduced set for the case of a RF board.

Data Set	No. of Samples	No. of Poles	Iterations	RMS Error	VECTFIT Time
Uniformly Sampled Set	2001	62	5	0.0028824	141.8377 s
Reduced Set	535	62	5	0.0029192	56.32506 s

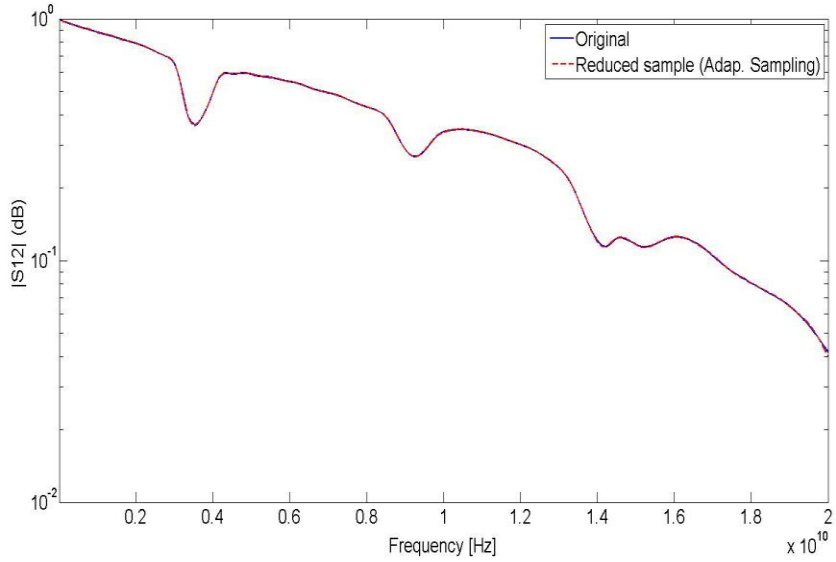

Figure 5.3: Comparison of magnitude of S12 for the original and reduced data set for the RF board.

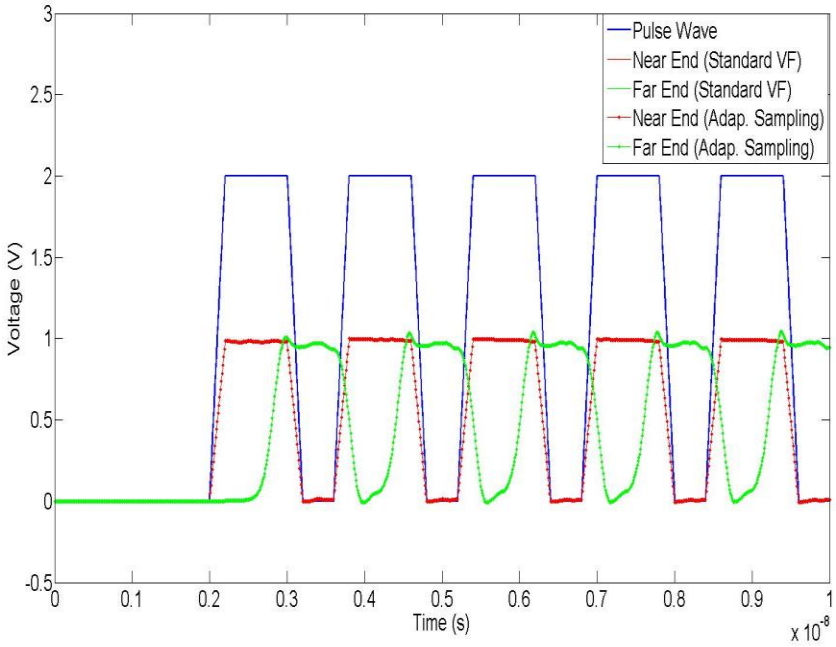

Figure 5.4: Comparison of calculated voltage transient responses using the synthesized SPICE netlists obtained using VECTFIT on the original and reduced frequency data sets of the RF board.

5.3.2 Two-port coupled line

The next example deals with measured data for a two-port scattering parameter matrix of a coupled line structure where the other two ports are terminated. The original data set contains

801 uniformly distributed samples over the range of 50 MHz to 5 GHz. The magnitude of the original ***S*** parameter data is shown in Figure 5.5. Adaptive sampling was applied to the measured data of 801 uniformly distributed samples. After four iterations, a set of 232 non-uniformly distributed points were selected, yielding a Blumer index of 92.9714 %, 98.2437 %, 97.8032 %, and 99.0874 % for S_{11}, S_{12}, S_{21}, and S_{22}, respectively. Twenty-six complex conjugate poles were selected initially as a result from local maxima and minima detection. VF was then used to fit the reduced set from the result of adaptive sampling, and the order of the system increased by 2 iteratively if RMS error of 3.5×10^{-3} was not met. Figures 5.6 and 5.7 depict the magnitude S_{11}, S_{12} and S_{21}, S_{22} of the adaptive sampling. A very good agreement between the original uniform sampled set and reduced set is observed. Then, original data with 801 samples and reduced data with 232 samples were both fitted with VF and the computation time was compared in Table 5.2.

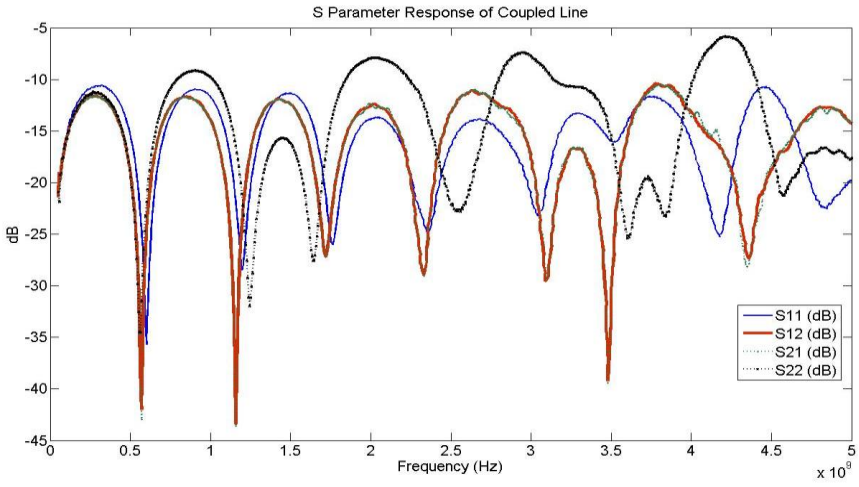

Figure 5.5: ***S***–parameter measurement (dB) of coupled line.

Table 5.2: Comparison of uniformly sampled set and reduced set for the case of a coupled line.

Data Set	No. of Samples	No. of Poles	Iterations (VECTFIT)	RMS Error	VECTFIT Time
Uniformly Sampled Set	801	78	5	0.00034985	111.203855 s
Reduced Set	232	70	5	0.00034617	53.184679 s

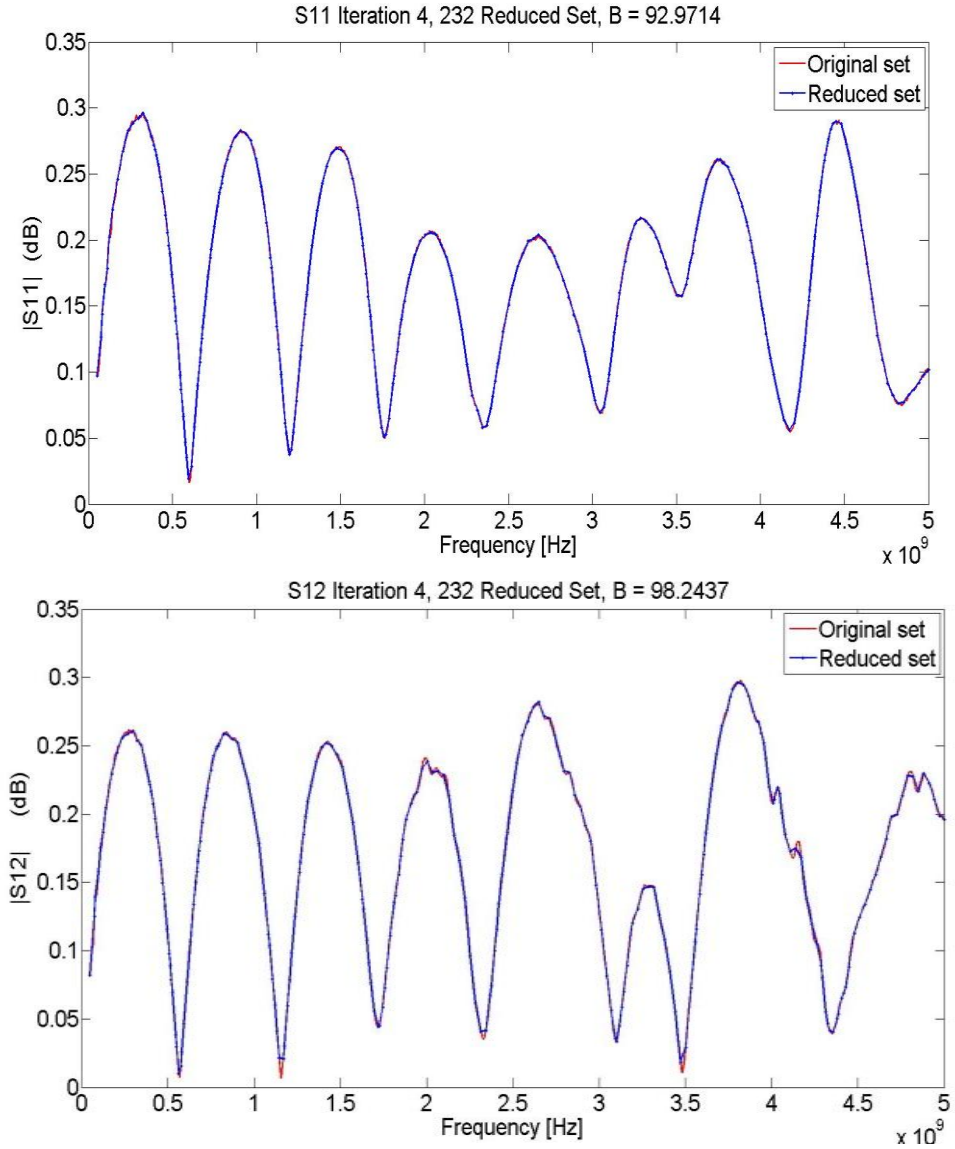

Figure 5.6: Magnitude of S_{11} and S_{12} (dB) from adaptive sampling after fourth iteration and corresponding Blumer index.

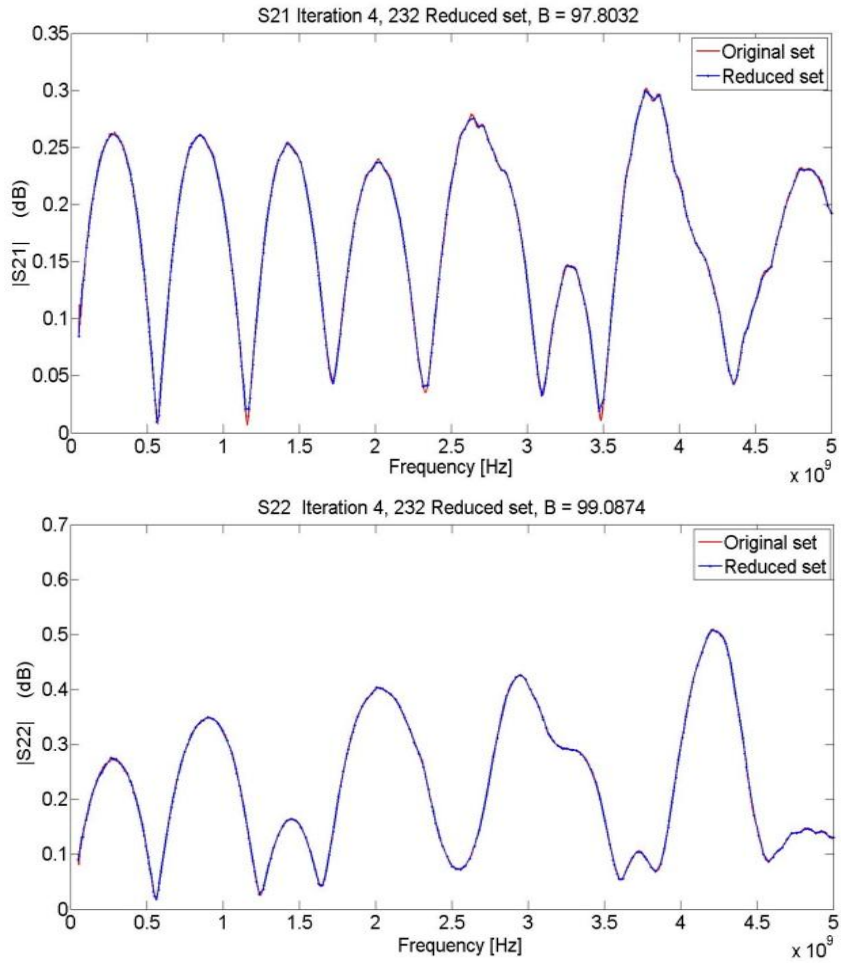

Figure 5.7: Magnitude of S_{21} and S_{22} (dB) from adaptive sampling after fourth iteration and corresponding Blumer index.

According to Table 5.2, the computation time for the uniformly sampled set was 111.203855 seconds, while the computation time for the reduced set was 53.184679 seconds.

Figure 5.8 shows the transient response of the original sampled set and adaptive sampled set, where a pulse train of 0.2 ns rise and fall time, 800 ps pulse width, and 1600 ps period is applied to port 1 while all other lines are terminated with 50 Ω. An excellent match between the macromodel obtained using the original data and the one obtained using a reduced set through adaptive sampling is observed.

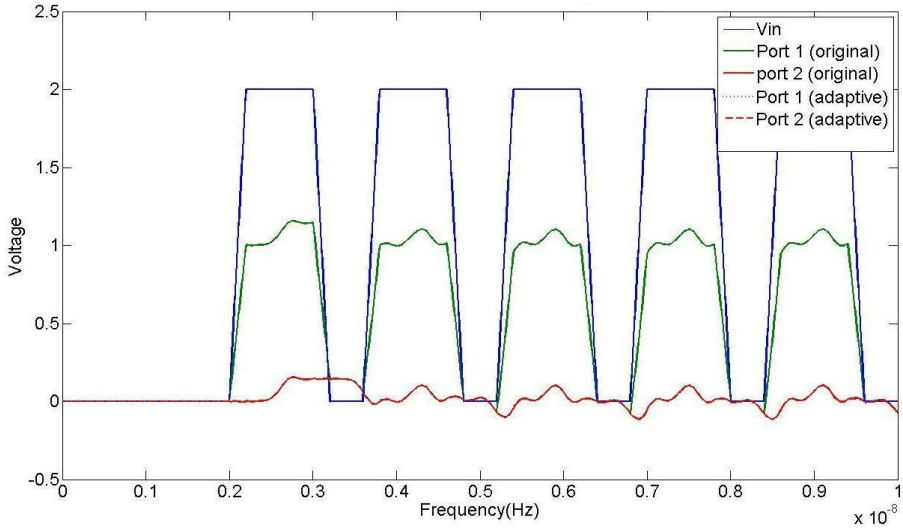

Figure 5.8: Transient response of original and adaptive sampled data of coupled line.

5.3.3 Two-port backplane measurement

Figure 5.9 depicts the magnitude plots of the two-port S-parameter measured data for backplane structure. The data consists of 801 uniformly distributed samples in the range 50 MHz to 4.05 GHz. Adaptive sampling is applied to four scattering parameters and reduced sets of 129 non-uniform samples are obtained after the 6^{th} iterations, with Blumer index of 95.2612 %, 98.6561 %, 98.3535 %, and 98.3535 %, respectively. Table 5.3 compares the original uniformly sampled set and the reduced set after VF. Again, rough estimate of initial number of order is found by detection of the number of local minima of the measured data. Twenty complex conjugate poles are used as initial poles, and the total number of poles is increased by 2 if RMS error after N_{iter} iterations (relocations of poles) does not meet the RMS error threshold. The application of VF to the rational fitting of the original data set was, as expected, time-consuming, requiring ~167.86 s of computation time for a 108-pole fit of the data, yielding RMS error of 0.0034983. On the other hand, rational fitting of our reduced data set through proposed

methodology only required 71.69277 s of computation time for a 96-pole fit of the data, yielding RMS error of 0.0033639. This amounts to a factor of 2.3414 reductions in computation time.

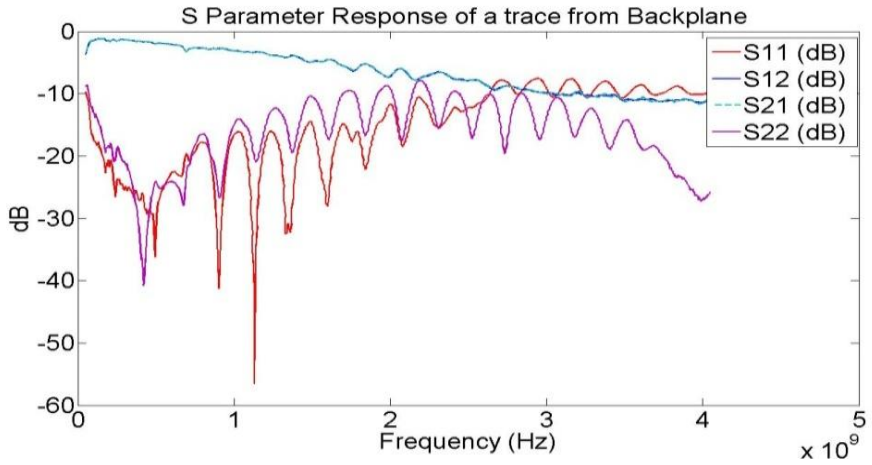

Figure 5.9: ***S***–parameter measurement (dB) of backplane.

Table 5.3: Comparison of uniformly sampled set and reduced set for the case of a backplane.

Data Set	No. of Samples	No. of Poles	Iterations (VECTFIT)	RMS Error	VECTFIT Time
Uniformly Sampled Set	801	108	5	0.0034983	167.86244 s
Reduced Set	129	96	5	0.0033639	71.69277 s

Figure 5.10 shows the iteration process of adaptive sampling for S_{12} and the steps of the added samples after each iteration starting from the top left. The total number of samples increases from 3 to 9, 17, 33, 65, and 129 from the first to the sixth iteration. Despite the fact that high Blumer index value of 98 is achieved on the third iteration, the adaptive curve of S_{12} is far from the original S_{12} curve and it takes full six iterations for the adaptive sampling process to satify the RMS error and Blumer index threshold.

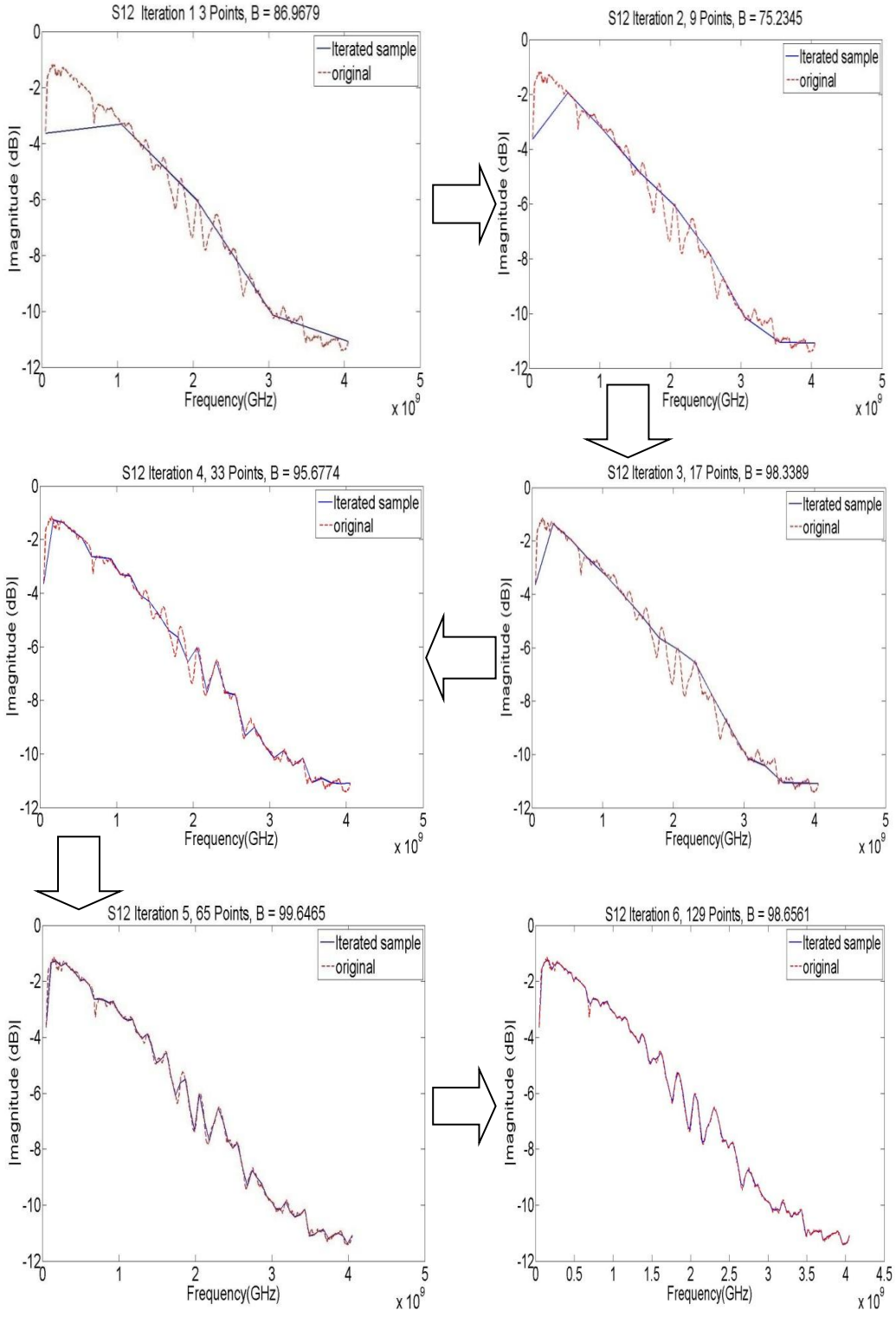

Figure 5.10: The iterative process (1~ 6th) of the number of a reduced set, with a Blumer index of S12.

5.4 Summary

In summary, we have presented a methodology for the systematic reduction of large sets of measured or calculated data quantifying the broadband frequency response of passive electromagnetic structures in this chapter. The proposed methodology makes use of the Hilbert transform constraints pertinent to the spectra of causal responses to replace the original set of frequency data with a reduced one that preserves the accuracy in the representation of the attributes of the electromagnetic response.

The proposed methodology is useful in improving computational efficiency, numerical robustness, and accuracy of rational function fitting and related approaches for the synthesis of equivalent circuit representations of interconnect structures from calculated or measured broadband frequency data. The adaptive sampling method can be done as a pre-processing step and combined with VF and passivity enforcement techniques such as iterative residue perturbation [63] to effectively approximate the data and preserve the physical consistency of the system.

CHAPTER 6

FAST RATIONAL FUNCTION FITTING OF BROADBAND MULTI-PORT RESPONSES VIA REPEATED RANDOM SAMPLING

6.1 Introduction

The robust and accurate rational approximation of broadband electromagnetic (EM) response of multi-port passive systems from tabulated data at a discrete set of frequencies is known to be a numerically challenging task. Several rational function fitting schemes have been proposed to improve both accuracy and computational efficiency of the fit [18]-[20]. For example, in [19], frequency band partitioning has been explored, as each partitioned band is modeled separately to identify the poles, with the residues solved in least squares sense by combining the poles. The accuracy of the fit is also improved in [19] by also introducing adaptive weighting, and column scaling along with the frequency band partitioning. Following the introduction of vector fitting (VF) [21] and further advances in its algorithm for handling large data sets, the numerical inaccuracies associated with the fitting of broadband responses of multiport systems have been significantly reduced [21]-[29]. Moreover, adaptive sampling [88] and frequency-partitioned VF [93],[94] had the further impact of reducing computation cost while guaranteeing superb accuracy in interpolation of complex broadband structures. The adaptive sampling has been combined with a robust and efficient passivity enforcement [86],[87] of the broadband data of the passive interconnects. The advancement of the algorithms has also been coupled with order estimation

techniques to further reduce the computational cost [91]-[94]. Recently, parallel VF [97] has been introduced to further improve computational efficiency by parallelizing the most CPU intensive section of the VF algorithm.

From Chapter 2, we have learned that the major computational cost in rational function approximation of the broadband data comes from handling the size of the matrix in the pole identification stage of least squares setting, which relies on the number of poles, the number of frequency samples, and the number of iterations to find the optimum pole order. In Chapter 5, adaptive sampling was suggested in an effort to reduce the computational cost of the rational function fit by reducing the number of frequency samples in broadband data. In this chapter, we propose a novel approach to improve the efficiency of rational function fitting of broadband passive multi-ports even further. The method uses several subsets of randomly selected frequency samples spanning the entire sampled bandwidth, and interpolates each subset separately to find the optimum order. The poles obtained from each subset are appropriately combined and used to approximate the original response of the broadband multiport system, and to solve for the residues of the final rational function fit. The proposed methodology reduces not only the number of frequency samples suggested in Chapter 5 but also the samples, the order of poles involved with each fit, and the overall cost by reducing the most computationally demanding pole identification stage in VF process. The effectiveness of the proposed approach is demonstrated by comparing the computational cost and fitting error of three examples of broadband multiport data with standard VF [21],[25],[27], adaptive sampling VF [88] and frequency partitioned VF [93],[94].

6.2 Vector Fitting via Repeated Random Sampling Methodology

We first start this section by reviewing the basic VF scheme briefly. We consider a stable and linear time invariant *N*-port *S* parameter matrix $\boldsymbol{S}(\mathrm{s_k})$ available in terms of a set of discrete frequency samples $s = \{\mathrm{j}\omega_1,\ldots, \mathrm{j}\omega_\mathrm{k}\}$, $k = \{1,2,\ldots,K\}$. Then the macromodel is recast in terms of a rational function as a sum of partial fractions in (6.1), where the VF will find the set of unknown poles $\tilde{p}_m$ and residues $\tilde{r}_{m,ij}$ to minimize the least squares distance of $N_e = \sum_{k=1}^{K}\left|S_{ij}(s_k) - \tilde{S}_{ij}(s_k)\right|^2$.

$$\left\{\tilde{S}(s_k)\right\}_{ij} = \sum_{m=1}^{N_p} \frac{\tilde{r}_{m,ij}}{s_k - \tilde{p}_m} + \tilde{d}_{ij} \tag{6.1}$$

The non-linear optimization problem in (6.1) is solved by iterative pole relocation procedure, based on Sanathanan-Koerner iteration using partial fraction functions. We define a weighting function $\boldsymbol{\sigma}^t(s)$ with set of poles $\{a_m^t\}$ and unknown residues $\{r_m^t\}$ and $(\boldsymbol{\sigma S})_{\tilde{n}}^t(s)$ with same set of poles but different residues, $\{\hat{r}_m^t\}$.

$$(\sigma S)_{i,j}^{(t)}(s) = \sum_{m=1}^{N_p}\left(\frac{\hat{r}_{m,ij}^{(t)}}{s-a_m^t}\right) + d_{ij} = \frac{\prod_{m=1}^{N_p-1}\left(s-z_{m,ij}^{(t)}\right)}{\prod_{m=1}^{N_p}(s-a_m^t)} \tag{6.2}$$

$$\sigma^{(t)}(s) = \sum_{m=1}^{N_p}\left(\frac{r_m^{(t)}}{s-a_m^t}\right) + d = \frac{\prod_{m=1}^{N_p}\left(s-z_{m,d}^{(t)}\right)}{\prod_{m=1}^{N_p}(s-a_m^t)} \tag{6.3}$$

The nonlinear problem is linearized in (6.4) in a least squares sense. The common poles from both functions (6.2) and (6.3) are cancelled out in the pole relocation step, and $\boldsymbol{S}(s)$ is defined as the fraction of the zeros of two functions. An iterative process is used to update the poles. Thus after iteration t, respective zeros, $z_{m,d}^{(t)}$, of the scaling function $\boldsymbol{\sigma}(\boldsymbol{s})$ in previous step are used as the relocated poles, $a_m^{(t+1)}$, in the subsequent iteration step.

$$(\boldsymbol{\sigma S})(s) = \boldsymbol{\sigma}(s)\boldsymbol{S}(s) \tag{6.4}$$

The zeros of $\boldsymbol{\sigma}(\boldsymbol{s})$ can be found by computing the eigenvalues in (6.5), where $\boldsymbol{A_\sigma}$, $\boldsymbol{B_\sigma}$, $\boldsymbol{C_\sigma}$ and $\boldsymbol{D_\sigma}$ are minimum state space representation [32] of $\boldsymbol{\sigma}(\boldsymbol{s})$**.** With the sufficient order N_p and appropriate number of pole relocations, RMS error of N_e will be minimized and $\{a_m^t\}$ will converge to $\{\tilde{p}_m\}$. Once the convergence is reached and $\tilde{p}_m$ is found in our original function (6.1), the least squares solution is used to find the residues, $\tilde{r}_{m,ij}$.

$$z_{m,d}^{(t)} = eig(\boldsymbol{A_\sigma} - \boldsymbol{B_\sigma D_\sigma^{-1} C_\sigma}) \tag{6.5}$$

Even though the details of the VF process for sparse and fast VF scheme have been covered in Chapter 2, the coverage was done with the main intention to highlight the computational advantage of the fast VF scheme over sparse VF. Therefore, not enough analysis was done with each individual step involved with fast VF process. It is known that the disadvantage of VF lies in its relatively poor scalability with the number of input/output ports *N*, and the number of poles *P*, used to approximate the broadband data. This becomes a serious limitation of VF where the number of ports becomes very large and the increase in the number of poles is significant when broadband data must be fit. Since our proposed methodology is based on the significant improvement of the computational cost of the standard fast VF process [27], we first give a proper review of each stage of fast VF and highlight the complexity involved with each VF step of fast VF scheme in this section, followed by introducing the details of our methodology.

6.2.1 Fast VF complexity

Figure 6.1 breaks down what percentage of the computation time is spent on each stage in the standard fast VF, for the case of approximating a 10-port network, 3996 using data at frequency samples and 50 complex conjugate poles. It shows that the pole identification stage of the fast

VF takes about 75 % of the overall VF time, which is computationally the most dominant stage out of the three stages in VF. Even though the figure only shows a case for a specific number of poles used in rational function fit to highlight the impact of each stage, the result is representative of the breakdown of the computational cost of each of the three stages. Based on many experiments with complicated passive broadband structure, it was observed that pole identification stage takes 70 % ~ 80 %, and the final residue identification stage takes 20 % ~ 30 % of the overall VF time, with increased percentage of time spent on pole identification stage as the number of poles, ports, or frequency samples increases.

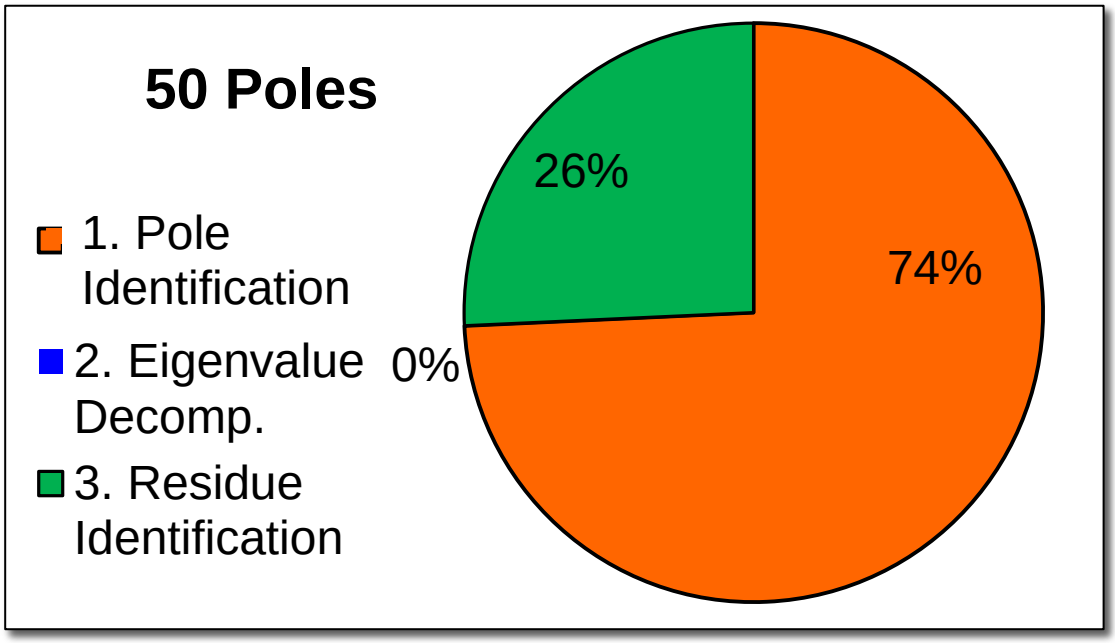

Figure 6.1: Computation time percentage distribution of standard fast VF when ten-port network with data at 3996 frequency samples (10 MHz ~ 10 GHz) is fitted with 50 complex conjugate poles.

In the next three sub-sections, the three stages of the fast VF are covered with regard to the matrix size, and the numbers of the floating-point operations (flop count) needed to measure the time involved in VF algorithm. Let us first define the parameters that will be used consistently in

the following sections. We express m as the number of iterations needed to find the number of poles for an accurate fit of the data; P_n as the number of poles used of the nth iteration; N as the number of ports; S as the number of frequency samples used in rational function fit; and N_{iter} as the number of iterations used in each fit for relocation of the poles.

6.2.1.1 Pole identification

From the least squares solution in Equation (6.1), the pole identification stage is further decomposed into three subsequent processes, namely QR decomposition, Q transposition, and least squares solution by back-substitution. Equations (6.6) and (6.7) show the least squares solution involved with QR stage, which is repeated N^2 times for all the elements in *S* matrix. The size of the least squares matrix *A* from (6.1) is ($2S$) × ($2P_n$+2). For each element of an *N*-port system, QR decomposition of (6.6) is carried out with orthogonal Q matrix and the upper triangular R matrix where the matrix size is defined as ($2S$) × ($2P_n$+2) and ($2P_n$+2) × ($2P_n$+2), respectively.

$$\boldsymbol{Ax} = [\boldsymbol{X} - \boldsymbol{H_v X}] \begin{bmatrix} \boldsymbol{C_v} \\ \widetilde{\boldsymbol{C}} \end{bmatrix} = \boldsymbol{b_1} = \boldsymbol{H_v}\widehat{\mathbf{1}} \tag{6.6}$$

$$[\boldsymbol{X} - \boldsymbol{H_v X}] = \boldsymbol{QR} = \boldsymbol{Q} \begin{bmatrix} \boldsymbol{R_{11}} & \boldsymbol{R_{12}} \\ \mathbf{0} & \boldsymbol{R_{22}} \end{bmatrix} \tag{6.7}$$

The number of floating-point operations (flops) needed for this QR decomposition of $\boldsymbol{A}$, where $\boldsymbol{A} \in \mathbb{C}^{m \times n}, m \geq n$ is given by $FC_{QR}(m, n) \approx 2\, mn^2$. Thus, for the size of our matrix A, flop count of QR stage is $FC_{QR}(2S, 2P_n + 2) = 16S(P_n + 1)^2 \times N^2$.

Next, the Q transposition stage, where the right- and left-hand sides of (6.7) are multiplied by $\boldsymbol{Q^T}$, is expressed by Equation (6.8). Pictorial description in Figure 6.2 also aids in understanding of the matrix computation involved. The total flop count with this stage with $\boldsymbol{Q^T} \in \mathbb{C}^{m \times n}, m \geq$

n is $FC_{\mathrm{Q^T}}(m,n) \approx 2\,mn$. Thus, for the size of our matrix $\boldsymbol{Q^T}$, the flop count involved will be $FC_{\mathrm{Q^T}}(2P_n + 2,2S) = 8S(P_n + 1) \times N^2$.

$$\begin{bmatrix} \boldsymbol{R_{11}} & \boldsymbol{R_{12}} \\ \boldsymbol{0} & \boldsymbol{R_{22}} \end{bmatrix} \begin{bmatrix} \boldsymbol{C_v} \\ \widetilde{\boldsymbol{C}} \end{bmatrix} = \boldsymbol{Q^T} \begin{bmatrix} \boldsymbol{b_1^1} \\ \boldsymbol{b_1^2} \end{bmatrix} = \begin{bmatrix} \boldsymbol{y_1^1} \\ \boldsymbol{y_1^2} \end{bmatrix} \tag{6.8}$$

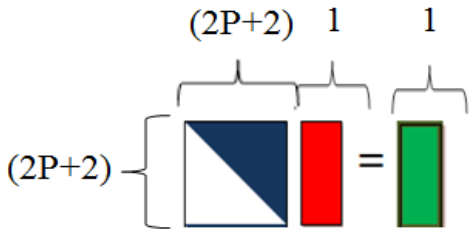

Figure 6.2: Sketch of the matrix structure for the Q transposition of the pole identification stage.

The final stage of pole identification is the least squares solution for pole estimation of the auxiliary function. This is done by collecting N^2 numbers of (P_n+1) × (P_n+1) upper triangular matrix $\boldsymbol{R_{22}^l}$, and by stacking up all the matrices for the least squares problem in (6.9). Figure 6.3 shows the pictorial description of the matrix structure for this stage. The dimension of $\boldsymbol{R_{22}^v}$, $\widetilde{\boldsymbol{C}}$, and $\mathbf{y}$ is N^2(P_n+1) × (P_n+1), (P_n+1) × 1, and N^2(P_n+1) × 1, respectively. The total flop count of least squares of the triangular system by back-substitution is $FC_{\mathrm{LS}}(m,n) \approx mn$. Therefore, total flop count of $FC_{\mathrm{LS}}(N^2(P_n + 1),(P_n + 1))$=$N^2(P_n + 1)^2$.

$$\begin{bmatrix} \boldsymbol{R_{22}^1} \\ \boldsymbol{R_{22}^2} \\ \vdots \\ \boldsymbol{R_{22}^{N^2}} \end{bmatrix} \widetilde{\boldsymbol{C}} = \begin{bmatrix} \boldsymbol{y_1^2} \\ \boldsymbol{y_2^2} \\ \vdots \\ \boldsymbol{y_{N^2}^2} \end{bmatrix} \tag{6.9}$$

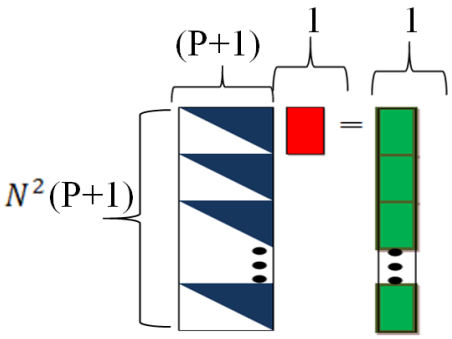

Figure 6.3: Sketch of the matrix structure for the least squares of the pole identification stage.

6.2.1.2 Eigenvalue decomposition

This stage concerns the eigenvalue computation of the auxiliary function in order to provide and replace the starting poles for the next iteration. The zeros of the auxiliary function (i.e. the next starting poles) are found by computing the eigenvalues in (6.5), and the flop count involved with this stage for an m by m matrix is accounted for by $FC_{\mathrm{EIG}}(m) \approx 10m^3$. Since our matrix $\boldsymbol{A}$ has the size $P_n \times P_n$, the total flop count for this process is $FC_{\mathrm{EIG}}(P_n) = 10{P_n}^3$.

6.2.1.3 Residue identification

The final stage of standard VF concerns the residue identification of our rational function of (6.1) in least squares sense. This concerns the computation of QR factorization, Q transposition, and the least squares solution of the triangular system by back-substitution, just like the pole identification stage. The size of the matrix $\boldsymbol{A}$ is $(2S) \times (P_n+1)$. In the QR stage, the number of flops counting the N^2 repetition is $FC_{QR,res}(2S, P_n + 1) = 4S(P_n + 1)^2N^2$. The flop count for Q transposition stage and the least squares stage is $FC_{\mathrm{Q^T},res}(P_n + 1,2S) = 4S(P_n + 1)N^2$, and $FC_{\mathrm{LS,res}}(N^2(P_n + 1)/2, (P_n + 1)/2) = N^2(P_n + 1)^2/4$, respectively. Table 6.1 summarizes the computational cost in terms of the flop count for each pole and overall flop count for the whole VF process by fixing the overall m numbers of iterations to find the optimum pole order and

assuming 5 iterations for pole relocation within VF. Table 6.1 provides a rough estimate of the computation time involved with each stage in VF and expresses the cost in terms of O function. Table 6.1 shows that the most computationally expensive and CPU intensive stage is the QR decomposition of the pole identification stage followed by the QR decomposition of the residue identification stage. These results collectively show that the primary goal in reducing the computational burden in VF should be focused on reducing the number of operations in these two stages. In the next section, we consider a methodology for achieving such flop count reduction.

6.2.2 VFRS methodology

The previous section covered the computation cost involved with each one of the fast VF stages, and identified the most CPU expensive one, by calculating the rough estimate of flops involved with each VF stage. In this section, we cover the details of our proposed methodology, Vector Fitting via Repeated Random Sampling (VFRS). Once again, we consider a stable and linear time-invariant *N*-port *S* parameter matrix $\boldsymbol{S}(\mathrm{s_k})$ available in terms of a set of discrete frequency samples $s = \{\mathrm{j}\omega_1,\ldots, \mathrm{j}\omega_\mathrm{k}\}$, $k = \{1,2,\ldots,K\}$. Three things need to be defined before using the VFRS algorithm. First, initial number of the poles for overall $\boldsymbol{S}(\mathrm{s})$ are estimated. This is done by locating the local maxima and minima of $|\boldsymbol{S}(\mathrm{s})|$. This initial number of poles, N_{init}, will be used to estimate the number of generated subsets, $\tilde{n}$, of data which are going to be fitted, and the number of randomly chosen samples, $r_{s,\tilde{n}}$, in each set.

Table 6.1: Computational cost of the VF process in terms of flop count

Stage	Function	Overall flop count
1. Pole identification		
1.1 QR	$O(SP_n{}^2N^2)$	$\sum_{n=1}^{m} 80S(P_n+1)^2 \times N^2$
1.2 Q^T Transpose	$O(SP_nN^2)$	$\sum_{n=1}^{m} 40S(P_n+1) \times N^2$
1.3 Least squares	$O(N^2P_n{}^2)$	$\sum_{n=1}^{m} 5N^2(P_n+1)^2$
2. Eigenvalue Decomposition		
2.1 Eigenvalue decomp.	$O(P_n{}^3)$	$\sum_{n=1}^{m} 50(P_n)^3$
3. Residue identification		
3.1 QR	$O(SP_n{}^2N^2)$	$\sum_{n=1}^{m} 20S(P_n+1)^2 \times N^2$
3.2 Q^T Transpose	$O(SP_nN^2)$	$\sum_{n=1}^{m} 20S(P_n+1) \times N^2$
3.3 Least squares	$O(N^2P_n{}^2)$	$\sum_{n=1}^{m} (5/4) \cdot N^2(P_n+1)^2$

The basic idea of VF via repeated random sampling (VFRS) is to obtain the poles of the multi-port system through the application of VF to each of the $\tilde{n}$ subsets, $\boldsymbol{S}(s)_{\tilde{n}}$, that contains $r_{s,\tilde{n}}$ randomly chosen samples from the original K samples. Thus, once $r_{s,\tilde{n}}$ and $\tilde{n}$ are defined, identification of each random subset $\boldsymbol{S}(s)_{\tilde{n}}$ is typically done using VF in (6.10), where $N_{p,\tilde{n}}$ denotes the order of the $\tilde{n}$th subset, and $\tilde{r}_{m,ij}$ and $\tilde{p}_m$ denotes residues and poles of the subset.

$$\left\{\tilde{S}(s_k)\right\}_{ij,\tilde{n}} = \sum_{m=1}^{N_{p,\tilde{n}}} \frac{\tilde{r}_{m,ij}}{s_k - \tilde{p}_m} + \tilde{d}_{ij,\tilde{n}} \tag{6.10}$$

Just as we defined the auxiliary function in standard VF, we define an auxiliary function $\boldsymbol{\sigma}^t(s)_{\tilde{n}}$ with set of poles $\{a_m^t\}$ and unknown residues $\{r_m^t\}$ and $(\boldsymbol{\sigma S})_{\tilde{n}}^t(s)$ with same set of poles as auxiliary function but with different residues $\{\hat{r}_m^t\}$ in (6.11) and (6.12).

$$(\sigma S)_{i,j,\tilde{n}}^{(t)}(s) = \sum_{m=1}^{N_{p,\tilde{n}}} \left(\frac{\hat{r}_{m,ij}^{(t)}}{s-a_m^t}\right) + d_{ij,\tilde{n}} = \frac{\prod_{m=1}^{N_{p,\tilde{n}}-1}\left(s-z_{m,ij}^{(t)}\right)}{\prod_{m=1}^{N_{p,\tilde{n}}}(s-a_m^t)} \tag{6.11}$$

$$\sigma^{(t)}(s)_{\tilde{n}} = \sum_{m=1}^{N_{p,\tilde{n}}} \left(\frac{r_m^{(t)}}{s-a_m^t}\right) + d_{\tilde{n}} = \frac{\prod_{m=1}^{N_{p,\tilde{n}}}\left(s-z_{m,d}^{(t)}\right)}{\prod_{m=1}^{N_{p,\tilde{n}}}(s-a_m^t)} \tag{6.12}$$

After parameterization, common poles from both functions are cancelled out and $\boldsymbol{S}(s)_{\tilde{n}}$ is defined as the fraction of the zeros of two functions for t iteration steps. Thus, respective zeros, $z_{m,d}^{(t)}$ of $\boldsymbol{\sigma}(\boldsymbol{s})_{\tilde{n}}$ in previous steps are used as the relocated poles, $a_m^{(t+1)}$ in the subsequent iteration step.

$$(\boldsymbol{\sigma S})_{\tilde{n}}(s) = \boldsymbol{\sigma}(s)_{\tilde{n}}\boldsymbol{S}(s)_{\tilde{n}} \tag{6.13}$$

The zeros of $\boldsymbol{\sigma}(\boldsymbol{s})_{\tilde{n}}$ can be found by computing the eigenvalues in (6.14), where $\boldsymbol{A}_{\boldsymbol{\sigma}_{\tilde{n}}}$, $\boldsymbol{B}_{\boldsymbol{\sigma}_{\tilde{n}}}$, $\boldsymbol{C}_{\boldsymbol{\sigma}_{\tilde{n}}}$ and $\boldsymbol{D}_{\boldsymbol{\sigma}_{\tilde{n}}}$ are minimum state space representation of $\boldsymbol{\sigma}(\boldsymbol{s})_{\tilde{n}}$. In each iteration, poles are relocated to reduce the weighted RMS error function (6.15) between $\boldsymbol{S}(s)_{\tilde{n}}$ and $\boldsymbol{S}_{\boldsymbol{fit}}(s)_{\tilde{n}}$. With a sufficient order $N_{p,\tilde{n}}$ and appropriate number of pole relocations, RMS error of N_e elements will be minimized and $\{a_m^t\}$ will converge to $\{\tilde{p}_m\}$.

$$z_{m,d}^{(t)} = eig\left(\boldsymbol{A}_{\boldsymbol{\sigma}_{\tilde{n}}} - \boldsymbol{B}_{\boldsymbol{\sigma}_{\tilde{n}}}\boldsymbol{D}_{\boldsymbol{\sigma}_{\tilde{n}}}^{-1}\boldsymbol{C}_{\boldsymbol{\sigma}_{\tilde{n}}}\right) \tag{6.14}$$

$$Error_{(\tilde{n})} = \sqrt{\frac{\sum_{m=1}^{N_e}\sum_{k=1}^{r_{s,\tilde{n}}}\left|\boldsymbol{S}(s_k)_{\tilde{n}} - \boldsymbol{S}_{\boldsymbol{fit}}(s_k)_{\tilde{n}}\right|^2}{r_{s,\tilde{n}} \cdot N_e}} \tag{6.15}$$

The identified poles for each set are compiled into one set of poles, which constitutes the set of $\tilde{p}_{total}$ poles for the system.

$$\tilde{p}_{total} = \{\tilde{p}_1, \tilde{p}_2, \dots, \tilde{p}_{\tilde{n}}\} \tag{6.16}$$

Then, VF is applied to find the respective residues. The total number of poles needs to be greater than the initially estimated poles, N_{init}, which are decided on the basis of the number of resonances in the response data. If the convergence of the fitting is not met, we simply interpolate another set that contains $r_{s,\tilde{n}+1}$ number of random samples to find $\tilde{p}_{\tilde{n}+1}$ number of poles, which will be added to $\tilde{p}_{total}$ to re-interpolate $\boldsymbol{S}(s)$ until it meets the RMS error criteria. Since it is possible to attain redundant number of poles, which have insignificant contribution to the final interpolated rational function, the spurious pole detection method can be used to eliminate the spurious poles [35]. Figures 6.4 and 6.5 summarize the complete VFRS methodology flow.

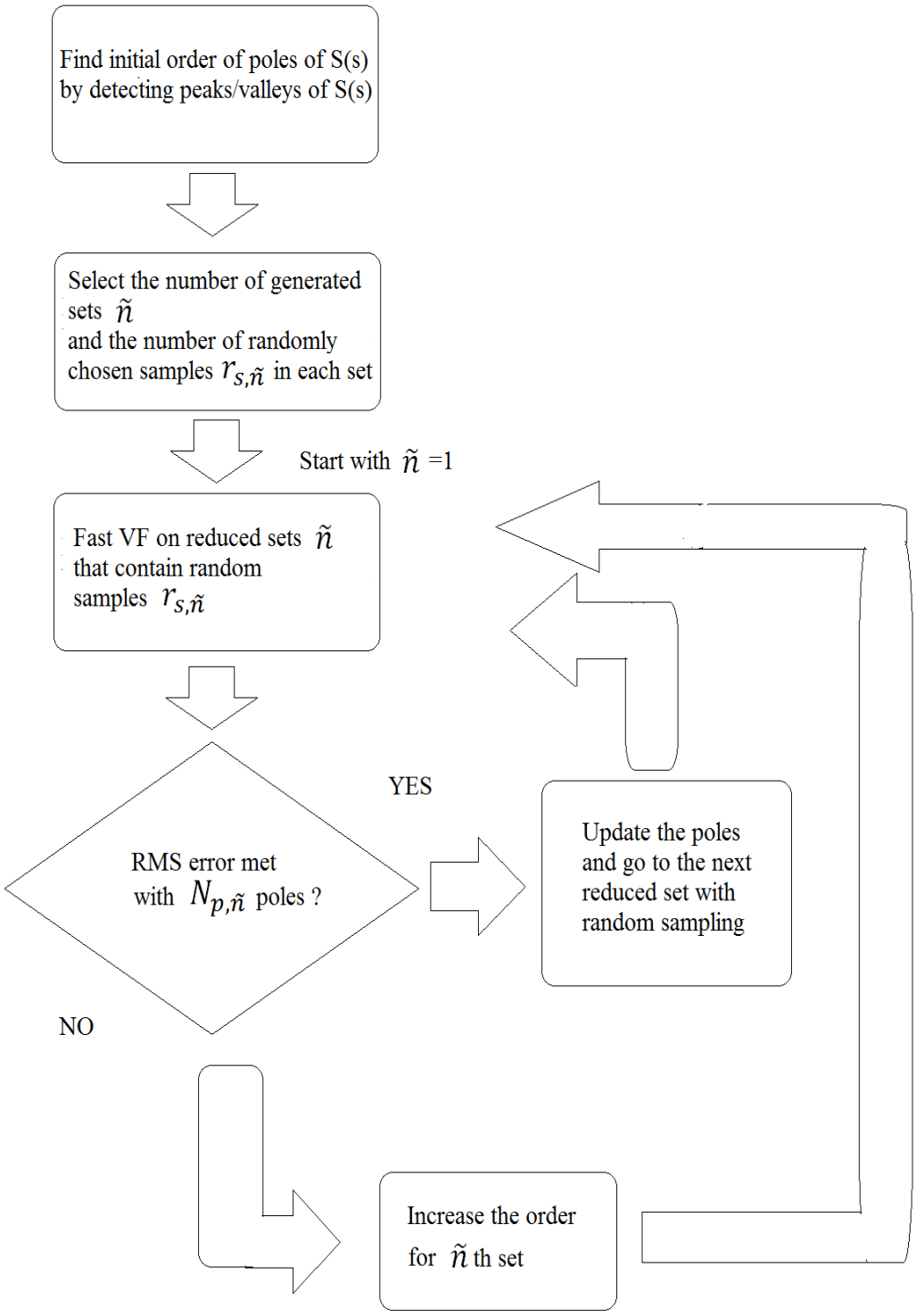

Figure 6.4: Complete VFRS flow 1.

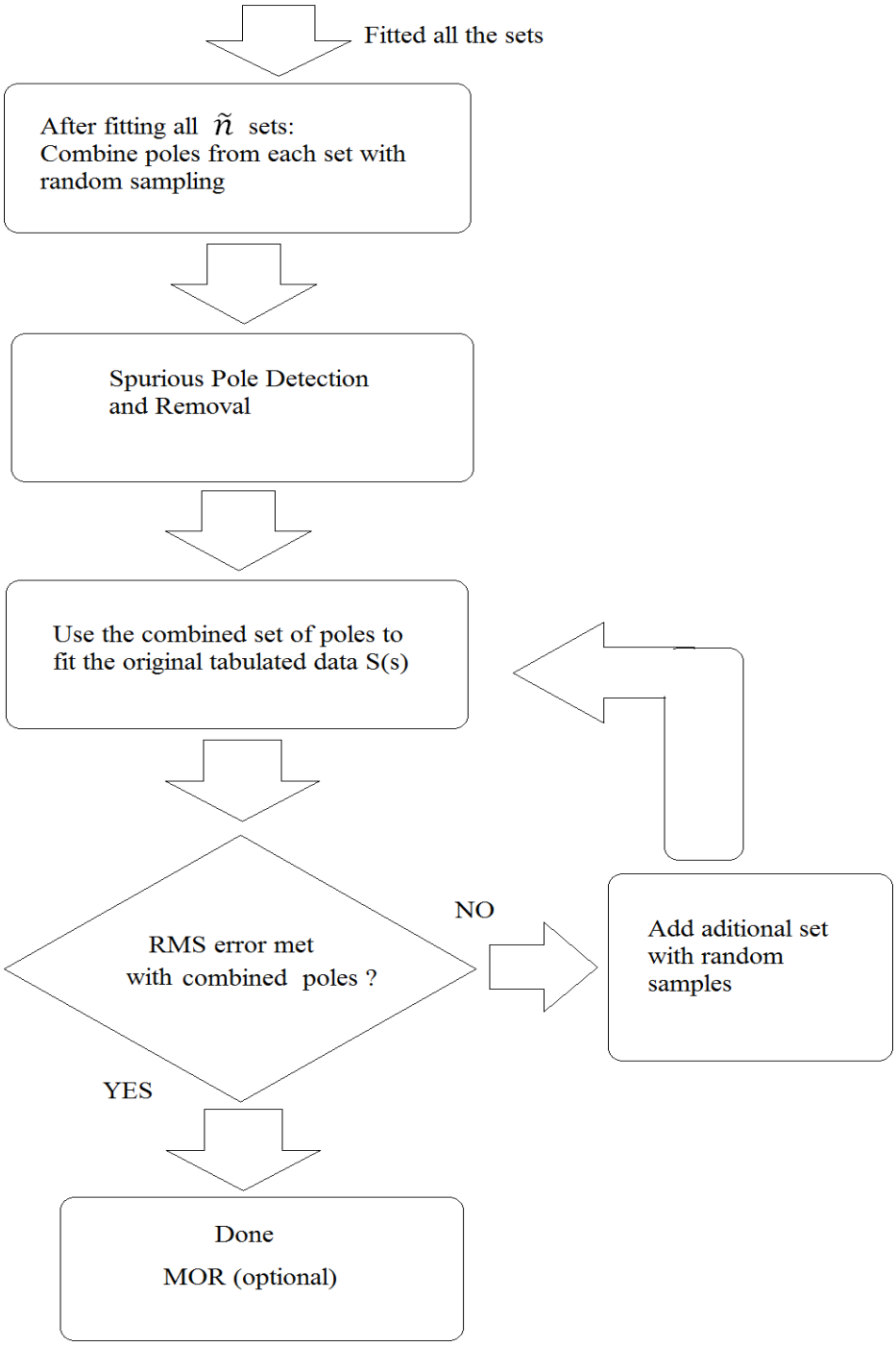

Figure 6.5: Complete VFRS flow 2.

6.2.3 Computational efficiency and comparison with other methods

In this section, we compare the proposed approach with other state-of-the-art methodologies that exist for the purpose of computationally efficient macromodeling of broadband data, such as adaptive sampling based VF method [88], and frequency paritioning VF (FPVF) [94]. We compare the total flop count from the QR step of the pole identification stage, the most computationally expensive stage of VF, to compare the efficiency of those other methods to VFRS. The adaptive sampling based VF approach reduces the number of frequency samples S as a preprocessing step before applying standard fast VF to the reduced set. It reduces the flop count by a factor of S/S_{adap} in the QR stage of fast VF. The normal reduction range of S_{adap} varies based on how sampling is done in our original data, but typically it amounts to 1/4 ~ 1/10 of the original samples. Thus, accounting for the time it takes to determine the reduced set, the overall computational cost is roughly 1/2~ 1/4 of standard VF.

FPVF, on the other hand, divides the whole frequency band into P frequency intervals, applies standard VF with the data in each frequency interval, gathers and combines the estimated poles from each interval, and uses the combined poles to obtain the residues of the fit for the data on the entire frequency band in least squares sense. Even though there is no direct means of comparing this approach with standard fast VF, we can obtain a rough estimate of the overall flop count of the QR stage from Table 6.1. For standard VF, the cost is $\sum_{n=1}^{m} 80S(P_n+1)^2\boldsymbol{N^2}$ for m sets of poles $\{P_1 < P_2 < \cdots < P_m\}$, where the number of poles is increasing from one to the next until convergence is reached. On the other hand, by using FPVF, we achieve the following overall flop count $\sum_{p=1}^{P}\sum_{n=1}^{m_{FPVF,p}} 80S_{FPVF,p}(P_{n,FPVF,p}+1)^2\boldsymbol{N^2}$. Since we have P frequency intervals, these are P different flop counts that must be considered. In each frequency partition, a significantly reduced number of $m_{FPVF,p}$ sets of increasing number of poles

$\{P_{1,FPVF,p} \leq P_{2,FPVF,p} \leq \cdots \leq P_{m,FPVF,p}\}$ is involved. However, these numbers are much smaller than the ones used when all frequency samples are fitted simultaneously. This is obvious by the fact that the number of samples involved now is $S_{FPVF,p}$. The cost will depend on how one partitions the frequency data, and this approach is often used with order estimation technique [94] as a pre-processing tool to further reduce the computational cost by reducing the number of $m_{FPVF,p}$ sets.

VFRS is similar to FPVF in terms of the primary target of reduction, which is the number of poles and the number of frequency samples used for the identification of the poles. Once the number of sets, $\tilde{n}$, and the number of randomly selected samples, $r_{s,\tilde{n}}$, in each set is determined, fast VF is used to fit each set, thus achieving the toal flop count of $\sum_{p=1}^{\tilde{n}} \sum_{n=1}^{m_{VFRS,p}} 80 r_{s,p}(P_{n,VFRS,p}+1)^2 N^2$ with a sigfinicantly reduced number of randomly selected frequency samples $r_{s,p}$, $m_{VFRS,p}$ sets, which is composed of significantly reduced number of poles $\{P_{1,VFRS,p} \leq P_{2,VFRS,p} \leq \cdots \leq P_{m,VFRS,p}\}$ for $p = \tilde{n}$ numbers of the sets. Thus, the cost will depend on how one chooses the number of sets with the number of randomly generated samples in a set. The major differences between VFRS and FPVF approaches are based on how one selects the reduced frequency sampled set. For example, FPVF selects *P* partitioned frequency samples, where each partition represents the local bandwidth of the global sampled set. In VFRS, this restriction is removed, and the frequency samples are randomly chosen from the global samples, not restricted to the local bandwidth.

Another difference between two methods is in the approximation of the reduced set. FPVF depends on accurate approximation of the partitioned set. The number and the location of poles generated from FPVF's local fit does not deviate much when compared to the number and the location of poles of the local frequency regime of the standard VF. This implies that both

approaches rely on accurate representation of the data. VFRS on the other hand, since it draws frequency samples in random manner from the original frequency set, yields a fit that emphasizes accuracy in the interpolation of the data in a local fashion, in the vicinity of the samples used in the randomly selected set. This does not matter, however, since the objective is to construct the overall set of poles to use for finding the residues of the fit for the entire set of data. Figure 6.6 uses the data from fitting a typical transfer function to demonstrate which stage is the most computationally dominant stage in VFRS. The original system had 1000 frequency samples. Twenty-five random samples were chosen in each of 12 sets. Using VF for the 12 sets with random sampling, 24 poles were used for each of the sets, resulting in a total of 288 poles. As can be seen in Figure 6.6, the computational cost of the sum of pole identification stage as well as the sum of residue identification stage is minor, since we are using significantly fewer number of poles and frequency samples in each fit. However, 86 % of the total computational cost was associated with the final stage of residue identification. This is reasonable as we are using least squares solution of the large number of poles gathered from the combined set, as well as the original frequency samples that span broadband data. The cost at the final residue identification stage can be further reduced by using parallelization and adaptive sampling. The most CPU dominant stages of VFRS are also summarized in Table 6.2.

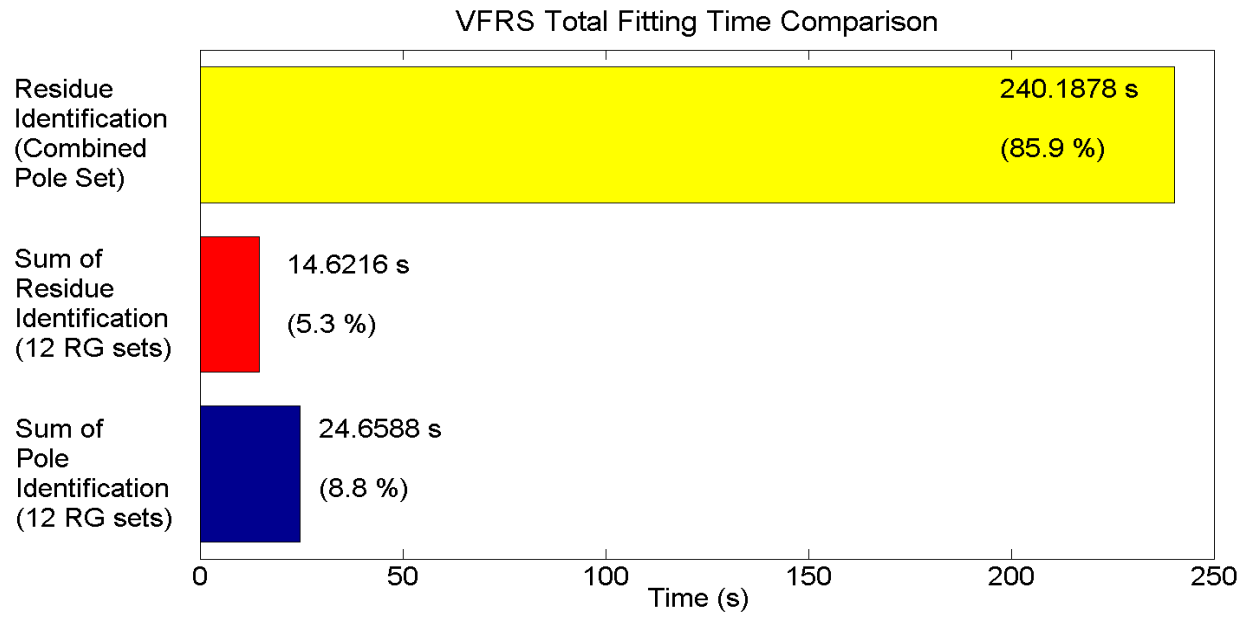

Figure 6.6: Computational cost percentage distribution in each stage of VFRS with 12 reduced set, each containing 25 randomly distributed samples.

Table 6.2: Computationally dominant stages of the VFRS process in terms of flop count.

Stage	Function	Overall flop count
1. Sum of Pole identification	$O\left(\tilde{n}r_{s,p}{P_{n,VFRS,p}}^{2}N^{\mathbf{2}}\right)$	$\sum_{p=1}^{\tilde{n}}\sum_{n=1}^{m_{VFRS,p}} 80r_{s,p}(P_{n,VFRS,p}+1)^{2}\times N^{\mathbf{2}}$
2. Sum of Residue identification	$O(\tilde{n}r_{s,p}{P_{n,VFRS,p}}^{2}N^{\mathbf{2}})$	$\sum_{p=1}^{\tilde{n}}\sum_{n=1}^{m_{VFRS,p}} 20r_{s,p}(P_{n,VFRS,p}+1)^{2}\times N^{\mathbf{2}}$
3. Residue identification of combined set	$O(S{P_n}^{2}N^{\mathbf{2}})$	$\sum_{n=1}^{m} 20S(P_n+1)^{2}\times N^{\mathbf{2}}$

6.3 Validation Studies

Three studies are used to demonstrate the efficiency of the proposed VFRS process and compare it to the standard VF and adaptive VF algorithms. All simulations were performed on a 2.93 GHz Xeon CPU server with 48 GB RAM.

6.3.1 Two-port blackbox model

The first study involved a two-port blackbox model described in terms of 801 uniform frequency samples in the frequency range 50 MHz ~ 5 GHz. The maximum number of iterations, N_{iter}, for pole relocation was set at 5. The RMS error ε_{rms} of the fit was set at 3.5×10^{-3}. The same RMS error threshold was applied to rational approximation of all random generation sets. The starting pole order is determined by a local minima and maxima estimation.

Table 6.3 shows the comparison of the standard VF, adaptive sampling VF, and six different implementations of VFRS methods with different choices of number of random sets and samples. The standard fast VF with relaxation required 78 complex conjugate pairs of poles to meet the RMS error threshold in 93.3 s, while adaptive sampling VF of 314 reduced sets of samples required 72 poles in 57.83 s. The rest of VFRS have different number of samples $r_{s,p}$ and number of sets $\tilde{n}$. The number of sets is the minimum number of sets required for rational function fit of VFRS to meet the RMS error. Based on the comparison, it is observed that VFRS with 10 randomly generated samples per set and 12 different sets had the best computation time of 17.88 s, which is a speedup of 5.22x and 3.23x over the standard VF and adaptive sampling VF, respectively. Figures 6.7 to 6.9 show the VFRS of {25 samples, 4 sets}, and {10 samples, 12 sets}. As the number of samples per set is reduced, the corresponding set will have different

representation of the magnitude compared to the original magnitude of function that contains full samples.

Table 6.3: Comparison of number of poles and corresponding RMS error of standard VF, adaptive sampling VF, and VF via randomly generated samples and sets (VFRS).

Method	No. of poles required	RMS error (ε_{rms}= 3.5×10^{-3})	Computation time (s)
Standard VF (801 samples)	78	0.0034985	93.383081
Adaptive Sampling VF (314 samples)	72	0.0034617	57.833803
VFRS (100 samples,2 sets)	136	0.0027179	64.527082
VFRS (50 samples,2 sets)	76	0.003581	49.090608
VFRS (25 samples,4 sets)	96	0.0034452	52.906699
VFRS (10 samples,12 sets)	96 (8 each)	0.0031653	17.888959
VFRS (5 samples,25 sets)	100	0.0031551	32.757989
VFRS (5 samples,30 sets)	120	0.0028349	34.249676

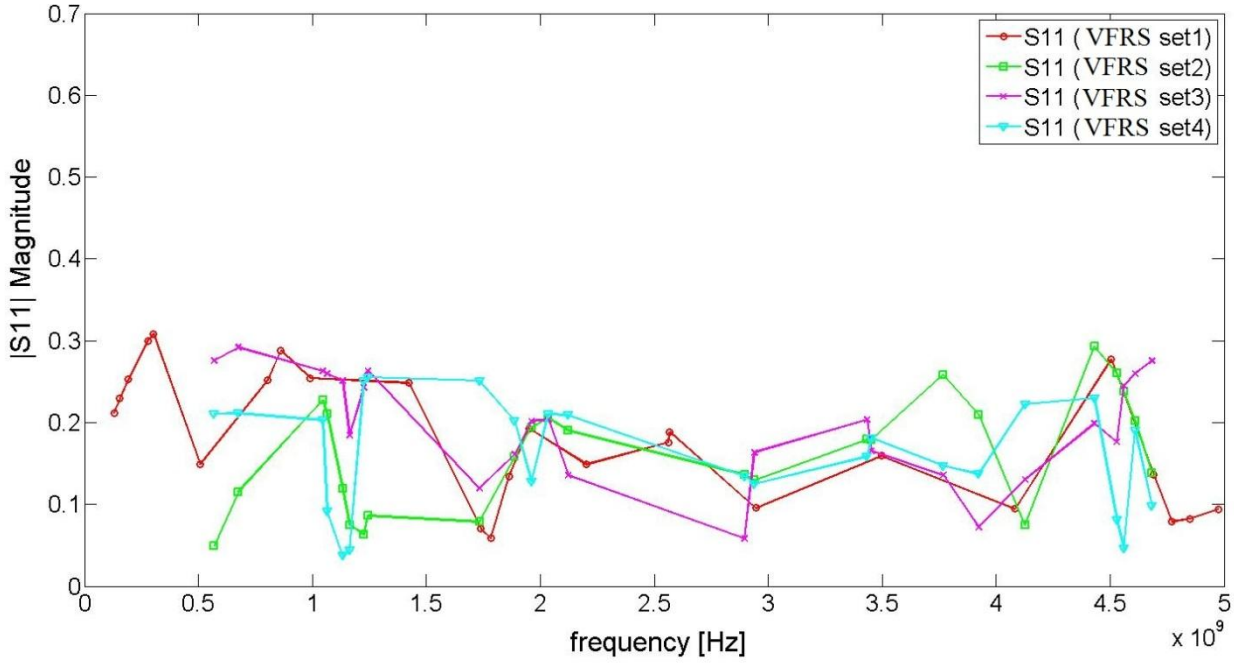

Figure 6.7: Magnitude of S_{11} of VFRS with $r_{s,p} = 25$ samples per set, $\tilde{n} = 4$ sets.

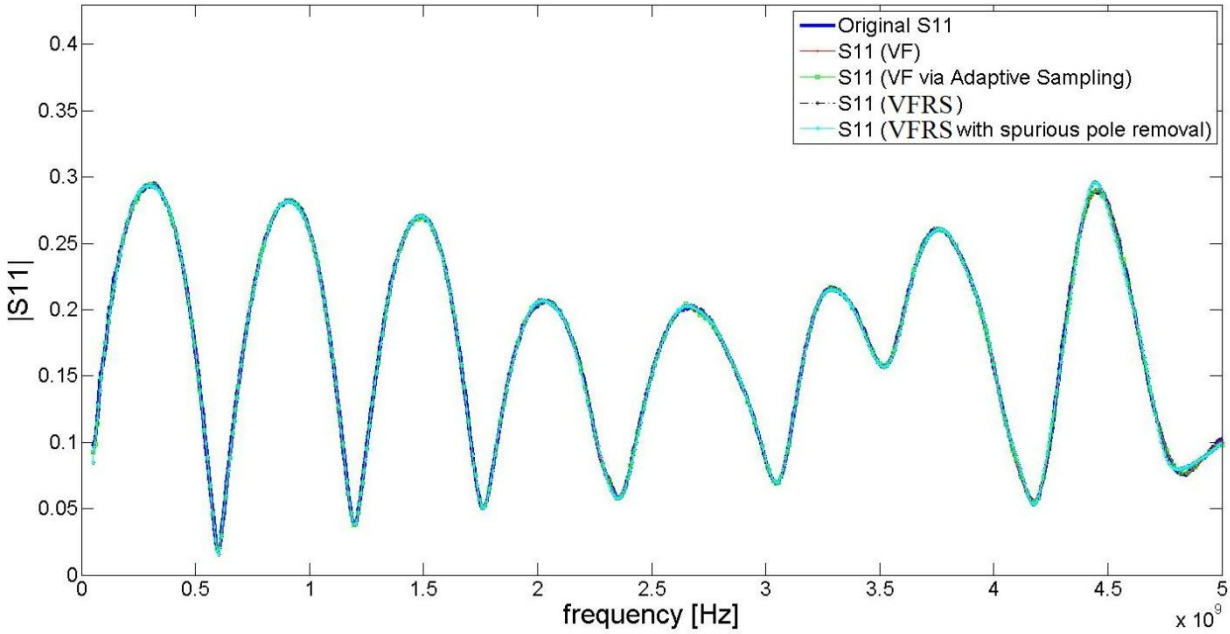

Figure 6.8: Comparison of magnitude of S_{11} standard VF, adaptive VF, VFRS $r_{s,p} = 25$ samples per set, $\tilde{n} = 4$ sets, and VFRS $r_{s,p} = 25$ samples per set, $\tilde{n} = 4$ sets after spurious pole removal.

Figure 6.8 compares the magnitude of measured S_{11}, fitted S_{11} with standard VF, adaptive sampling, VFRS {25 samples, 4 sets}, and VFRS of {25 samples, 4 sets} after spurious pole removal. Excellent agreement among all the methodologies is observed, and this proves VFRS is an effective method that preserves the accuracy of the fit. Figure 6.8 shows 4 sets out of 12 random generated sampling of S_{11} and S_{12} and fitted magnitude of S_{11} and S_{12} due to random generation sampling for {10 samples, 12 sets}. The difference of the magnitude of S_{11} and S_{12} based on standard VF and VF via random generation is minimal, as RMS error for VF of {10 randomly generated samples / 12 sets} meets the RMS threshold.

Table 6.4 shows the RMS error of VFRS of 4 reduced sets with 25 random samples, and the overall RMS error of VFRS with combined set of poles from 4 sets. The RMS error from each random generation set fails to meet the RMS error of 3.5×10^{-3}. Therefore, for each set, the number of poles is constrained by the number of randomly chosen samples. In this example, 24 complex conjugate pole pairs can be used for each randomly generated set of 25 samples, and 4 sets of 24 complex conjugate pole pairs are combined to form a total of 96 poles. These final 96 complex conjugate common pole pairs are used for least squares fit of the 2-port matrix with VFRS, reducing not only the number of frequency samples S, but all the critical parameters that control the computation time of the least squares fit.

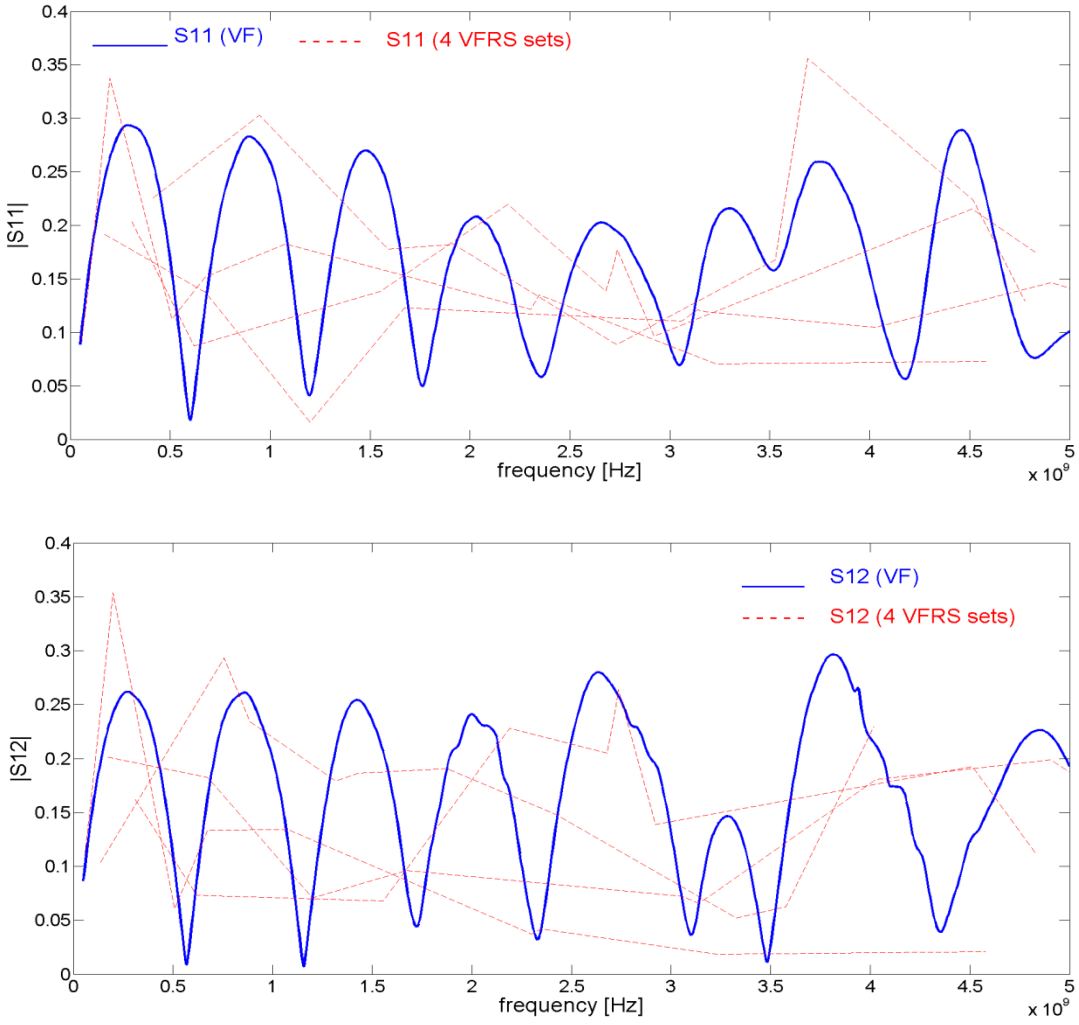

Figure 6.9: Magnitude of S_{11} (top) and S_{12} (bottom) due to VFRS {10 samples per set, 12 sets}, and 4 of 12 randomly generated sets.

Table 6.4: RMS error for VF of {25 randomly generated samples per set, 4 sets }.

{25/4} VFRS	RMS Error
Set 1	0.04051618
Set 2	0.00647947
Set 3	0.00977175
Set 4	0.01070029
VFRS (combination of poles from set 1, 2,3,4)	0.00344517

Figure 6.10 shows the RMS error (top) and the computation time (bottom) with respect to the number of randomly generated sets for 10 samples per set. As the number of random sets with 10 randomly generated samples increases, the number of total poles used for rational function fit will also increase, and the RMS error of the fit will decrease. Likewise, the overall computation time will increase linearly with respect to the added random sets. Figure 6.11 gives a nice summary of the computation time for all the methods of Table 6.3. It shows that, at least for this specific fitting study, VFRS is the most computationally efficient method.

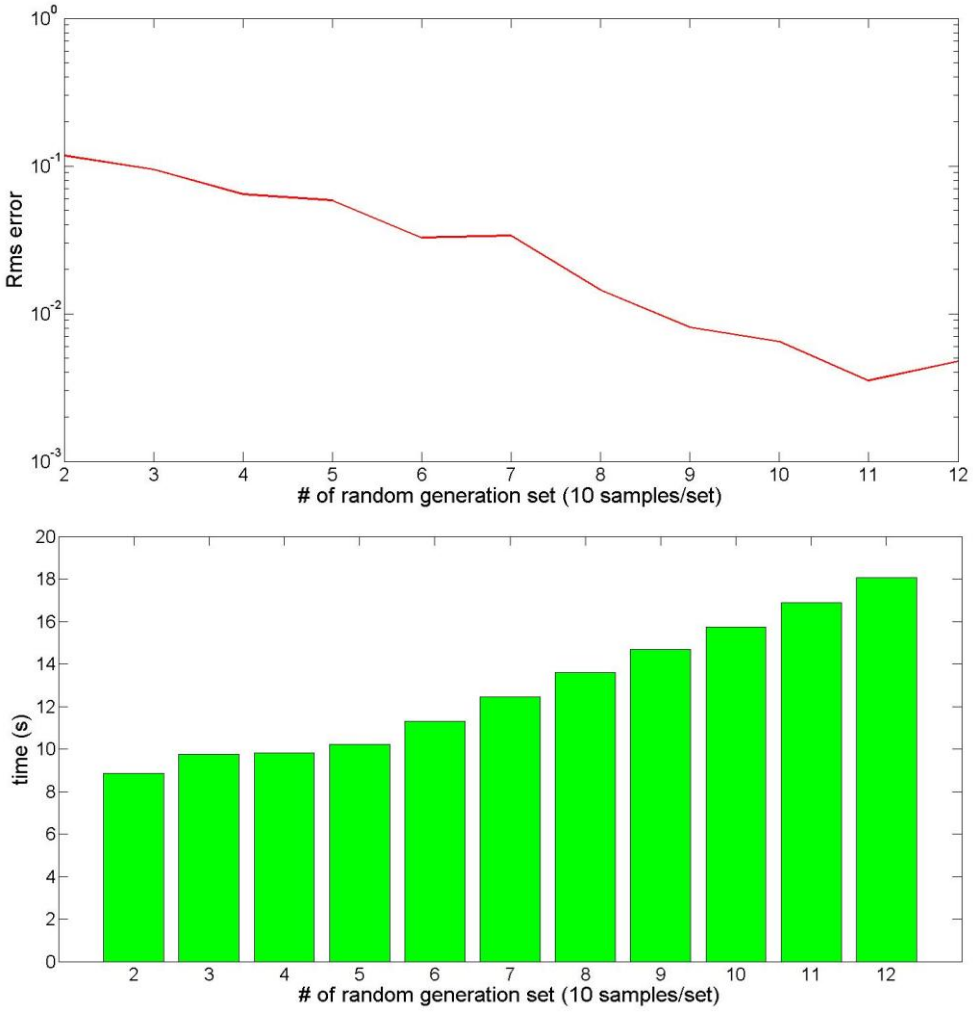

Figure 6.10: RMS error vs. the number of random generation set (10 samples/set) (top) and the computation time vs. the number of random generation set (10 samples/set) (bottom).

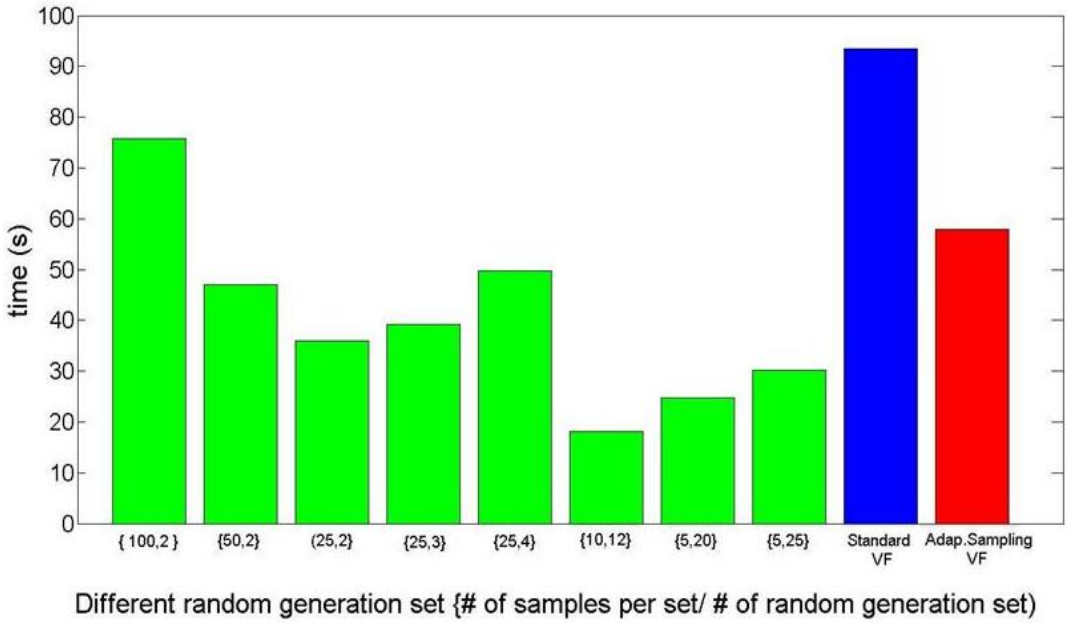

Figure 6.11: Computation time comparison of standard VF, adaptive sampling VF, and several implementations of VFRS.

6.3.2 Ten-port five-coupled microstrip lines

The second case considered concerns the fitting of the response of the scattering parameters of 10-port network associated with a set of five coupled microstrip lines. Frequency data for the S-parameters were obtained using a full-wave 3D field solver. The data involve 3996 frequency samples uniformly selected over the 10 MHz - 10 GHz bandwidth. Figure 6.12 compares the magnitudes of the original S(1,1) ~ S(1,10) responses with those obtained using a VFRS implementation that utilize 6 subsets of data with 25 samples each. A total of 114 complex conjugate poles were used in the final fit with spurious pole detection and removal. The resulting RMS error of the VFRS fit was 1.1541×10^{-4}, which was well below the target value of 3×10^{-4}.

Figure 6.13 depicts how each one of the subsets performs in fitting the sampled points involved in it for the case of the $S(1,1)$ parameter. As expected, the reduced number of samples

in each set achieves nothing else but a locally effective fit of the entire response. However, with enough subsets, the process results in the accurate computation of the poles for the system, thus facilitating a highly accurate fit, as Figure 6.12 illustrates, with superior computational efficiency compared to standard VF.

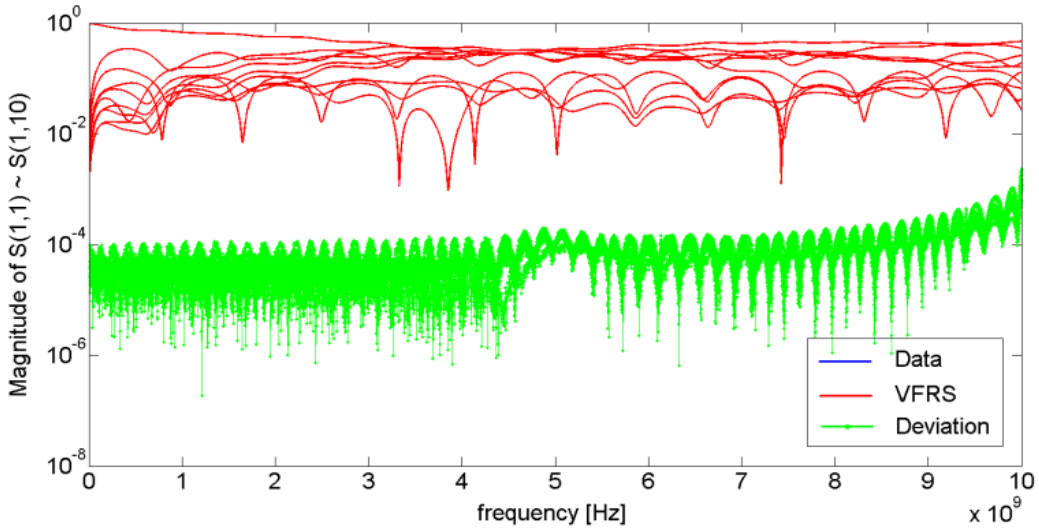

Figure 6.12: Magnitude of original and fitted S(1,1) ~ S(1,10) for a five coupled microstrip ten-port.

The distribution of the poles of standard VF, adaptive sampling VF, and VFRS after spurious pole removal is compared in Figure 6.14. As expected, the pole distributions for the standard and adaptive VF are very close. VFRS, while yielding a very accurate approximation of the original S matrix, requires a slightly larger number of poles to achieve its accurate fit.

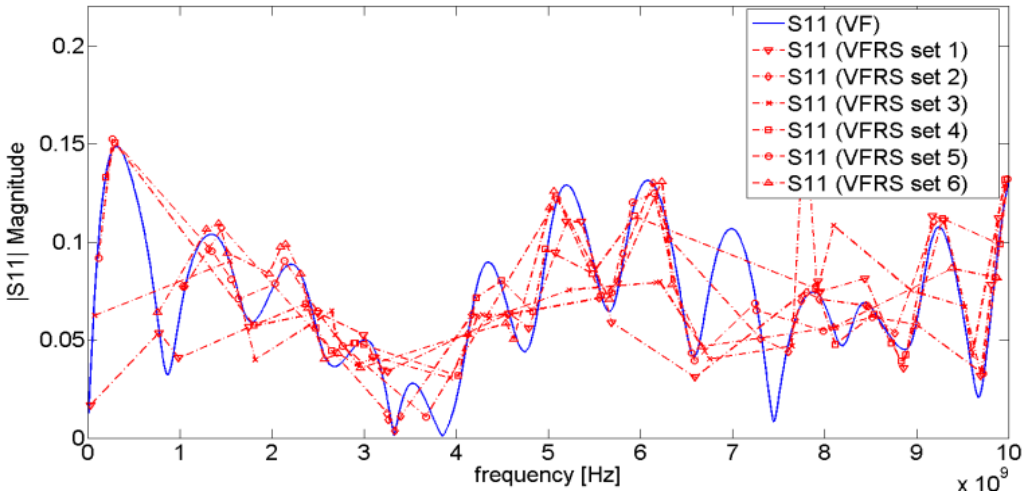

Figure 6.13: Illustration of the fitting performance for each one of the subsets used in VFRS.

Table 6.5 compares the pole order, RMS error, and the computational cost of the standard VF, adaptive sampling VF, and several choices of number of subsets and number of samples in each subset for VFRS. The same RMS target of 3×10^{-4} was used for the simulation criteria. All sets in Table 6.5 meet the RMS criteria and are the optimum number of sets without over-fitting the data. It can be seen from Table 6.5 that VFRS with 6 random sets and each set having 25 randomly chosen samples is computationally the most efficient approach out of all other sets. It achieves a speed-up factor of 25 and 6.8, respectively, compared to standard VF and adaptive sampling VF.

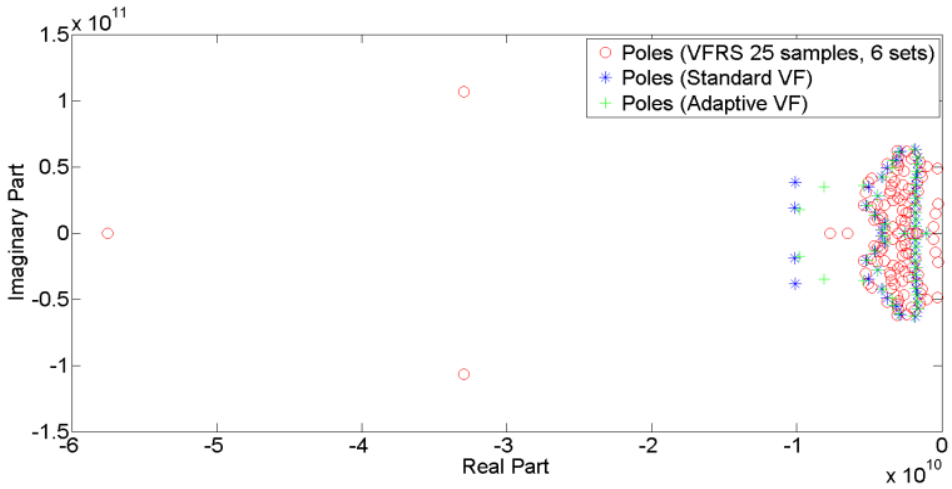

Figure 6.14: Comparison of pole distribution for standard VF, adaptive sampling VF, and VFRS (25 samples, 6 sets).

Figure 6.15 compares the computational time and speed-up factor of standard VF (labeled as VF), adaptive sampling VF (labeled as adap VF), and several different VFRS sets, according to their number of random samples and number of sets with and without spurious pole removal. It shows that a careful choice of randomly chosen samples can improve the computational efficiency of the fit by 15 ~ 25 for five-coupled microstrip interpolation problem compared with the standard VF. Note that computation time comparison is a subjective one. For example, initial number of poles assigned to both methods was 2. Each time both methods did not converge, 4 complex conjugate poles were added in the subsequent iteration steps for both methods. Thus, it took 13 iterations with increasing number of poles {2,6,10,14,….,50} used in pole identification, eigenvalue decomposition, and residue identification process for VF. We note that the final speed-up factor between VFRS and VF is based not on the computation time spent with VF with 50 complex conjugate poles, but on the 13 iterations needed to find the right number of poles to converge. Since the size of the matrices in least squares of VFRS is significantly reduced compared to VF, increasing the iterations to find the poles will not affect the overall computation time for VFRS. However, since the computational cost of the VF process with original data is

dependent on number of iterations needed to find the number of poles that will converge, this will add additional computational complexity. Therefore, the comparison of the two methods is subjective. Had we known the number of poles that would bring convergence to our fit prior to fitting, we would have used fewer iterations for poles, and the speed-up factor of VFRS would have decreased. On the other hand, if we needed more iterations for both method to converge, the speed-up factor of VFRS compared to VF would have increased. Hence, when considering the increase of the number of poles for standard VF and VFRS, we considered reasonable increase in number of poles.

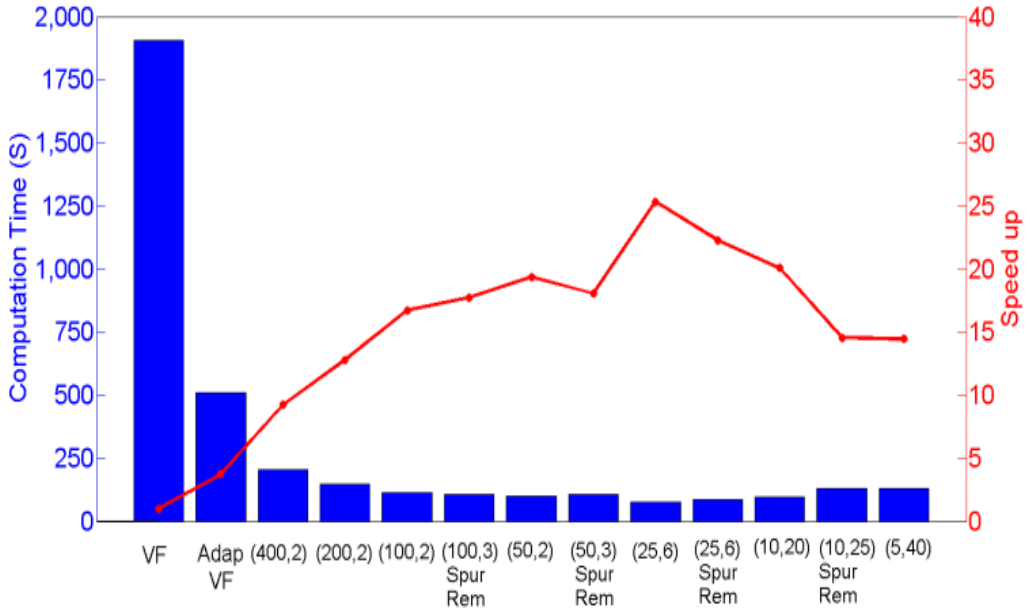

Figure 6.15: Comparison of computation time (left) and speed up w.r.t. VF (right) of several choices of number of samples per set and number of sets in VFRS.

Table 6.5: Comparison of order, RMS error and computation time of standard VF (fast VF), adaptive sampling VF, and different sets of VFRS (with and without spurious pole removal).

Method	No. of poles	RMS error	Computation time (s)
Standard VF (3996 samples)	50	9.9831×10^{-6}	1907.4743
Adaptive Sampling VF (1216 samples)	50	2.8574×10^{-4}	510.8488
VFRS {400,2} (spurious poles removal)	50	3.4771×10^{-5}	239.5485
VFRS {400,2}	100	9.9335×10^{-6}	206.5614
VFRS {200,2} (spurious poles removal)	50	1.5608×10^{-5}	152.5384
VFRS {200,2}	100	9.9314×10^{-6}	149.0372
VFRS {100,3} (spurious poles removal)	58	1.0945×10^{-4}	107.4767
VFRS {100,2}	100	9.9377×10^{-6}	114.1316
VFRS {50,3} (spurious poles removal)	92	1.3353×10^{-4}	105.6333
VFRS {50,2}	96	1.0863×10^{-5}	98.4449
VFRS {25,6} (spurious poles removal)	114	1.1154×10^{-4}	85.5948
VFRS {25,6}	120	1.3019×10^{-4}	75.2751
VFRS {10,25} (spurious poles removal)	172	1.3589×10^{-4}	130.8755
VFRS {10,20}	160	1.6106×10^{-5}	95.0192
VFRS {5, 80} (spurious poles removal)	267	1.0907×10^{-5}	246.1891
VFRS {5, 40}	160	9.8170×10^{-5}	131.8349

6.3.3 A 32-port board interconnect structure

The third study considers the fitting of the response of a set of 16 tightly coupled traces on a two-layer board. The lengths of the traces vary from 3500 mils to 5000 mils, with some of the coupled striplines from the bottom layer transitioning to microstrip lines on top layer by vias. Figure 6.16 demonstrates the accuracy of VFRS fitting for a set of the S-parameters for the case of RMS target of 1.5×10^{-3}. Similar accuracy was observed for all S-parameters.

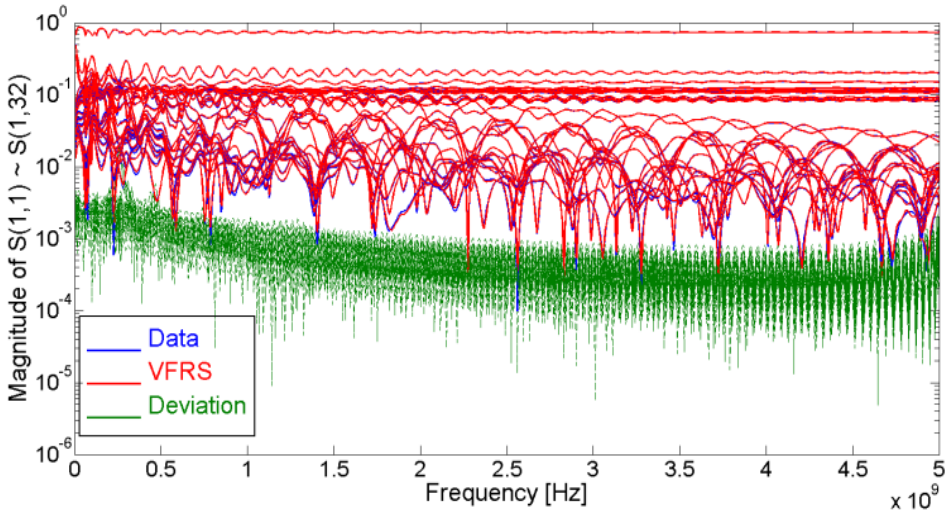

Figure 6.16: Magnitude of original and fitted S(1,1) ~ S(1,32) for a 32-port board interconnect network.

In order to reduce the number of iterations and the CPU time to find the optimum number of poles, the number of resonances in the magnitude of $S(1,1) \sim S(1,32)$ were detected and were used as an initial estimate of the number of poles before using standard VF and adaptive sampling VF. This number was 206. Five sets of iterations N_{iter} for pole relocation were used, with the number of poles in subsequent interpolation increasing by 10. Table 6.6 compares the pole order, RMS error and the computation time of standard VF, adaptive sampling VF, frequency partitioned VF (FPVF), and VFRS with several choices of number of subsets and number of samples per set, as well as VFRS combined with frequency partitioning. It shows that VFRS significantly improves the computational cost of the fit, with the choice of 6 sets and 50 random samples per set leading to a speed-up factor of 35 compared to standard VF. The performance of VFRS in general was comparable to or slightly better than FPVF. Two different cases of frequency partitioning (FP) have also been explored in the use of VFRS to test whether its use can further reduce the computation time. The first case divides the original frequency spectrum in 10 intervals, with each interval having 100 frequency samples. The second case

divides the spectrum in 20 intervals, with each interval having 50 frequency samples. In each interval, VFRS is applied. It is observed that with 10 frequency regimes, with one subset of 32 samples used in each interval, the computation time is 258.8914 s, which amounts to 48x speed-up compared to standard VF, and 1.4x speed-up compared to FPVF with 10 frequency regimes. This improvement in numerical efficiency is due to VFRS further reducing the number of frequency samples in a subset that is already reduced by FP, and capturing the accurate spread poles in each subset. Figure 6.17 shows pictorially the computation time and the speed-up factor involved with VFRS, standard VF, adaptive VF, FPVF, and FP-VFRS approaches.

Table 6.6: Comparison of order, RMS error and computation time of standard VF (fast VF), adaptive sampling VF, frequency partitioned Vector Fitting (FPVF) and different sets of VFRS and frequency partitioned VFRS.

Method	No. of poles	RMS error	Computation time (s)
Standard VF (1000 samples)	308	0.0012949	12425.821
Adaptive Sampling VF (469 samples)	306	0.0013546	3844.534
10 Freq Partition	320	0.0011464	373.321939
20 Freq Partition	440	0.0011489	464.702175
VFRS {100,4}	392	0.0014152	546.636
VFRS {50,6}	288	0.0013596	354.829
VFRS {50,7}	336	0.0012365	440.037
VFRS {25,12}	288	0.0012331	397.488
VFRS {25,13}	312	0.0012855	434.329
VFRS {10,38}	304	0.0013598	626.869
10 FP(VFRS{25,2})	480	0.0010592	457.4885
10 FP(VFRS{32,1})	300	0.0011286	258.8914
20 FP(VFRS{10,2})	320	0.0012357	404.49857
20 FP(VFRS{32,1})	600	0.0011637	620.37183

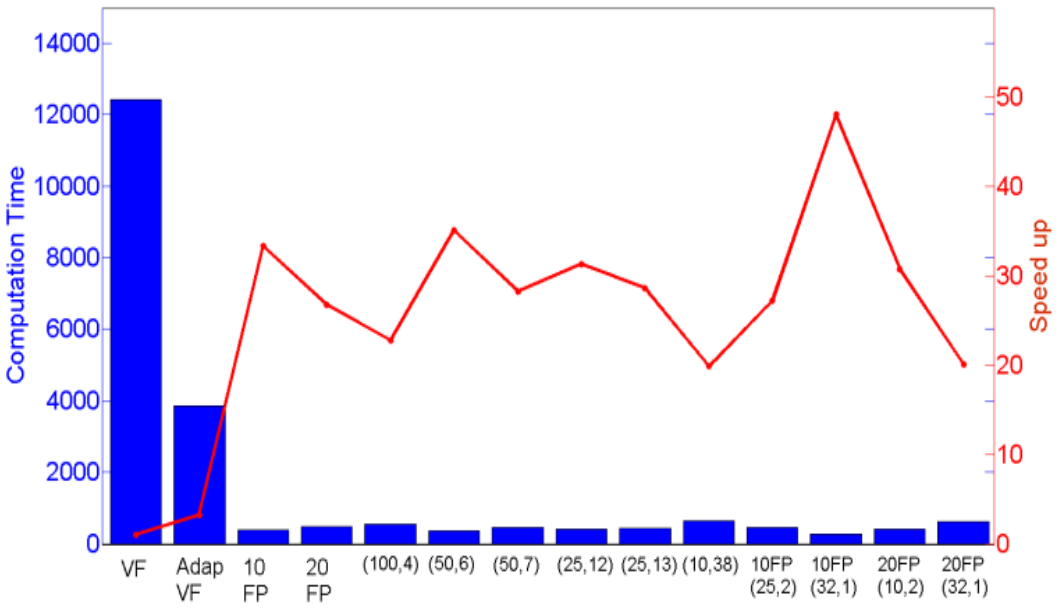

Figure 6.17: Comparison of computation time (left) and speed up w.r.t. VF (right) of several choices of number of samples per set and number of sets in VFRS with and without frequency partitioning.

6.4 Summary

In summary, we have proposed Vector Fitting via Repeated Random Sampling (VFRS) as an algorithm for expedient rational function fitting of broadband electromagnetic responses of multi-port passive networks. VFRS uses VF for rational fitting of the data in each subset. The poles thus generated are compiled into one set of poles that, after spurious pole removal, are used to retrieve the respective residues through vector fitting of the entire response. Since pole calculation, the most expensive component of the VF process, is carried out working with small data sets, VFRS yields significant reduction in the overall computational cost of rational function fitting compared to both standard VF and adaptive VF. The effectiveness and improved computational efficiency of VFRS is demonstrated through its application to the fitting of broadband S-parameters for three complex multi-ports interconnect structures. As shown by

examples in this chapter, the effectiveness of VFRS is maximized for a large set of measured/simulated broadband responses. Furthermore, it is shown that even better computational cost can be achieved with combining a similar reduction technique such as frequency partitioning with VFRS. Through our studies, it was observed that the most cost-effective number of samples per set was 10 ~ 25. Use of post-processing techniques was also discussed, and it was verified that the removal of the spurious poles could further decrease the order without affecting the quality of the overall rational function fit. Reduction of the number of the finalized poles is important as the increasing number of spurious poles can decrease the numerical conditioning of the system, and even result in violation of passivity if the poles are too close or if multiplicity of the poles occurs.

CHAPTER 7

FAST ASSESSMENT OF THE IMPACT OF SURROUNDING WIRING ON THE TRANSMISSION PROPERTIES OF HIGH-SPEED INTERCONNECT CHANNELS

7.1 Introduction

At this point, we turn our attention to another important issue of electromagnetic macromodeling, namely, the development of frequency-dependent macromodels of interconnect structures in the presence of uncertainty or statistical variability in their geometric and material properties. As a concrete example of why such macromodeling is needed, let us consider the noise-aware design of a high-speed channel in the early stages of design. Noise-aware routing of the signal distribution network is a key concern of the signal integrity designer in minimizing interconnect-induced signal distortion in the channel, especially with the increase in switching speed and the higher functionality integration both on chip and in the package. While a great deal of care goes into the design of the channel interconnects to ensure its electrical performance according to the desired signal integrity specifications, such design, especially in the early stages of design, is often performed with only partial information about the specifics of the substrate wiring in the immediate neighborhood of the channel after insertion. Thus, the electromagnetic (capacitive and inductive) loading that the channel interconnects experience due to neighboring

wires that are not part of the channel and thus are not accounted for during design cannot be assessed with specificity until the final layout and routing are known.

A possible way to account for such electromagnetic (EM) loading early in the design phase is through EM simulations that include several possible layouts of the wiring in the vicinity of the channel of interest. Such an approach lends itself to a statistical quantification of the impact of such loading on the signal integrity of the channel. A way in which such an analysis can be performed in a manner that is computationally efficient yet accurate for the resulting statistics to be useful to the signal integrity engineers is presented in this chapter.

Statistical EM analysis of interconnect electrical performance is a well-examined topic [98]. Design of experiments (DoE) [101],[102], which is known for optimal selection of the important subset of model parameters, is useful for yield estimation and design refinement of the parameters, and is a well-established method for statistical high-speed channel and link simulation [99],[100]. However, its use in tackling the uncertainty of the anticipated wiring layout in the neighborhood of the channel after insertion is hindered by the high dimensionality of the random space involved [103]. As an alternative, several stochastic modeling approaches have been under investigation recently [103]-[118]. However, thus far these approaches are focused on geometric, material, or even layout uncertainty of the wiring in the channel itself, rather than on the uncertainty of the layout of the surrounding wiring.

Instead, our focus is on how to account, in a quantitative statistical manner, for the impact of the surrounding wires in the transmission properties of the channel. We propose a methodology [113] for the fast assessment of the impact of electromagnetic loading by surrounding wiring on the signal transmission properties of a high-speed interconnect channel. The proposed methodology is aimed at alleviating the computational complexity of the electromagnetic

modeling of the channel including the details of the wiring in its surrounding that, more often than not and especially in the early stages of design are not well defined and thus are best accounted for through a Monte Carlo analysis. Instead, use of a stochastic macromodel for the channel is proposed that incorporates the electromagnetic attributes of the surrounding wiring through a statistical description of its loading on the interconnects of the channel. The proposed method makes use of parametric rational interpolation [119]-[123] to develop a frequency-dependent macromodel that is valid over the multi-dimensional space that describes the uncertainty of the neighboring layout topography. Making use of stochastic collocation [111],[112], the channel macromodel lends itself to fast quantitative analysis of the channel transmission properties and signal degradation in both the frequency and the time domain. While reviewing the big scope of the overall research goal, the proposed methodology also improves the three major challenges in the macromodeling field in the context of stochastic macromodeling.

This chapter is organized as follows. We begin with the introduction of the framework behind the fast stochastic macromodeling technique in frequency and time domain. A problem statement of the stochastic modeling of the channel is given, followed by the introduction of the stochastic collocation method. Then the way stochastic modeling and parametric macromodeling are combined to generate passive stochastic macromodels is discussed. The chapter then concludes with numerical studies with multi-port single-ended channel and differential pair channel that allow us to demonstrate the development and application of the proposed stochastic macromodel with emphasis on its key attributes and its usefulness as a computer-aided tool for noise-aware wiring layout planning.

7.2 Stochastic Macromodeling

This section covers the detailed interconnect channel theoretical framework for the stochastic macromodeling of a channel in the presence of surrounding wiring of uncertainty in its geometry. To facilitate presentation and without loss of generality, we consider the channel to consist of a set of parallel wires, with its overall span partitioned into p segments each one of which constitutes a unit cell of the overall structure. Our approach uses rational interpolation and stochastic collocation for sampling and interpolation of the random spaces describing the m-port unit-cell in frequency domain. The obtained unit-cell scattering matrix is converted to unit-cell transmission matrix, $\boldsymbol{T}_{unit,}$ and the p transmission matrices are concatenated to obtain the transmission matrix of the channel, $\boldsymbol{T}_{inter}$. Then, $\boldsymbol{T}_{inter}$ is converted back to the scattering matrix for the channel**.**

7.2.1 Problem statement

Figure 7.1 (a) depicts the cross-sectional geometry of a generic interconnect structure of N active wires. From the depicted wires, only the center one is the wire of the channel. The other *N-1* wires surrounding the channel are external wires for which only partial uncertain information is available about their geometry and layout. The straightforward way to analyze the channel transmission properties in frequency and time domain in the presence of such uncertainty is through Monte Carlo (MC) analysis [99]-[102]. With inclusion of ensembles of all random realizations for the random inputs, MC analysis relies on repetitive deterministic simulations to solve for the channel transmission properties accounting for the uncertainty of the adjacent wiring topology. Despite its simplicity, MC suffers from slow convergence [111].[112]. Brute-force MC converges asymptotically at a rate $1/\sqrt{K}$ with K number of realizations.

Alternatives to brute-force MC have been proposed recently, where polynomial chaos interpolation over the random space and stochastic collocation are used to provide for a faster, yet accurate, calculation of the statistics of the response [103]-[118]. While successful in reducing the computational cost of brute-force MC, such approaches need to tackle the complexity resulting from the high dimensionality of the random space when the number of random variables needed to describe uncertainty becomes very large. For example, in the context of the interconnect depicted in Figure 7.1 (a), the dimensionality of the random space starts increasing fast with the number of adjacent wires if conductor width, spacing and thickness are to be included in the definition of the random space.

This high-dimensionality complexity can be circumvented by recognizing that, since we are interested only in electromagnetic loading by adjacent wiring, the key effects of such loading, namely capacitive and inductive coupling, can be represented through an equivalent set of only a few interconnect wires adjacent to the channel, of width, thickness and spacing chosen such that their resulting loading effect accurately represent the loading effect of more complicated multi-wire configurations. For example, Figure 7.1 (b) shows a set of two wires, one on either side of the channel wire in the center, are one such choice of an equivalent set. Thus, the conjecture is made that the effect of EM loading of the channel due to a numbers of wires in its vicinity can be described using two adjacent wires with uncertainty in their widths and spacing from the channel, being the governing random variables with properly selected probability density functions (pdf).

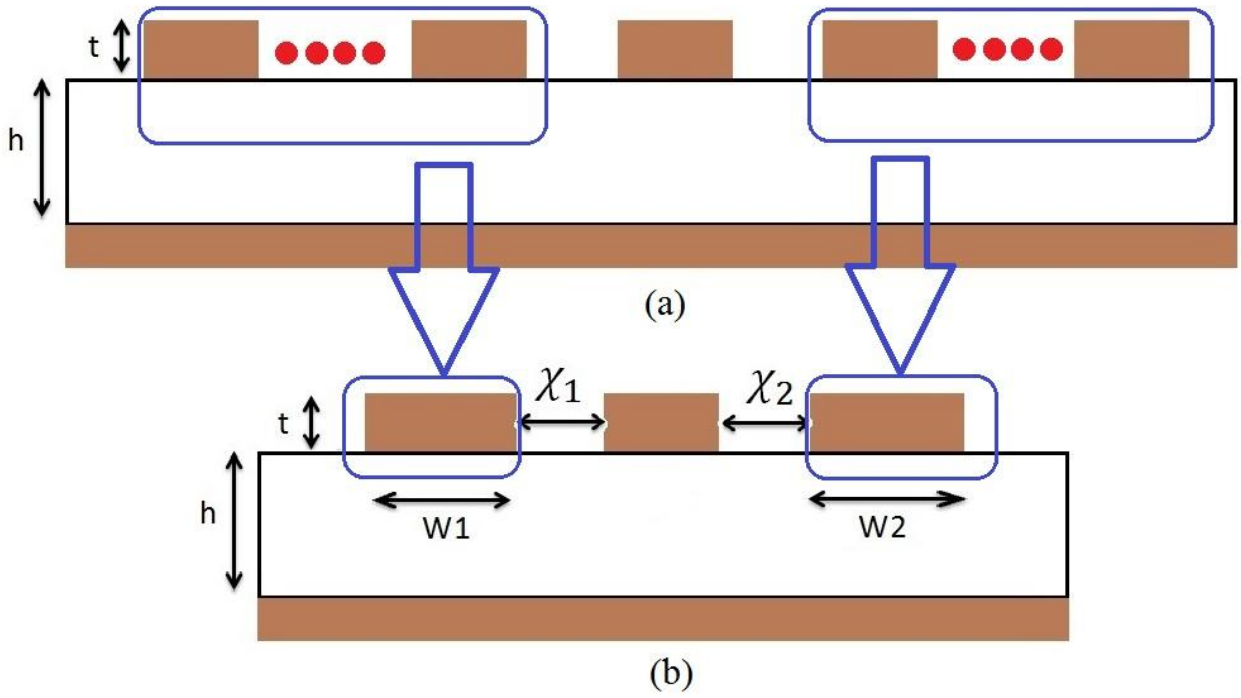

Figure 7.1: (a) Cross-sectional geometry of a generic interconnect structure where the center single-ended channel is surrounded by other wires of uncertainty in their routing. (b) An equivalent reduced model of where the loading by multiple wires on either side of center single-ended channel is represented in only a single wire.

A priori study in Tables 7.1 and 7.2 shows the impact of the per-unit-length short-circuit capacitance and per-unit-length inductance of the channel with increasing number of wiring in the vicinity of the channel and the per-unit-length short-circuit capacitance and per-unit-length inductance of the channel with increasing the width of the adjacent wires. The study shows for both models the tendency that per-unit-length parameter values of the channel will converge and will not be affected much after reaching convergence. These studies support our conjecture that adjacent wiring topography can be approximately represented in terms of just two wires with random variables taken to be the wire width and their spacing from the channel.

Table 7.1: Per-unit-length capacitance (pF/cm) and per-unit-length inductance (nH/cm) (at 1GHz) values of the channel wire with increasing number of adjacent wiring (2 – 14). All wires are of same width (0.3 mm) and thickness (0.03 mm). Adjacent wire spacing is 0.1 mm.

Number of adjacent wires	2	4	6	8	10	12	14
Pul. capacitance	1.2137	1.2195	1.2214	1.2297	1.2285	1.2360	1.2367
Pul. inductance	2.8185	2.8136	2.8130	2.8129	2.8130	2.8131	2.8132

Table 7.2: Per-unit-length capacitance (pF/cm) and per-unit-length inductance (nH/cm) (at 1GHz) values of the wire channel with 2 adjacent wires with variable width and spacing from channelwire. Two sets of adjacent wire width 0.4 mm and 0.5 mm were considered while spacing from channel wire was varied from 0.05 – 0.3 mm.

Distance (mm)	0.05	0.1	0.15	0.2	0.25	0.3
Pul. Capacitance (a)	1.4234	1.2782	1.2208	1.1996	1.1897	1.1898
Pul. Inductance (a)	2.4964	2.7055	2.797	2.8436	2.8696	2.8792
Pul. Capacitance (b)	1.4215	1.2709	1.2208	1.1991	1.1940	1.1937
Pul. Inductance (b)	2.4438	2.6756	2.7793	2.8329	2.8621	2.8912

Let us again review Figure 7.1 (b), which shows the single-ended microstrip channel model with adjacent wirings. For the sake of simplicity but without loss of generality, the substrate dielectric constant (ε_r), and the length (L), width (W), and thickness (t) of both the channel and the external wires as well as the thickness of the substrate (h) are fixed. The external wiring

uncertainty is defined in terms of the distance of each of the wires from the channel. Thus, given the maximum and minimum values of these distances and a known probability density function (pdf) for their description, the uncertainty of the external wiring for this specific case is completely described. Assuming that the random variables are uniformly distributed, normalized random variables, ξ_i, over the interval [–1,1] may be used

$$\chi_i = \frac{1}{2}\left(\chi_{i,min} + \chi_{i,max}\right) + \xi_i \frac{1}{2}\left(\chi_{i,min} - \chi_{i,max}\right), i = 1,2. \quad (7.1)$$

In the following, the physical random variables are used in the development of the mathematical foundation of the model. With the random space defined, the goal is to build a stochastic macromodel $\boldsymbol{S}(s, \vec{\chi})$ that represents the channel accounting for adjacent random wiring loading over the frequency bandwidth of interest.

7.2.2 Stochastic collocation

Several different approaches are available for numerical solutions with uncertainty in system parameters, inputs, and boundary conditions. Monte Carlo (MC) is a very well known sampling method that relies on repetitive deterministic solutions for each realization. As mentioned before, the convergence rate of MC is slow. Another popular method such as perturbation method expands the random inputs via Taylor series around their mean and truncates at a certain order. Because of the existing problem with the convergent series of expansion, this method works for small random inputs and outputs and their application is limited [111]. Stochastic Galerkin method, which is a generalization of Wiener-Hermite polynomial chaos expansion, establishes a good convergence for problems with large random inputs and outputs. It also reaches a fast convergence rate with increasing order of the expansions. However, the equations used with stochastic Galerkin are often coupled and care needs to be taken to design an efficient solver [111]. The equations can also become very complicated if they have a non-linear form.

In this chapter, the stochastic collocation method is introduced. Stochastic collocation combines the strength of Monte Carlo and stochastic Galerkin methods. Just like stochastic Galerkin, stochastic collocation achieves fast convergence when there are small numbers of random variables, and the solution possesses sufficient smoothness in random space. Also, just like Monte Carlo, stochastic collocation has a very straight implementation as this method only requires solutions of the corresponding deterministic problems at each interpolation point in the random space [111],[112].

Stochastic collocation relies upon interpolations in the multidimensional random space. Going back to section 7.1 for a single-ended microstrip channel example with two uniform random variables (distance between channel and adjacent wiring) and their random space defined over the rectangular domain $[\chi_{i,min}, \chi_{i,max}]^2$, and i=1,2, the next step is to define a sampling grid over the random space using a deterministic Cartesian-product rule. Since the computational complexity of the stochastic collocation depends on the number of collocation nodes, a careful choice needs to be made with nodal set with fewest possible number of points for a prescribed accuracy. One typical way to choose the nodal set is the tensor product of one-dimensional set defined in Equation (7.2), if we can construct a one-dimensional interpolation based on the nodal sets $\theta_1^i = (\chi_1^i, \dots, \chi_{m_i}^i) \subset [\chi_{i,min}, \chi_{i,max}]$, where the basis function $a_k^i \equiv a_k(\chi^i)$ [111].

$$\boldsymbol{S}(s, \chi^i) = \sum_{k=1}^{m_i} S(s, \chi_k^i) \cdot a_k^i \tag{7.2}$$

Assuming that we use the same number of points for the two random variables, $m_{i_1} = m_{i_2} = m$, two-dimensional interpolation is expressed as tensor products of the one-dimensional nodal set as shown in (7.3). The total number of nodes used for two-dimensional interpolation is $M = m^2$.

$$\boldsymbol{S}(s,\chi^1,\chi^2)=\sum_{k_1=1}^{m}\sum_{k_2=1}^{m}\boldsymbol{S}\left(s,\chi_{k_1}^{(1)},\chi_{k_2}^{(2)}\right)\cdot\left(a_{k_1}^1\otimes a_{k_2}^2\right) \tag{7.3}$$

7.2.3 Root macromodeling / passivity enforcement

From the previous section, we defined an equidistant set of *m* points $(\chi_n)_{n=1}^m$ in random space $[\chi_{i,min},\chi_{i,max}]$ for each one of the two random variables. Next, use is made of a 2D/2.5D/3D EM solver to extract electromagnetic models for the interconnect for each grid sampling point in the random space. More specifically, given that the interconnect is assumed uniform, the model is obtained for an interconnect structure of length small compared to the minimum wavelength of interest. Thus, the total length of the structure is obtained as the concatenation of *p* unit-cells. Next, the system frequency response, $\{\boldsymbol{H}(s,\vec{\chi})_k\}_{k=1}^K$, obtained at *K* frequency points for each one of the sample points in the random space is used to construct a rational interpolation. The VF algorithm is used to produce a pole/residue form using an iterative pole relocation procedure. Each pole/residue model is of the form

$$\boldsymbol{R}(s_k,\chi_{k_1}^{(1)},\chi_{k_2}^{(2)})=\sum_{n=1}^{N}\frac{\boldsymbol{r}_n}{s_k-p_n} \tag{7.4}$$

Note that all the models in random space are fitted with common poles [120]-[122]. Two choices of the poles were tested in rational function approximation of the random space, and both have shown excellent results. First, common poles with linear displacement over the available bandwidth were used for all our macromodels sampled with tensor grid. As shown in (7.5), the complex pole pairs have small real parts and their imaginary parts linearly spaced over the parameter range of interest. In the absence of resonances, common poles with real poles can be distributed with linear displacement over the entire bandwidth instead of complex conjugate poles in (7.5). In the second option, one of the model poles was re-used to fit all other models.

Reference [123] reports possible bifurcation effects with direct parameterization of the model poles. However, our choice of common poles is based on the following rationale. First, since we are considering the macromodeling of an electrically small unit-cell structure, rational interpolation of either choice of direct common-poles fitting will lead to a smooth rational function fitting. Second, since indirect parameterization of the poles/residues or state space representation will lead to an increase in the number of iterations of the VF process, the overall cost of rational function fitting for each sample in the random space is higher. Therefore, use of common poles is preferable.

$$-b_v = -\alpha_v + j\beta_v, -b_{v+1} = -\alpha_v - j\beta_v,\ \alpha_v = 0.01\beta_v \tag{7.5}$$

For the choice of our common poles above, stability is enforced with a pole-flipping scheme [21], and passivity is enforced with a well-known iterative residue perturbation method [63]. The constructed rational models are the root macromodels [119]-[121], from which an interpolated stochastic macromodel over the entire random space will be generated.

7.2.4 Stochastic multivariate interpolation in frequency domain

Once the root macromodel of the unit-cell of interconnects is available and passivity is enforced, we make use of the properties of positive interpolation kernels [119]-[121] to preserve passivity of our stochastic model. The multivariate representation of our stochastic response can then be modeled as we employ univariate interpolation, and can be extended to a multivariate setting by filling up the entire space dimension by dimension. This is accomplished with tensor product interpolation in (7.6) with piecewise multi-linear interpolation [119]-[121] as our kernels $l_k(\chi)$ in Equation (7.6) and (7.7).

$$\boldsymbol{S}(s,\chi^1,\chi^2)=\sum_{k_1=1}^{K_1}\sum_{k_2=1}^{K_2}\boldsymbol{S}\left(s,\chi^{(1)},\chi^{(2)}\right)\times l_{k_1}\left(\chi^{(1)}\right)l_{k_2}\left(\chi^{(2)}\right) \tag{7.6}$$

$$\frac{\chi^{(i)}-\chi^{(i)}_{k_i-1}}{\chi^{(i)}_{k_i}-\chi^{(i)}_{k_i-1}},\chi^{(i)}\in\left[\chi^{(i)}_{k_i-1},\chi^{(i)}_{k_i}\right],k_i=2,\dots,K_i,\qquad i=1,2$$

$$\frac{\chi^{(i)}_{k_i+1}-\chi^{(i)}}{\chi^{(i)}_{k_i+1}-\chi^{(i)}_{k_i}},\chi^{(i)}\in\left[\chi^{(i)}_{k_i},\chi^{(i)}_{k_i+1}\right],k_i=1,\dots,K_i-1,\quad i=1,2$$

$$0,\text{ otherwise} \tag{7.7}$$

Note that the interpolation is in regards to the residues of our macromodels, where our collocated nodes are defined. Once we obtain residues of our macromodels from common-pole fitting, piecewise multi-linear interpolation is used to interpolate the residues for the entire random space. The tensor product and piecewise linear kernel scheme in (7.6) and (7.7) completes the interpolation of the stochastic response for the unit-cell $\{\boldsymbol{H}(s,\vec{\chi})_k\}_{k=1}^{K}$ with *K* data samples over complex frequency, $s=j\omega$. Figure 7.2 shows the piecewise linear interpolation kernel of a random variable that spans the 1-D random space with five nodes. The interpolation kernels $l_k(\chi)$ are scalar functions that satisfy the following constraints in (7.8) [124].

$$l_k(\chi)\geq 0$$

$$l_k(\chi_i)=\delta_{k,i}$$

$$\sum_{k=1}^{K_1}l_k(\chi)=1 \tag{7.8}$$

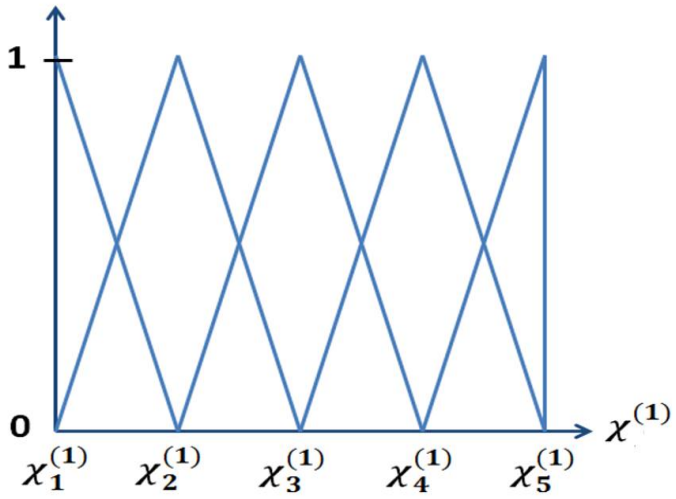

Figure 7.2: Piecewise linear interpolation basis functions in one-dimensional random space.

If our scattering matrix $\boldsymbol{S}(s,\chi^{(1)},\chi^{(2)})$ is passive, then the properties of the positive interpolation from the above equation (7.8) guarantee that (7.7) is simply a linear combination of stable and passive multivariate models by positive interpolation kernels. Therefore, this type of interpolation preserves the passivity of the model in the whole random space. Let us once again show the passivity preservation condition of a linear network defined by the scattering matrix in (7.9).

(a) $\boldsymbol{S}(s^*) = \boldsymbol{S}^*(s)$ for all s, where "*" is the complex conjugate

(b) $\boldsymbol{S}(s)$ is analytic in $\Re e(s) > 0$

(c) $\boldsymbol{I} - \boldsymbol{S^t}(s^*)\boldsymbol{S}(s) \geq 0$ for all s, and where in $\Re e(s) > 0$ (7.9)

Conditions (a) and (b) in (7.9) are automatically satisfied with our root macromodels, since all complex pole/residues are considered with their conjugates to enforce realness, and stability condition is imposed by pole-flipping within VF algorithm. Both conditions (a) and (b) are also preserved with multivariate extensions with positive interpolation. Equation (7.6) is a weighted sum with real nonnegative weights, thus preserving condition (a), and it is also a weighted sum

of strictly stable rational macrmodels, thus preserving condition (b). As passivity condition is enforced as a post-processing step for all the root macromodels, the positive interpolation also preserves the passivity condition of (c) in (7.9) for the entire random space. This can also be explained by observing the largest singular value of $\boldsymbol{S}(s,\chi^1,\chi^2)$. Since the largest singular value is $\|\boldsymbol{S}(s,\chi^1,\chi^2)\|_\infty \leq 1$**,** any non-negative linear combination of positive real matrix will also be a positive real matrix.

$$\|\boldsymbol{S}(s,\chi^1,\chi^2)\|_\infty \leq \sum_{k_1=1}^{K_1}\sum_{k_2=1}^{K_2}\left\|\boldsymbol{S}\left(s,\chi_{k_1}^1,\chi_{k_2}^2\right)\right\|_\infty l_{k_1}\left(\chi^{(1)}\right)l_{k_2}\left(\chi^{(2)}\right)$$

$$\leq \sum_{k_1=1}^{K_1}\sum_{k_2=1}^{K_2} l_{k_1}\left(\chi^{(1)}\right)l_{k_2}\left(\chi^{(2)}\right) = 1 \tag{7.10}$$

7.2.5 Response statistics

The statistics of our scattering parameters $\boldsymbol{S}\left(s,\chi^{(1)},\chi^{(2)}\right)$ and input/out voltage $\boldsymbol{V}\left(t,\chi^{(1)},\chi^{(2)}\right)$ response in the case of transient simulations are calculated using quadrature rules for the expedient calculation of their moments [111]. In this section, the statistics of $\boldsymbol{S}$ matrix are shown, but the same rule applies to the input/output voltage our channel. First, recognizing that the (*j*,*k*) entry of $\boldsymbol{S}\left(s,\chi^{(1)},\chi^{(2)}\right)$ is a combination of real and imaginary response of $S_{mn}\left(s,\chi^{(1)},\chi^{(2)}\right)$, the response of the expectations and the variance can be summarized as follows:

$$\boldsymbol{E}\left\{S_{mn}\left(s,\chi^{(1)},\chi^{(2)}\right)\right\} = \boldsymbol{E}\left\{Re\left\{S_{mn}\left(s,\chi^{(1)},\chi^{(2)}\right)\right\}\right\} + j\boldsymbol{E}\left\{Im\left\{S_{mn}\left(s,\chi^{(1)},\chi^{(2)}\right)\right\}\right\}$$

$$\boldsymbol{var}\left\{S_{mn}\left(s,\chi^{(1)},\chi^{(2)}\right)\right\} = \boldsymbol{var}\left\{Re\left\{S_{mn}\left(s,\chi^{(1)},\chi^{(2)}\right)\right\}\right\} + j\boldsymbol{var}\left\{Im\left\{S_{mn}\left(s,\chi^{(1)},\chi^{(2)}\right)\right\}\right\}$$

$$= \boldsymbol{E}\begin{Bmatrix} S_{mn}\left(s,\chi^{(1)},\chi^{(2)}\right) \\ -E\left\{S_{mn}\left(s,\chi^{(1)},\chi^{(2)}\right)\right\}\end{Bmatrix} \tag{7.11}$$

The definition of the expectation of the real part of S_{mn}, for example, involves calculation of (7.12). The expectation of the imaginary part of S_{mn} can be obtained in the same manner, and with defining the covariance matrix and correlation between the real and the complex random variables in (7.13), this completes the stochastic macromodeling process of multi-port interconnect structure in frequency domain.

$$\boldsymbol{E}\left\{Re\{S_{mn}(s,\chi^{(1)},\chi^{(2)})\}\right\}$$

$$= \sum_{k_1=1}^{K_1}\sum_{k_2=1}^{K_2} Re\{S_{mn}(s,\chi^{(1)},\chi^{(2)})\} \int_{\chi_{1,min}}^{\chi_{1,max}} \int_{\chi_{2,min}}^{\chi_{2,max}} l_{k_1}(\chi^{(1)})\, l_{k_2}(\chi^{(2)})$$

$$\times p(\chi^{(1)}) \times p(\chi^{(2)}) d\chi^{(1)} d\chi^{(2)} \tag{7.12}$$

$$Cov_{S_{mn}}$$

$$= \begin{bmatrix} var[Re\{S_{mn}(s,\chi^{(1)},\chi^{(2)})\}] & cov[Re\{S_{mn}(s,\chi^{(1)},\chi^{(2)})\}, Im\{S_{mn}(s,\chi^{(1)},\chi^{(2)})\}] \\ cov[Re\{S_{mn}(s,\chi^{(1)},\chi^{(2)})\}, Im\{S_{mn}(s,\chi^{(1)},\chi^{(2)})\}] & var[Im\{S_{mn}(s,\chi^{(1)},\chi^{(2)})\}] \end{bmatrix}$$

$$\rho\left(S_{mn}(s,\chi^{(1)},\chi^{(2)})\right) = \frac{cov[Re\{S_{mn}(s,\chi^{(1)},\chi^{(2)})\}, Im\{S_{mn}(s,\chi^{(1)},\chi^{(2)})\}]}{\sigma(Re\{S_{mn}(s,\chi^{(1)},\chi^{(2)})\})\sigma(Im\{S_{mn}(s,\chi^{(1)},\chi^{(2)})\})} \in [-1,1] \tag{7.13}$$

Figure 7.3 shows the complete flowchart of the stochastic macromodeling of interconnect structure that contain both channel and wiring in the frequency domain.

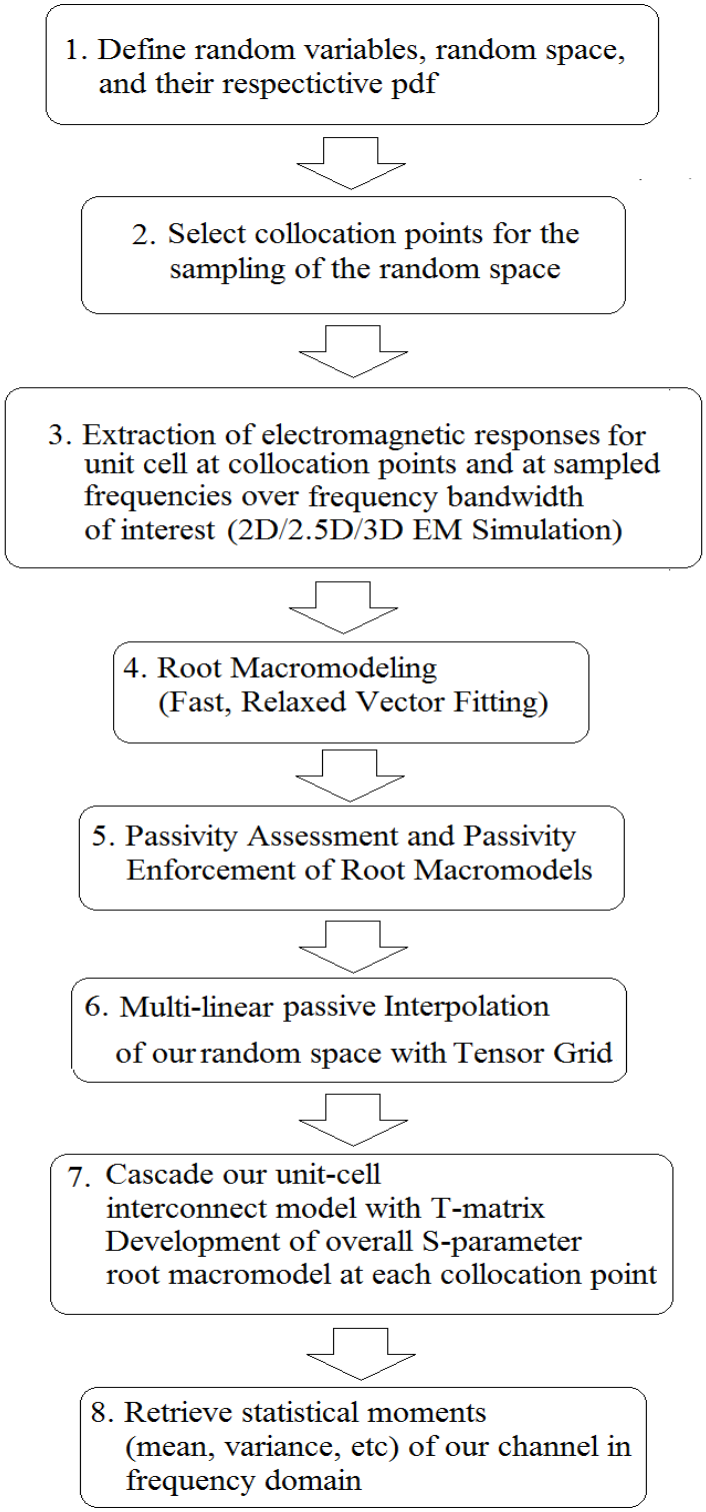

Figure 7.3: Complete flow of stochastic macromodeling of interconnects with channel and wiring in the vicinity of the channel in frequency domain.

7.2.6 Stochastic multivariate interpolation in time domain

Once the stochastic macromodel of *m*-port interconnects is defined in frequency domain, our primary interest is in stochastic modeling of the transient response of our channel due to the uncertainty in EM loading of the wires. Therefore, we apply discretized convolution [75] or IFFT, and extract *n*-port ***S*** parameter sub-matrix to model our input and output voltage of the channel in the time domain by making use of appropriate terminal conditions. Figure 7.4 shows the complete flow of the stochastic modeling of the channel model in time domain.

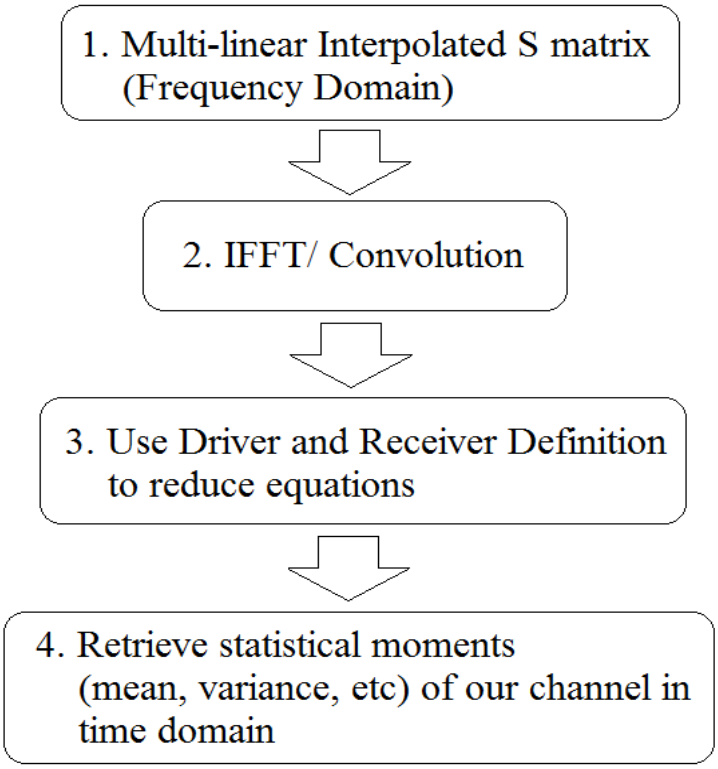

Figure 7.4: Complete flow of stochastic macromodeling of interconnects with channel and wiring in the vicinity of the channel in time domain.

7.3 Demonstration Studies

Next two examples, a single-ended channel, differential-pair channel are given as demonstration studies of the proposed stochastic macromodeling in frequency and time domain.

7.3.1 Single-ended microstrip channel

The cross-section of the single-wire microstrip channel is depicted in Figure 7.5. All wires have a fixed width w= 300 μm, conductor thickness t = 30 μm, and a dielectric constant ε_r = 4.2 with loss tangent of 0.02. The length of the unit-cell is L_{unit} = 1 mm and the thickness of the substrate dielectric is h = 160 μm. The overall length of the channel, as well as the length of the adjacent wiring, is L = 100 mm. The uniform random variables $\chi^{(1)}$ and $\chi^{(2)}$ are distances of the adjacent wiring on the right and the left end of the single-wire channel. Their values are in the interval [100, 300]μm. The scattering matrix $\boldsymbol{S}(s, \chi^{(1)}, \chi^{(2)})$ is computed using quasi-static 3D EM tool [131] from DC to 5 GHz with uniform sampling using 501 frequency samples.

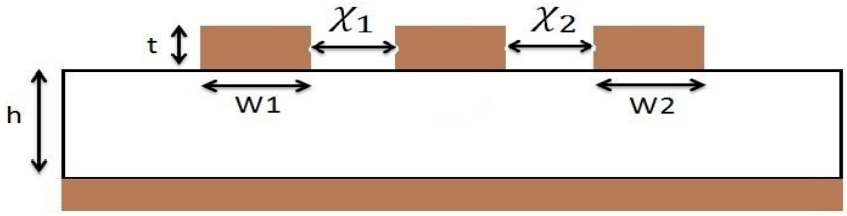

Figure 7.5: A cross-section of the single-wire channel (middle) and adjacent coupled microstrip wiring.

A 5 by 5 estimation grid with equidistant spacing of 50 μm has been chosen for our random variables as the estimation grid of each random variable's domain defined as [100,300] μm. Therefore, 25 $\boldsymbol{S}$ matrix models are involved in the estimation grid and Vector Fitting is used to form 25 root macromodels, each using 10 common poles. After passivity of each root

macromodel of our unit-cell has been checked and enforced, $\boldsymbol{S}_{unit}$ matrix is converted into $\boldsymbol{T}_{unit}$ matrix. One hundred $\boldsymbol{T}_{unit}$ matrices are cascaded to obtain the $\boldsymbol{T}$ matrix for the channel, which is then reconverted to an $\boldsymbol{S}$ matrix. Then piecewise linear interpolation is used to interpolate the stochastic scattering matrix $\boldsymbol{S}(s, \chi^{(1)}, \chi^{(2)})$ over the estimation grid in the random space. The interpolated $\boldsymbol{S}$ matrix from our estimation grid is then used to assess the interpolation capability of a denser 9 by 9 validation grid with equidistant spacing of 25 μm in [100,300] μm. Figure 7.6 depicts how the ports numbering has been defined for the single-ended channel.

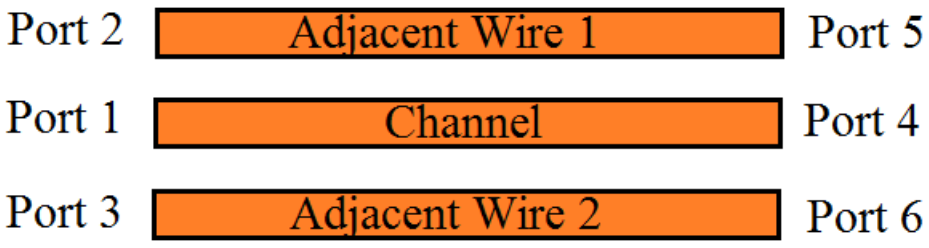

Figure 7.6: Port numbering definitions for the channel and adjacent wires.

Figures 7.7 and 7.8 depict the comparison of the magnitude of the interpolated crosstalk, $S_{13}(s, \chi^{(1)}, \chi^{(2)})$ and insertion loss, $S_{14}(s, \chi^{(1)}, \chi^{(2)})$ of the unit-cell and S_{13} and S_{14} from Q3D over the validation grid with fixed $\chi^{(1)} = 100\ \mu$m and $\chi^{(2)} = 100 \sim 300\ \mu$m. Clearly, the accuracy of the interpolation is satisfactory. Figures 7.9 and 7.10 show the comparison of the magnitude of the interpolated return loss, $S_{11}(s, \chi^{(1)}, \chi^{(2)})$ and insertion loss, $S_{14}(s, \chi^{(1)}, \chi^{(2)})$ for the entire channel, and the magnitudes from Q3D over the validation grid with fixed $\chi^{(1)} = 100\ \mu$m and $\chi^{(2)} = 100 \sim 300\ \mu$m, after we have cascaded the 100 unit-cell structures. Again, these results validate the accuracy of the proposed interpolation over the random space.

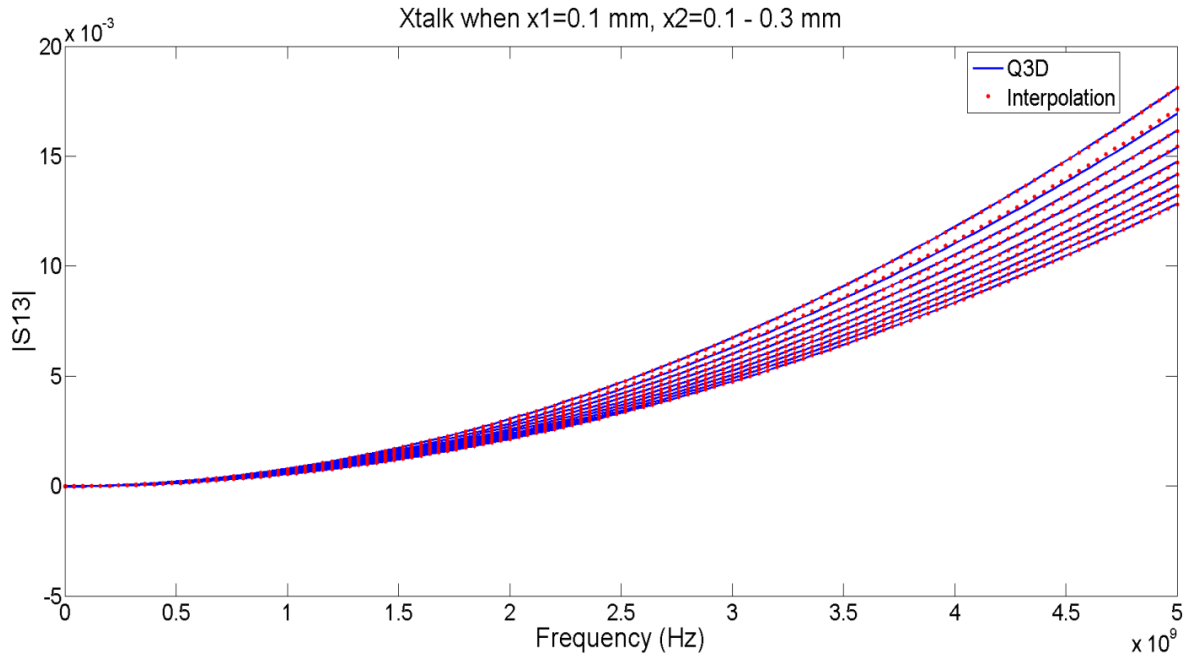

Figure 7.7: Magnitude comparison of the crosstalk |S13| of the unit-cell of the interpolation and Q3D with fixed $\chi^{(1)} = 100\ \mu$m and $\chi^{(2)} = 100 \sim 300\ \mu$m.

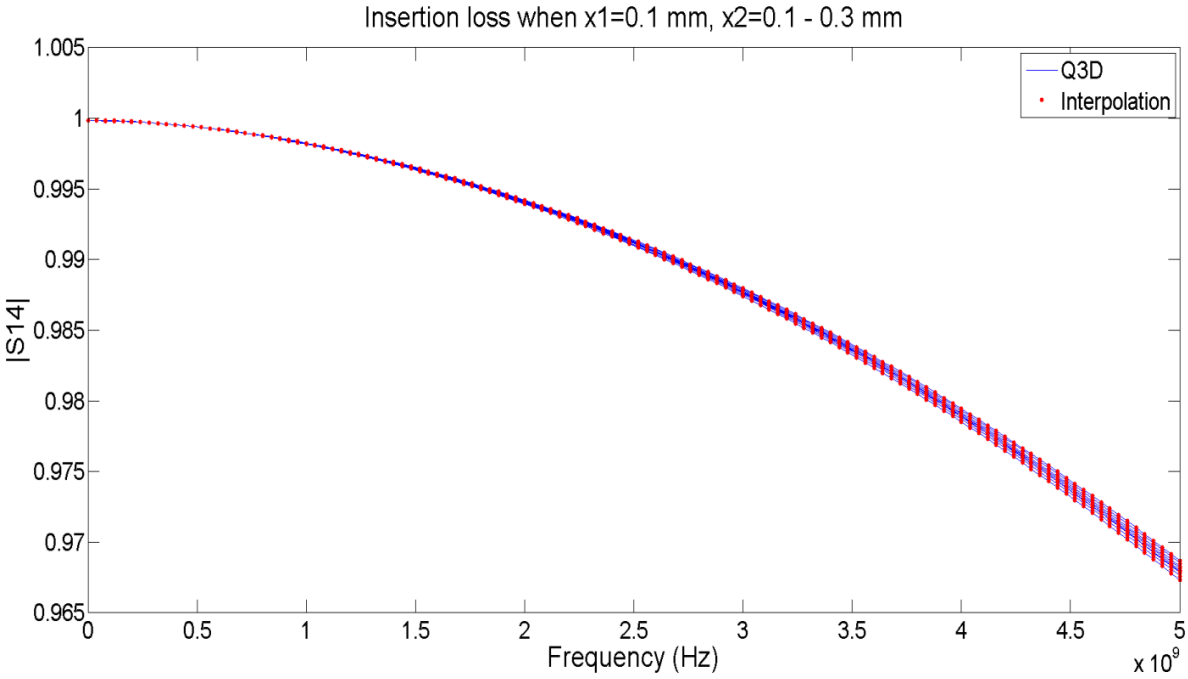

Figure 7.8: Magnitude comparison of the insertion loss |S14| of the unit-cell of the interpolation and Q3D with fixed $\chi^{(1)} = 100\ \mu$m and $\chi^{(2)} = 100 \sim 300\ \mu$m.

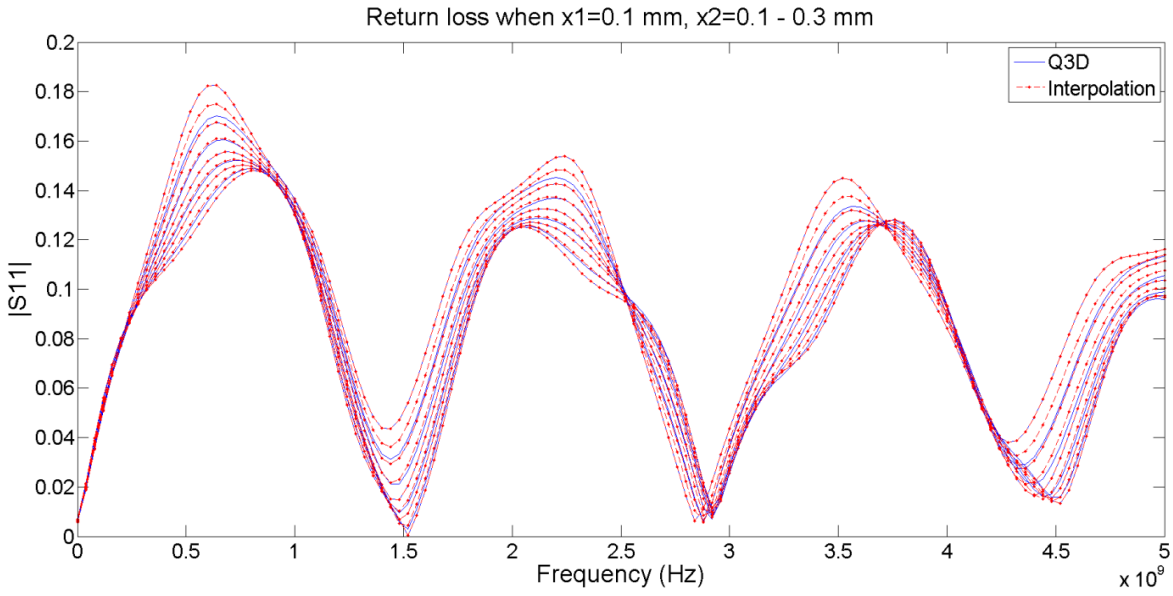

Figure 7.9: Magnitude comparison of the return loss |S11| of the interconnect (L= 100 mm) of the interpolation and Q3D with fixed $\chi^{(1)} = 100\ \mu$m and $\chi^{(2)} = 100 \sim 300\ \mu$m.

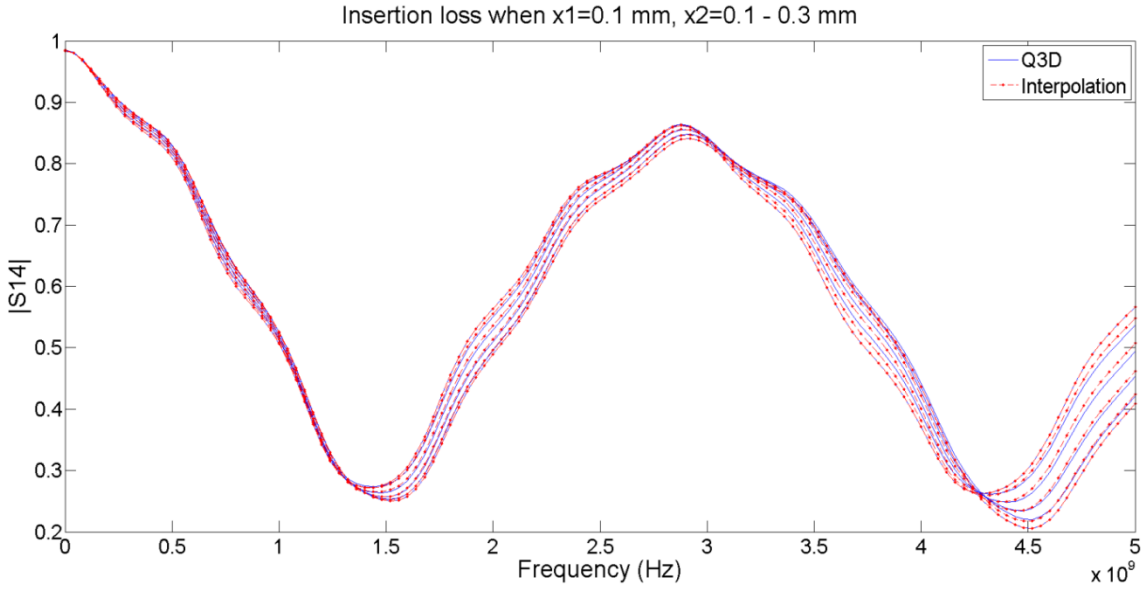

Figure 7.10: Magnitude comparison of the insertion loss |S14| of the interconnect (L=100 mm) of the interpolation and Q3D with fixed $\chi^{(1)} = 100\ \mu$m and $\chi^{(2)} = 100 \sim 300\ \mu$m.

Figure 7.11 depicts the relative error of the mean value of the real part of insertion loss at 2 GHz from Monte Carlo analysis with 1500 realizations, where relative error of the mean value is

defined as $Err_{rel} = \|\mu(N) - \mu(N-1)\|/\|\mu(N)\|$ and $\mu(N)$ denotes the mean value of N samples from Monte Carlo. The MC solution converges at the rate of $1/\sqrt{N}$, and the relative error decreases with the increase of the samples. For this example, we choose our reference solution with 1500 realizations, which is in an interval where fluctuation of the relative error is below 10^{-3}.

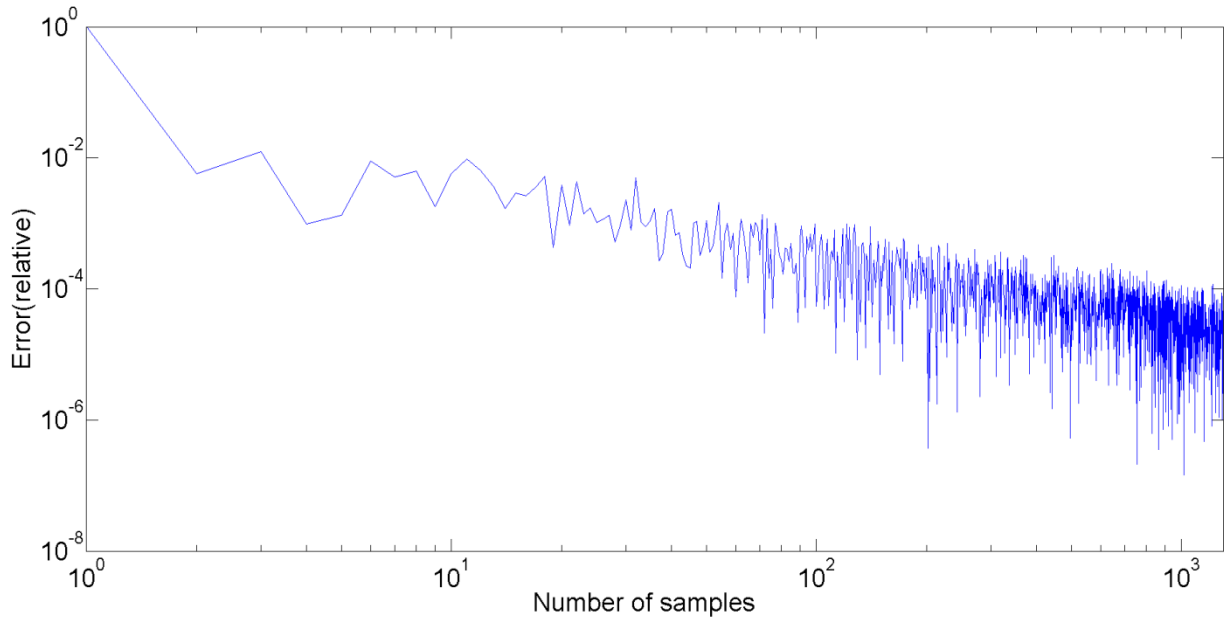

Figure 7.11: Relative mean error of Monte Carlo with respect to the number of samples.

Figures 7.12 and 7.13 depict the mean and the standard deviation for the real and imaginary parts of $S_{21}(s, \chi^{(1)}, \chi^{(2)})$ obtained using the proposed stochastic collocation method and compared with those obtained using Monte Carlo from 1500 sample points. The error bar indicates the $\pm\sigma$ (standard deviation) of stochastic collocation and Monte Carlo method. The calculated mean and the standard deviation obtained using stochastic collocation are in very good agreement with those obtained using Monte Carlo.

Table 7.3 compares the average and the worst case error between the mean and the standard deviation values of the real and the imaginary insertion loss based on the result of stochastic collocation and Monte Carlo. We see a very good agreement between the mean value of the MC and SC result, while the MC provides the bounds of the standard deviation.

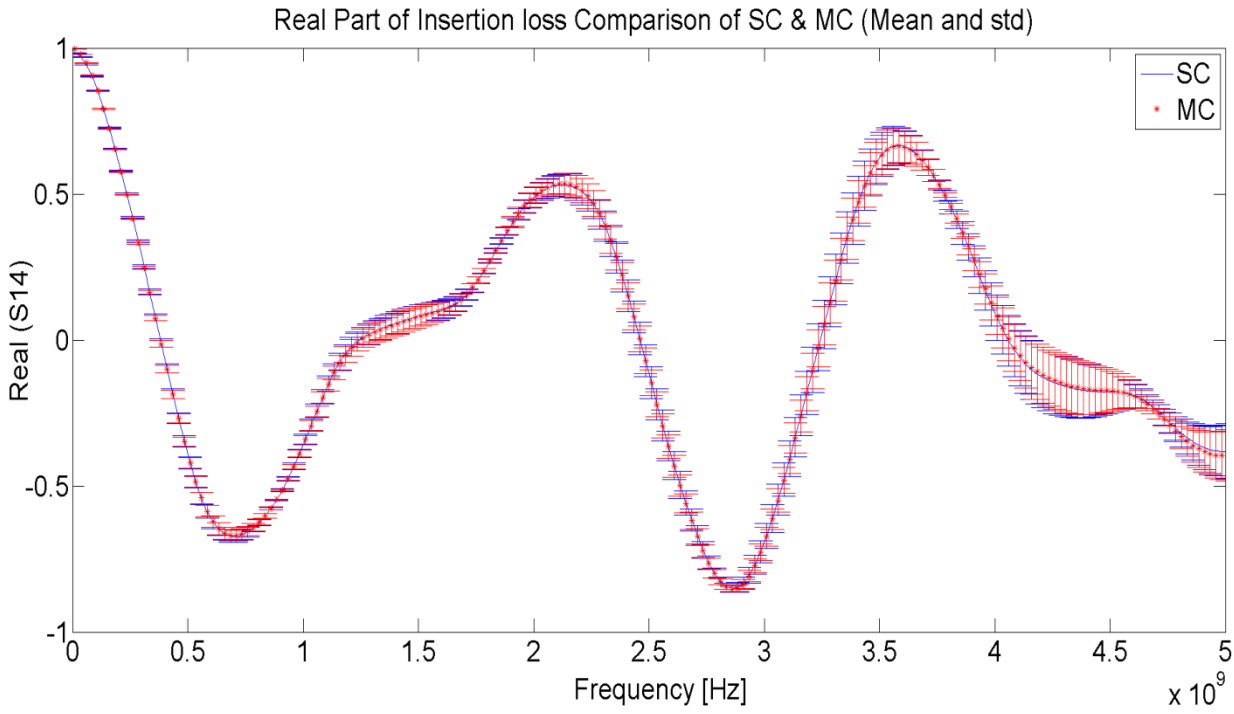

Figure 7.12: Comparison of the mean and the standard deviation of stochastic collocation and Monte Carlo for real part of insertion loss.

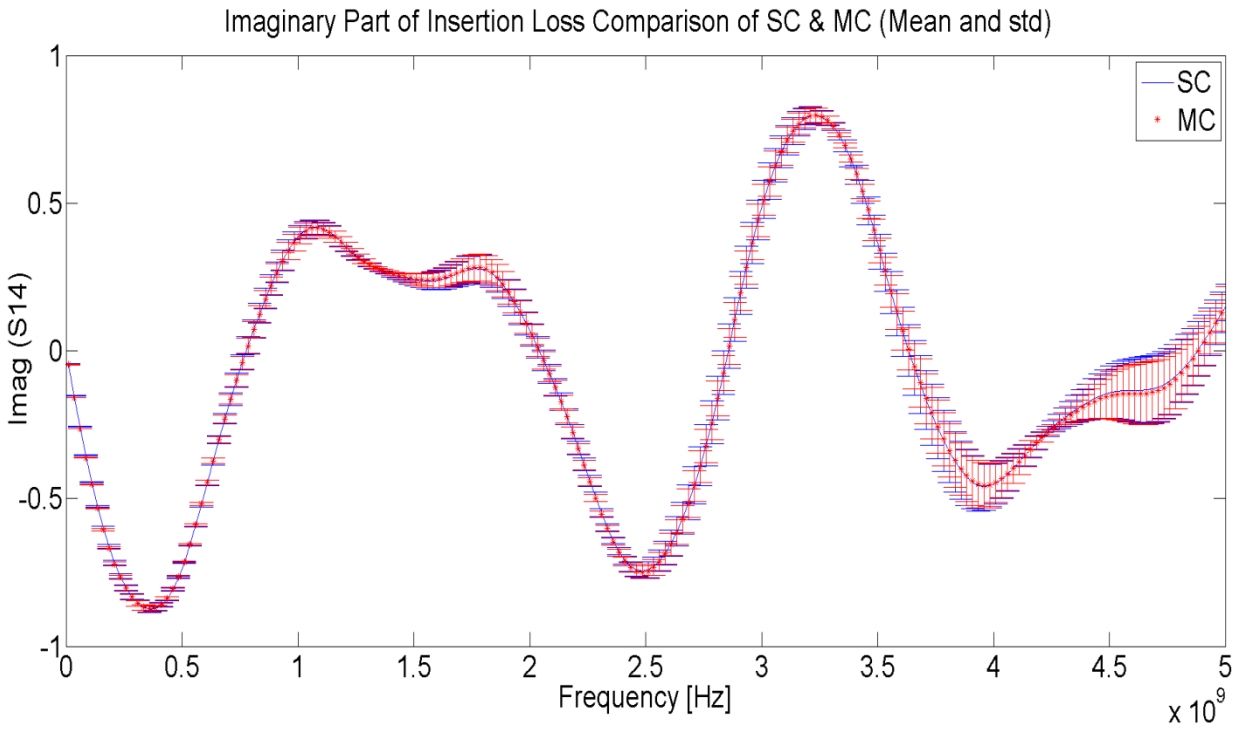

Figure 7.13: Comparison of the mean and the standard deviation of stochastic collocation and Monte Carlo for imaginary part of insertion loss.

Table 7.3: Comparison of the difference of the mean and standard deviation values of stochastic collocation and Monte Carlo analysis of the real and the imaginary values of insertion loss.

	Difference between Mean(Real(S14)) For SC & MC	Difference between Std(Real(S14)) For SC & MC	Difference between Mean(Imag(S14)) For SC & MC	Difference between Std(Imag(S14)) For SC & MC
Mean error (DC – 5 GHz)	0.0035	0.0055	0.0034	0.0057
Maximum error	0.0145	0.0167	0.0115	0.0175

Next, we turn our attention to the assessment of the impact of adjacent wiring loading on the transient response of the channel. Figure 7.14 shows the time-domain stochastic modeling setup. Input port of the channel model is match terminated with 50 Ω while all the other ports are left

open. The terminal conditions of the interconnect structure are represented by reflection coefficient matrix (**Γ**) and transmission coefficient matrix (**T**) in Figure 7.14. As stated in the previous section, we use the terminal conditions from the transmitter and the receiver to reduce the transient analysis equation to only input and output channel response. Pertinent equations are given in (7.13), where we use the relation of the incident and reflected voltage wave response from the frequency response, and combine terminal condition equation of the incident wave expressed in terms of reflection coefficient, reflected wave, transmission coefficient and input voltage response.

$$\boldsymbol{b}\left(s,\ \chi^{(1)},\chi^{(2)}\right) = \boldsymbol{S}\left(s,\ \chi^{(1)},\chi^{(2)}\right)\boldsymbol{a}(s)$$

$$\boldsymbol{a}(s) = \Gamma\boldsymbol{b}\left(s,\ \chi^{(1)},\chi^{(2)}\right) + \boldsymbol{T}\boldsymbol{g} \tag{7.13}$$

The channel voltage response at frequency domain is summarized as (7.14) after reduction of the equations. Then, IFFT is applied in (7.15) to our channel for observation of the time-domain response at output channel voltage. Note that both reflection coefficient and transmission coefficient matrices can be introduced with uncertainty, which prompts uncertainty in source and load conditions.

$$\boldsymbol{V_{ch}}\left(s,\ \chi^{(1)},\chi^{(2)}\right) = \boldsymbol{a_{ch}}(s) + \ \boldsymbol{b_{ch}}\left(s,\ \chi^{(1)},\chi^{(2)}\right) \tag{7.14}$$

$$\boldsymbol{V_{ch}}\left(t,\ \chi^{(1)},\chi^{(2)}\right) = \boldsymbol{IFFT}(\boldsymbol{V_{ch}}\left(s,\ \chi^{(1)},\chi^{(2)}\right)) \tag{7.15}$$

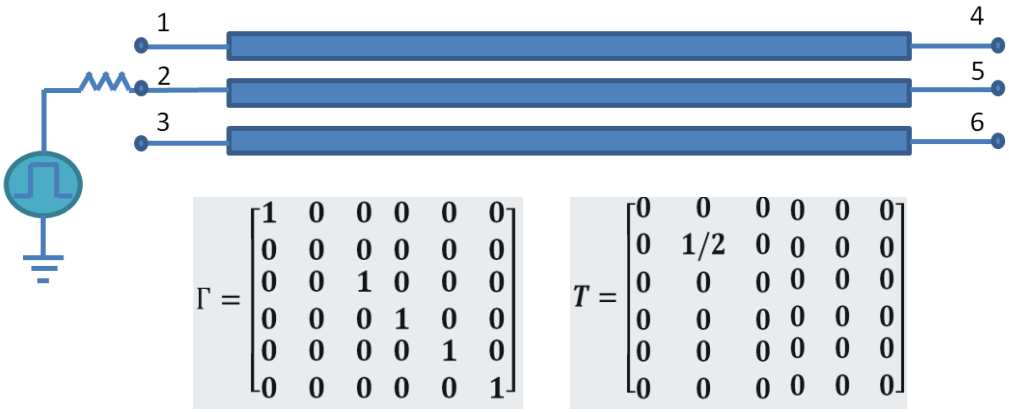

Figure 7.14: Transient simulation set-up for single-ended microstrip channel.

Figure 7.14 compares the mean input voltage response obtained using stochastic collocation with that obtained using Monte Carlo when a trapezoidal pulse that switches from 0 to 1.5 V with time delay $t_d = 2$ ns, rise and fall time $t_r = t_f = 0.2$ ns, and pulse width $t_w = 2$ ns is applied to the channel, while 50 Ω source impedance and open load condition are used to terminate the channel and the wiring. Similar to the frequency domain, Monte Carlo was used with 1500 realizations. Table 7.4 compares the error value of mean and standard deviation between Monte Carlo and stochastic collocation from DC to 15 ns. Again, we see a very good agreement with our SC method in time domain with Monte Carlo simulation.

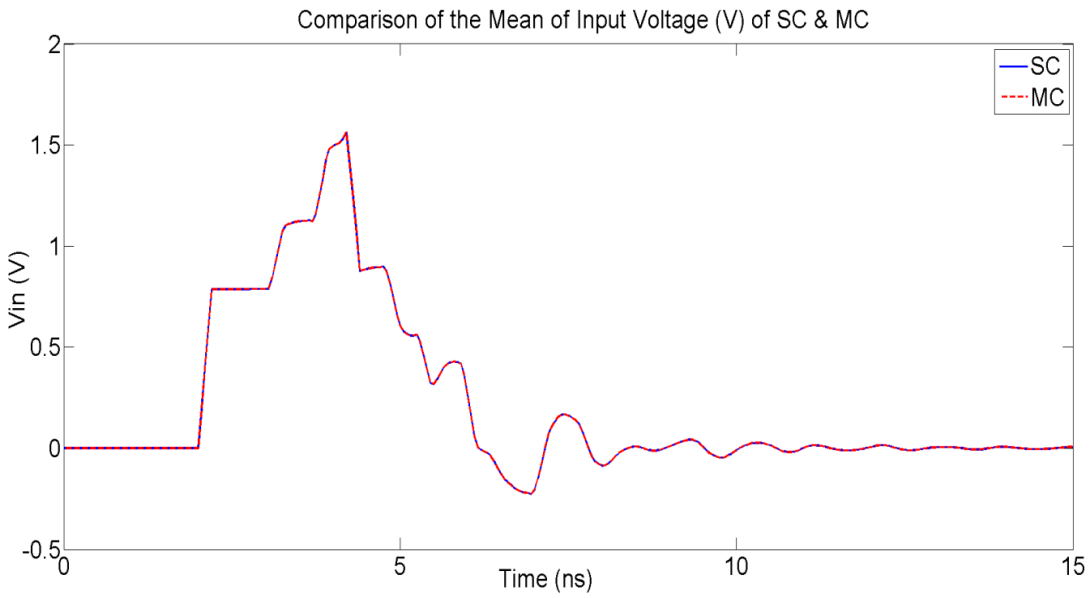

Figure 7.15: Comparison of the mean input voltage of stochastic collocation (SC) and Monte Carlo (MC) for the channel response with source of the channel terminated with 50 ohms while the load is left open.

Table 7.4: Comparison of the difference of the mean and standard deviation values of the input voltage Vin (V) for stochastic collocation and Monte Carlo analysis.

	Difference of Mean(Vin) For SC & MC	Difference of Std(Vin) For SC & MC
Mean difference (0 – 15 ns)	1.4343×10^{-5}	5.5442×10^{-4}
Maximum difference	3.6×10^{-3}	6.3×10^{-3}

Figure 7.16 compares the mean and the $\pm 3\,\sigma$ for the time-domain output voltage response of stochastic collocation and Monte Carlo. The $\pm 3\sigma$ is shown through the error bar. Table 7.5 compares the difference between the mean value and the standard deviation value of stochastic collocation and Monte Carlo from DC – 15 ns. As far as computation time is concerned, the 1500 Monte Carlo simulations required 44 hours 37 minutes to 53 minutes 34 seconds required for 25 samples used for the tensor grid stochastic collocation solution on Intel core i7-2670QM platform.

Once again, the result verifies the accuracy and computational efficiency of the proposed method over Monte Carlo.

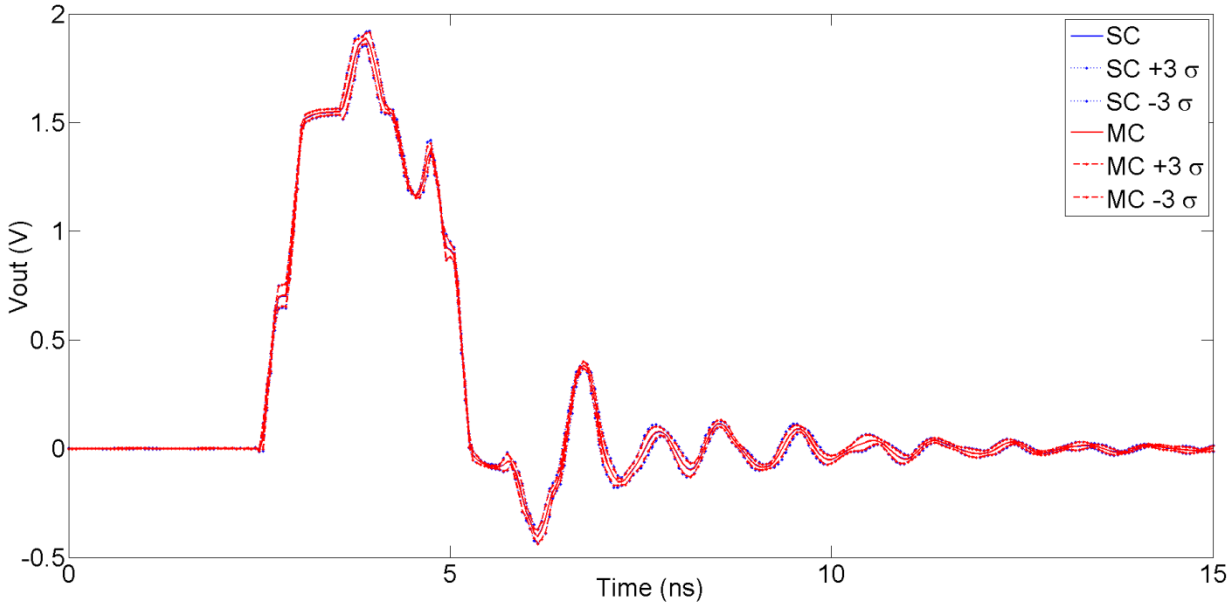

Figure 7.16: Comparison of the mean and $\pm 3\sigma$ for output voltage of stochastic collocation (SC) and Monte Carlo (MC) of the channel response with source of the channel terminated with 50 ohms while the load is left open.

Table 7.5: Comparison of the difference of the mean and standard deviation values of the output voltage Vout (V) for stochastic collocation and Monte Carlo analysis.

	Difference of Mean(Vout) For SC & MC	Difference of Std(Vout) For SC & MC
Mean difference (0 – 15 ns)	1.4606×10^{-5}	9.0271×10^{-4}
Maximum difference	4.1×10^{-3}	8.3×10^{-3}

7.3.2 Differential pair microstrip channel

The second study considers an interconnect structure of a differential pair microstrip channel in the presence of adjacent wiring. Figure 7.17 shows the cross-section of the differential pair

microstrip channel. All wires have a fixed width w= 300 μm, conductor thickness t = 30 μm, and substrate dielectric constant ε_r = 4.2 with loss tangent of 0.02. The length of the unit-cell is L_{unit} = 1 mm and the thickness of the dielectric substrate is h = 160 μm. The spacing between the wires in the differential pair is s = 200 μm. The overall length of the channel as well as the wiring is L = 100 mm. The uniform random variables $\chi^{(1)}$ and $\chi^{(2)}$ are distances of the adjacent wiring on the right and the left end of the differential pair channel, and assume values over the interval [100, 400]μm. We have chosen a 7 by 7 sampling grid on the random space with equidistant spacing of 50 μm. Eighty one scattering matrices $\boldsymbol{S}(s, \chi^{(1)}, \chi^{(2)})$ were computed using quasi-static 3D EM tool [131] from DC to 5 GHz in 501 frequency samples, and 16 common poles were used for the root macromodels generated for each one of the 81 $\boldsymbol{S}$ matrix. Passivity enforcement via residue perturbation was applied to the root macromodels.

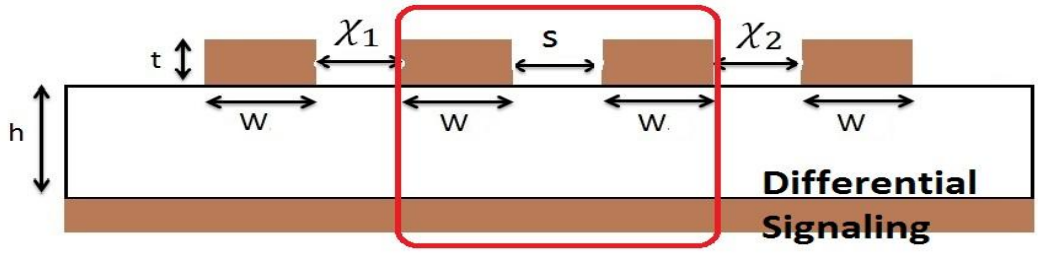

Figure 7.17: A cross-sectional geometry of the differential pair channel (middle) and adjacent coupled microstrip wiring.

Figure 7.18 shows the terminal and port definitions of the differential pair channel and the wirings in the vicinity of the channel. In this example, we are interested in looking at the mode conversion occuring in the differential pair channel due to asymmetrical EM loading caused by uncertainties in distances between the channel and adjacent wiring. Equation (7.16) below is used to change the standard $\boldsymbol{S}$ matrix into a mixed modal $\boldsymbol{S}$ matrix form, which has a combination of mixed-mode (differential mode and common mode) and single-ended $\boldsymbol{S}$

parameters [129]. The upper four rows of $\boldsymbol{M}$ in (7.17) contain definitions of single-ended $\boldsymbol{S}$ parameters in terminal 3,4,7 and 8. The lower four rows of $\boldsymbol{M}$ contains a 4 by 4 submatrix that is the conversion matrix for standard four-port $\boldsymbol{S}$ parameters to two-port mixed mode $\boldsymbol{S}$ parameters. Mixed mode port 1 is defined by terminals 1 and 2, and mixed mode port 2 is defined by terminals 5 and 6.

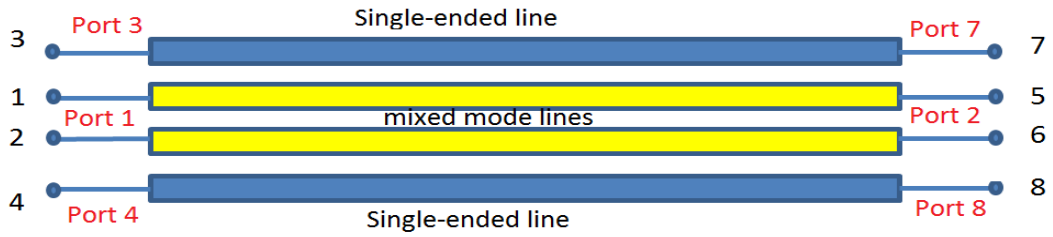

Figure 7.18: Mixed mode S matrix conversion for the differential pair channel (middle) and adjacent coupled single-ended wiring.

$$\boldsymbol{S}^{mm} = \boldsymbol{M}\boldsymbol{S}^{std}\boldsymbol{M}^{-1} \tag{7.16}$$

$$\boldsymbol{M} = \frac{1}{\sqrt{2}}\begin{bmatrix} 0 & 0 & \sqrt{2} & 0 & 0 & 0 & 0 & 0 \\ 0 & 0 & 0 & \sqrt{2} & 0 & 0 & 0 & 0 \\ 0 & 0 & 0 & 0 & 0 & 0 & \sqrt{2} & 0 \\ 0 & 0 & 0 & 0 & 0 & 0 & 0 & \sqrt{2} \\ 1 & -1 & 0 & 0 & 0 & 0 & 0 & 0 \\ 0 & 0 & 0 & 0 & 1 & -1 & 0 & 0 \\ 1 & 1 & 0 & 0 & 0 & 0 & 0 & 0 \\ 0 & 0 & 0 & 0 & 1 & 1 & 0 & 0 \end{bmatrix} \tag{7.17}$$

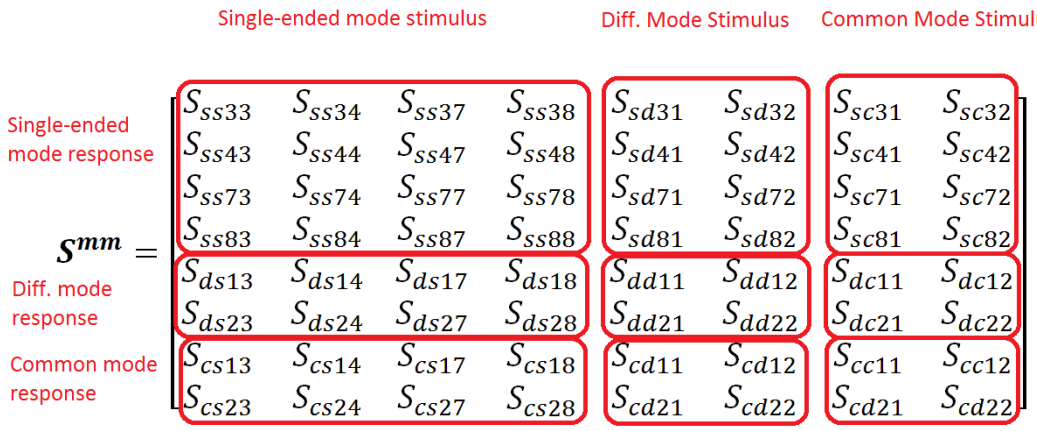

Figure 7.19: Mixed mode S matrix representing four interconnects network of differential channel and two single-ended wiring in Figure 7.17.

Figure 7.19 depicts the mixed mode ***S***-matrix of the interconnect structure. The mixed mode matrix is divided into nine different blocks. Let us name the block rows as upper, middle, and low, and the block columns as right, middle, and left to aid in defining the blocks. The upper left block is single-ended to single-ended ***S***-matrix, and the upper middle and upper right blocks are differential mode to single-ended mode, and common mode to single-ended mode, ***S***-matrix parameters, respectively. Our ultimate interest is on the low middle block, which is the differential mode stimulus to common mode response. This is called the mode conversion due to asymmetry in the channel, which is the amount of the mode conversion in the frequency domain due to the uncertainty in the distance of adjacent wiring to the differential pair. The middle block, which is the differential mode stimulus to differential mode response, is the transmission loss or return loss the differential mode suffices, and it is closely related to the mode conversion. For example, the larger the mode conversion noise in the insertion loss of the differential channel, the higher the differential mode insertion loss in the differential channel[128],[130].

Figure 7.20 compares results obtained using stochastic collocation (SC) and Monte Carlo (MC) for differential mode insertion loss (a) and differential to common mode insertion loss (b). A total of 1450 samples were chosen for Monte Carlo. Table 7.6 summarizes the difference between SC and MC in the calculated mean values and standard deviation values in dB. We see an excellent agreement between SC and MC for differential to differential insertion loss. As for the differential to common mode conversion, the mode converted insertion loss value in the entire frequency band is very small compared to the differential to differential insertion loss. This is expected, as the mode conversion is the undesirable noise coming from the asymmetry in the geometry of our channel model. Due to the fact that it is small, matching differential to common insertion loss for SC and MC is a more difficult task than that of differential to differential insertion loss. This is evident from Table 7.6 by observing the mean and the maximum mean and standard deviation values of SC and MC. However, the general trend of the mean value of the magnitude of SC and MC of the mode conversion of insertion loss is similar and the actual values of insertion loss for the two methods are reasonably close to one another, as is seen for the differential-to-differential modal insertion loss. In order to increase the accuracy of our SC further, it is important to increase the number of collocation points in SC to make a denser tensor grid. This will increase the accuracy of prediction of the mean and the standard deviation values of mode conversion. MC with 1450 realizations reaches convergence for the mean and the standard deviation values as comparison with MC with 2500 realizations in Table 7.7 and Figure 7.21 verifies that introducing more samples with MC does not change the mean and the standard deviation values. A time-domain simulation for prediction of the statistical moments of the common mode noise with denser SC grid and comparison with MC approach is left as a future work.

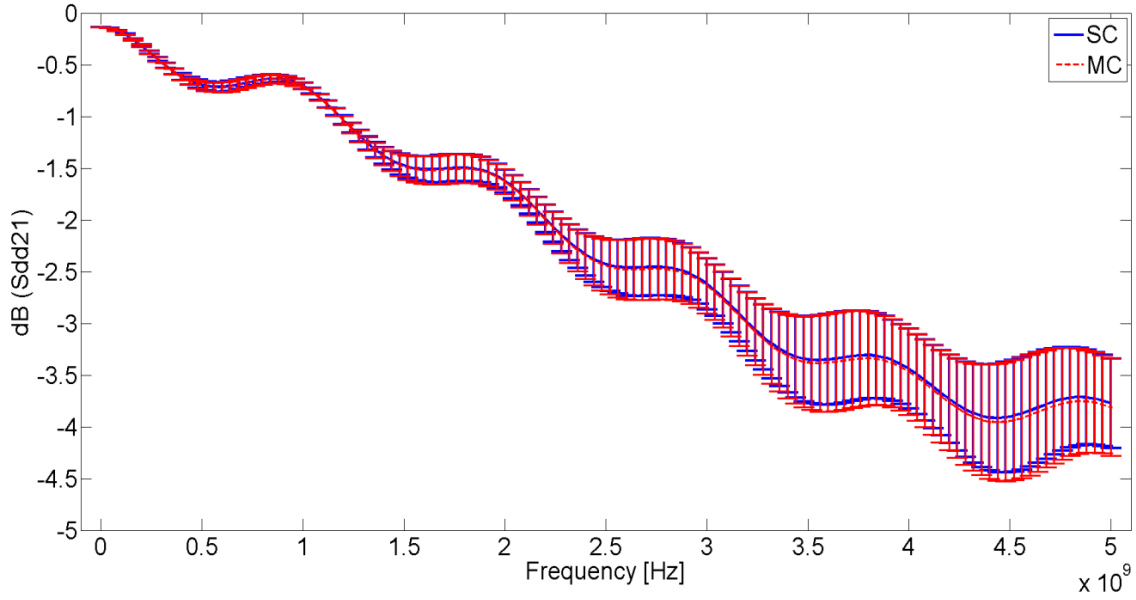

(a)

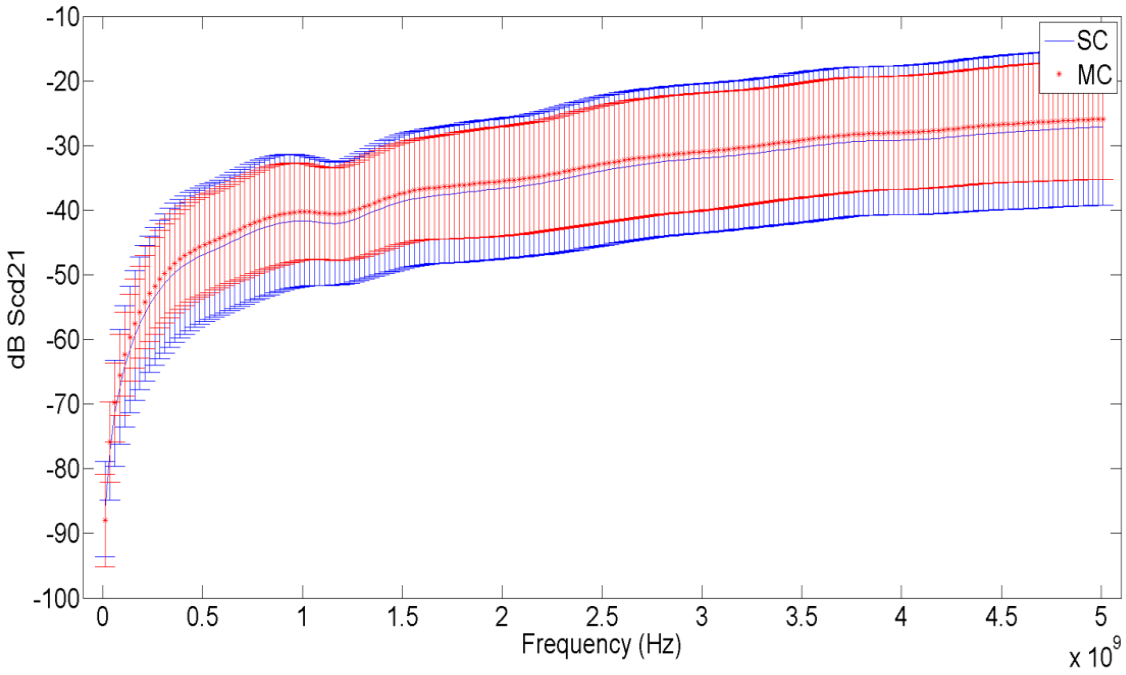

(b)

Figure 7.20: Comparison of the mean and the standard deviation values computed using stochastic collocation and Monte Carlo for differential to differential mode insertion loss (a), and differential to common mode insertion loss (b).

Table 7.6: Comparison of stochastic collocation and Monte Carlo results for the difference of the mean and standard deviation values of the magnitude of the mode conversion (Scd21) and differential to differential mode (Sdd21) insertion loss.

(dB)	Difference of Mean (Scd21) For SC & MC	Difference of Std (Scd21) For SC & MC	Difference of Mean (Sdd21) For SC & MC	Difference of Std (Sdd21) For SC & MC
Mean difference	1.2281	2.6413	0.0180	0.0065
Maximum difference	1.8179	3.2108	0.1068	0.0211

Table 7.7: Comparison of Monte Carlo results with different realizations (1450, 2500) for the difference of the mean and standard deviation values of the real part and the imaginary part of the mode conversion (Scd21) insertion loss.

	Difference of Mean Re(Scd21) For MC(1450) & MC(2500)	Difference of Std Re(Scd21) For MC(1450) & MC(2500)	Difference of Mean Im(Scd21) For MC(1450) & MC(2500)	Difference of Std Im(Scd21) For MC (1450) & MC (2500)
Mean difference	1.5198×10^{-5}	3.8128×10^{-4}	1.0074×10^{-5}	4.1632×10^{-4}
Maximum difference	2.2896×10^{-4}	0.0013	3.2671×10^{-4}	0.0015

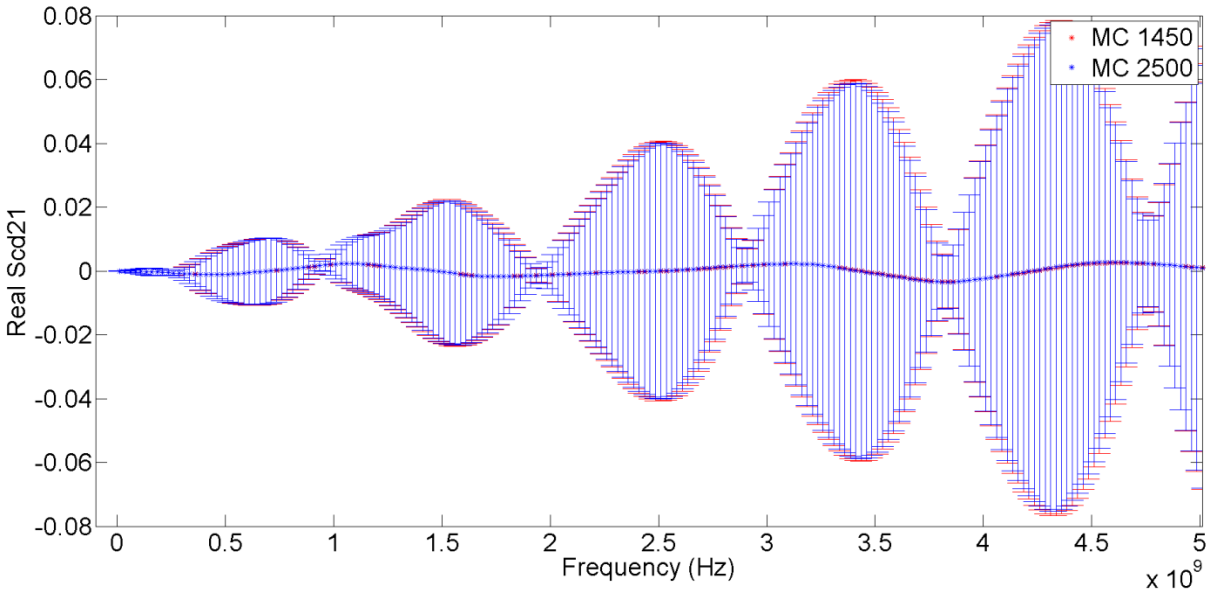

(a)

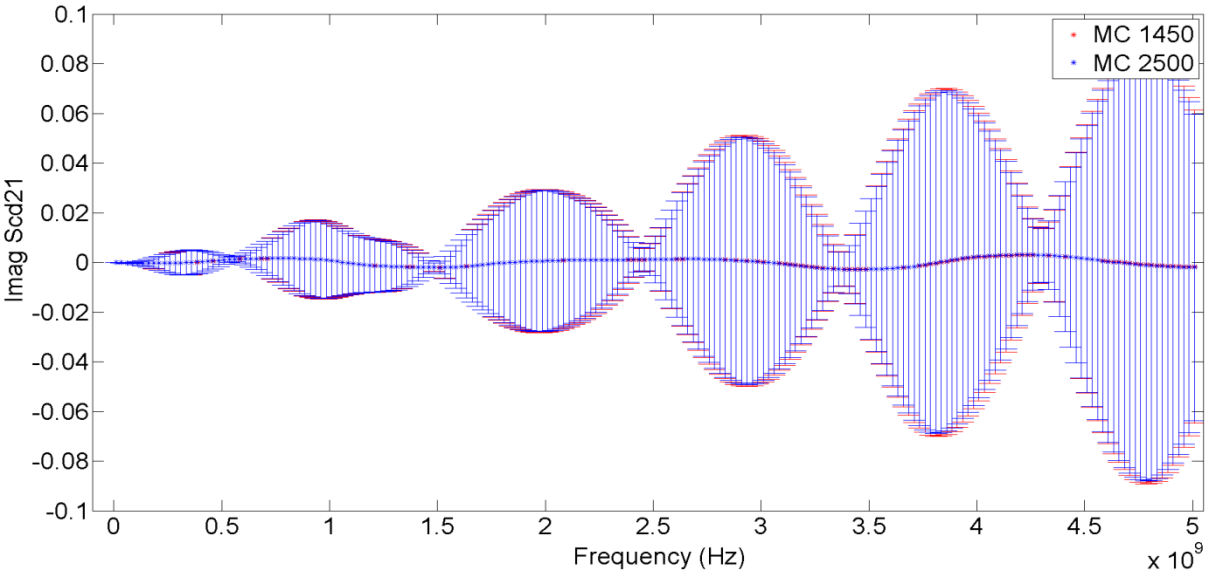

(b)

Figure 7.21: Comparison of the mean and the standard deviation of MC with 1450 and 2500 realizations for the real part of differential to common mode insertion loss (a) and the imaginary part of differential to common mode insertion loss (b).

7.4 Summary

In summary, we have presented a fast stochastic macromodeling in the frequency and time domain to quantify the impact of uncertainty in the wiring routing adjacent to the channel on its transfer characteristics. The proposed methodology offers an expedient approach for the modeling of the change in the channel signal transmission properties due to its electromagnetic loading by the adjacent wiring. For validation purposes, a simple one-wire straight single-ended channel and a differential pair channel were chosen to demonstrate the proposed stochastic macromodeling methodology. Comparisons with reference results obtained using Monte Carlo method were used to demonstrate the accuracy of the proposed method. We note that the major issue in stochastic collocation lies in the selection of the set of interpolation points, and in particular, making sure that a sufficient number of samples has been selected to ensure accuracy based on the comparison with Monte Carlo. Our choice appears to be of sufficient accuracy, at least for the numerical studies considered.

The complexity and, hence, the computational cost of the proposed approach are intimately coupled to the dimensionality of the random space used for describing the uncertainty of the adjacent wiring topography. Our conjecture that an equivalent description of adjacent wiring geometry in terms of just two wires, one on either side of the channel under consideration, was justified through studies that compared the loading of channel interconnect parameters (e.g. per-unit length capacitance and inductance) to that obtained due to the presence of multiple wires on either side. These comparisons showed that an equivalent reduced geometry, consisting of two wires with properly selected width and spacing from the channel wires, provided sufficient accuracy in describing a more complicated multi-wire configuration. For those cases where a more complicated adjacent topography becomes necessary to describe accurately the

environment in which the channel will be used, the resulting higher dimensionality of the associated random space will necessitate the use of sparse grid sampling techniques [111],[112],[114],[115] for its efficient representation in the context of the proposed stochastic collocation framework.

CHAPTER 8

CONCLUSION AND FUTURE WORK

8.1 Conclusion

The main goal of this research was to develop physically consistent macromodeling techniques that accurately approximate a large set of passive frequency-domain broadband interconnect responses in a computationally efficient manner. The possibility of such methodology development with three distinct goals was explored in both deterministic and stochastic macromodeling frameworks.

A computationally efficient methodology was presented in Chapter 3 for the synthesis of electrically small dispersive multi-port bond wires combining a magneto-quasi-static RLGC extractor and VF over frequency bandwidths for which the wire length is small compared to the wavelength. The main idea was to compute $\boldsymbol{R}(\omega)$ and $\boldsymbol{L}(\omega)$ matrices of the bond wires at the low- and high-frequency band through the use of magneto-quasi-static RLCG 3D solver, and use VF to interpolate the reduced sets of frequency samples over the entire frequency bandwidth of interest and generate the desired multi-port SPICE equivalent netlist. For low frequency band, use of a low-density volumetric grid at a subset of frequencies at which the skin depth is larger than or at most comparable with wire cross-sectional dimensions result in fast computation of frequency-dependent resistance and inductance matrices. For high-frequency band, a surface impedance boundary condition was applied to eliminate the need for volumetric discretization of

the wires, since the skin-depth is substantially smaller than the cross-sectional dimensions of the wires.

To reduce the computational effort in interpolating multi-port broadband interconnect data and to preserve physical consistency of the macromodel, the feasibility of an element-by-element, and block-wise rational function interpolation with passivity enforcement was investigated through sparse and fast VF solver in Chapter 4. In the fast VF solver, though element-by-element fitting reserved the best accuracy of the fit, it was considered computationally the most expensive approach out of the three. Block-wise fitting was considered as an alternative for common-pole fitting and it provided accuracy while reducing the computational cost of the fit. The computational cost of the three fitting techniques for the global passivity assessment and enforcement was investigated as well. As the size of the state space matrix involved with the passivity check and enforcement of the element-by-element and the block-wise fitting is generally larger than that of the common-pole fitting, common-pole fitting and passivity enforcement is the preferred approach. An iterative residue perturbation technique was applied to all three types of fitting techniques to detect the violation of passivity band by checking their singular values over the entire bandwidth of interest and enforce passivity by perturbing residues.

A methodology that systematically reduces large sets of measured or calculated broadband frequency response of passive network was presented in Chapter 5. Adaptive sampling method was applied systematically to reduce the large set of broadband frequency samples, making use of the Hilbert transform and energy conservation constraints pertinent to the causal electromagnetic responses to replace the original set of frequency data. This method effectively reduces the number of samples needed to preserve the accuracy of the original response while also providing means to quickly check the causality of the original system.

Another methodology, Vector Fitting via Repeated Random Sampling (VFRS), was proposed in Chapter 6 for expedient rational function fitting of broadband electromagnetic responses of multi-port passive networks. The number of sets and number of randomly chosen sample data in each set are defined first within VFRS process, and standard VF is carried out for rational function fitting of the data in each subset. Thus, the poles generated in each set are compiled into one set of poles, and after spurious pole removal they are used to retrieve the respective residues through vector fitting of the entire bandwidth of interest. Since pole identification of VF is the most computationally expensive stage in the VF process, VFRS works with reduced numbers of data sets and poles to yield significant reduction in the overall computational cost of rational function fitting compared to standard VF.

A fast stochastic macromodeling in the frequency and time domain to quantify the impact of uncertainty in the wiring routing adjacent to the channel on its transmission properties was presented in Chapter 7. The proposed methodology introduced stochastic collocation to select a sufficient number of interpolation points in random space described by adjacent wiring, and it made use of passivity-preserving parametric rational interpolation to interpolate the multi-dimensional random space that describes the uncertainty of the adjacent wiring topography. The computational complexity and cost of assessing the impact of channel signal transmission properties due to its electromagnetic loading is directly dependent on the dimensionality of the random space used for describing the uncertainty of the neighborhood wiring topography. Therefore, in order for an efficient stochastic simulation in frequency and time domain, the high dimensionality problem of the original random space was replaced by a reduced geometry, which consists of two adjacent wires with variability in their width and spacing from the channel. The studies proved that the reduced model with two wires can accurately describe the equivalent

complicated high-dimensionality multi-wire configuration by comparing the loading of the channel interconnect parameters (e.g. per-unit-length capacitance and per-unit-length inductance). The proposed methodology gave good accuracy based on the comparison of two channel models with Monte Carlo.

8.2 Future Work

The methodologies presented in this work especially highlight the computational improvement over the existing methodologies. However, there are additional works that could be done for further improvements. Three future works regarding VFRS, stochastic macromodeling, and VF with electrically small structures are worth noting here.

First, regarding VFRS, since the combined number of poles generated from VFRS is in general greater than the number of poles for standard VF, the size of the final state space matrix is greater than that in standard VF. Even though VFRS significantly reduces the computational complexity of the QR factorization stage of the pole relocation and residue relocation step within the VF process, the increased size of the state space matrix would result in more computational cost in the ensuing passivity enforcement stage. Therefore, it may be advisable to combine deterministic adaptive sampling and random sampling to reduce the final number of poles. In this manner, some poles from the VFRS will exactly fit the resonances of the original data. This can reduce the number of overall poles such that it would bring less computational burden in the post-processing stage.

Another useful algorithm would be to group the elements of the transfer function that have similar magnitude. Once the groups are chosen, VFRS is called to each group by choosing randomly selected samples and sets. Machine learning techniques have to be used to identify the similarity between the ***S***-parameter elements and group them together. This will increase the

efficiency of VFRS even further, since we are reducing the number of elements in each fit. A priori knowledge of model order estimation would also be helpful in deciding how many sets are required in VFRS. In this document, rough estimate of the order of the system was possible by detecting the peaks and the valleys. However, a more rigorous, yet efficient method needs to be developed that detects the order of the system.

Finally, since the major cost of VFRS is with the least squares solution stage when we use combined set of poles to obtain the residues (~ 85 %), further cost reduction of that stage can significantly bring down the overall cost involved with VFRS. One way to achieve the reduction would be parallelization, and another way to achieve the reduction would be using adaptive sampling to reduce the frequency samples.

As for the stochastic macromodeling, a better measure for reducing the random variables needs to be developed using statistical measures, such that more efficiency in stochastic modeling can be achieved, reducing the number of random variables. In an effort to increase the computational efficiency involved with higher dimensionality, adaptive sparse grid needs to be used to reduce the total number of samples in our multi-dimensional grid.

Positive interpolation was used to preserve the passivity of the channel over the entire random space. The adaptive sparse grid also needs to be modified such that it preserves the passivity of the macromodel over the entire random space.

Since the examples we considered were 2D problems, extension of 3D channel application (e.g. DDR3/4, PCI Express) would be desirable to see the changes of the transmission properties of channel model from the uncertainties of the neighboring wires and other 3D discontinuities. Since the complexity of the 3D model and the computational time for solving it increase, a semi-analytical method needs to be developed to model some of the known 3D structures. For

example, a physics-based analytical model of vias and a package/BRD model can be used in combination with the existing 2D EM tool to reduce the computational cost of stochastic modeling of the channel.

The current method also needs to be compared to the industry standard DOE, response surface method (RSM) and its derivatives for channel modeling such that advantages of our method can be clearly exemplified. Lastly, automated scripts that invoke commercial tools such as Q3D/HFSS/HSPICE or a 2D EM extractor tool needs to be written to accommodate our method and to compare with the rigorous Monte Carlo simulation.

As for VF modeling with electrically short bond wires, the current methodology needs to be expanded to appropriately model electrically longer multi-port bond wires. Other applications such as flip-chip or BGA structures could also be considered as validation study. It is also necessary find the optimum and appropriate SPICE compatible circuit representation for each structure. This has to be combined with the advanced EM extractor that can correctly represent the frequency dependent resistance and inductance matrices of 3D structure.

REFERENCES

[1] A. E. Ruehli and A. C. Cangellaris, "Progress in the methodologies for the electrical modeling of interconnects and electronic packages," *Proc. IEEE*, vol. 89, pp. 740-771, May 2001.

[2] R. Achar and M. Nakhla, "Simulation of high-speed interconnects," *Proc. IEEE*, vol. 89, 693-728, May 2001.

[3] H. B. Bakoglu, *Circuits, Interconnections and Packaging for VLSI*. Reading, MA: Addison-Wesley, 1990.

[4] A. Deustsch, "Electrical characteristics of interconnections for high-performance systems," *Proc. IEEE*, vol. 86, pp. 315-355, Feb. 1998.

[5] C. Paul, *Analysis of Multiconductor Transmission Lines, 2nd ed.*, New York: John Wiley and Sons, Inc., 2007.

[6] C. Paul, *Introduction to Electromagnetic Compatibility, 2nd ed.*, New York: John Wiley and Sons, Inc., 2006.

[7] M. Celik, N. Pileggi, and A. Odabasioglu, *IC Interconnect Analysis*. Kluwer Aacademic Publishers, 2002.

[8] S. H. Hall, G. W. Hall, J. A. McCall, *High-Speed Digital System Design: A Handbook of Interconnect Theory and Design Practices*, New York, NY: John Wiley and Sons, Inc., 2000.

[9] H. W. Johnson and M. Graham, *High-Speed Signal Propagation: Advanced Block Magic*, Englewood Cliffs, NJ: Prentice-Hall, 2003.

[10] S. H. Hall, and H. L. Heck, *Advanced Signal Integrity for High-Speed Digital Design.* Hoboken, NJ: Wiley, 2009.

[11] E. Bogatin, *Signal and Power Integrity – Simplified, 2nd ed.*, Upper Saddle River, NJ: Prentice-Hall, 2009.

[12] T. L. Quarles, "The SPICE3 implementation guide," Univ. California, Berkeley, Tech. Rep., ERL-M89/44, 1989.

[13] J. Vlach and K. Singhal, *Computer Methods for Circuit Analysis and Design*, New York: Van Nostrand, 1983.

[14] A. V. Oppenheim and R. W. Schafer, *Discrete-Time Signal Processing*, Upper Saddle River, NJ: Prentice Hall, 1999.

[15] E. C. Levi, "Complex curve fitting," *IEEE Trans. Autom. Control*, vol. AC-4, no. 1, pp. 37-43, Jan. 1959.

[16] C. K. Sanathanan and J. Koerner, "Transfer function synthesis as a raio of two complex polynomials," *IEEE Trans. Autom. Control*, vol. AC-8, no. 1, pp. 56-58, Jan. 1963.

[17] M. Elzinga, K. L. Virga, L. Zhao, and J. L. Prince, "Pole-residue formulation for transient simulation of high-frequency interconnects using householder LS curve-fitting techniques," *IEEE Trans. Adv. Packag.*, vol. 25, no. 2, pp. 142-147, May 2000.

[18] S. -H. Min and M. Swaminathan, "Construction of broadband passive macromodels from frequency data for simulation of distributed interconnect networks," *IEEE Trans. Electromagn. Compat.*, vol. 46, no. 4, pp. 544-558, Nov. 2004.

[19] T. Noda, "Identification of a multiphase network equivalent for electromagnetic transient calculations using partitioned frequency response," *IEEE Trans. Power Del.*, vol. 20, no. 2, pp. 1134-1142, Apr. 2005.

[20] R. Gao, Y. S. Mekonnen, W. T. Beyene, "Orthonormal vector fitting: A robust macromodeling tool for rational approximation of frequency domain responses," *IEEE Trans. Adv. Packag.*, vol. 30, no. 2, pp. 216-225, May 2007.

[21] B. Gustavsen and A. Semlyen, "Rational approximation of frequency domain responses by vector fitting," *IEEE Trans. Power Del.*, vol. 14, no. 3, pp. 1052-1061, Jul. 1999.

[22] A. Semlyen and B. Gustavsen, "Vector fitting by pole relocation for the state equation approximation of nonrational transfer matrices," *Circuits Syst. Signal Process.*, vol. 19, no. 6, pp. 549-566, 2000.

[23] B. Gustavsen, "Computer code for rational approximation of frequency dependent admittance matrices," *IEEE Trans. Power Del.*, vol. 17, no. 4, pp. 1093-1098, Oct. 2002.

[24] D. Deschrijver, T. Dhaene, "Univariate rational macromodeling of high-speed passive components: A comparative study," *Applied Computatoinal Electromagnetics Society Journal*, vol. 20, no. 2, pp. 35-60, July 2005.

[25] B. Gustavsen, "Improving the pole relocating properties of vector fitting," *IEEE Trans. Power Del.*, vol. 21, no. 3, pp. 1587-1592, Jul. 2006.

[26] B. Gustavsen, "Relaxed vector fitting algorithm for rational approximation of frequency domain responses," in *Proc. 10th IEEE Workshop Signal Propagation Interconnects*, Berlin, Germany, May 9-12, pp. 97-100, 2006.

[27] D. Deschrijver, M. Mrozowski, T. Dhaene, and D. De Zutter, "Macromodeling of multiport systems using a fast implementation of the vector fitting method," *IEEE Microw., Wireless Compon. Lett.*, vol. 18, no. 6, pp. 383-385, Jun. 2008.

[28] D. Deschrijver, B. Haegeman, and T. Dhaene, "Orthonormal vector fitting: A robust macromodeling tool for rational approximation of frequency domain responses," *IEEE Trans. Adv. Packag.*, vol. 30, no. 2, pp. 216-225, May 2007.

[29] D. Deschrijver, B. Gustavsen, and T. Dhaene, "Advancements in iterative methods for rational approximation in the frequency domain," *IEEE Trans. Power Del.*, vol. 22, no. 3, pp. 1633-1642, Aug. 2007.

[30] W. Hendrickx and T. Dhane, "A discussion of "Rational approximation of frequency domain responses by vector fitting"," *IEEE Trans. Power Syst.*, vol.21, no. 1, pp. 441-443, Feb 2006.

[31] W. Hendrickx, D. Deschrijver, T. Dhaene, "Some remarks on the vector fitting iteration," in Post Conf. Proc. EMCI 2004, Mathematics in Industry, 2006, vol. 8, pp. 134-138.

[32] F. Ebert and T. Stykel, "Rational interpolation, minimal realization and model reduction," Tech. Rep. 371-2007, DFG Research Center MATHEON, 2007.

[33] I. Kocar, J. Mahseredjian, and G. Olivier, "Weighting method for transient analysis of underground cables," *IEEE Trans. Power Del.*, vol. 23, no. 3, pp. 1629-1635, Jul. 2008.

[34] D. Deschrijver, and T. Dhaene, "Rational fitting of S-parameter frequency samples with maximum absolute error control," *IEEE Microw., Wireless Compon. Lett.*, vol. 20, no. 5, pp. 247-249, May 2010.

[35] S. Grivet-Talocia, M. Bandinu, "Improving the convergence of vector fitting for equivalent circuit extraction from noisy frequency responses," *IEEE Trans. Electromagn. Compat*, vol. 48, no. 1, pp. 104-120, Feb. 2006.

[36] S. Grivet-Talocia, M. Bandinu, and F. Canavero, "An automatic algorithm for equivalent circuit extraction from noisy frequency responses," in *Proc. IEEE Int. Symp. EMC*, pp. 163-168, 2005.

[37] C. U. Lei, Y. Wang, Q. Chen and N. Wong, "On vector fitting methods in signal/power integrity applications," in *Lecture Notes in Engineering and Computer Science: Proc. International Multiconference of Engineers and Computer Scientists (IAENG IMECS-ICEE)*, pp. 1407-1412, Mar. 2010.

[38] C. U. Lei, Y. Wang, Q. Chen and N. Wong, "A decade of vector fitting development: application on signal/power integrity," *IAENG Transactions on Engineering Technologies*, vol 5, pp. 435-449, Oct. 2010.

[39] P. Triverio,"Self consistent, efficient and parametric macromodels for high-speed interconnects design" Ph.D. dissertation, Politecnico di Torino, Italy, 2009.

[40] P. Triverio, S. Grivet-Talocia, M. S. Nakhla, F. G. Canavero, and R. Achar, "Stability, causality, and passivity in electrical interconnect models," *IEEE Trans. Adv. Packag.*, vol. 30, pp. 795-808, Nov. 2007.

[41] A. H. Zemanian, "An N-port realizability theory based on the theory of distributions," *IEEE Trans. Circuit Theory*, vol. CT-10, pp. 265-274, Oct. 1963.

[42] B. D. O. Anderson and S. Vongpanitlerd, *Network Analysis and Synthesis: A Modern Systems Theory Approach*. Upper Saddle River, NJ: Prentice-Hall, 1973.

[43] D. C. Youla, L. J. Catriota, and H. J. Carlin, "Bounded real scattering matrices and the foundations of linear passive network theory," *IRE Trans. Circuit Theory*, vol. CT-6, pp. 102-124, Mar. 1959.

[44] E. J. Beltrami, "Linear dissipative systems, nonnegative definite distributional kernels, and the boundary values of boundary-real and positive-real matrices," *J. Math. Analysis Applic.*, vol. 19, pp. 231-246, 1967.

[45] H. A. Kramers, "La diffusion de la lumiere par les atoms," in *Collected Scientific Papers.* Amsterdam, The Netherlands: North-Holland, 1956.

[46] R. Krönig, "On the theory of dispersion of x-rays," *J. Opt. Soc. Amer.*, vol. 12, pp. 547-557, 1926.

[47] M. Kamon, M. J. Tsuk, and J. K. White, "FASTHENRY: A multipole-accelerated 3D inductance extraction program," *IEEE Trans. Microw., Theory Tech.*, vol. 42, no. 9, pp. 1750-1758, Sept. 1994.

[48] K. M. Coperich, J. Morsey, V. I. Okhmatovski, A. C. Cangellaris and A.E. Ruehli, "Systematic development of transmission-line models for interconnects with frequency-dependent losses," *IEEE Trans. Microw. Theory Tech.*, vol. 49, no. 10, pp. 1677-1685, Oct. 2001.

[49] K. M. Coperich, J. Morsey, A. C. Cangellaris, "Physically consistent transmission line models for high-speed interconnects in lossy dielectrics," *IEEE Trans. Adv. Packag.*, vol. 25, no. 2, May 2002.

[50] J.A. Stratton, *Electromagnetic Theory.* New York: McGraw-Hill, 1941.

[51] J. H. Chung, V. Okhamtovski, and A. C. Cangellaris, "A fast methodology for the synthesis of dispersive multi-port equivalent circuit model of multiple coupled bond wires," *Proc. IEEE 18th Topical Meeting on Electrical Performance of Electronic Packaging*, pp. 163-166, Oct. 2009.

[52] S. Grivet-Talocia, "On driving non-passive macromodels to instability," *International Journal of Circuit Theory and Applications*, vol. 37, no. 8, pp. 863-886, Jun. 2008.

[53] B. Gustavsen and A. Semlyen, "Enforcing passivity for admittance matrices approximated by rational functions," *IEEE Trans. Power Del.*, vol 16, no. 1, pp. 97-104, Feb. 2001.

[54] B. Gustavsen, "Fast passivity enforcement for pole-residue models by perturbation of residue matrix eigenvalues," *IEEE Trans. Power Del.*, vol 23, no. 4, pp. 2278-2285, Oct. 2008.

[55] B. Gustavsen, "Passivity enforcement of rational models via modal perturbation," *IEEE Trans. Power Del.*, vol. 23, no. 2, pp. 768-775, Apr. 2008.

[56] S. Moon and A.C. Cangellaris, "Passivity enforcement via quadratic programming for element-by-element rational function approximation of passive network matrices," *Proc. IEEE 17TH Topical Meeting on Electrical Performance of Electronic Packaging*, pp. 203-206. Oct. 2008.

[57] C. P. Coelho, J. R. Phillips, and L. M. Silveira, "A convex programming approach for generating guaranteed passive approximations to tabulated frequency-data," *IEEE Trans. Computer Aaided Design of Int. Circuits and Systems*, vol. 23, issue 2, pp. 293-301, Feb. 2004.

[58] D. Saraswat, R. Achar, and M. Nakhla "Global passivity enforcement algorithm for macromodels of interconnect subnetworks characterized by tabulated data," *IEEE Trans. Very Large Scale Integr. (VLSI) Syst.*, vol. 13, no. 7, Jul. 2005.

[59] S. Grivet-Talcia, "Passivity enforcement via perturbation of Hamiltonian matrices," *IEEE Trans. Circuits Syst. I, Reg. Papers*, vol. 51, no. 9, pp. 1755-1769, Sep. 2004.

[60] D. Saraswat, R. Achar, and M. S. Nakhla, "Fast passivity verification and enforcement via reciprocal systems for interconnects with large order macromodels," *IEEE Trans. Very Large Scale Integr. (VLSI) Syst*., vol. 15, no. 1, pp. 48-59, Jan. 2007.

[61] A. Lamecki and M. Mrozowski, "Equivalent SPICE circuits with guaranteed passivity from nonpassive models," *IEEE Trans. Microw. Theory Tech.*, vol. 55, no. 5, pp. 526-532, Mar. 2007.

[62] D. Deschrijver and T. Dhaene, "Fast passivity enforcement of S-parameter macromodels by pole perturbation," *IEEE Trans. Microw. Theory Tech.*, vol. 57, no. 3, Mar. 2009.

[63] T. Dhaene, D. Deschrijver, and N. Stevens, "Efficient algorithm for passivity enforcement of S-parameter based macromodels," *IEEE Trans. Microw. Theory Tech.*, vol. 57. no. 2, pp.415-420, Feb. 2009.

[64] D. Deschrijver and T. Dhaene, "DC-preserving passivity enforcement for S-parameter based macromodels," *IEEE Trans. Microw. Theory Tech.*, vol. 58, no 4, Apr. 2010.

[65] S. Grivet-Talocia and A. Ubolli, "Passivity enforcement with relative error control," *IEEE Trans. Microw. Theory Tech.*, vol. 55, no. 11, pp. 2374-2383, Nov. 2007.

[66] S. Grivet-Talocia and A. Ubolli, "A comparative study of passivity enforcement schemes for linear lumped macromodels," *IEEE Trans. Adv. Packag.*, vol. 31, no. 4, pp. 673-683, Nov. 2008.

[67] S. Grivet-Talocia, "On the generation of large passive macromodels for complex interconnect structures," *IEEE Trans. Adv. Packag*., vol. 29, no. 1, pp. 39-54, Feb. 2006.

[68] A. Chinea and S. Grivet-Talocia, "Perturbation schemes for passivity enforcement of delay-based transmission line macromodels," *IEEE Trans. Adv. Packag.*, vol. 31, no. 3, pp. 568-578, Aug. 2008.

[69] A. Y. Woo and A. C. Cangellaris, "Passive rational fitting of a network transfer function from its real part," *International Journal of RF and Maicrowave Computer-aided Engineering*, vol 18, no. 3 pp. 209-218, 2008.

[70] J. Morsey and A. C. Cangellaris, "Passive realization of interconnect models from measured data," *Proc. IEEE 10th Topical Meeting on Electrical Performance of Electronic Packaging*, pp. 47-50, 2001.

[71] S. Boyd, V. Balakrishnan, and P. Kabamba, "A bisection method for computing the H_∞ norm of a transfer matrix and related problems," *Math. Control, Signals, Syst.*, vol. 2, pp. 207-219, 1989.

[72] A. Semlyen and B. Gustavsen, "A half-size singularity test matrix for fast and reliable passivity assessment of rational models," *IEEE Trans. Power Delivery*, vol. 24, no. 1, Jan. 2009.

[73] E.-P, Li, E.-X. Liu, L.-W. Li, and M.-S. Leong, "A coupled efficient and systematic full-wave time-domain macromodeling and circuit simulation method for signal integrity analysis of high-speed interconnects," *IEEE Trans. Adv. Packag.*, vol. 27, no. 1, pp. 213-223, Feb. 2004.

[74] J. Schutt-Aine, J. Tan, and C. Kumar, "Use of Smith Chart to Compensate for Missing Data on Network Performance at Lower Frequency," patent application, October 2007.

[75] T. J. Brazil, "Causal-convolution – a new method for the transient analysis of linear systems at microwave frequencies," *IEEE Trans. Microw. Theory Tech*. vol. 43, no. 2, pp. 315-323, Feb. 1995.

[76] T. J. Brazil, "Accurate and efficient incorporation of frequency-domain data within linear and non-linear time-domain transient simulation," *Microwave Symposium Diget., 2005 IEEE MTTS International*, pp. 4, Jun. 2005.

[77] J. H. Chung and A. C. Cangellaris, "Causality enforcement in numerically or experimentally obtained microwave netowork transfer function," *GOMAC-Tech*, Reno, NV, Mar. 2010

[78] P. Triverio, and S. Grivet-Talocia, "Robust causality characterization via generalized dispersion relations," *IEEE Trans. Aadv. Packag.*, vol. 31, no. 3, Aug. 2008.

[79] R. Mandrekar, K. Srinivasan, E. Engin, and M. Swaminathan, "Causality enforcement in transient co-simulation of signal and power delivery networks," *IEEE Trans. Adv. Packag*., vol 30, no. 2 pp. 270-278, May 2007.

[80] J. Schutt-Aine, T. Jilin, C. Kumar, and F. Al-Hawari, "Blackbox macromodel with S-parameters and fast convolution," *Proc. 12th IEEE Workshop Signal Propag. Interconnects*, pp. 1-4 May 2008.

[81] S. N. Lalguldi, E. Engin, G. Casinovi, and M. Swaminathan, "Accurate transient simulation of interconnect characterized by band-limited data with propagation delay enforcement in a modified nodal analysis framework," *IEEE Trans. Electromag. Compatibility*, vol. 50, no. 3, pp. 715-729, Aug. 2008.

[82] S.-J. Moon and A. C. Cangellaris, "SPICE-compatible representation of S-parameter matrices of passive networks with transport delay," *Proc. IEEE 16th Topical Meeting on Electrical Performance of Electronic Packaging*, pp. 59-62, Oct. 2007.

[83] M. J. Choi and A. C. Cangellaris, "A quasi-three-dimensional distributed electromagnetic model for complex power distribution networks," *IEEE Trans. Adv. Packag.*, vol. 25, no. 1, pp. 28-34, Feb. 2002.

[84] D. Deschrijver and T. Dhaene, "Efficient GA-inspired macro-modeling of general LTI multi-port systems," *Proc. 8th IEEE Workshop Signal Propagation Interconnects*, pp. 95-98, 2004.

[85] D. Deschrijver and T. Dhaene, "Adaptive knot placement for rational spline interpolation of sparse EM-based data," *17th International Conference on Applied Electromagnetics and Communications (ICECOM)* pp. 433-436, 2003.

[86] S. Grivet-Talocia, "An adaptive sampling technique for passivity characterization and enforcement of large interconnect macromodels," *IEEE Trans. Adv. Packag*., vol. 30, no. 2, pp. 226-234, May 2007.

[87] D. Deschrijver, T. Dhaene, "Passivity-based sample selection and adaptive vector fitting algorithm for pole-residue modeling of sparse frequency-domain data," *Proc. IEEE Int. Conf. Behavioral Modeling Simulation (BMAS'2004)*, pp. 68-73, 2004.

[88] J. H. Chung and A. C. Cangellaris, "Accuracy-preserving adaptive sampling of broadband electromagnetic spectra of interconnect structures," *Proc. IEEE 17th Topical Meeting on Electrical Performance of Electronic Packaging*, pp. 335-338, Oct. 2008.

[89] F. M. Tesche, A. W. Kalin, M. Nyffeler and B. R. Brandli, "Representation of wide-band EMC spectra using an adaptive, non-uniform sampling scheme," *Proc. of the 13th International Zurich Symposium on EMC*, Zurich, Switzerland, Mar. 1997.

[90] W. Blumer and W. Johl, "Coupling to transmission line systems: Theoretical background and TLS code," *Supplement to the Proceedings of the 11th International Zurich Symposium on EMC*, Zurich, Switzerland, March 7-9, 1995.

[91] Y. S. Mekonnen, J. E. Schutt-Aine, J. Tan, C. Kumar, and D. Milosevic, "Combining rational interpolation with the vector fitting method," *Proceedings of IEEE 14th Topical Meeting on Electrical Performance of Electrical Packaging*, pp. 51-54, Oct. 2005.

[92] S-H. Min, H. Lee, E. Song, Y-S. Choi, T-J. Cho, S-Y. Kang, S-Y. Oh, and M. Swaminathan,"Moder-order estimation and reduction of distributed interconnects via improved vector fitting," *Proc. IEEE 14th Topical Meeting on Electrical Performance of Electronic Packaging*

[93] D. Deschrijver, B. Gustavsen and T. Dhaene, "Fast broadband modeling of frequency-domain responses by piecewise interpolation," *Electric Power Systems Research,* vol. 79, no. 11, pp. 1574-1578, 2009.

[94] D. Deschrijver, B. Gustavsen, T. Dhaene, "Fast algorithm for broadband macromodeling of high-order frequency responses,"*15th IEEE Mediterranean Electrotechnical Conference*, Valletta (Malta), pp. 359-362, April 2010.

[95] J. H. Chung and A. C. Cangellaris, "Fast rational function fitting of broadband multi-port responses via repeated random sampling," *Proc. IEEE 20th Topical Meeting on Electrical Performance of Electronic Packaging and Systems*, pp. 49-52, Oct. 2011.

[96] G. H. Golub and C. F. Van Loan, *Matrix Computations*, 3rd ed. London, U.K. : The Johns Hopkins University Press, 1996.

[97] A. Chinea, S. Grivet-Talocia, "On the parallelization of vector fitting algorithms," *IEEE Trans. on Componen. Packag. Manufac. Tech.*, vol. 1, no. 11, Nov. 2011, pp. 1761-1773.

[98] D. Bellan, S.A. Pignari, G. Spadacini, "Characterisation of crosstalk in terms of mean value and standard deviation," *IEE Proc.-Sci. Meas. Technol.*, vol. 150, no. 6, pp. 289-295, Nov. 2003.

[99] Q. Zhang, J. J. Liou, J. McMacken, J. Thomson, P. Layman, "Development of robust interconnect model based on design of experiments and multiobjective optimization," *IEEE Trans. Electron Devices*, vol. 48, no. 9, pp. 1885 – 1891, Sep. 2001.

[100] E. Matoglu, N. Pham, D. N. de Araujo, M. Cases, and M. Swaminathan, "Statistical signal integrity analysis and diagnosis methodology for high-speed systems," *IEEE Trans. Adv. Packag.*, vol. 27, no. 4, pp. 611-629, Nov. 2004.

[101] M. D. Morris and T. J. Mitchell, "Exploratory designs for computer experiments," *J. Stat. Plann. Inference*, no. 43, 381-402.

[102] A. A. Giunta, S. F. Wojtkiewicz, and M. S. Eldred, "Overview of modern design of experiments methods for computational simulations," Forty-first AIAA Aerospace Sciences Meeting and Exhibit, Reno, NV, 6-9 Jan. 2003; AIAA – 2003-0649.

[103] P. Manfredi, M. Fontana, I.S. Stievano, and F. G. Canavero, "Comparison of stochastic methods for the variability assessment of technology parameters," *Radio Science,* vol. 47, pp.1-8, 2012.

[104] I. S. Stievano, P. Manfredi, and F. G. Canavero, "Parameters variability effects on multiconductor interconnects via hermite polynomial chaos," *IEEE Trans. Comp. Pack. Man. Tech.*, vol. 1, no. 8, pp. 1234-1239, Aug. 2011.

[105]P. Manfredi, I. S. Stievano, F. G. Canavero, "Stochastic evaluation of parameters variability on a terminated signal bus," *Proc. 10th Int. Symp. on Electromag. Compat.*, 2011, pp. 362-367, Sep. 2011.

[106] I. S. Stievano, P. Manfredi, and F. G. Canavero, "Stochastic analyis of multiconductor cables and interconnects," *IEEE Trans. Electromagn. Compat.*, vol. 53, no. 2, pp. 501-507, May 2011.

[107] I. S. Stievano, P. Manfredi, and F. G. Canavero, "Parameters variability effects on multiconductor interconnects via hermite polynomial chaos," *IEEE Trans. on Comp. Pack. & Man. Tech.*, vol. 1, no. 8, pp. 1234-1239, Aug. 2011.

[108] P. Manfredi, I. S. Stievano, and F. G. Canavero, "Transient analysis of PCB lines with the inclusion of parameters uncertainties," in *Proc. IEEE Int. Symp. Electromagn. Compat.*, Aug. 2011, pp. 146-149.

[109] P. Manfredi, I. S. Stievano, and F. G. Canavero, "Alternative SPICE implentation of circuit uncertianties based on orthogonal polynomials," in *Proc. IEEE 20th Conf. Electr. Perform. Electron. Pack. Sys.*, Oct. 2011, pp. 41-44.

[110] P. Manfredi, I. S. Stievano, F. G. Canavero, "Time- and frequency-domain evaluation of stochastic parameters on signal lines," in *Adv. Electromag. Symp. AES 2012*, 16-19 Apr. 2012.

[111] D. Xiu, "Fast numerical methods for stochastic computations: A Review," *Commum. Comput. Phys.*, vol. 5, pp. 242-272, Feb. 2009.

[112] D. Xiu and J. S. Hesthaven, "Higher order collocation methods for differential equations with random inputs," *SIAM J. Scientific Computing*, vol. 27, pp. 1118-1139, 2005.

[113] J. H. Chung and A. C. Cangellaris, "Fast assessment of the impact of surrounding wiring on the transmission properties of high-speed interconnect channels," in *Proc. IEEE 21st Conf. Electr. Perform. Electron. Pack. Sys.*, Oct. 2012, pp. 69-72.

[114] M. S. Eldred, "Recent advances in non-intrusive polynomial-chaos and stochastic collocation methods for uncertainty analysis and design," in *Proc. 50th AIAA/ASME/ASCE/AHS/ASC Struct., Structural Dynam., Mat. Conf.*, Palm Springs, CA, May 2009, Art. ID AIAA, pp. 2009-2274.

[115] M.S. Eldred, J. Burkardt, "Comparison of non-intrusive polynomial chaos and stochastic collocation methods for uncertainty quantification," AIAA Paper 2009-0976, 2009; 1-20.

[116] J. d S. Azevedo, S. P. Oliveira, "A numerical comparison between quasi-Monte Carlo and sparse grid stochstic collocation methods," *Commun. Comput. Phys.*, vol. 10, pp. 1-19, Sep. 2011.

[117] A. Rong, A. C. Cangellaris, "Interconnect transient simulation in the presence of layout and routing uncertainty," *Proc. 19th IEEE Conf. Electri. Perfor. Electron. Pack. Sys.*, pp. 157-160, Oct. 2011.

[118] P. Sumant, H. Wu, and A. C. Cangellaris, "Reduced-order models of finite element approximations of electromagnetic devices exhibiting statistical variability," *IEEE Trans. Antennas Propagat.*, vol. 60, no. 1, pp. 301-309, Jan. 2012.

[119] F. Ferranti, L Knockaert, and T. Dhaene, "Parameterized S-parameter based macromodeling with guaranteed passivity," *IEEE Microw. Wireless Componon. Lett.*, vol. 19, no 10, pp. 608-610, Oct. 2009.

[120] F. Ferranti, L. Knockaert, and T. Dhaene, "Guaranteed passive parameterized admittance-based macromodeling," *IEEE Trans. Adv. Packag.*, vol. 33, pp. 623-629, Aug. 2010.

[121] F. Ferranti, G. Antonini, T. Dhaene, and L. Knockaeret, "Parametric macromodeling of lossy and dispersive multiconductor transmission lines," *IEEE Trans. Adv. Packag.*, vol. 33, no. 2, pp. 481-491, May 2010.

[122] F. Ferranti, L. Knockaert, T. Dhaene, and G. Antonini, "Parametric macromodeling for S-parameter data based on internal nonexpansivity," *Int. J. Numer. Model.* vol. 25, pp. 1-13, Feb. 2012.

[123] P. Triverio, S. Grivet-Talocis, and M. S. Nakhla, "A parameterized macromodeling strategy with uniform stability test," *IEEE Trans. Adv. Packag.*, vol. 32, pp. 205-215, Feb. 2009.

[124] G. Allasia, "A class of interpolating positive linear operators: Theoretical and computational aspects," in *Recent Developments in Approximation Theory, Wavelets and Applications*, S. P. Singh, Ed. Norwell, MA: Kluwer, 1995, pp. 1-36.

[125] F. Ferranti, L. Knockaert, T. Dhaene, and G. Antonini, "Passivity-preserving parametric macromodeling for highly dynamic tabulated data based on lur'e equations," *IEEE Trans. Microw. Theory Tech.*, vol. 58, no. 12, pp. 3688-3696, Dec. 2010.

[126] T. Dhaene, D. Deschrijver, "Stable parametric macromodeling using a recursive implementation of the vector fitting algorithm," *IEEE Microwave and Wireless Components Letters*, vol. 19, no. 2, pp. 59-61, Feb. 2009.

[127] F. Ferranti, D. Deschrijver, L. Knockaert and T. Dhaene, "Hybrid algorithm for compact and stable macromodeling of parameterized frequency responses," *Electron. Lett.*, vol. 45, no. 10, pp. 493-495, may 2009.

[128] G.-H. Shiue, W.-D. Guo, C.-M. Lin, and R.-B. Wu, "Noise reduction using compensation capacitance for bend discontinuities of differential transmission lines," *IEEE Trans. Adv. Packag.*, vol. 29, no. 3, pp. 560-569, Aug. 2006.

[129]D. Bockelman and W. R. Einsenstadt, "Combined differential and common-mode scattering parameters: Theory and simulation," *IEEE Trans. Microw. Theory Tech.*, vol. 43, no. 7, pp. 1530-1539, Jul. 1995.

[130] F. Xiao and Y. Kami, "Modeling and analysis of crosstalk between differential lines in high-speed interconnects," *PIERS Online*, vol. 3, no. 8, 1293-1297, 2007.

[131] Q3D Extractor, Ansoft Corp, Pittsburgh, PA, www.ansoft.com.